7-10-2013

Using oxygen and carbon stable isotopes, 53Mn-53Cr isotope systematics, and petrology to constrain the history of carbonates and water in the CR and CM chondrite parent bodies

Mark Tyra

Recommended Citation

Tyra, Mark. "Using oxygen and carbon stable isotopes, 53Mn-53Cr isotope systematics, and petrology to constrain the history of carbonates and water in the CR and CM chondrite parent bodies." (2013). https://digitalrepository.unm.edu/eps_etds/93

Mark Anthony Tyra
Candidate

Earth and Planetary Sciences
Department

This dissertation is approved, and it is acceptable in quality and form for publication:

Approved by the Dissertation Committee:

Adrian J. Brearley , Chairperson

Ian D. Hutcheon

Rhian H. Jones

Zachary D. Sharp

Charles K. Shearer

USING OXYGEN AND CARBON STABLE ISOTOPES, 53MN-53CR ISOTOPE SYSTEMATICS, AND PETROLOGY TO CONSTRAIN THE HISTORY OF CARBONATES AND WATER IN THE CR AND CM CHONDRITE PARENT BODIES

by

MARK ANTHONY TYRA

B.S., Geology, University of Kentucky, 2000
M.S., Geology, University of Maryland, 2005

DISSERTATION

Submitted in Partial Fulfillment of the
Requirements for the Degree of

Doctor of Philosophy in
Earth and Planetary Sciences

The University of New Mexico
Albuquerque, New Mexico

May, 2013

DEDICATION

Education, on the other hand, means emancipation. It means light and liberty. It means the uplifting of the soul of man into the glorious light of truth, the light only by which men can be free. To deny education to any people is one of the greatest crimes against human nature. It is to deny them the means of freedom and the rightful pursuit of happiness, and to defeat the very end of their being. –Frederick Douglass

ACKNOWLEDGEMENTS

This work is the direct result of many people who have lent their support. I first would like to thank my dissertation advisor, Dr. Adrian Brearley. His support, challenges, conversations, insight, and guidance have helped my growth as a writer and a scientist. I consider him both a mentor and a friend.

I also wish to thank my dissertation committee Drs. Ian Hutcheon, Rhian Jones, Charles Shearer, and Zachary Sharp for their advice, feedback, and discussion.

I also am grateful for the support of Drs. Benjamin Jacobson, Jennifer Matzel, Erick Ramon, and Peter Weber at Lawrence Livermore National Laboratory for their support and ideas. Similarly, the support of Dr. Yunbin Guan at the California Institute of Technology Center for Microanalysis was essential for much of the work presented here.

At the University of New Mexico, I would like to express my sincere thanks to friends and colleges who helped in a myriad of ways. This includes Dr. Mike Spilde and Ara Kooser at the EPS Electron Microbeam Facility and Drs. Ying-Bing Jiang, Shenghong Huang, and Corentin Le Guillou in the TEM lab. Furthermore, support from the administrative staff, Mary Bennett, Mabel Chavez, Cindy Jaramillo, and Paula Pascetti, has been essential during my stay here. I also am grateful for the many colleagues and friends at the E&PS department who have helped in so many ways.

I also must acknowledge my friends and family for all that they have done. I am also grateful for my parents and brother, who love a good argument, a good story, and have supported me in uncounted ways. Lastly I would like thank my wife Jennifer for her support, patience, and love throughout this process. Her support underlies every phrase in this work.

PREFACE

This work is primarily the work of the author. Each chapter, however, is the culmination of work of multiple workers and will be submitted to professional journals as multi-author works. As requested by the Department of Earth and Planetary Sciences, the input of each additional worker is noted below.

Chapter 1 will be submitted as a paper with A. J. Brearley[1], J. Matzel[2], I. D. Hutcheon[2], and E. Ramon[2] as coauthors. A.J. Brearley provided data interpretation, funding, and editing. J. Matzel and E. Ramon collected NanoSIMS data and provided data interpretation. I.D. Hutcheon provided funding, editing, and data interpretation.

Chapter 2 will be submitted for publication along with coauthors A. J. Brearley[1], J. Matzel[2], and I. D. Hutcheon[2]. A.J. Brearley helped design and fund the project, provided data interpretation, and edited the manuscript. J. Matzel helped collect Mn-Cr data, provided data interpretation, and edited the manuscript. I. D. Hutcheon provided funding, ideas, and editorial handling.

Chapter 3 will be submitted to a journal as a multi-author paper. Adrian Brearley[1] secured funding and edited this work. Yunbin Guan[3] provided guidance and helped acquire isotope data using SIMS.

Chapter 4 coauthors include Adrian Brearley[1], who provided ideas, editing, and support, and Yunbin Guan[3], who provided SIMS data and interpretation.

[1] *Dept. of Earth and Planetary Sciences, University of New Mexico, Albuquerque, NM 87131, USA (matyra@unm.edu),* [2] *Glenn T. Seaborg Institute, Chemical Sciences Division, Lawrence Livermore National Laboratory, Livermore, CA 94551.* [3] *Division of Geological and Planetary Sciences, California Institute of Technology, Pasadena, CA 91125*

USING OXYGEN AND CARBON STABLE ISOTOPES, ^{53}MN-^{53}CR ISOTOPE SYSTEMATICS, AND PETROLOGY TO CONSTRAIN THE HISTORY OF CARBONATES AND WATER IN THE CM AND CR CHONDRITE PARENT BODIES

by

Mark Anthony Tyra

B.S., Geology, University of Kentucky, 2000

M.S., Geology, University of Maryland, 2005

Doctor of Philosophy in Earth and Planetary Sciences

University of New Mexico, May 2013

ABSTRACT

I carried out a petrologic and Mn-Cr isotopic study of carbonates in the paired CM1 chondrites, ALH 84049 and ALH 84051, in an effort to understand the origin and chronology of formation of carbonates in the most heavily altered CM chondrites. Dolomite is strongly compositionally zoned (Ca, Mg, Fe, Mn), indicating very heterogeneous formation conditions, yet all carbonate Mn-Cr analyses form individual isochrons. In this study, I also analyzed the Mn-Cr isotope systematics of the CR1 chondrite GRO 95577 and determined that siderite is the youngest secondary mineral yet observed in carbonaceous chondrites. This has implications for the CR parent body as it either was large enough to retain heat for long periods of time or was heated by impact after most aqueous alteration in carbonaceous chondrites had ceased. This study also presents analyses of carbonates in the same samples (ALH 84049 and GRO 95577) in-situ for their oxygen, and, in ALH 84049, carbon isotope composition to constrain aqueous alteration. The results show that multiple generations of carbonates must have occurred in ALH 84049 from a carbon source with either heterogeneous carbon isotopes or with changing carbon isotope compositions from ongoing methane formation. Furthermore, in GRO 95577, the oxygen isotope values suggest that calcite precipitated before siderite if CR chondrite fluids followed a closed system oxygen isotope evolution path similar to CM chondrites.

TABLE OF CONTENTS

CHAPTER 2. Very late timing of CR1 GRO 95577 aqueous alteration: a NanoSIMS ^{53}Mn-^{53}Cr study of siderite……………………………………………………..83

CHAPTER 3. Distinct C and O Isotope Compositions Show Carbonate Precipitation Was Episodic in the CM Chondrite ALH 84049: An Ion Microprobe Analysis

CHAPTER 4. Siderite and calcite oxygen isotope composition in CR1 chondrite GRO 95577: a SIMS approach

CHAPTER 1

Origin and chronology of formation of carbonates in the most heavily altered CM chondrites

1 ABSTRACT

We have carried out a petrologic and Mn-Cr isotopic study of carbonates in the paired CM1 chondrites, ALH 84049 and ALH 84051 in an effort to understand the origin and chronology of formation of carbonates in the most heavily altered CM chondrites. Both meteorites contain calcite and dolomite grains (grains of both minerals are 10-50μm in size) with morphologies and textural occurrences similar to those described in ALH 84034 and ALH 83100; all four meteorites are paired. In addition, ALH 84051 contains large (up to 400 μm) dolomite aggregates and distinct crosscutting veins of disseminated dolomite that extend for lengths of up to ~1cm as observed within the thin section. Almost all dolomite grains in both samples show extensive chemical zoning in $CaCO_3$, $MgCO_3$, $MnCO_3$, and $FeCO_3$ (intragrain variability up to ~5 mol%). This zoning is patchy and complex; some grains, for example, have Fe-rich cores while the opposite is observed in other grains. Nevertheless, linear covariance of the major cations indicates that the carbonates precipitated from a single evolving fluid or dissolution – reprecipitation buffered fluid. The Mn-Cr isotopic compositions of several dolomite grains measured by NanoSIMS give a $(^{53}Mn/^{55}Mn)_o$ of $(3.35 \pm 0.74) \times 10^{-6}$ (2σ) for ALH 84049 and $(4.68 \pm 1.22) \times 10^{-6}$ (2σ) for ALH 84051.These findings suggest the rapid chemical evolution of water and that carbonate precipitated within a ≤ 4 million-year timespan. These ages, along with Mn-Cr carbonate ages previously reported in other CM1 and CM2 chondrites, are consistent with dolomite precipitation in one event throughout the CM parent body.

2 INTRODUCTION

Chondritic meteorites record processes that occurred during the earliest stages of Solar System history. This record extends from the formation of the first solids at high temperatures to processes where solids interacted with volatile compounds such as water at low temperatures. The importance of water in the cosmochemical evolution of chondritic meteorites has been widely recognized, and the effects of the interaction of aqueous fluids on chondritic meteorites continue to be an important area of research

(Brearley, 2006; Krot et al., 2006; Rubin et al., 2007). During alteration, water reacted with primary mineral phases and also acted as a mass transfer agent (Brearley, 2006; Zolensky et al., 2008). Despite efforts to understand the role of water in the alteration of chondrites, a number of questions remain. These include learning if alteration was a single event, episodic, or prolonged; how temperature changed during alteration; if alteration occurred in an open or closed system; and whether brecciation occurred before, during, or after alteration. Simply put, knowing the mechanisms and timing of water activity on meteorite parent bodies is essential to establish a full understanding of early Solar System history.

CM chondrites are composed of chondrules and refractory inclusions that formed at high temperatures, embedded in a hydrated, fine-grained matrix (Brearley and Jones, 1998). Following the classification scheme of van Schmus and Wood (1967), CM chondrites range from heterogeneously hydrated (petrologic type 2) to completely hydrated (petrologic type 1) (Zolensky et al., 1997; Clayton and Mayeda, 1999). CM1 chondrites rank among the most aqueously altered types of chondrites, where almost all primary phases have been replaced by phyllosilicates, magnetite, carbonates, and other secondary phases (Browning et al., 1996; Zolensky et al., 1997; Krot et al., 2005; Rubin et al., 2007).

CM1 chondrites may represent the end of a continuum of progressive alteration from CM2s to CM1s (e.g., Zolensky et al., 1997; Rubin et al., 2007). This implies a genetic relationship between the two meteorite subgroups. Botta et al. (2007) used amino acid abundances to show that CM1 chondrites share more affinities with CM2 chondrites than with CI1 chondrites. The authors note, however, that CM1 chondrites contain lower concentrations of amino acids than CM2 chondrites and that one, LAP 02277, has a unique amino acid profile. Additionally, petrographic, isotopic, and extracted amino-acid compositional constraints imply that CM1 chondrites experienced a different alteration history than CM2 chondrites. For example, Zolensky et al. (1997) calculate that CM1 chondrites had water/rock ratios akin to the least-altered CM2s, and stand apart from the most-altered CM2s. Furthermore, Glavin et al. (2006) note that amino acid profiles in ALH 83100, which is paired with the chondrites studied here, are “strikingly different” enough to be consistent with CM1 chondrites being from a different parent body than CM2 chondrites.

Carbonate mineral populations also reflect a difference between CM1 and CM2 chondrites, both in terms of carbonate type and, potentially, in abundance. The principal carbonate phases in CM chondrites are calcite and dolomite; minor carbonate phases include aragonite and breunnerite (Fuchs et al., 1973; Bunch and Chang, 1980; Llorca and Brearley, 1992; Zolensky et al., 1997; Rubin et al., 2007; Lee et al., 2012). Most CM chondrites are moderately altered and only contain calcite (Rubin et al., 2007). More altered CM chondrites have a progressively complicated carbonate mineralogy. For example, the highly-altered CM2 sample QUE 93005 contains calcite, breunnerite, and two varieties of dolomite (Lee et al., 2012). In addition, some studies suggest that the abundance of carbonate minerals in CM2 chondrites increases with their degree of alteration (Grady et al., 1988; Zolensky et al., 1997). These trends, however, are not supported by more recent work (Benedix et al., 2003; de Leuw et al., 2010): in particular, Benedix et al., 2003 note that CO_2 yields from acid reactions in multiple aliquots of Murchison (CM2) show significant modal variability within a single meteorite (Benedix et al., 2003). Reports of possible trends in carbonate abundance with increasing degrees of alteration, therefore, must be treated with caution.

In this study, we focus on the textural, mineralogic and Mn-Cr isotopic systematics of carbonates in the paired CM1 chondrites ALH 84049 and ALH 84051 to constrain the processes and timing of aqueous alteration that have affected the CM1 chondrites. Our goals are (1) to determine the chemical variability in CM1 carbonates and use these data to constrain the behavior of fluids in the CM1 parent body and (2) to determine the chronology of carbonate formation. This study builds on previous carbonate Mn-Cr studies in the CM1 chondrites ALH 84034 and ALH 83100 which are paired with the samples studied here (Brearley and Hutcheon, 2000; Krot et al., 2006; de Leuw et al., 2009; Fujiya et al., 2012). CM chondrites are complex breccias that contain clasts of intimately mixed CM material with different histories (e.g. Metzler et al., 1992). Therefore, paired samples may superficially appear to share similarities but in detail consist of a diverse sampling of materials. Although the original spatial relationship between individual samples in a pairing are unknown, analyzing the set as a whole provides a more comprehensive view of carbonate history within the CM parent body.

3 SAMPLES AND METHODS

3.1 Samples

Mineralogic, petrographic, and isotopic studies were carried out on two 1-inch polished petrographic thin sections of CM1 chondrites ALH84049 (weathering grade Ae, fracturing grade B) and ALH 84051 (weathering grade A/Be, fracturing grade B) (Score and Lindstrom, 1990). Both are paired with ALH 83100 and were provided by the Antarctic Meteorite Working Group from the Antarctic Meteorite Collection at NASA Johnson Space Center. The studied meteorites were listed as CM 1/2 chondrites by Score and Lindstrom (1990). However, Llorca and Brearley (1992) showed that ALH 84034 (also paired with ALH 83100) is completely hydrated and consistent with a CM1 classification. Although rare fragmented olivine grains can be found, out of hundreds of chondrule pseudomorphs, only two in ALH 84049 and one in ALH 84051 retain original olivine. Therefore, both ALH 84049 and ALH 84051 can be considered CM1 chondrites.

Rubin et al. (2007) classified CM chondrites according to degree of alteration; they did not follow the van Schmus and Wood (1967) classification where fully-hydrated meteorites are designated as petrologic type 1. In the Rubin et al. scheme, hypothetical petrologic type 3.0 chondrites represent the least altered chondrites and increasing aqueous alteration is denoted by progressively decreasing numbers. Fully hydrated CMs are classified as 2.0. Existing CM2 chondrites range from petrologic type 2.1 to 2.6. Although the Rubin et al. (2007) classification proposes useful criteria for distinguishing between CM chondrites with different degrees of alteration, we think that the type 1 designation for fully altered chondrites remains useful. Van Schmus and Wood (1967) define diagnostic properties of type 1 chondrites by '*their lack of chondrules and high volatile contents; the meteorite consists wholly of very fine-grained material.'* Although pseudomorphs of relict grains remain in CM1s, large anhydrous grains in chondrules have now been replaced by serpentines of variable composition. Also, the designation of completely hydrated chondrites as petrologic type 2.0 chondrites is inconsistent with one of the major criteria used by van Schmus and Wood (1967); specifically a type 2 chondrite has '*olivine and pyroxene of widely variable composition.*' These phases are essentially absent in CM1 chondrites. We therefore retain the type 1 designation for the

CM chondrites and follow the original identification and classification of meteorites with these characteristics by Zolensky et al. (1997).

3.2 Analytical Methods

3.2.1 Petrographic analyses

Petrographic studies to locate and characterize carbonates were carried out by optical microscopy, scanning electron microscopy (SEM), and electron microprobe analysis. We created full photographic mosaics of each thin section by optical microscopy in plane-polarized light, cross-polarized light, and reflected light. To construct the mosaics, individual images were stitched together using the Hugin [Sourceforge] panoramic software package. The stitched montages were then pegged in ArcGIS to a flat-scanned image to remove distortion that may have occurred during stitching. These images, particularly the cross-polarized images, are useful to identify carbonate grains. In crossed-polarized light, carbonates have high order birefringence colors and are far brighter than surrounding phyllosilicates.

After locating carbonates with the optical images, individual grains were characterized by backscattered electron (BSE) imaging. We used a JEOL 5800LV scanning electron microscope (SEM), operating in high vacuum mode at an accelerating voltage of 20 kV. Carbonate phases were identified by qualitative X-ray analyses using an Oxford Instruments ISIS 200 energy dispersive X-ray (EDS) analysis system. Cathodoluminescence (CL) images of carbonate grains were also obtained in the SEM using an Oxford Instruments CL detector. Cathodoluminescence imaging was carried out at an accelerating voltage of 10kV, at a working distance Z = 15.5 mm, and with a variable detector gain that depended upon grain response. Due to the slow rate of decay of cathodoluminscence in carbonates, 1600-to-3200 μs/pixel dwell times were used during image collection to avoid ghosting in the CL images. The CL response of carbonate grains is sensitive to subtle compositional variations and is a useful qualitative technique for identifying fine scale minor and trace element zoning within carbonates (Brearley, 1998; Brearley et al., 1999).

We determined carbonate modal abundance at a 2 µm pixel resolution using a FEI Quanta 3D Field Emission Gun SEM/Focused Ion Beam (FIB) instrument. Each thin section was mapped using full X-ray spectral imaging with an EDAX Apollo 40 SDD EDS. Instrumental operating conditions for the X-ray maps were 30kV accelerating voltage and a 23 nA beam current, conditions that provided X-ray count rates exceeding 100,000 cps. Dead time was ~30% for ALH 84054 and ~25% for ALH 84049. Each thin section X-ray map consists of multiple images taken at 165X at 2.2 μm/pixel resolution with an X-ray dwell time of 200 μs and 2 frames per X-ray map. For ALH 84049, 56 individual maps were taken and stitched. For ALH 84051, 88 maps were taken and stitched.

A JEOL 8200 Superprobe Electron Probe Micro-analyzer (EPMA) was used to create semi-quantitative X-ray maps and spot analyses of individual calcite and dolomite grains in ALH 84051 and ALH 84049. This instrument is located within the University of New Mexico EPS/IOM Electron Microbeam Facility and is equipped with five wavelength dispersive spectrometers (WDS). Standards used for elemental calibration for the quantitative analyses and X-ray maps were dolomite (Ca, Mg), siderite (Fe), celestite (Sr), and spessartine (Si, Mn). All X-ray maps and individual quantitative analyses were performed with a 1-2 μm spot size, 20 nA beam current and an accelerating voltage of 15 kV.

Multiple EPMA spot analyses were performed in each carbonate grain (~1:45 minutes per spot). In ALH 84049, 116 spots from 13 dolomite grains were used after discarding analyses that overlapped with adjacent phases as indicated by Si contents. Any analysis with > 1 wt% SiO_2 was discarded. In ALH 84051, 149 spots from 14 dolomite and 2 calcite grains were used and 62 spots discarded. The following detection limits were attained: 0.01wt% (Ca), 0.03wt% (Mg), 0.01 (Fe), 0.01 wt% (Sr), 0.02wt% (Si), and 0.01wt% (Mn) after ZAF correction.

We found that the analytical conditions for EPMA spot analyses (15 kV, 20 nA) of dolomite resulted in considerable damage (pits and halos coincident with electron beam interaction volume damage and carbonate decomposition). We had chosen these conditions to ensure accurate analyses of Fe and Mn, both elements which are important to this study. In sample ALH 84051, this electron beam damage affected the later NanoSIMS analyses, because damaged areas exhibited enhanced sputtering rates possibly due to decarbonization. Although NanoSIMS-measured Mn/Cr ratios in beam-damaged regions are within the range of values obtained from adjacent undamaged areas, we chose to avoid carrying out EPMA spot analyses prior to NanoSIMS studies for ALH 84049. Instead, a combination of CL imaging and X-ray mapping (25 ms dwell time/pixel) were used to characterize carbonates before NanoSIMS analyses. Only after NanoSIMS analysis was completed did we perform the EPMA spot analyses of dolomite in sample ALH 84049.

X-ray maps of Ca, Mg, Mn, Fe, Sr, and Si were obtained for individual carbonate grains using WDS spectrometers in order to provide details of the compositional zoning observed in CL images. Although Si is not present in the carbonate, X-ray maps of Si were used to determine the locations of inclusions and the edges of carbonate grains. The combination of CL images and EPMA X-ray maps was used to select grains or large areas within grains with the highest Mn concentrations for Mn-Cr analyses by NanoSIMS.

3.2.2 NanoSIMS analyses

Isotopic studies of the dolomite grains were carried out using the NanoSIMS 50 ion microprobe at Lawrence Livermore National Laboratory (LLNL) during two sessions 8 months apart. Conditions in the primary column changed over time and led to slight changes in operating conditions between the two sessions. During the first session, secondary ion images were collected by rastering a 90 pA $^{16}O^-$ beam over 15-50 μm^2 areas. Positive secondary ions were acquired by combining multicollection with magnetic field peak-jumping: In one magnetic field, five electron multipliers collected $^{26}Mg^+$, $^{28}Si^+$, $^{44}Ca^+$, $^{52}Cr^+$, and $^{55}Mn^+$ counts, and then the field parameters were changed to collect $^{53}Cr^+$ and $^{56}Fe^+$. Measured secondary ion intensities were next corrected for background and counting-system dead time. The corrected $^{55}Mn/^{53}Cr$ ratios were converted to atomic ratios using a relative sensitivity factor of 1.12 determined from repeated measurements of San Carlos olivine standard. A mass resolving power of ~3600 was attained during the analysis of three dolomite grains in ALH 84051 in this session.

Because the primary beam ion optics had deteriorated slightly, for the second session a lower primary beam current of 70 pA was used to attain a measured beam size of 400-500 nm. The same ion species were measured, with similar corrections, and the relative sensitivity factor was calculated to be 1.08. The calculated mass resolving power was ~3600, sufficient to resolve potential interferences. This session included two replicate analyses of areas analyzed in the prior session, four additional dolomite grains from ALH 84051, and seven from ALH 84049.

Isochrons were constructed by plotting measured ^{55}Mn/^{52}Cr vs. ^{53}Cr/^{52}Cr. We used Williamson weighted least-square methodology to determine regressions (in both x and y axis) in the NanoSIMS data (e.g. Ogren and Norton, 1992). The L'Image software package (written by L. Nittler) was used to view isotope ratio images, define regions of interest (ROIs), and quantify data within these ROIs. As data were obtained in raster mode, ROIs were determined graphically (using L'Image) by binning different ^{55}Mn/^{52}Cr values. For example, the examined area of grain 13-b2 of ALH 84049 was divided into four ROIs, the first with ^{55}Mn/^{52}Cr ranging from 0 to 5000, the second from 5000 to 10000, the third from 10000 to 15000 and the fourth encompassed all data greater than 15000, which in this case averaged about 40000 (see Table 1 in the Results). ROIs with small areas contain fewer counts and therefore also have higher errors, which explain larger errors reported for the higher ^{55}Mn/^{52}Cr ratio ROIs. The software allowed data from sub-micrometer inclusions to be excluded, which removed high Cr areas and increased the observed spread in ^{55}Mn/^{52}Cr ratios. The approach using the NanoSIMS and L'Image to determine ROIs allows us to select a very wide range of Mn/Cr ratios, much larger than with conventional SIMS, and this is an advantage of the NanoSIMS technique.

Grains were selected for NanoSIMS analysis based on several criteria. Large grains were preferred (>50 μm) as they provided more area to analyze and were easier to locate. We chose grains that had a range of Mn concentrations (zoning) which could allow a large spread in Mn/Cr ratios. We also sampled carbonates with different morphologies or from different textural environments for comparison. In ALH 84051, three vein carbonates, 2 carbonate aggregates, and 2 matrix carbonates were analyzed. In ALH 84049, only matrix dolomite grains were analyzed; no veins or aggregate dolomites were observed in this sample. Examples of grain environments and morphologies are shown in the Results section.

4 RESULTS

4.1 General Petrography

Almost all of the original phases in chondrules in both ALH 84049 and ALH 84051 have been replaced by alteration minerals. In plane polarized light, both meteorites are a distinct pale green color that is consistent with a high abundance of serpentine. Numerous spherical to irregular-shaped objects up to a millimeter in size consisting predominantly of serpentine are distributed throughout both thin sections. In the X-ray maps shown in Figures 1a and 1b, these are clearly visible as light green (high Mg) objects. These objects resemble chondrules that have been pseudomorphed into secondary phases, as originally suggested by Llorca and Brearley (1992) and Zolensky et al. (1997). Figures 2a and b show BSE images of two of these chondrule pseudomorphs in which the outlines of pseudomorphed crystals, probably olivine, up to 250 μm in size are clearly defined. Fine-grained rims on individual chondrules, a distinct feature of CM2 chondrites, are rare.

Not all chondrules or chondrule fragments have been replaced, however. Rare, large (up to 200 μm in diameter) fragments of isolated olivine grains are dispersed through ALH 84049 and ALH 84051. X-ray map pixel counting indicates that forsteritic olivine abundances are 0.12 vol% in ALH 84049 and 0.07 vol % in ALH 84051. No detectable pyroxene was found in either meteorite. Many olivine grains show partial dissolution and subsequent replacement (Figs. 2c and 2d). Furthermore, ALH84049 also contains several large forsteritic olivine grains (e.g., Fig. 2c) surrounding a central region of serpentine and carbonate which may represent altered mesostasis glass. The BSE image of the chondrule in Figure 2c also shows two distinct serpentine compositions indicated by different Z-contrast. The darker gray (lower Z) serpentine may represent alteration of the forsterite. Embedded within the darker serpentine are smaller olivine grains that show evidence of partially pseudomorphic replacement around their peripheries. The olivine grains shown in Figures 2c and 2d may represent clasts introduced by regolith gardening.

Mineral compositions abundances change with proximity to the dolomite vein in ALH 84051. For example, in Figure 1a it is apparent that serpentine minerals adjacent to the dolomite veins are lower in Fe and higher in Mg than the general matrix. Forsterite is generally constrained to the upper third of the ALH 84051 thin section. The upper box in Figure 1a contains 0.60 vol% calcite, 0.63 vol% dolomite, and 0.39 vol% forsterite, while the average modal abundance of minerals in ALH 84051 is 0.3 vol% calcite, 1.4 vol% dolomite, and 0.07 vol% forsterite. Differences in carbonate and olivine abundance, however, could arise due to heterogeneous mineral distribution independent of proximity to veins. Carbonates and olivine in ALH 84049, distant from dolomite veins, are distributed randomly.

Although chondrule pseudomorphs are distinctive in thin section, both meteorites are dominated by matrix. Rather than the opaque matrix often seen in CM2 chondrites, the matrix consists of translucent to transparent secondary phyllosilicates with opaque sulfide minerals. These secondary minerals are relatively coarse-grained (typically <5μm in diameter) which allows some light transmission through the slides; CM2 matrix serpentine grains typically are 10-100 nm diameter (Barber, 1981). Although we have not focused our analyses on the matrix mineralogy of either meteorite, our observations are consistent with those of Zolensky et al. (1997) who reported that the matrix mineralogy of CM1 meteorites is dominated by secondary serpentine with lower abundances of pentlandite, pyrrhotite, magnetite, and carbonate. Embedded within the matrix are 20 – 50 μm diameter aggregates of serpentine. These aggregates are rimmed by a thin (1-2 μm) high atomic number layer that has EDS spectra consistent with Fe-rich serpentine. Locally these rimmed objects may abut one another and form a honeycomb or mudcrack-like texture (Figs. 2d and 3a).

4.2 Carbonate Petrography

Here we summarize our observations on the occurrence and texture of carbonate grains in ALH 84049 and ALH 84051. We assume that the Ca-carbonate is probably calcite, although compositional data alone cannot differentiate calcite from the polymorphic phases vaterite or aragonite. Lee and Ellen (2008) note that aragonite is a minor phase in the CM2 chondrite Murray. Dolomite and calcite modal abundances measured from X-ray maps of ALH 84049 using the FEI FEGSEM are 0.8 vol% and 0.9

vol%, respectively. Carbonate modal abundances for ALH 84051, also determined using FEI FEGSEM combined X-ray maps, are 1.4 vol% dolomite and 0.3 vol% calcite.

Backscattered electron images of representative carbonate grains are shown in Figures 2d, 3, and 4. Most individual calcite and dolomite grains are 20-50 μm in size and are distributed randomly throughout the matrix. In both ALH 84049 and ALH 84051, calcite and dolomite occur predominantly within the matrix, the exception being two dolomite grains within a partially-replaced chondrule fragment (Fig. 2c) and one (Fig. 3b) that may represent a replaced CAI or chondrule. Calcite and dolomite grains are usually separate, but there are rare cases where calcite lies in contact with dolomite (e.g., Fig. 4c). Carbonate grains have angular-to-subrounded morphologies, may show partial development of crystal facets, and commonly exhibit well-developed cleavages (Figs. 3 and 4). Some carbonate grains, however, show corroded or embayed margins, a feature that is more common in calcite (e.g., Fig. 4f). In addition, many dolomite grains contain distinct zones with submicron sized pores (e.g., Fig. 3b), some of which may follow cleavage traces. Unlike carbonates in CM2 chondrites, no rims of tochilinite/cronstedtite occur on any carbonate grain in either meteorite.

In addition to individual carbonate grains, ALH 84051 contains discontinuous dolomite veins that span the width of the section (Fig. 1a). One vein is ~0.5 cm long; another vein is ~0.9 cm long. Individual grains that constitute the veins are similar to dolomite matrix grains described above: 20-50 μm diameters with angular-to-subrounded morphologies. In some areas, such as that shown in Figure 3c, individual grains are arranged contiguously. Disseminated veins like that in Figure 3d, however, are more typical. X-ray maps of the entire thin section (Fig. 1a) show that serpentine adjacent to these veins has lower Mg and higher Fe contents than typical matrix serpentine up to 2 mm in width. This is the first time that large-scale dolomite veining has been noted in a CM chondrite, although recently an extensive calcite vein was reported in the CM2 chondrite LON 94101 (Lindgren et al., 2011) and micrometer scale (dolomite and breunnerite) veins in QUE 93005 (Lee et al., 2012).

Rare, large (up to 300 μm diameter) dolomite aggregates also occur in ALH 84051, but have not been observed in ALH 84049. Figure 3e shows an example of a dolomite aggregate in ALH 84051 (also visible in Fig. 1a as the left-most denoted aggregate). This aggregate has a 10-20 μm rim of Fe-rich serpentine and numerous cracks. Overall, aggregates consist of individual grains up to 30 μm in diameter and have a complex poikilitic texture in which dolomite encloses 1-40 μm serpentine-rich inclusions and 1-5μm sulfide grains (Fig. 3f).

4.2.1 Dolomite Zoning and Chemistry

Calcite and dolomite in both ALH 84049 and ALH 84051 have complex zoning that is apparent in CL imaging in calcite and by both CL imaging and X-ray mapping in dolomite. Details of the compositional zoning exhibited by major and minor elements in carbonate grains in the two meteorites are shown in Figure 4 (a-f), which shows BSE and CL images along with Fe and Mn X-ray maps for six different dolomite grains.

Cathodoluminescence images (Fig. 4) display CL intensity and do not provide spectral information. Manganese is generally considered to be an activator of CL in carbonates, and Fe is recognized to quench CL (Have and Heijnen, 1985). For some grains, as discussed below, there is a correlation between high CL and high Mn, but for many examples this is not the case. It is clear that Mn is not the only possible activator of CL and further study would be required to fully understand the origin of CL variations in these grains.

There appear to be three distinct types of zoning revealed by CL. First, dolomite may have complex, patchy zoning, often with low CL cores and higher CL overgrowths (Figs. 4a-c). Second, rare dolomite grains also have low CL cores, but the cores have well-defined outlines which may be original growth faces (Figure 4d). These grains also have high CL rims or overgrowths. Third, many dolomites exhibit relatively low CL over most of the grains, but locally have distinct, much higher CL regions that can be regular or patchy in shape (Figures 4e and f). These grains lack high CL overgrowths. Details of these different grains are discussed below.

Figures 4a-c show examples of grains with low CL cores; these can be rounded to euhedral in shape with high CL rims. Figure 4a illustrates a group of three dolomite crystals that are separated by cracks which may have developed during sample preparation. CL within the grain is very complex, with areas of low CL coincident with areas of elevated Fe. The central section has well-defined margins with preserved cleavage traces (visible in the BSE image) dividing an area of high porosity and CL from an area with fewer pores and low CL. Manganese concentration gradually changes across the central grain. Elevated Mn may correspond with porous areas in the central grain. The grain shown in Figure 4b has a corroded appearance and resides within a euhedral rectangular outline that is well defined in the BSE image and in the Fe X-ray map. This may be evidence of serpentine replacement of dolomite. Zoning of Mn and Fe in dolomite is patchy, and there seems to be little correlation between CL response and Fe or Mn concentration. In Figure 4c, calcite and dolomite coexist. Furthermore, there seem to be multiple dolomite grains: one subgrain displays patchy zoning, where the upper area has high Mn and Fe, and the lower subgrain (with well-preserved facets) is lower in Mn and Fe. Low CL intensity is correlated with elevated Fe.

Figure 4d is an example of a composite grain consisting of two distinct zones, both with variable CL. The upper part of the grain has an asymmetric low CL core region with well-defined facets that appear to define the original crystal shape of an earlier growth phase. The high CL region (low Fe, high Mn) is on the exterior of the upper part of the grain and may represent an overgrowth on the core of the grain. The smaller, lower part of the grain also has asymmetric zoning, with a low CL region which is in direct contact with the matrix. Fractures are visible in the BSE image, but these fractures are not correlated with CL zoning and are clearly not original crystal boundaries. The X-ray maps show that higher Fe concentrations correlate with low CL zones in both grains. Additionally, the high CL outer zones usually correlate with the highest concentrations of Mn, but this correlation is not perfect. For example, the CL images indicate that there is a narrow, continuous high CL zone overgrowing the low CL core in the upper part of the grain. This zone, however, is not enriched in Mn in the X-ray map, suggesting that another activator is responsible for the elevated CL.

Figures 4e and 4f are examples of carbonates with relatively low CL intensity across much of the individual grains, but which locally exhibit small regions of high CL. Figure 4e is a single crystal with an irregular high CL region on the edge of the grain; this area is not elevated in Mn but is depleted in Fe. The crystal also has a euhedral zone in the lower part of the grain that is enriched in Mn. This area does not show significantly enhanced CL intensity, possibly because of its relatively high Fe content. Figure 4f illustrates an example of a euhedral dolomite grain with well-developed facets with two irregularly-shaped regions of higher CL adjacent to the grain edge. In contrast to the grain shown in Figure 4e, the high CL regions are reasonably well correlated with higher Mn contents and low Fe.

Individual grains in both dolomite aggregates (Figs. 4g-4h) and in vein dolomite (Figs. 4i-4k) also are compositionally zoned. In Figure 4g-4k, we show only Mn X-ray maps and CL images, but these grains are zoned in Fe, Mg, and Ca as well. The dolomite aggregate in Figure 4g (also Fig. 3e) contains many subgrains of variable composition. High Mn grains are found in the upper, right, and lower sections of the aggregate. Low Mn grains are found in the center of the aggregate and in grains outside the serpentine rim of the aggregate. Figure 4h shows a larger (150x400 μm) dolomite aggregate that also displays patchy Mn zoning. Unlike the aggregate in Figure 4g, this aggregate does not have a thick serpentine rim, although numerous phyllosilicate (light gray) and sulfide (white) inclusions are visible in the BSE image. Vein dolomite in Figure 4i has patchy zoning in the dolomite grains bisecting the image. The euhedral grain in the upper right has a Mn-rich rim. Figure 4j shows two large vein dolomite grains: the right grain is generally uniform in Mn composition, although the upper left and lower right show some enrichment. The left grain has an area strikingly higher in Mn than surrounding areas. This high Mn zone is porous which may represent dissolution and subsequent recrystallization. Figure 4k shows a dolomite vein aggregate with Mn-enriched zones on the outside edges.

To quantify the compositional zoning in the dolomite grains in more detail, zoning profiles were measured by EPMA across individual grains. Analyses with low totals or SiO_2 contents higher than 1 wt% were removed from consideration to eliminate analyses that overlapped adjacent silicate grains or inclusions. Figure 5 shows compositional profiles for three dolomite grains to illustrate the variability in zoning styles. Cathodoluminescence images were obtained first for individual grains and were used to orient the zoning profiles to transect zones with different CL intensities. In Figure 5a, BSE and CL images of a dolomite grain show distinct zoning. Grain margins have high CL intensities with a lower intensity core region. The EPMA traverse shows that the core region is higher in MgO and FeO and lower in CaO than the rim of the grain, although the zoning is asymmetrical. Although the transition from high CL margins to low CL core looks sharp in the image, there is no evidence of a sharp compositional transition in the microprobe data. For example, the MnO concentration is uniform from rim to core. The grain shown in Figure 5b displays patchy zoning in the CL image; although the central area has lower CL intensity than the margins. In two transects across the same grain, the cores contain slightly higher MnO and FeO than the rims. MgO and CaO show the opposite relationship. Figure 5c shows another grain with patchy CL. The EPMA transect of this grain shows a core high in CaO and low in FeO. MnO is variable and does not follow the smooth core-to-rim transition of CaO, MgO, and FeO. The resolution, ~10μm per spot, may overlook some variability at a finer spatial scale, however.

4.2.2 Dolomite major elemental composition

Figure 6 uses a ternary diagram to compare, in mol%, the $MgCO_3$, $CaCO_3$, and $(Fe+Mn)CO_3$ components of dolomite. The data include 63 EPMA analyses from ALH 84049 and 167 analyses from ALH 84051; all data also reported in the Appendix. All analyses with low analytical totals or with SiO_2 contents >1 wt% were rejected. Rejected analyses may have hit cracks, inclusions, or adjacent matrix materials. Figure 6 demonstrates that dolomites in both samples have comparable compositional ranges. Pure dolomite compositions do not occur in either meteorite. Instead, significant substitution of $FeCO_3$ and $MnCO_3$ into the dolomite structure is evident. The $CaCO_3$ component in these dolomite grains ranges from 44 to 59 mol% in ALH 84049 and from 36 to 57 mol% in ALH 84051. $MgCO_3$ ranges from 32 to 48 mol% in ALH 84049 and from 32 to 53 mol% in ALH 84051. $FeCO_3$ ranges from 3 to 9 mol% in ALH 84049 and from 3 to 12 (with two outliers of 14 and 18) mol%. $MnCO_3$ ranges from 1 to 8 mol% in ALH 84049 and from 1 to 10 mol% in ALH 84051. Compositional means for both samples are similar: 48 (± 3.0) mol% $CaCO_3$, 41.8 (± 3.1) mol% $MgCO_3$, 7.4 (± 2.3) mol% $FeCO_3$, and 2.9 (± 1.8) mol% $MnCO_3$ in ALH 84051 and 49.8 (± 2.7) mol% $CaCO_3$, 42.1(± 2.8) mol% $MgCO_3$, 4.74 (± 1.5) mol% $FeCO_3$, and 3.3 (± 1.8) mol% $MnCO_3$ in ALH 84049. Dolomite matrix grains, aggregates, and veins do not exhibit any significant compositional difference.

The spread in composition shown in Figure 6 can be partially explained by either Fe-Ca substitution or Mg-Ca substitution. Cation substitution relations in dolomite for the same dataset as Figure 6 are explored in detail in Figure 7. The only significant correlations are between the cation pairs Mg-Ca and Fe-Ca, which show negative correlations (Figs. 7a and 7b). Figure 7a (Mg-Ca) gives a linear regression that has a slope of -0.53 ($R^2 = 0.3$) for ALH 84049 and -0.37 ($R^2= 0.15$) for ALH 84051. Figure 7b shows a stronger correlation between Fe and Ca with a slope of -1.2 ($R^2= 0.4$) for ALH 84049 and a slope of-0.8 ($R^2= 0.4$) for ALH 84051. It appears that the calcite component is replaced by either magnesite (Fig. 7a) or siderite (Fig. 7b) components; there is considerable solid solution between these components. However, neither Mn-Ca, Mg-Mn, Mg-Fe, nor Mn-Fe pairs covary (Figs. 7c – 7f). In addition to evaluating substitutional relationships, Figure 7 confirms that there is significant compositional overlap and little difference between dolomite compositions in ALH 84051 and ALH 84049.

The analyses show that although Mg/Ca and Fe/Ca ratios covary when considering the entire data set, they do not necessarily do so clearly on an individual grain level. Figure 6c, 6d, and 6e show compositions of three dolomite grains in ALH 84051. These are the same grains that were transected in Figure 5. On the ternary diagram, compositions of analyses that were either within the interpreted core of a dolomite grain or within a rim are plotted. These data shows that compositional variability in individual grains does not encompass the entire spread found in the compiled data set on the left (Fig. 6a). Furthermore, it shows that no definitive core – rim relationship can be ascertained. We noted similar variability in other grains not shown here.

4.3 Mn-Cr isotopic systematics

Mn-Cr isotope systematics were measured, as discussed previously, from ALH 84049 and matrix, aggregate, and vein dolomite grains from ALH84051. Data for dolomites in both ALH 84049 and ALH 84051 show excesses in ^{53}Cr that covary with ^{55}Mn/^{52}Cr ratios, consistent with in-situ decay of live ^{53}Mn. The Mn and Cr data for dolomites in ALH 84049 and ALH 84051 are tabulated in Tables 1 and 2 and are shown plotted in Figure 8a and 8b respectively. Tables 1 and 2 report calculated ^{55}Mn/^{52}Cr ratios for each ROI. Individual grain analyses have regression errors that are too high to permit a useful comparison between isochrons; therefore the isochron shown in Figure 8 represents a combination of all the NanoSIMS data obtained from all the grains analyzed. This assumes all grains formed, within error, concurrently.

The NanoSIMS Mn-Cr data for ALH84049 are plotted in Figure 8a and reported in Table 1; these data represent seven individual matrix dolomite grains. Each dolomite grain was subdivided into three or four regions of interest based on ^{55}Mn/^{52}Cr ratio, and each data point on the isochron represents the ^{55}Mn/^{52}Cr ratio from one of these defined ROIs (see Methods). Grains were chosen for variable Mn compositions and were located within a 9 mm^2 area of the thin section. The isochron, calculated using the combined regions of interest from all of the grains, indicates a ^{53}Cr excess, expressed as δ^{53}Cr, that correlates with ^{55}Mn/^{52}Cr ratio and indicates in-situ decay. Regression of these data gives a slope of (3.35 ± 0.74) x 10^{-6} (2σ) for the (^{53}Mn/^{55}Mn)$_0$ ratio.

For ALH 84051, ^{55}Mn/^{52}Cr ratios were determined from the NanoSIMS isotopic data from a total of 37 different ROIs (Table 2). The regressed slopes using data for seven different dolomite grains define the initial ^{53}Mn/^{55}Mn ratio (^{53}Mn/^{55}Mn)$_0$ as (4.68 ± 1.22) x 10^{-6} (2σ). This slope is within error of that for ALH 84049 and, as reported by Tyra et al. (2009), dolomite within ALH 84034 (4.27 ± 0.50) x 10^{-6}. Table 2 lists the morphology of each dolomite grain (matrix grain, vein dolomite, or aggregate); all three grain types form a single isochron. The calculated (^{53}Mn/^{55}Mn)$_0$ from this dataset for ALH 84051 is significantly different from the preliminary data reported in Tyra et al. (2009) of 9.4 ± 1.95 x 10^{-6}, where only 3 dolomite grains were analyzed.

5 DISCUSSION

We have used NanoSIMS techniques to obtain high spatial resolution Mn-Cr isotopic compositions of dolomites in the paired CM1 chondrites ALH 84051 and ALH 84049. The high spatial resolution of the NanoSIMS avoids analytical problems caused by the presence of inclusions within the carbonate grains and expands the range of Mn/Cr ratios that can be used to define the isochrons. Here we discuss the implications of the Mn-Cr results and relate them to observed complex chemical zoning in dolomite within both studied samples. We also examine the differences and similarities between the occurrence and compositions of carbonates in these two meteorites. Although dolomite grains in both paired samples are compositionally similar, ALH 84051 contains large dolomite aggregates and carbonate veins that are not observed in ALH 84049. We also discuss the chemical setting and timing of carbonate formation in the ALH 83100 paired set of chondrites.

5.1 Mn-Cr Systematics

Previous studies (e.g., Hoppe et al., 2004; Hoppe et al., 2007) of CI chondrites have shown that NanoSIMS is a powerful technique for high spatial resolution analysis of Mn-Cr isotopes in carbonates. Here we have applied the NanoSIMS to study dolomites from CM chondrites in a petrologic context. Hoppe et al. (2007) used SIMS to analyze Mn/Cr within dolomite and breunnerite grains ranging from 100 μm to 400 μm in size from CI chondrites. Because of their large grain size, multiple analyses of each carbonate grain were possible, enabling isochrons to be measured for individual carbonate grains. These data were of sufficiently high quality to demonstrate that dolomite and breunnerite formed at different times within the CI chondrites studied.

There are advantages in using the NanoSIMS for Mn-Cr dating of carbonates in CM chondrites. The high spatial resolution of the instrument compared with conventional SIMS techniques has enabled us to obtain multiple analyses of the small (20-50 μm), complex carbonate grains in the CM1 chondrites ALH 84049 and ALH 84051. In particular, the NanoSIMS dataset can be processed so that Cr-rich inclusions within the dolomite can be removed from the analytical data set. We delimited ROIs by Mn/Cr ratio to construct a well-defined isochron that is not compromised by overlap of the ion beam by inclusions. This approach proved particularly useful for analyzing aggregate dolomite in ALH 84051. These aggregate dolomites typically contain widely dispersed micron-to-submicron inclusions such as serpentine (identified by FEGSEM) that contain significantly higher concentrations of Cr than dolomite, and hence analyses would overlap with these grains. Another disadvantage of conventional SIMS is that a large beam size dilutes the Mn/Cr values to the average of that within the beam. A limited Mn/Cr spread could be the result of overlap of high and low Mn areas by the large SIMS beam size. The small beam of the NanoSIMS allows a wider range in measured Mn/Cr to be delineated within individual grains. The tradeoff, however, is that as measured Mn/Cr ratios expand, the uncertainties increase commensurately as the relative counts of measured Cr decrease.

5.1.1 All CM dolomite ages are cogenetic

Calculated (^{53}Mn/^{55}Mn)$_o$ values from our measurements compare well with data obtained from dolomites in other CM1 chondrites. The calculated (^{53}Mn/^{55}Mn)$_o$ for ALH 84049 is (3.35 ± 0.74) x 10^{-6} and that for ALH 84051 is (4.68 ± 1.22) x 10^{-6}. Reported SIMS dolomite analyses of chondrites paired with those analyzed here, ALH 83100 and ALH 84034, are similar. ALH 83100 dolomite has a measured (^{55}Mn/^{53}Mn)$_o$ of (5.0 ± 1.7) x 10^{-6}(de Leuw et al., 2009) and ALH 84034 dolomite (5.0 ± 1.5) x 10^{-6} (Brearley and Hutcheon, 2000) and (4.27 ± 0.5) x 10^{-6} (Tyra et al., 2009). QUE 93005, another CM1 chondrite, contains dolomite grains with (^{53}Mn/^{55}Mn)$_o$ of (4.1 ± 1.2) x 10^{-6}, also indistinguishable within error (de Leuw et al., 2009). Although carbonates measured in ALH 84049, ALH 83100, ALH 84034, and QUE 93005 are what we define in this paper as matrix grains, measured (^{55}Mn/^{53}Mn)$_o$ values are all within error to that of ALH 84051 which has mixed dolomite morphologies. Results from Fujiya et al. (2012), using a new carbonate standard, also give similar ages, though (^{55}Mn/^{53}Mn)$_o$ values are slightly lower: (2.66 ± 0.79) x 10^{-6} for the Murchison (CM2) calcite, (3.40 ± 0.74) x 10^{-6} for Y791198 (CM2) calcite, (2.79 ± 0.47) x 10^{-6} for ALH 83100 (CM1) dolomite, and (3.38 ± 0.40) x 10^{-6} for Sayama (CM1/2) dolomite.

To establish the absolute age of formation of carbonates using the Mn-Cr system requires calibration using initial (^{53}Mn/^{55}Mn)$_0$ for samples whose ages are known from high accuracy long-lived radioisotope dating. The choice of early solar system materials that are used for this calibration has been the subject of some debate in the literature. The angrite LEW86010 has been used to anchor most calibrations of the Mn-Cr system for dating secondary carbonates (Krot et al., 2006; Hoppe et al., 2007; Fujiya et al., 2012) because its formation age has been determined using very high precision Pb-Pb dating and its (^{53}Mn/^{55}Mn)$_o$ is also very well constrained (Lugmair and Shukolyukov, 1998; Kita et al., 2005; Shukolyukov and Lugmair, 2006; Amelin, 2008). An alternative approach is to use the initial solar system ^{53}Mn/^{55}Mn ratio of 9.1 x 10^{-6} at 4568 (± 1) Ma of CAIs, assuming that ^{53}Mn was ubiquitous and distributed homogeneously in the solar system and that this value applies to CM chondrites (Nyquist et al., 2009; Petitat et al., 2011b). The solar nebula, however, may not have been homogeneous in initial (^{53}Mn/^{55}Mn)$_o$ (Shukolyukov and Lugmair, 2000). Furthermore, spallation-produced ^{53}Mn could occur when CAIs traveled near the proto-sun (Nyquist et al., 2009), and secondary alteration has affected most Allende CAIs (Keller and Buseck, 1991; Jones and Brearley, 2006). Consequently, we choose to use LEW86010 for calculation of absolute age from measured (^{53}Mn/^{55}Mn)$_o$, because (1) LEW86010 is a time anchor for multiple radioisotopic systems (e.g., Kita et al., 2005), (2) initial Solar system (^{53}Mn/^{55}Mn)$_o$ values still need refinement, and (3) LEW86010 is well established as a reference for the comparison of formation ages of secondary minerals in carbonaceous chondrites dated using the Mn-Cr system (Hutcheon et al., 1998; Brearley and Hutcheon, 2000; Krot et al., 2006; Hoppe et al., 2008; Fujiya et al., 2012).

A second problem with Mn-Cr analysis of carbonates originates in calculated relative sensitivity factor (RSF) during SIMS analysis. Most published SIMS analyses of carbonates within carbonaceous chondrites use San Carlos olivine as a standard (e.g., Hoppe et al., 2007; de Leuw et al., 2009; Petitat et al., 2011b); natural terrestrial carbonates simply incorporate too little Cr into their structures to provide useful standards for SIMS analysis (<30 ppm for terrestrial carbonate; Frei et al., 2011). A recently synthesized calcite doped with Cr has been used in Mn-Cr analysis of carbonates by SIMS (Fujiya et al., 2010; Sugiura et al., 2010b). The Mn^+/Cr^+ RSF of this carbonate (0.79) differs from the San Carlos olivine (0.95) and represents a calculated age ~2.2 Myr younger (Sugiura et al., 2010a). Relative ages of carbonates determined using San Carlos olivine as a standard, however, will not change.

Assuming that $(^{53}Mn/^{55}Mn)_o$ was distributed homogeneously within the CM parent body and using the traditional LEW 86010 anchor, we have calculated the formation ages of the analyzed carbonates. Figure 9 compares our new data with previously published formation ages for carbonates in CM chondrites. Reported secondary carbonate ages for ALH 83100, ALH 84034, ALH 84049, ALH 84051, Murchison, QUE 93005, and Y 791198 average 4564.1 ± 0.9 use our data produced here and that of Fujiya et al. (2012), Brearley and Hutcheon (2000), Tyra et al. (2009), de Leuw et al. (2009), and Lee et al. (2012). Additionally, all CM secondary carbonate ages are similar regardless of whether San Carlos olivine or the new calcite standard of Fujiya et al. (2012) is used (see Fig. 9a). We performed a T test assuming unequal variance on the four ages reported by Fujiya et al. (2012) that used the calcite standard (mean age = $4563.4 \frac{+0.4}{-0.5}$ Ma) compared to seven additional ages by other workers (mean age = 4564.5 ±0.8 Ma, references reported in Fig. 9a) that used San Carlos olivine as a standard. The difference is probably significant (significant at a 0.05 level but not at a 0.01 level, p= 0.03), but the <1 Myr difference we calculate (both values are actually within error) is less than the 2.2 million years calculated by Sugiura et al. (2010b) based on different RSFs for the synthesized calcite and San Carlos olivine. This comparison is based upon a small number of analyses, however, and more data needs to be collected to better determine the impact of using the calcite standard of Sugiura et al. (2010b).

The carbonate ages determined for ALH 84049 and ALH 84051 are consistent with a single pulse of precipitation within the resolution of the Mn-Cr data. Furthermore, all CM chondrite carbonate ages are cogenetic regardless of the alteration extent reported by Rubin et al. (See Fig. 9b; 2007). If we assume that the beginning of the Solar System is 4568 (± 1) Ma, determined by analyzing CAIs (Nyquist et al., 2009), then aqueous alteration of the CM parent body occurred ~4 Myrs later. Errors reported about the average of all CM data also indicate that the duration of aqueous alteration with carbonate precipitation was <1 Myr.

5.2 Composition and Petrography

5.2.1 Total dolomite compositional variability

Dolomite compositions in CM chondrites are variable (Johnson and Prinz, 1993; Zolensky et al., 1997; de Leuw et al., 2010) and the entire chemical variability of dolomite in CM chondrites is represented in ALH 84049 and ALH 84051. As would be expected with paired samples, ALH 84049 and ALH 84051 dolomite compositions are similar to ALH 83100 reported by Zolensky et al. (1997) and Lee et al. (2012) but differ slightly in Mg/Ca compared with compositions reported by de Leuw et al. (2010). The dolomite compositions are also similar to that reported in the highly altered CM2 QUE 93005 (Lee et al., 2012). The spread in compositions observed here is slightly larger (Fig. 6a) than that reported in CM chondrites by the workers cited above: we report 63 dolomite analyses in ALH 84049 and 167 in ALH 84051.

There are differences between this data set and other reported dolomite compositions. Johnson and Prinz (1993) analyzed the CM2 chondrites Boriskino, Cold Bokkeveld, Essebi and Nogoya. With dolomite containing greater than 50 mol% $CaCO_3$, Johnson and Prinz (1993) suggest that dolomite compositions in CM2 chondrites are non-stoichiometric and metastable (Fouke and Reeder, 1992). Riciputi et al. (1994) confirmed excess $CaCO_3$ in CM2 chondrite dolomites and noted that they are distinct from dolomite in CI1 chondrites, which have less than 50% $CaCO_3$. Furthermore, de Leuw et al. (2010) observed dolomite with excess $CaCO_3$ in the CM1 chondrites ALH 83100 and QUE 93005. Conversely, Zolensky et al. (1997) did not observe non-stoichiometric dolomite in the CM1 chondrites ALH 83100, Y82042, and EET 83334. We report that average dolomite in ALH 84051 has 48.0 ± 3.0 mol% $CaCO_3$ and ALH 84049 is 49.8 ± 2.7 mol% $CaCO_3$, which suggests that the composition of dolomite in ALH 84049 and ALH 84051 is stoichiometric overall. Some individual grains, however, may have excess $CaCO_3$, the result of dolomite formation either occurring at low temperatures or under briny conditions (Fouke and Reeder, 1992; Riciputi et al., 1994).

5.2.2 Chemical zoning in dolomite

The wide range of compositions in ALH 84049 and ALH 84051 is not simply a reflection of dolomite grains of different composition, but is, in part, due to the great compositional heterogeneity within individual grains. As shown in Figure 6b, c, and d, there is considerable compositional heterogeneity within individual grains that make up a large percentage of the total dolomite compositional range observed in both samples. For example, the single grain 6-b6 (see Appendix) has a $(Fe+Mn)CO_3$ content that ranges from 6.5 to ~16 mol% while all previously reported dolomite compositions in CM1 chondrites range from 0 to ~17 mol% (Zolensky et al., 1997); one grain has ~60% of the compositional variability of all previously described CM1 dolomites.

ALH 84049 and ALH 84051 dolomite grains have complex zoning. Chemical zoning in dolomite grains was first reported in the CM1 chondrite ALH 84034 (Brearley and Hutcheon, 2000; 2002). Other studies of carbonates in the CM1 chondrites QUE 93005 and ALH 83100 by de Leuw et al. (2009) did not identify the compositional zoning that we find to be a ubiquitous feature of dolomite grains in ALH 84049 and ALH 84051. These studies, however, were focused on general compositional trends within individual meteorites (often with just one EPMA analysis per grain) and may have overlooked the significant chemical variability that is present in every dolomite grain that we have analyzed here. Chemical zoning in minerals that grew from fluids in aqueously altered meteorites can provide significant insights into the compositional evolution of the fluids from which they grew. It is therefore important to characterize this zoning in detail, in order to unravel the complex alteration histories of these meteorites.

Three general zoning patterns are common to many of the grains studied. First, the zoning is consistently asymmetric, suggesting that carbonate grains nucleated on the edges of a fluid-filled pore and grew inward. In some cases, we observe two or three grains in an aggregate that all have asymmetric cores, suggesting that nucleation of more than one grain on the pore edges occurred (Fig.4c). Second, in some grains, the CL image and X-ray maps clearly reveal ghost euhedral rhombohedral zones within the dolomite grains, again developed asymmetrically in the grain. This provides compelling evidence that growth of these carbonate grains occurred unimpeded into fluid-filled pore space, such that euhedral grains with progressive growth zones have developed. In the example shown in Figure 4d, distinct compositional zones are present, with a low CL core that is richer in $FeCO_3$, overgrown by thinner zones with higher CL and higher $MnCO_3$. The transition between the more Fe-rich core and the overgrowth is sharp. We interpret this feature as indicating that the carbonate grew in at least two distinct episodes from fluids of different compositions. Third, we also observe examples of dolomite grains that have rounded or subrounded, irregularly shaped regions, which we interpret as being the corroded original cores. The subrounded texture of these core regions suggests that these grains have undergone dissolution at some period in their history, before being overgrown by a later stage of carbonate growth (Fig. 4j). Alternately, the high Mn areas often are porous (Fig 4j, again) which suggests that recrystallization may have occurred and a later, Mn-rich fluid, facilitated later carbonate growth (Putnis, 2009). Either scenario suggests that carbonates grew in at least two different periods, but unlike the grains with euhedral cores and subsequent growth, these two episodes of growth may have been separated by a period of dissolution.

There are few consistent core-to-rim compositional relationships, in part due to the asymmetry of the zoning. This asymmetry makes identification of the core of some of the grains ambiguous. However, in cases where we think the core-rim relationships are clear, there appear to be two general, but distinct, types of zoning behavior. In the first case, the cores of the grains have higher Mn contents: examples of such grains are shown in Figures 4b, 4i, and 4j. The cores of these grains can be either euhedral or corroded. In the second case, the cores of the grains are lower in Mn and there is a transition to higher Mn contents at the edges of the grains, such as those shown in Figures 4e, 4d, and 4k. This observation signifies a progressive increase in Mn as fluids evolved and became more saline perhaps due to the consumption of water by silicate hydration reactions. Higher Mn concentrations at carbonate peripheries have also been reported in ALH 84034 (Brearley and Hutcheon, 2000). We observed no noticeable differences in zoning complexity between ALH 84049 and ALH 84051, which is consistent with their pairing (and therefore similar asteroidal setting within the parent body). Nor do we see a difference in zoning style of either vein or aggregate dolomite: each display zoning as complex as that seen in small matrix grains.

The variability of texture and composition from one dolomite grain to another indicates that the process of carbonate growth is complex and diverse. For example, chemical zoning can occur because of crystal growth structure controls; one face may incorporate more Mn or Fe during active growth than another (Fouke and Reeder, 1992). This sector zoning can result in zones that vary by as much as 3 mol% of the $CaCO_3$ component. Zoning observed in CM chondrites, however, is much more extensive than can be explained by sector zoning. Carbonates with sector zoning are not observed. A chemically-variable fluid like that reported by Riciputi et al. (1994) which clearly varied at a at least a sample scale (cm-scale) is more consistent with our observations.

5.2.3 Implications of carbonate zoning for the nature of fluid

We explore a framework that may explain dolomite compositional heterogeneity in ALH 84049 and ALH 84051. Except for a relationship between Ca-Mg and Ca-Fe, compositional zoning in dolomite is very complex. For example, in many grains, the mol% $MnCO_3$ increases on the outside of grains or within porous, potentially recrystallized, areas, indicating evolution towards a high Mn fluid. Other grains, however, show the reverse with etched, Mn-rich cores enclosed within Mn-poor dolomite. The seemingly chaotic nature of dolomite precipitation could arise if water was abundant early and the meteorite parent body was relatively permeable when calcite precipitated. Then, as alteration continued, the availability of water progressively diminished as it was consumed by serpentinization reactions. Fluid permeability would diminish as pores were filled by secondary minerals. In this scenario, chemical microenvironments would dominate which may be manifested in the chemical variability observed in dolomite. If this interpretation is correct, then the carbonate assemblage in ALH 84049 and ALH 84051 may have progressed from an open system at the millimeter scale to a closed system as the permeability of the rock decreased.

In ALH 84049 and ALH 84051, pervasively etched margins of calcite and inclusions of calcite within dolomites (e.g., Fig. 1d and Fig. 4c) may signify that calcite predated dolomite or that fluid pH decreased slightly out of the stability field of calcite, but not of dolomite. Oxygen isotope compositions also imply that, in general, calcite predated dolomite in CM chondrites (Benedix et al., 2003). In terrestrial waters, $CaCO_3$ is kinetically favored to precipitate (Arvidson and Mackenzie, 1999), until the Mg/Ca ratio reaches high enough values to permit dolomite precipitation. Increasing Mg/Ca ratios in the fluid could result from progressive dissolution of forsterite (Mg_2SiO_4), which would supply Mg to the fluid. Calcite, however, may not always precipitate first; Lee et al. (2012) note that in the highly altered CM2 chondrite QUE 93005 dolomite precipitated first, then breunnerite, Ca-poor dolomite, and finally calcite. Furthermore de Leuw et al. (2010) suggest that the absence of dolomite in some CM1 chondrites is the result of a dedolimization processes that removed dolomite and re-precipitated calcite. Although increasing Mg/Ca ratios can increase the likelihood that dolomite will precipitate, compositional heterogeneities in the fluid within CM chondrites was also important.

As alteration progressed, evidence from carbonaceous chondrites indicates that the precipitation of dolomite became more likely. For example, dolomite is found only within more altered CM2 chondrites (Rubin et al., 2007). In CI chondrites, the carbonate precipitation sequence has been determined to be first calcite, then dolomite, and then more complex carbonates (Endress and Bischoff, 1996; Zito et al., 1998; Petitat et al., 2009). Similar alteration grade, water content (Clayton and Mayeda, 1999), compositionally similar (matrix-dominated) starting material (Zolensky et al., 1989), and temperatures (Cody et al., 2008), suggest that it is likely that CM1 chondrites experienced a similar precipitation progression (e.g., Lee et al., 2012). (2) Calcite precipitation is favored until Mg/Ca ratios become high enough to precipitate dolomite (Tucker and Wright, 1990; Wright and Wacey, 2004). The fine-grained chondrule mesostasis hosts Ca and would alter early, adding Ca to the fluid (e.g., Sears et al., 1992). Late alteration, alternatively, is characterized by serpentinization of forsteritic olivine phenocrysts in chondrules, which are generally resistant to alteration (Hanowski and Brearley, 2001). Forsterite replacement by serpentine would increase Mg concentrations in the fluid adjacent to altering chondrules (Sleep et al., 2004; Oze and Sharma, 2007). This argument is consistent with calcite predating dolomite. (3) Dolomite often forms from brines, which is likely to be present once much of water has been consumed by serpentinization (Adams and Rhodes, 1960; Machel and Mountjoy, 1986; Tucker and Write, 1990; Arvidson and Mackenzie, 1999). Furthermore, trace element analyses show brines were present during late alteration in CM chondrites (Riciputi et al., 1994).

Brearley et al. (2006) suggested that the heterogeneous mineralogy and local water-mineral reactions in CM chondrites would create geochemical microenvironments. Although we do not treat this subject rigorously here, we have observed compositional heterogeneities ($CaCO_3$, $MgCO_3$, FeCO3, and $MnCO_3$) in dolomite grains separated by only tens of micrometers. Such heterogeneity in composition would require that cation mobility was restricted; otherwise the compositional zoning style in adjacent dolomite grains would be similar. Bland et al. (2009) related fluid permeability to the very small grain size of minerals in CI1 and CM2 chondrites and calculated permeabilities for carbonaceous chondrites in the range 10^{-19} to $10^{-17} m^2$, which is up to six orders of magnitude smaller than previous estimates (e.g., Young et al., 2003). When these calculated permeabilities are used as input for asteroidal flow models (Cohen and Coker, 2000; Young et al., 2003; Grimm, 2007), the authors estimated fluid flow would range from <10 μm (for $P = 10^{-19}$ m^2) to <1000 μm (for $P = 10^{-17}$ m^2). The specific flow value depends, in part, upon location within a hypothetical 50 km radius body. The hydraulic radius parameter in permeability calculations is related to tortuosity, which contrasts the actual distance between two points that a molecule would travel compared to the direct distance if there were no intervening particles. Permeability also implicitly accounts for viscosity increases (α) that occur adjacent to surfaces, especially as conduit diameter decreases. The effective diffusivity (D') is related to tortuosity (τ), α, and the electrostatic attraction of a cation to surfaces (γ) by the equation:

$$D' = D_o \tau \alpha \gamma$$

where D_o is the natural diffusion coefficient of a cation through a fluid (Olsen and Kemper, 1968). Because the three impedance factors (τ, α, and γ) are difficult to quantify

(Nye, 1980; Jungk and Claassen, 1997), an approximation can be made where cation diffusion was slower than fluid flow. This may be a valid approximation because α, the attraction of cations to conduit surfaces (generally phyllosilicates in CM chondrites), is not factored into permeability. If we, therefore, assume permeability is faster than diffusion, the observed length-scales of dolomite compositional heterogeneity are consistent with the calculated permeability and resultant fluid flow length-scale of Bland et al. (2009).

Although Bland et al. (2009) calculated very low permeabilities for CM chondrites, the relative lack of compositional heterogeneity in calcite in comparison with dolomite suggests that permeability was higher during calcite formation than during later dolomite precipitation. Furthermore, calcite is found in almost all CM chondrites, especially the least altered (Fuchs et al., 1973; Johnson and Prinz, 1993; Riciputi et al., 1994; Benedix et al., 2003; de Leuw et al., 2010). This may indicate that widespread calcite in CM chondrites formed early in one or two discreet events as postulated by Tyra et al. (2012) and Benedix et al. (2003). Below we conceptualize the steps that may have occurred that relate to carbonate precipitation in the CM parent body.

1. Calcite grains in most CM2 chondrites are nearly identical compositionally indicating that during calcite precipitation Ca^{2+} was distributed relatively uniformly across both samples (mm-to-cm scale). This indicates that permeability early in the history of aqueous alteration in CM chondrites may have not been as low as calculated by Bland et al. (2009) and that Ca^{2+}cation diffusivity was relatively high ($D_o \rightarrow D'$).

2. The compositionally heterogeneous dolomite indicates that the effective diffusion (D’) rate slowed considerably after calcite formation. This can be explained by the reaction of chondrule minerals, primarily forsterite, with water to form serpentine. Observations of chondrule pseudomorphic replacement by serpentine appear to have involved no discernible volume change (Hanowski and Brearley, 2001; Velbel et al., 2012). However, serpentinization reactions involve a volume increase of 25-55 vol%, so that isovolumetric replacement of chondrule forsterite requires the movement of SiO_{2aq} and Mg^{2+} outside of chondrules, possibly reacting to form serpentine there (Coleman, 1971; O'Hanley, 1992; Putnis, 2009). This phenomenon has been observed terrestrially, where serpentine has precipitated as fracture fillings exterior to serpentinized peridotite bodies (O'Hanley, 1992; Lafay et al., 2012). Serpentine formation outside of chondrules would fill pore space and reduce the fluid connectivity of the chondrite.
3. Although all dolomite compositions are constrained to a limited area in Ca, Mg, and Fe+Mn compositional space (see ternary diagram, Fig. 6), pervasive zoning in dolomite grains indicates that Mg/Ca, Mn/Ca, and Fe/Ca ratios were spatially heterogeneous in the fluid. Ongoing infill of interconnected pores by serpentine formation reduced D’ and limited cation migration and homogenization to tens of microns. Fluid interactions with the heterogeneous, on a micron scale, mineralogy in CM chondrites (e.g., Brearley, 1998) therefore could dominate fluid composition.

5.2.4 Significance of veins

The studied thin section of ALH 84051, unlike ALH 84049, contains dolomite veins. The observed dolomite veins are extraterrestrial in origin and not the result of Antarctic weathering. The primary evidence that the dolomite veins are extraterrestrial is their Mn-Cr isotope composition and resultant inferred age.

Fluid flow through cracks may have occurred during vein formation. Cracks may have resulted from impact fracturing (Rubin, 2012), hydrodynamic fracturing (Wilson et al., 1999), or to accommodate mineral volume changes during serpentinization (O'Hanley, 1992). Evidence for flow through cracks primarily lies with the serpentine adjacent to the cracks having a different composition (less Fe, more Mg, Fig. 1) than serpentine further from the veins. If a fluid flowed through a fracture with a different composition than the fluid within the general pore space, it could have facilitated dissolution–reprecipitation reactions in phyllosilicates near the veins. Fluid flow of limited scope and duration may have allowed alteration of the matrix adjacent to these veins. The low abundance of olivine near the veins could be related to enhanced availability of water in the host rock immediately adjacent to the vein, causing local, more extensive alteration of forsterite.

Conversely, the absence of olivine in this region may simply be because there is inherently a heterogeneous distribution of unaltered olivine in the host rock. Unlike the calcite vein in LON 94101 (Lindgren et al., 2011), there is no obvious depletion of Mg from nearby to account for concentrated dolomite in the vein; as noted above, matrix proximal to the veins is Mg-rich. Dolomite veins could have resulted from fracture infill by a stagnant fluid and not the result of large-scale fluid flow. The Mg-rich serpentine around veins could be the result of cation diffusion through a non-flowing fluid. Furthermore, the dolomite vein infill composition is indistinguishable from both aggregates and matrix grains, and the zoning in vein dolomite is just as complex as matrix and aggregate grains. These observations suggest that at the time of dolomite formation, microenvironments in the veins were just as prevalent as elsewhere, perhaps closure of the cracks reduced permeability similar to elsewhere in the host chondrite.

6 Conclusions

We have studied the general petrology and carbonate petrology of the CM1 chondrites ALH 84049 and ALH 84051 to constrain some aspects of aqueous alteration. Both samples contain widespread, small calcite and dolomite grains interspersed through the matrix. ALH 84051 also contains large dolomite aggregates and cm-scale disseminated dolomite veins. Regardless of the morphology and sample, dolomite grains show extensive compositional zoning in $CaCO_3$, $MgCO_3$, $FeCO_3$, and $MnCO_3$; the compositional variability in some individual grains covers up to 60% of the observed compositional variability of CM1 dolomite. Compositional zoning in dolomite is heterogeneous with no consistent core-to-rim relationships in either sample: this observation is consistent with dolomite growth within isolated, fluid-filled pores with very limited communication between pores. Our observations are most consistent with at least two stages of carbonate growth; calcite precipitated first, followed by dolomite, from late stage concentrated brines with high Mg/Ca ratios, produced by advanced serpentinization of forsterite in chondrules. The volume change associated with serpentinization may have caused a reduction in porosity as a result of the growth of product phases in pore space in the matrix. Once pores became isolated, localized dissolution reactions would have controlled the fluid chemistry, resulting in the observed variations in dolomite compositions. Mn-Cr results for dolomite record evidence of excess ^{53}Cr indicative of in-situ decay of the short-lived radionuclide ^{53}Mn. These data show that, regardless of morphology, dolomites, in ALH 84049 and ALH 84051 are cogenetic. The calculated ages for carbonate formation are consistent with those of other highly altered CM chondrites (Brearley and Hutcheon, 2000; de Leuw et al., 2009; Tyra et al., 2009; Fujiya et al., 2012; Lee et al., 2012).

7 ACKNOWLEDGEMENTS

We thank Mike Spilde, Ara Kooser, Ben Jacobsen, and Peter Weber for their assistance. We also acknowledge support from NASA NAG5-9798 (A.J. Brearley, PI), NM Space Grant (M. Tyra), and further support under the auspices of the Dept. of Energy by Lawrence Livermore National Laboratory, contract DE-AC52-07NA27344.

8 BIBLIOGRAPHY

Adams J. E. and Rhodes M. L. (1960) Dolomitization by seepage refluxion. *AAPG Bulletin* **44**, 1912-1920.

Amelin Y. (2008) U–Pb ages of angrites. *Geochimica et Cosmochimica Acta* **72**, 221-232.

Arvidson R. S. and Mackenzie F. T. (1999) The dolomite problem: Control of precipitation kinetics by temperature and saturation state. *American Journal of Science* **299**, 257-288.

Barber D. J. (1981) Matrix phyllosilicates and associated minerals in CM2 carbonaceous chondrites. *Geochimica et Cosmochimica Acta* **45**, 945-970.

Benedix G. K., Leshin L. A., Farquhar J., Jackson T., and Thiemens M. H. (2003) Carbonates in CM2 chondrites: Constraints on alteration conditions from oxygen isotopic compositions and petrographic observations. *Geochimica et Cosmochimica Acta* **67**, 1577-1588.

Birck J.-L. and Allegre C. J. (1988) Manganese-chromium isotope systematics and the development of the early Solar System. *Nature* **331**, 579-584.

Bland P. A., Jackson M. D., Coker R. F., Cohen B. A., Webber J. B. W., Lee M. R., Duffy C. M., Chater R. J., Ardakani M. G., McPhail D. S., McComb D. W., and Benedix G. (2009) Why aqueous alteration in asteroids was isochemical: High porosity ≠ high permeability. *Earth and Planetary Science Letters* **287**, 559-568.

Botta O., Martins Z., and Ehrenfreund P. (2007) Amino acids in Antarctic CM1 meteorites and their relationship to other carbonaceous chondrites. *Meteoritics & Planetary Science* **42**, 82-92.

Brearley A. J. (1998) Carbonates in CM carbonaceous chondrites: Complex zoning revealed by high resolution cathodoluminescence studies. *Lunar and Planetary Science XXIX*. LPI, Houston, TX.

Brearley A. J. and Jones R. H. (1998) Chondritic Meteorites. In: Papike, J. J. (Ed.), *Planetary Materials*. The Mineralogical Society of America, Washington, DC.

Brearley A. J., Saxton J. M., Lyon I. C., and Turner G. (1999) Carbonates in the Murchison CM chondrite: CL characteristics and oxygen isotopic compositions. *Lunar and Planetary Science* **XXX**, 1301.pdf.

Brearley A. J. and Hutcheon I. D. (2000) Carbonates in the CM1 chondrite ALH84034: Mineral chemistry, zoning and Mn-Cr systematics. *Lunar and Planetary Science Conference* **XXXI**, abstract #1407.

Brearley A. J. and Hutcheon I. (2002) Carbonates in the Y791198 CM2 chondrite: Zoning and Mn-Cr systematics. *Meteoritics & Planetary Science* **37**, A23.

Brearley A. J. (2006) The action of water. In: Lauretta, D. S., Leshin, L. A., and McSween, H. Y. Eds.), *Meteorites and the early solar system II*. University of Arizona Press, Tucson, AZ.

Brearley A. J., Weber P., and Hutcheon I. D. (2006) Trace element zoning in CM chondrite carbonates: Insights from compositional mapping using NanoSIMS. *Annual Meteoritical Society Meeting* **69**, abstract # 5365.

Browning L., McSween H., and Zolensky M. (1996) Correlated alteration effects in CM carbonaceous chondrites. *Geochimica et Cosmochimica Acta* **60**, 2621-2633.

Bunch T. E. and Chang S. (1980) Carbonaceous chondrites .2. Carbonaceous chondrite phyllosilicates and light-element geochemistry as indicators of parent body processes and surface conditions. *Geochimica et Cosmochimica Acta* **44**, 1543-1577.

Clayton R. and Mayeda T. (1999) Oxygen isotope studies of carbonaceous chondrites. *Geochimica et Cosmochimica Acta* **63**, 2089-2104.

Cody G. D., Alexander C. M. O. D., Yabuta H., Kilcoyne A. L. D., Araki T., Ade H., Dera P., Fogel M., Militzer B., and Mysen B. O. (2008) Organic thermometry for chondritic parent bodies. *Earth and Planetary Science Letters* **272**, 446-455.

Cohen B. and Coker R. F. (2000) Modeling of liquid water on CM meteorite parent bodies and implications for amino acid racemization. *Icarus* **145**, 369-381.

Coleman R. G. (1971) Petrologic and Geophysical Nature of Serpentinites. *Geological Society of America Bulletin* **82**, 897-918.

de Leuw S., Rubin A. E., Schmitt A. K., and Wasson J. T. (2009) ^{53}Mn-^{53}Cr systematics of carbonates in CM chondrites: Implications for the timing and duration of aqueous alteration. *Geochimica et Cosmochimica Acta* **73**, 7433-7442

de Leuw S., Rubin A. E., and Wasson J. T. (2010) Carbonates in CM chondrites: Complex formational histories and comparison to carbonates in CI chondrites. *Meteoritics & Planetary Science* **45**, 513-530.

Endress M. and Bischoff A. (1996) Carbonates in CI chondrites: Clues to parent body evolution. *Geochimica et Cosmochimica Acta* **60**, 489-507.

Fouke B. W. and Reeder R. J. (1992) Surface structural controls on dolomite composition - Evidence from sectoral zoning. *Geochimica et Cosmochimica Acta* **56**, 4015-4024.

Frei R., Gaucher C., Døssing L. N., and Sial A. N. (2011) Chromium isotopes in carbonates — A tracer for climate change and for reconstructing the redox state of ancient seawater. *Earth and Planetary Science Letters* **312**, 114-125.

Fuchs L. H., Olsen E., and Jensen J. (1973) Mineralogy, mineral-chemistry, and compositon of the Murchison (C2) meteorite. *Smithsonian Contributions to the Earth Sciences* **10**, 1-38.

Fujiya W., Sugiura K., Ichimura K., Takahata N., and Sano Y. (2010) Mn-Cr ages of carbonates in Murchison and ALH 83100 CM chondrites *LPSC*. LPI, Houston.

Fujiya W., Sugiura N., Hotta H., Ichimura K., and Sano Y. (2012) Evidence for the late formation of hydrous asteroids from young meteoritic carbonates. *Nat Commun* **3**, 627.

Glavin D. P., Dworkin J. P., Aubrey A., Botta O., Doty J. H., Martins Z., and Bada J. L. (2006) Amino acid analyses of Antarctic CM2 meteorites using liquid chromatography-time of flight-mass spectrometry. *Meteoritics & Planetary Science* **41**, 889-902.

Grady M. M., Wright I. P., Swart P. K., and Pillinger C. T. (1988) The carbon and oxygen isotopic composition of meteoritic carbonates. *Geochimica et Cosmochimica Acta* **52**, 2855-2866.

Grimm R. E. (2007) Fluid flow on carbonaceous chondrite parent bodies. *Lunar Planet.l Sci. Conf.* ***XXXVIII***.

Hanowski N. P. and Brearley A. J. (2001) Aqueous alteration of chondrules in the CM carbonaceous chondrite, Allan Hills 81002: Implications for parent body alteration. *Geochimica et Cosmochimica Acta* **65**, 495-518.

Have T. and Heijnen W. (1985) Cathodoluminescence activation and zonation in carbonate rocks: an experimental approach. *Geologie en Mijnbouw* **64**, 297-310.

Hoppe P., Ott U., and Lugmair G. W. (2004) NanoSIMS, the new tool of choice: Al-26, Ti-44, V-49, Mn-53, Fe-60, and more. *New Astronomy Reviews* **48**, 171-176.

Hoppe P., Macdougall D., and Lugmair G. W. (2007) High spatial resolution ion microprobe measurements refine chronology of carbonate formation in Orgueil. *Meteoritics & Planetary Science* **42**, 1309-1320.

Hoppe P., Macdougall D., and Lugmair G. W. (2008) Extinct manganese-53 in carbonates from the Orgueil meteorite. *New Astronomy Reviews* **52**, 467-470.

Hutcheon I. D., Krot A. N., Keil K., Phinney D. L., and Scott E. R. D. (1998) ^{53}Mn-^{53}Cr dating of fayalite formation in the CV3 chondrite Mokoia: Evidence for asteroidal alteration. *Science* **282**, 1865-1867.

Johnson C. A. and Prinz M. (1993) Carbonate compositions in CM and CI chondrites, and implications for aqueous alteration. *Geochimica et Cosmochimica Acta* **57**, 2843-2852.

Jones C. L. and Brearley A. J. (2006) Experimental aqueous alteration of the Allende meteorite under oxidizing conditions: Constraints on asteroidal alteration. *Geochimica et Cosmochimica Acta* **70**, 1040-1058.

Jungk A. and Claassen N. (1997) Ion diffusion in the soil-root system. In: Donald, L. S. (Ed.), *Advances in Agronomy*. Academic Press.

Keller L. P. and Buseck P. R. (1991) Calcic micas in the Allende meteorite - Evidence for hydration reactions in the early solar nebula. *Science* **252**, 946-949.

Kita N. T., Huss G. R., Tachibana S., Amelin Y., Nyquist L. E., and Hutcheon I. D. (2005) Constraints on the origin of chondrules and CAIs from short-lived and long-lived radionuclides. In: Krot, A. N., Scott, E. R. D., and Reipurth, B. Eds.)*Chondrites and the Protoplanetary Disk*. Astronomical Society of the Pacific, Kaua'i, Hawai'i.

Krot A. N., Keil K., Goodrich C. A., Scott E. R. D., and Weisberg M. K. (2005) Classification of meteorites. In: Davis, A. N. (Ed.), *Meteorites, Comets, and Planets*.

Krot A. N., Hutcheon I. D., Brearley A. J., Pravdivtseva O. V., Petaev M. I., and Hohenberg C. M. (2006) Timescales and settings for alteration of chondritic meteorites. In: Lauretta, D. S., Leshin, L. A., and McSween, H. Y. Eds.), *Meteorites and the early solar system II*. University of Arizona Press, Tucson, AZ.

Lafay R., Montes-Hernandez G., Janots E., Chiriac R., Findling N., and Toche F. (2012) Mineral replacement rate of olivine by chrysotile and brucite under high alkaline conditions. *Journal of Crystal Growth* **347**, 62-72.

Lee M. R. and Ellen R. (2008) Aragonite in the Murray (CM2) carbonaceous chondrite: Implications for parent body compaction and aqueous alteration. *Meteoritics & Planetary Science* **43**, 1219-1231.

Lee M. R., Lindgren P., Sofe M. R., O'D Alexander C. M., and Wang J. (2012) Extended chronologies of aqueous alteration in the CM2 carbonaceous chondrites: Evidence from carbonates in Queen Alexandra Range 93005. *Geochimica et Cosmochimica Acta* **92**, 148-169.

Lindgren P., Lee M. R., Sofe M., and Burchell M. J. (2011) Microstructure of calcite in the CM2 carbonaceous chondrite LON 94101: Implications for deformation history during and/or after aqueous alteration. *Earth and Planetary Science Letters* **306**, 289-298.

Llorca J. and Brearley A. J. (1992) Alteration of chondrules in ALH 84034, an unusual CM2 carbonaceous chondrite. *Lunar and Planetary Science Conference XXIII*. LPI, Houston, TX.

Lugmair G. W. and Shukolyukov A. (1998) Early solar system timescales according to 53Mn-53Cr systematics. *Geochimica et Cosmochimica Acta* **62**, 2863-2886.

Machel H.-G. and Mountjoy E. W. (1986) Chemistry and Environments of Dolomitization —A Reappraisal. *Earth-Science Reviews* **23**, 175-222.

Metzler K., Bischoff A., and Stoffler D. (1992) Accretionary dust mantles in CM chondrites: Evidence for solar nebula processes. *Geochimica et Cosmochimica Acta* **56**, 2873-2897.

Nye P. H. (1980) Diffusion of ions and uncharged solutes in soils and soil clays. In: Brady, N. C. (Ed.), *Advances in Agronomy*. Academic Press.

Nyquist L. E., Kleine T., Shih C. Y., and Reese Y. D. (2009) The distribution of short-lived radioisotopes in the early solar system and the chronology of asteroid accretion, differentiation, and secondary mineralization. *Geochimica et Cosmochimica Acta* **73**, 5115-5136.

O'Hanley D. S. (1992) Solution to the volume problem in serpentinization. *Geology* **20**, 705-708.

Ogren P. J. and Norton J. R. (1992) Applying a simple linear least-squares algorithm to data with uncertainties in both variables. *Journal of Chemical Education* **69**, A130-A131.

Olsen S. R. and Kemper W. D. (1968) Movement of nutrients to plant roots. In: Norman, A. G. (Ed.), *Advances in Agronomy*. Academic Press.

Oze C. and Sharma M. (2007) Serpentinization and the inorganic synthesis of H2 in planetary surfaces. *Icarus* **186**, 557-561.

Petitat M., McKeegan K. D., Gounelle M., Mostefaoui S., Marrocchi Y., Meibom A., and Leshin L. A. (2009) Duration and sequence of carbonate crystallization on the Orgueil protolith: ^{53}Mn-^{53}Cr systematics of their evolution in O can C isotopic composition. *Lunar and Planetary Science Conference XL*. LPI, The Woodlands, TX.

Petitat M., Marrocchi Y., McKeegan K. D., Mostefaoui S., Meibom A., Zolensky M., and Gounelle M. (2011) ^{53}Mn-^{53}Cr ages of Kaidun carbonates. *Meteoritics & Planetary Science* **46**, 275-283.

Putnis A. (2009) Mineral Replacement Reactions. In: Oelkers, E. H. and Schott, J. Eds.), *Thermodynamics and Kinetics of Water-Rock Interaction*. Mineralogical Society of America, Chantilly.

Riciputi L. R., McSween H. Y., Jonson C. A., and Prinz M. (1994) Minor and trace-element concentrations in carbonates of carbonaceous chondrites, and implications for the compositions of co-existing fluids. *Geochimica et Cosmochimica Acta* **58**, 1343-1351.

Rubin A. E., Trigo-Rodriguez J. M., Huber H., and Wasson J. T. (2007) Progressive aqueous alteration of CM carbonaceous chondrites. *Geochimica et Cosmochimica Acta* **71**, 2361-2382.

Rubin A. E. (2012) Collisional facilitation of aqueous alteration of CM and CV carbonaceous chondrites. *Geochimica et Cosmochimica Acta* **90**, 181-194.

Score R. and Lindstrom M. M. (1990) Guide to the U.S. collection of Antarctic meteorites 1976-1988. *Antarctic Meteorite Newsletter* **13**, 40,41,88.

Sears D. W. G., Lu J., Benoit P. H., Dehart J. M., and Lofgren G. E. (1992) A compositional classification scheme for meteoritic chondrules. *Nature* **357**, 207-210.

Shukolyukov A. and Lugmair G. W. (2000) Chromium-isotopic anomalies in the carbonaceous chondrites Allende and Orgueil and a potential connection between chromium-54 and oxygen isotopes. *Meteoritics & Planetary Science* **35**.

Shukolyukov A. and Lugmair G. W. (2006) Manganese-chromium isotope systematics of carbonaceous chondrites. *Earth and Planetary Science Letters* **250**, 200-213.

Sleep N. H., Meibom A., Fridriksson T., Coleman R. G., and Bird D. K. (2004) H2-rich fluids from serpentinization: Geochemical and biotic implications. *P Natl Acad Sci USA* **101**, 12818-12823.

Sugiura K., Ichimura K., Fujiya W., and Takahata N. (2010a) A progress report on the Mn/Cr relative sensitivity for carbonate measured with a NanoSIMS. *Lunar and Planetary Science Conference* Houston.

Sugiura N., Ichimura K., Fujiya W., and Takahata N. (2010b) Mn/Cr relative sensitivity factors for synthetic calcium carbonate measured with a NanoSIMS ion microprobe. *Geochem J* **44**, E11-E16.

Tucker M. and Write V. P. (1990) Dolomites and dolomitization models, *Carbonate Sedimentology*. Blackwell Science, Malden, MA.

Tucker M. E. and Wright V. P. (1990) *Carbonate Sedimentology*. Blackwell Science Ltd., Oxford.

Tyra M. A., Brearley A. J., Hutcheon I. D., Ramon E., Matzel J., and Weber P. (2009) Carbonate formation timescales vary between CM1 chondrites ALH84051 and ALH84034. *Lunar and Planetary Science Conference XL*. Lunar Planet. Inst., Houston, TX.

Tyra M. A., Farquhar J., Guan Y., and Leshin L. A. (2012) An oxygen isotope dichotomy in CM2 chondritic carbonates—A SIMS approach. *Geochimica et Cosmochimica Acta* **77**, 383-395.

van Schmus R. and Wood J. A. (1967) A chemical-petrologic classification for chondritic meteorites. *Geochimica et Cosmochimica Acta* **31**, 747-765.

Velbel M. A., Tonui E. K., and Zolensky M. E. (2012) Replacement of olivine by serpentine in the carbonaceous chondrite Nogoya (CM2). *Geochimica Et Cosmochimica Acta* **87**, 117-135.

Wilson L., Keil K., Browning L., Krot A., and Bourcier W. (1999) Early aqueous alteration, explosive disruption, and reprocessing of asteroids. *Meteoritics & Planetary Science* **34**, 541-557.

Wright D. T. and Wacey D. (2004) Sedimentary dolomite: a reality check. *Geological Society, London, Special Publications* **235**, 65-74.

Young E. D., Zhang K. K., and Schubert G. (2003) Conditions for pore water convection within carbonaceous chondrite parent bodies – implications for planetesimal size and heat production. *Earth and Planetary Science Letters* **213**, 249-259.

Zito K. L., McKeegan K. D., Kerridge J. F., Hutcheon I. D., and Leshin L. A. (1998) Aqueous alteration on the CI parent-body evidence from oxygen and carbon isotopic studies of single carbonate grains from Orgueil. *Meteoritics & Planetary Science* **33**, A171-A172.

Zolensky M. E., Bourcier W. L., and Gooding J. L. (1989) Aqueous alteration on the hydrous asteroids - Results of Eq3/6 computer-simulations. *Icarus* **78**, 411-425.

Zolensky M. E., Mittlefehldt D. W., Lipschutz M. E., Wang M. S., Clayton R. N., Mayeda T. K., Grady M. M., Pillinger C. T., and Barber D. (1997) CM chondrites exhibit the complete petrologic range from type 2 to 1. *Geochimica et Cosmochimica Acta* **61**, 5099-5115.

Zolensky M. E., Krot A. N., and Benedix G. (2008) Record of low-temperature alteration in asteroids, *Oxygen in the Solar System*.

9 Tables

Table 1. Mn-Cr results for seven dolomite grains from ALH 84049.

Grain	type*	^{55}Mn/^{52}Cr	2σ err	δ^{53}Cr**	2σ err	Ref
13-b2, a	m	40558	17941	1443	1810	Fig. 4d
	m	15696	4222	1078	988	
	m	9657	1527	227	416	
	m	134	1	-1	22	
13-b5, a	m	10657	1626	382	431	Fig. 4f
	m	2834	148	-163	110	
	m	8	0	15	4	
13-b4, a	m	83597	50706	9298	7464	Fig. 4e
	m	13001	3151	-59	544	
	m	15	0	-80	5	
6-b10a-1, a	m	76311	15235	1466	822	Fig. 4c
	m	18074	1834	662	322	
	m	25	0	8	4	
6-b10b, a	m	40653	9869	1842	1102	Fig. 4b
	m	18189	2526	656	440	
	m	8390	810	282	261	
	m	16	0	-3	5	
6-b9, a	m	66082	13738	3242	1259	Fig. 4a
	m	21922	2167	470	291	
	m	9079	1059	293	317	
	m	274	3	-8	26	
6-b4, a	m	43351	21730	3149	2987	--
	m	19836	5221	1276	1026	
	m	8115	1123	499	412	
	m	44	0	37	8	

* m, small matrix dolomite; a, large dolomite aggregate; v, vein dolomite .

** δ^{53}Cr = (Rx/Rs-1)1000, where Rx = ^{53}Cr/^{52}Cr$_{sample}$ and Rs = ^{53}Cr/^{52}Cr$_{std}$ =0.113457 (Birck and Allegre 1988)

Table 2. Mn-Cr results for seven dolomite grains from ALH 84051

Grain	type	^{55}Mn/^{52}Cr	2σ err	δ^{53}Cr	2σ err	Ref
12-b8d, a	m	896	120	175	343	Fig. 5a
	m	420	21	61	118	
	m	25	0	-14	10	
12-b8d, b	m	36546	10280	1975	1318	Fig. 5a
	m	13519	1896	724	456	
	m	505	8	21	35	
12-b8d, c	m	14296	1372	2	223	Fig. 5a
	m	26	0	-3	5	
12-b3, a	a	10253	1872	648	577	Fig. 4h
	a	2216	189	-144	181	
	a	4	0	-3	3	
20a-b16, a	v	9129	3395	524	1118	--
	v	1583	156	118	244	
	v	23	0	-3	11	
20a-b16, b	v	8860	1680	331	524	--
	v	4926	663	78	327	
	v	24	0	-4	9	
12-b5c	a	4492	639	294	386	Fig. 4g
	a	768	27	-30	82	
	a	9	0	2	3	
12-b5e	m	7	0	-7	3	--
20a-b9	v	6195	277	705	248	
	v	1746	78	285	120	
	v	438	20	71	52	
	v	2	0	11	3	
20a-b16, c	v	6093	272	308	192	--
	v	1352	60	153	73	
	v	371	17	-3	40	
	v	9	0	6	4	
	v	240	11	1	32	
	v	397	18	60	52	
20a-b12	v	11752	525	993	575	--
	v	2837	127	193	127	
	v	529	24	42	56	
	v	1	0	-4	3	
	v	12	1	0	15	
	v	12	1	-7	11	

* m, small matrix dolomite; a, large dolomite aggregate; v, vein dolomite .

** δ^{53}Cr = (Rx/Rs-1)1000, where Rx = ^{53}Cr/^{52}Cr$_{sample}$ and Rs = ^{53}Cr/^{52}Cr$_{std}$ =0.113457 (Birck and Allegre 1988)

10 Figures

Figure 1. Stitched composite Ca (red) Mg (green) Si (blue) RGB X-ray maps of ALH 84051 (a) and ALH 84049 (b). Calcite appears as red, dolomite orange, forsterite neon-green, and serpentine varying shades of green depending upon Mg and Fe abundance; lighter greens are more iron-rich. The circular pale blue-green features are chondrule pseudomorphs. The linear vein features in the lower third of the image shown in (a) are dolomite veins. The serpentine around the veins is lighter green (i.e. more Fe-rich) than serpentine within most of the matrix. Some prominent dolomite aggregates are also labeled; these only occur in ALH 84051 (a). Matrix carbonates are small and dispersed throughout the sample. The two lower boxes in (a) denote areas shown in Fig. 2 g and h. The mineralogy of the area in the upper box is discussed in the text. Rounded black features in (a) are areas plucked during sample preparation.

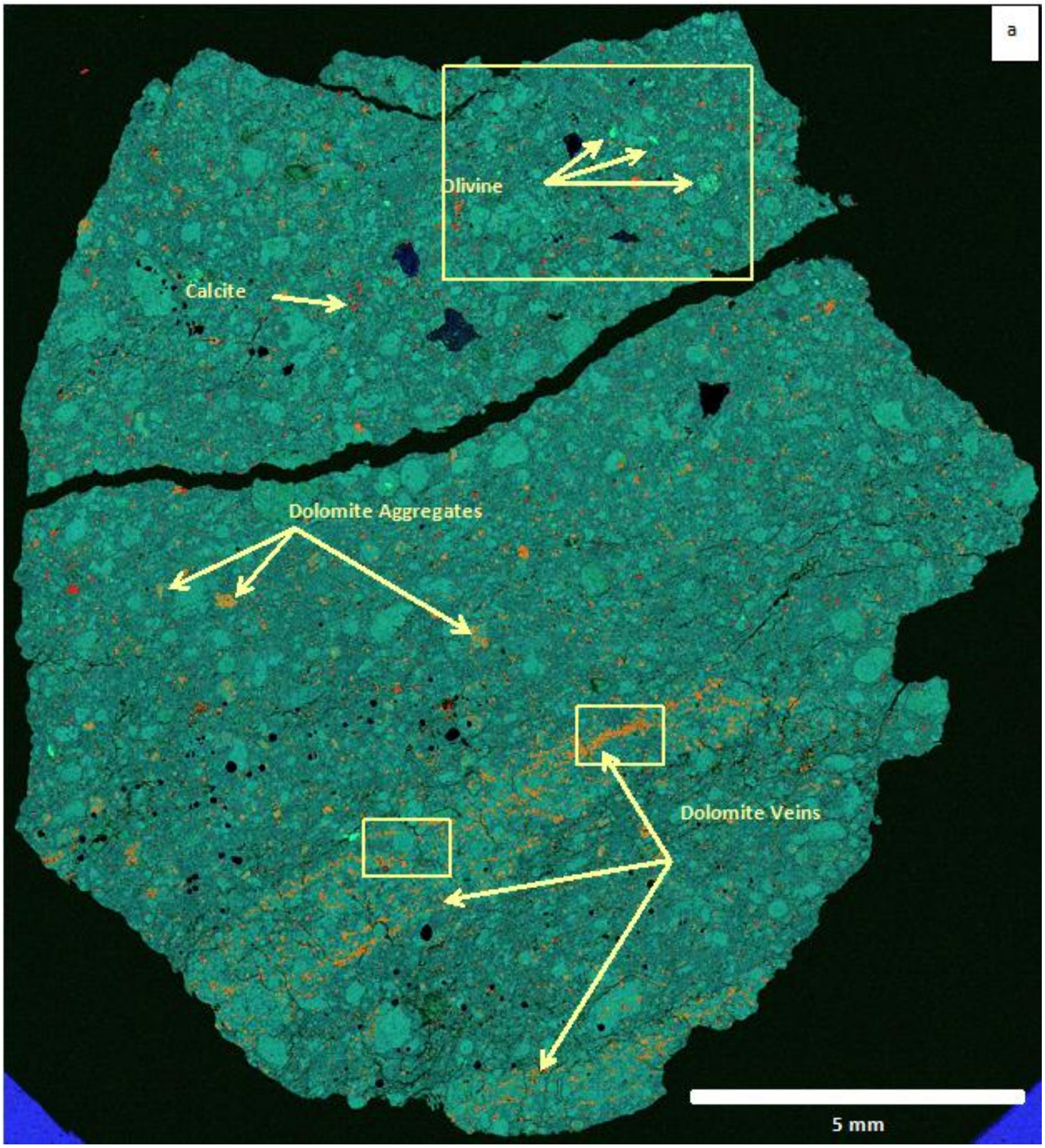
a
Olivine
Calcite
Dolomite Aggregates
Dolomite Veins
5 mm

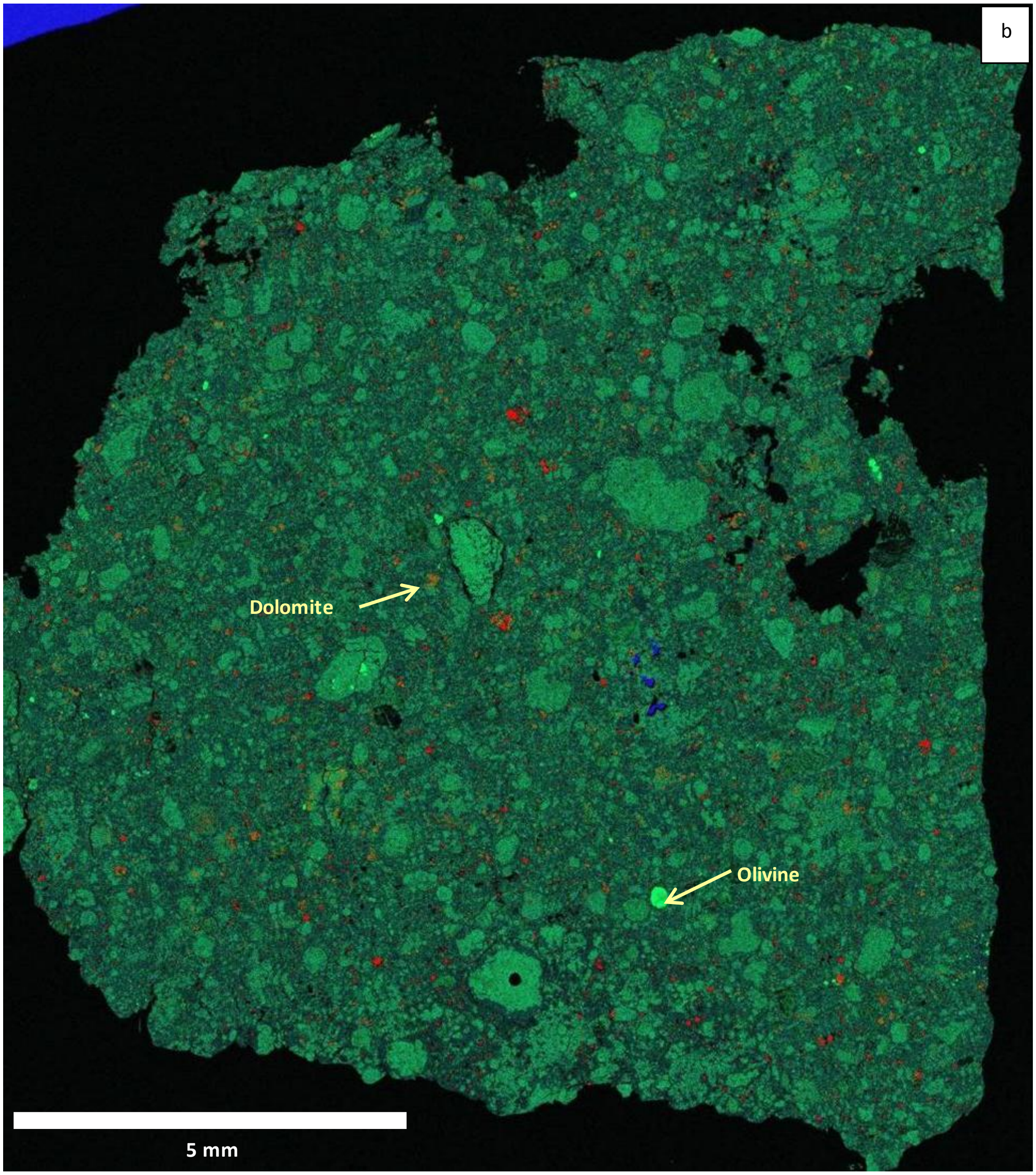
b
Dolomite
Olivine
5 mm

Figure 2. BSE images showing representative examples of the textures and occurrence of chondrules and chondrule pseudomorphs in ALH 84049 and ALH 84051.

a) BSE image showing an example of a chondrule in ALH 84051 which has been completely replaced by secondary phases. Pseudomorphic replacement of chondrule phenocrysts, probably olivine, by serpentine has occurred (arrowed). Based on BSE contrast, the serpentine replacement products of olivine appear to more Fe-poor than serpentine that has replaced the surrounding mesostasis (indicated). The very bright, high Z phase distributed through the chondrule and as a rim around the periphery of the chondrule pseudomorph is Fe sulfide.

b) BSE image of a completely altered chondrule in ALH 84049. The distinct continuous crack defines the periphery of the chondrule pseudomorph. The chondrule pseudomorph consists of medium-to-fine-grained phyllosilicates. There is no fine-grained rim around the chondrule and unlike the chondrule in Fig. 2a, no sulfide rim is evident.

c) BSE image of a probable fragment of an incompletely altered chondrule from ALH 84049. The fragment consists primarily of forsteritic olivine with sparse 1-5 μm metal blebs within the forsterite (white in image). The interior of the chondrule has undergone probable dissolution and replacement by Mg-rich serpentine (darker) and more Fe rich serpentine (lighter). Two dolomite grains (one ~5μm and the other ~20 μm diameter) are also found within the altered interior. No fine grain rim is observed.

d) Area of ALH 84049 showing isolated carbonates, sulfide, forsteritic olivine, and matrix. The ~150 μm olivine grains are fractured and phyllosilicate is present in the chondrule interior. A ~80 μm sulfide grain (white) lies near the olivine. Calcite grains are 20-30 μm diameter, are un-rimmed, and appear to have etched edges. Dolomite appears more pristine than calcite with straight, cleavage-defined edges. Also note the honeycombed, mudcracked (mc) matrix texture throughout the field of view that is defined by white lines.

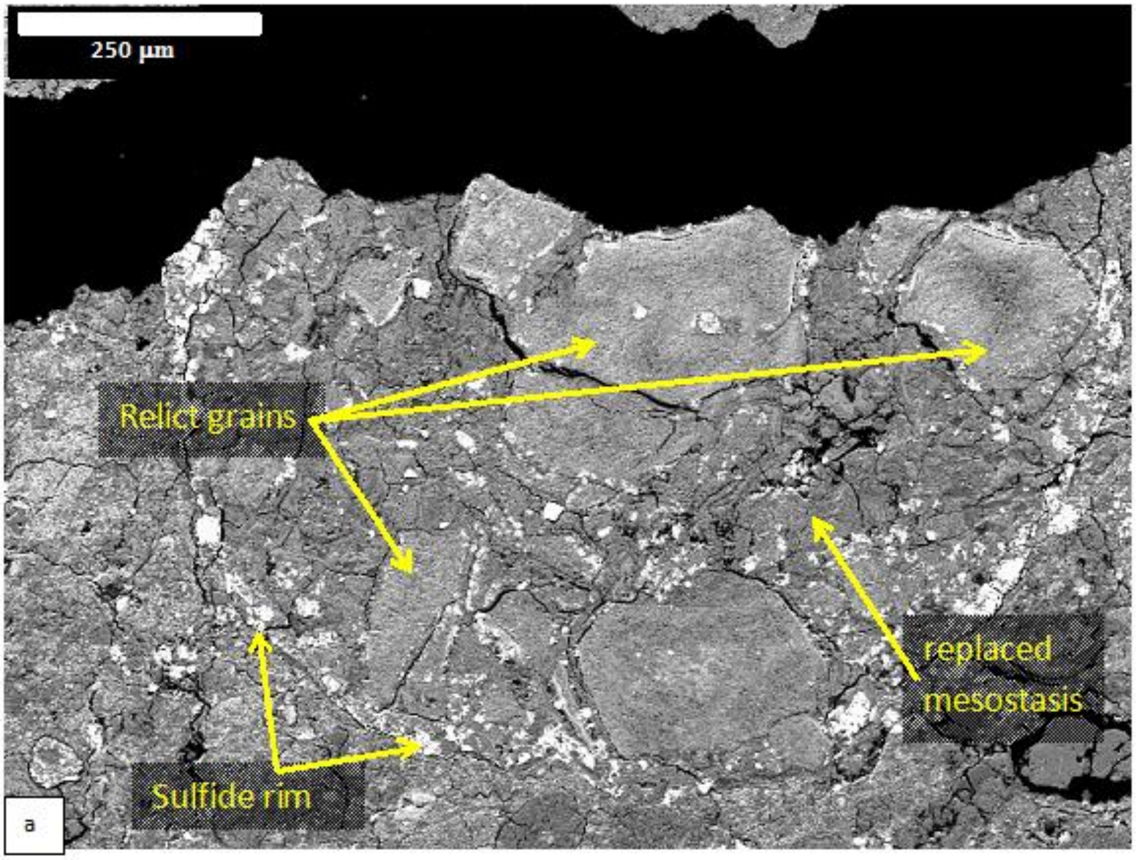
250 µm
Relict grains
replaced mesostasis
Sulfide rim
a

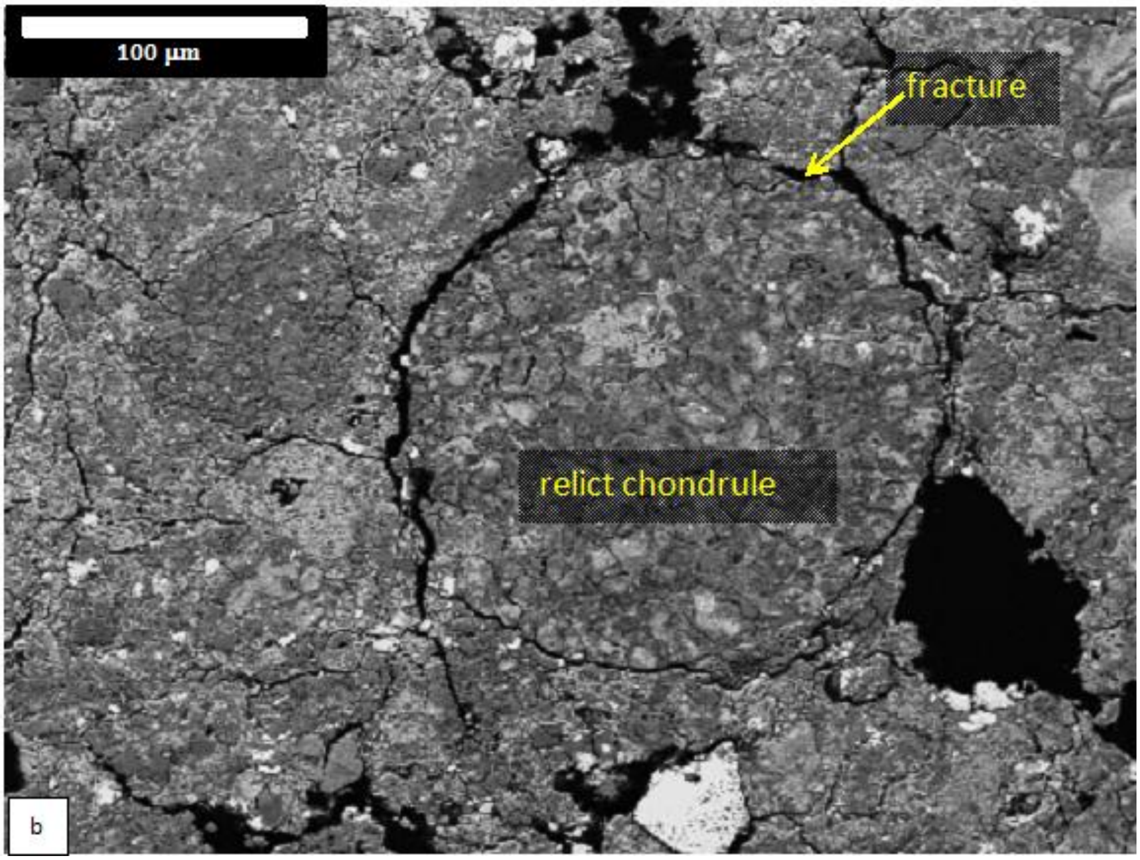
100 µm
fracture
relict chondrule
b

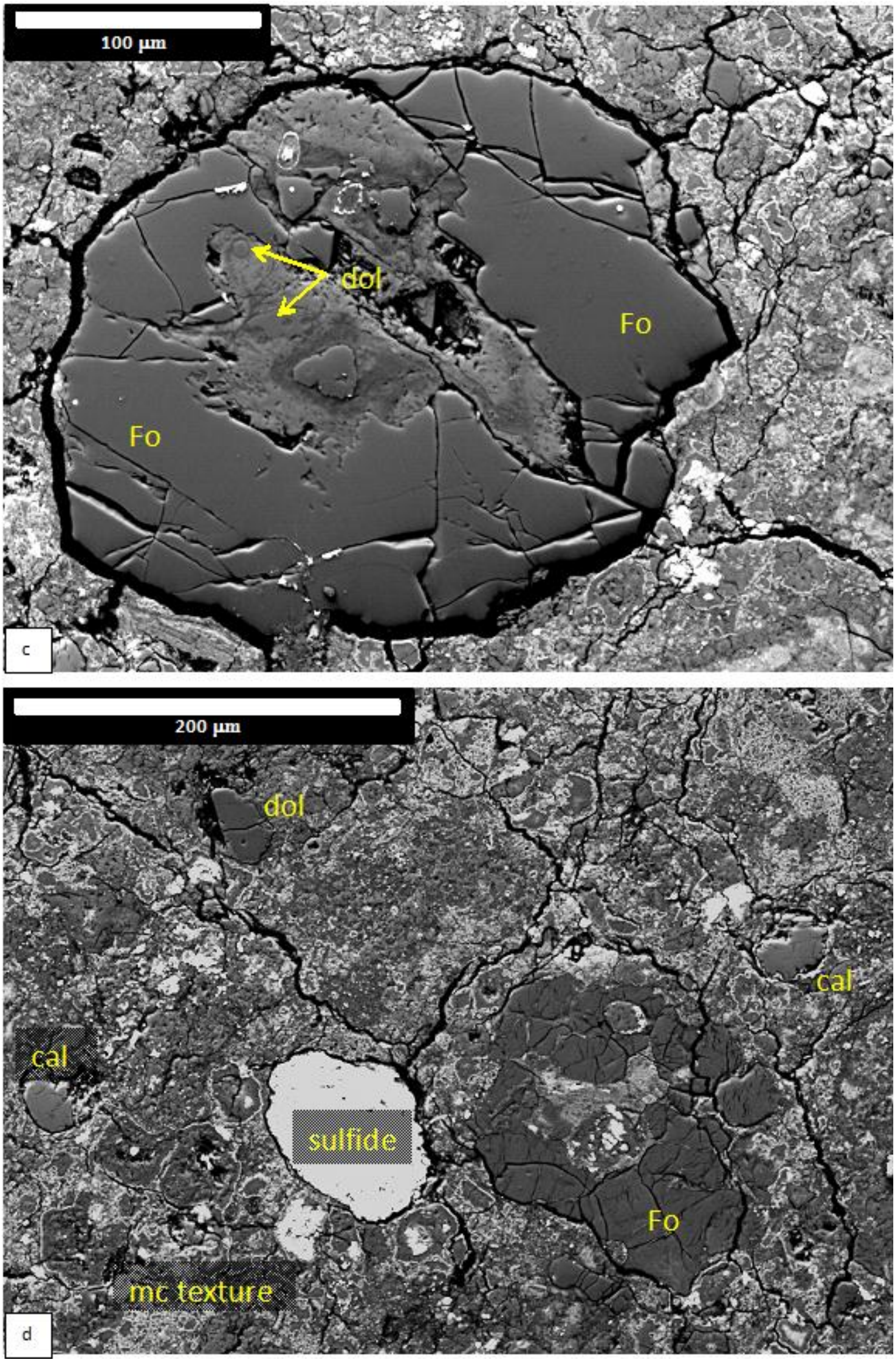
100 µm
dol
Fo
Fo
c
200 µm
dol
cal
cal
sulfide
Fo
mc texture
d

Figure 3. BSE images of individual carbonate grains, dolomite veins, and dolomite aggregates.

a) Representative region of matrix showing examples of the typical occurrence of carbonates (ALH 84049). Four dolomite grains are present, ranging from 10 to 50 μm in diameter. Most dolomite is fractured but unaltered. An exception is the round 50 μm dolomite at the bottom left, where the core of the grain is porous, which may indicate alteration. As in Fig. 2d, a mudcrack-like (mc) texture is apparent throughout the matrix. A single calcite grain (20-30 μm diameter) is present in this figure.

b) Polyphase aggregate of porous dolomite, sulfide, and phyllosilicate that may represent a replaced CAI or chondrule in ALH 84049. The aggregate is almost completely rimmed by a very narrow layer of a high Z phase that is consistent with Fe-rich serpentine. Dolomite grains range from ~20 μm to 100 μm diameter. Although some areas are clean, most dolomites have porous areas, some which form linear features that may follow cleavage traces.

c) Image of an exceptionally well-defined dolomite vein consisting of 10-50 μm diameter subgrains. The field of view of this image is marked on Fig. 1a, the right boxed area of ALH 84051. In this area, the vein is ~100μm in width.

d) Examples of more typical, disseminated dolomite veins from Fig. 1a in the lower left boxed area from ALH 84051. As in Fig. 3c, the veins are also composed of smaller dolomite subgrains, but unlike Fig. 3c the dolomites do not necessarily abut one another in this two-dimensional section. The vein widths are variable, but are generally less than 50 μm wide. The dolomite vein seems to wrap around a relict 200 μm diameter chondrule.

e) A large dolomite aggregate with a 10-20 μm Fe-rich serpentine rim. The aggregate appears to have corroded margins alongside the rim. Other nearby dolomite grains are indicated; these are typically 10-25 μm diameter, rimless, matrix dolomite grains.

f) A dolomite aggregate at high magnification. The entire field of view is dolomite with the exception of Mg-rich serpentine inclusions (arrowed and delineated by white lines).

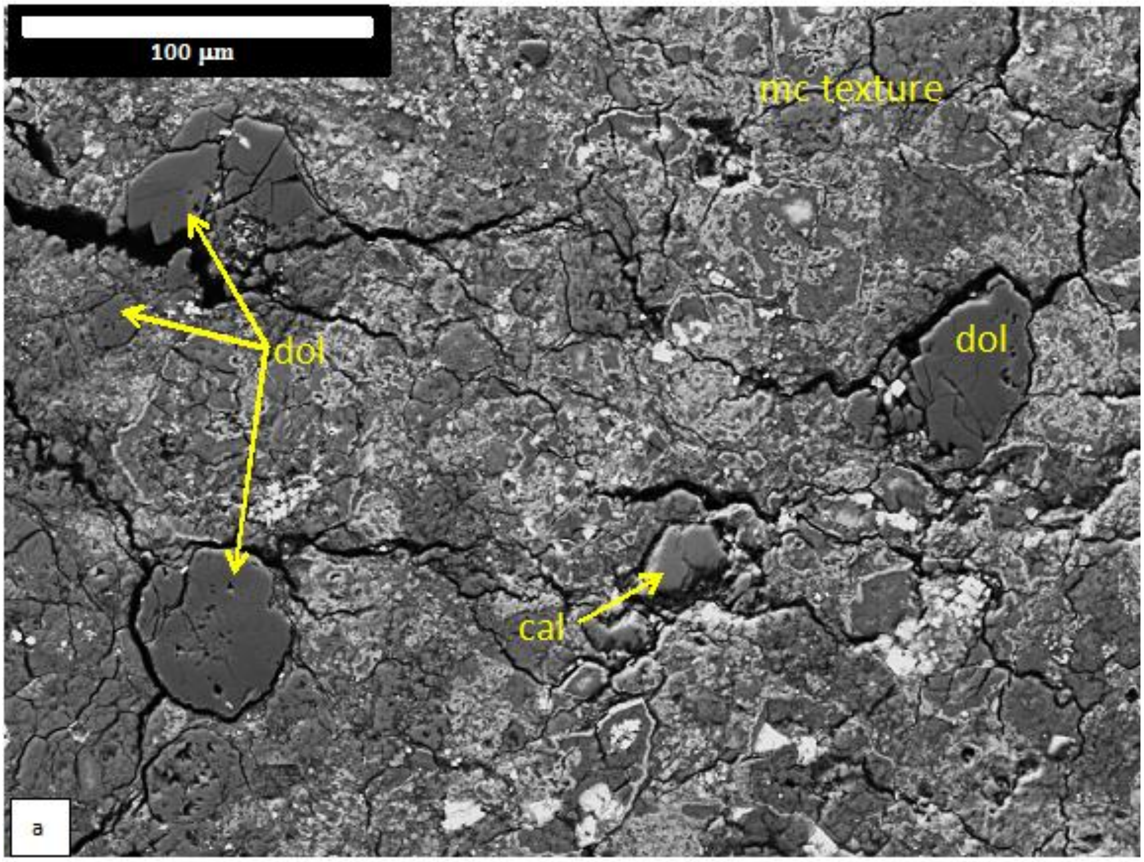
100 µm
mc texture
dol
dol
cal
a

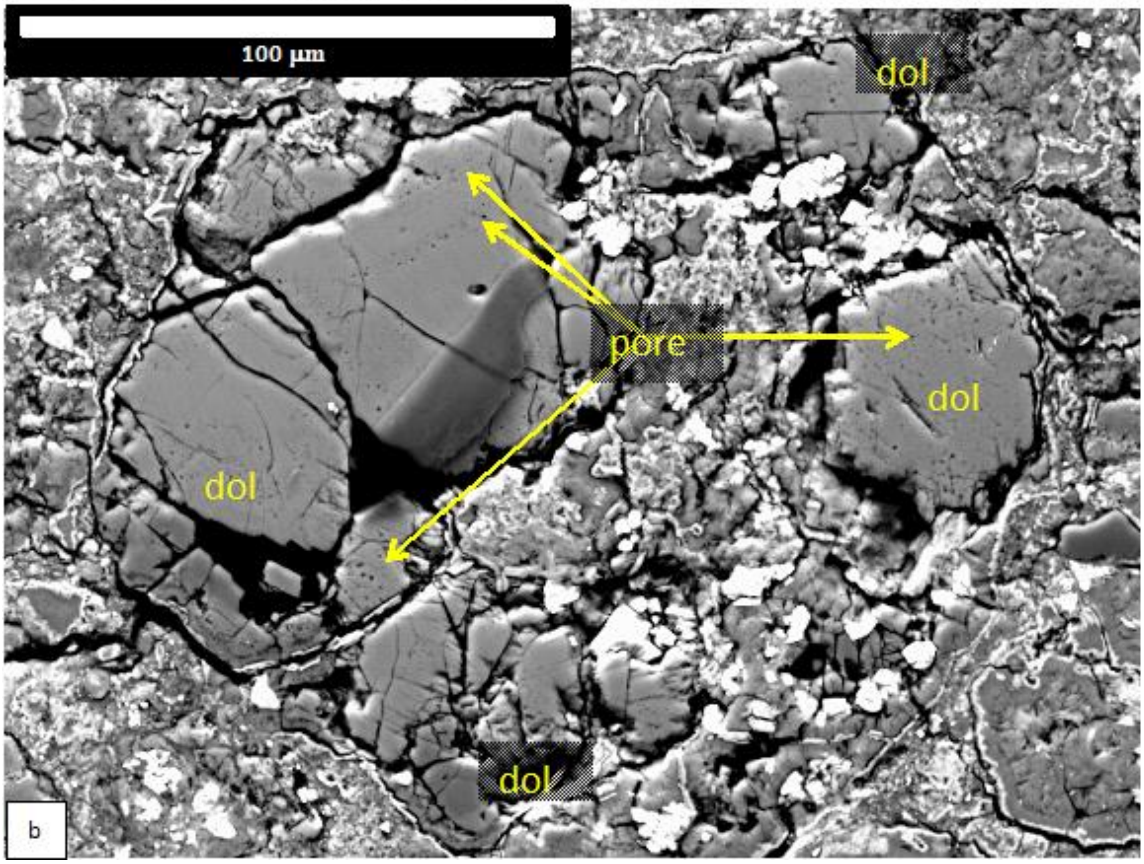
100 µm
dol
pore
dol
dol
dol
b

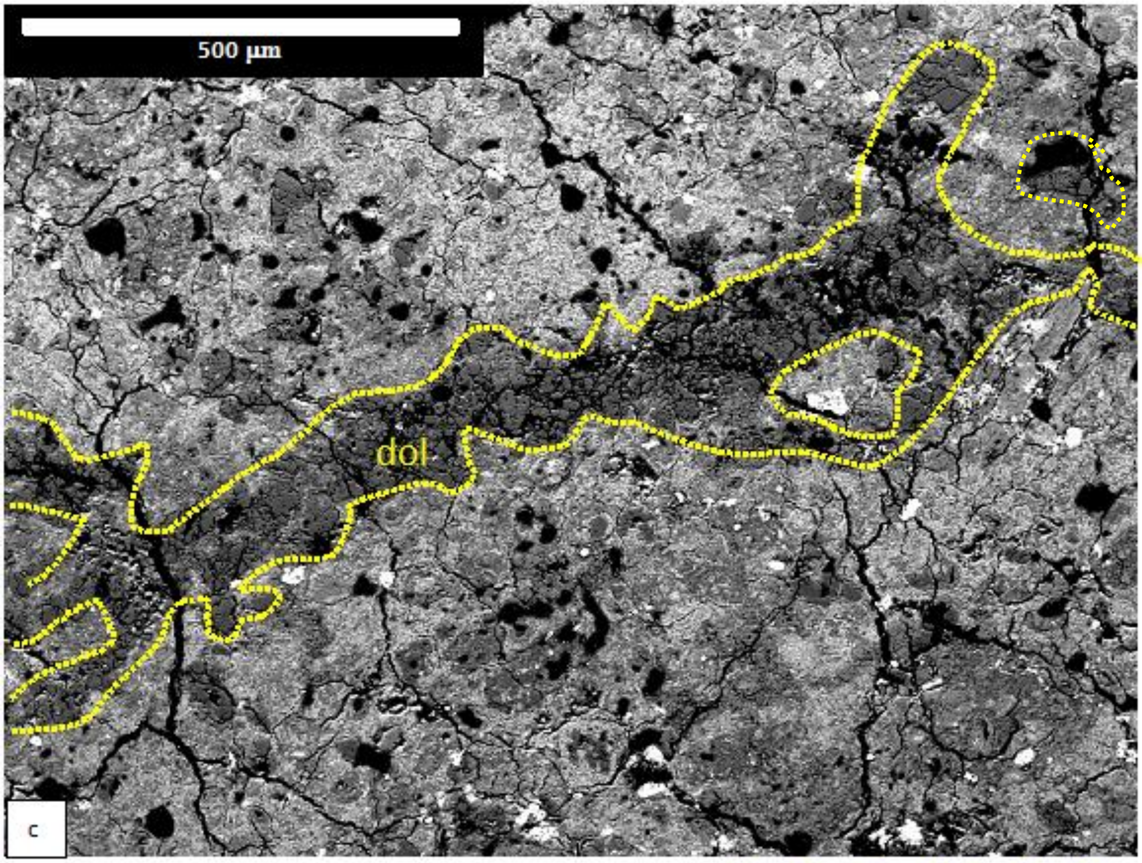
500 µm
dol
c

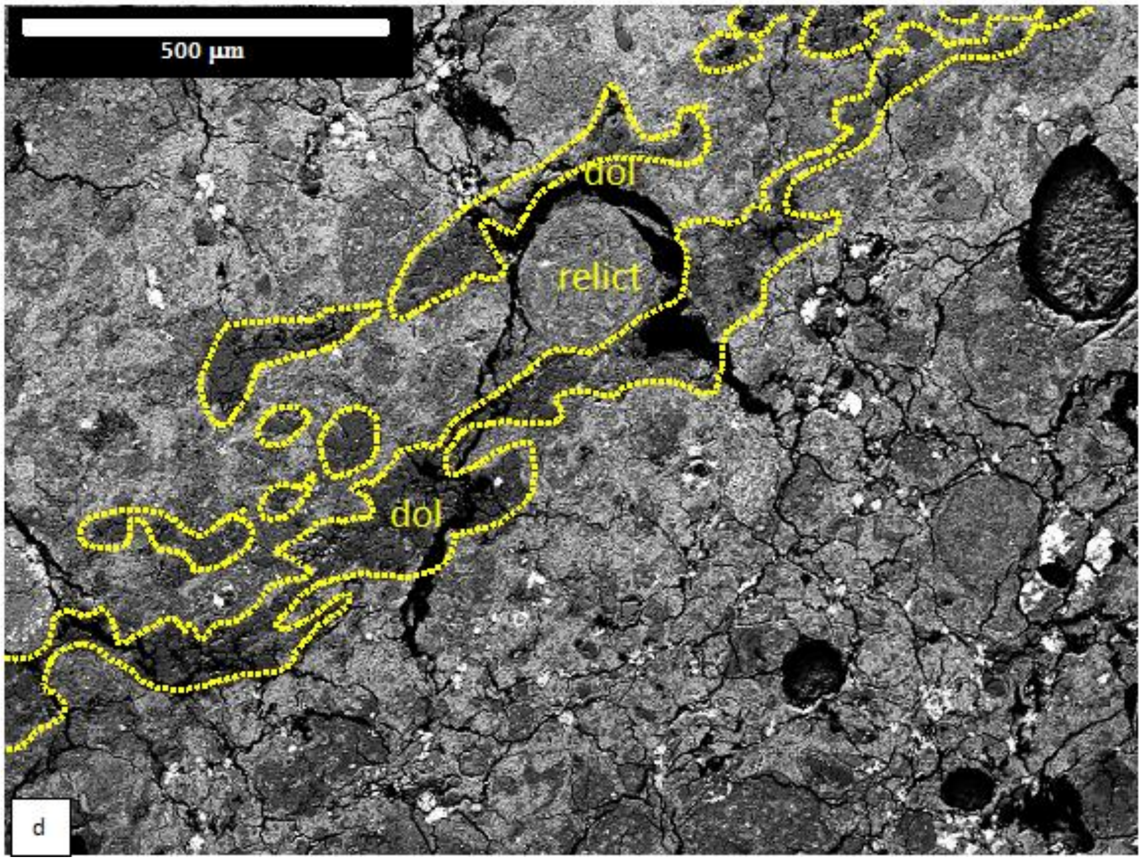
500 µm
dol
relict
dol
d

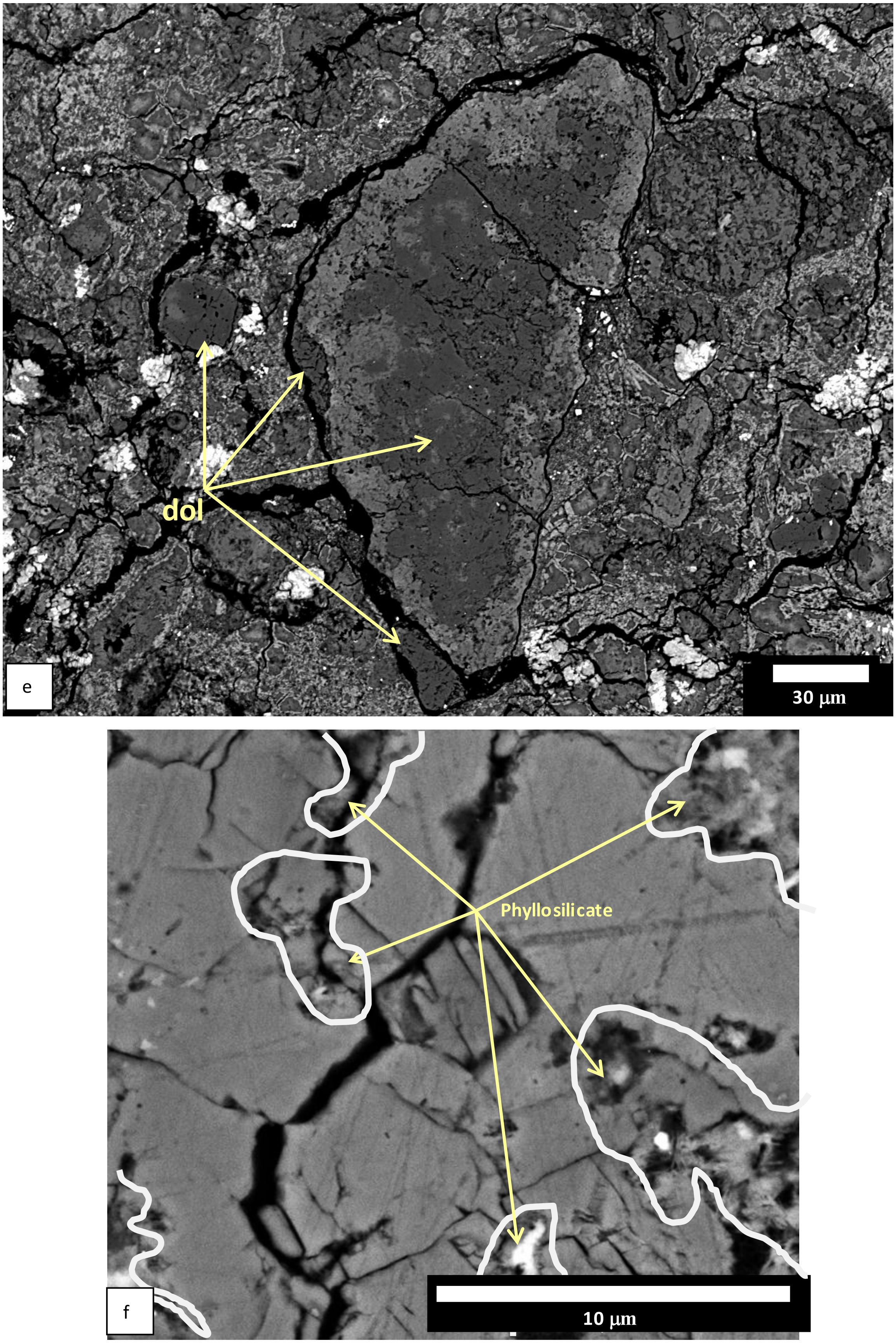
dol
e
30 μm
Phyllosilicate
f
10 μm

Figure 4. Figures 4a-4f show BSE images, CL images, Mn X-ray maps, and Fe X-ray maps of individual dolomite grains from ALH 84049. Figures 4g-4k contrast BSE images with the Mn X-ray map in ALH 84051. Scales and rotation of grains in images are generally equivalent, although some FOV shift or rotation may be apparent (such as the CL image in Fig. 4e). Colors in the X-ray maps are scaled with composition. Cathodoluminescence images, such as Fig. 4e and 4f show an artifact due to electrical interferences.

Zoning in CL is apparent and correlates roughly with presence of Mn and lack of Fe (Fig. 4e is an exception and CL correlates solely with the absence of Fe). Calcite has a much higher CL response than dolomite. Figures 4a-c exhibit complex, patchy zoning, occasionally with low CL in cores and higher CL in rims. Fig. 4a shows extensive porosity and Fig. 4c a small 5x10 μm calcite grain (extremely bright CL) enclosed within the dolomite grain. Figure 4d also has an area with low CL; this grain exhibits well expressed overgrowths clearly visible in CL image and in both X-ray maps. Conversely, Figures 4e and 4f have areas with low CL on grain peripheries. Figures 4g and 4h show two dolomite aggregates with compositional zoning. Figures 4i-4k show individual dolomite grains from dolomite veins; these also are compositionally zoned.

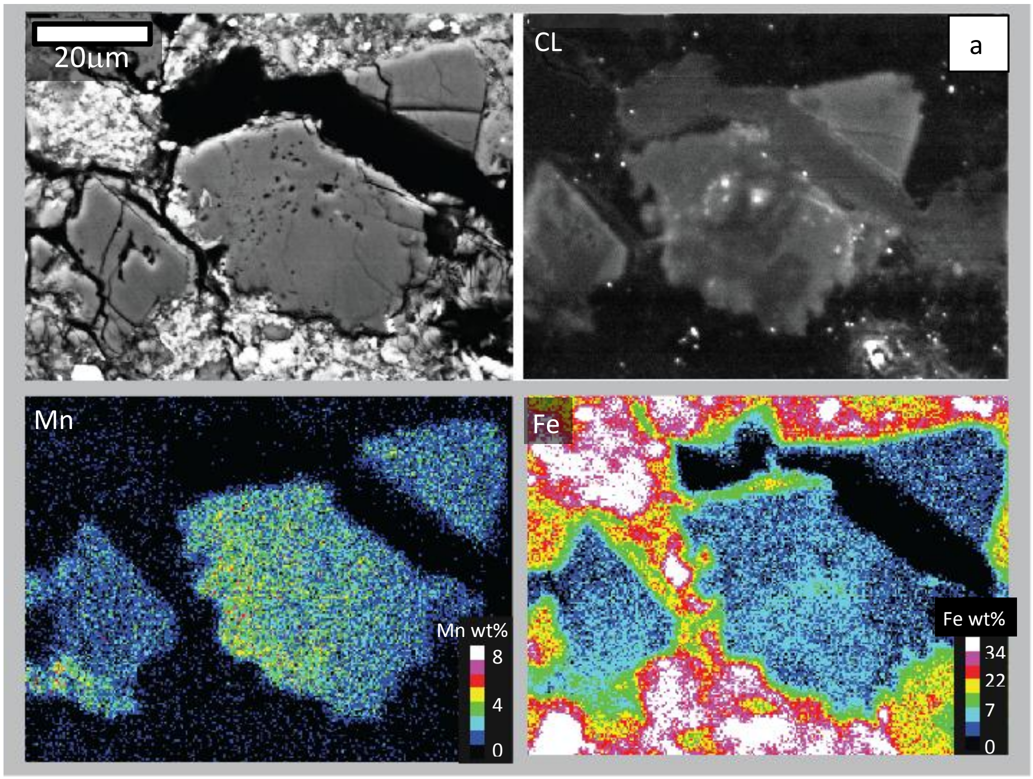
20µm
CL
a
Mn
Mn wt%
8
4
0
Fe
Fe wt%
34
22
7
0

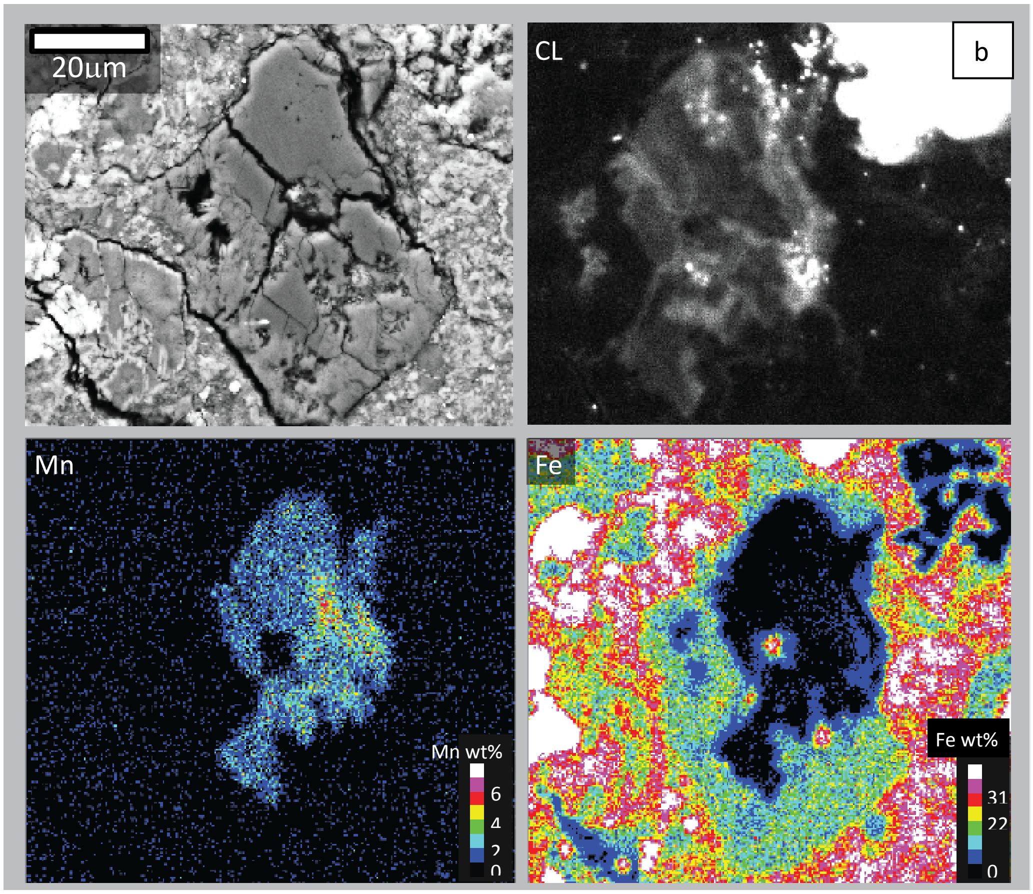
20µm
CL
b
Mn
Mn wt%
6
4
2
0
Fe
Fe wt%
31
22
0

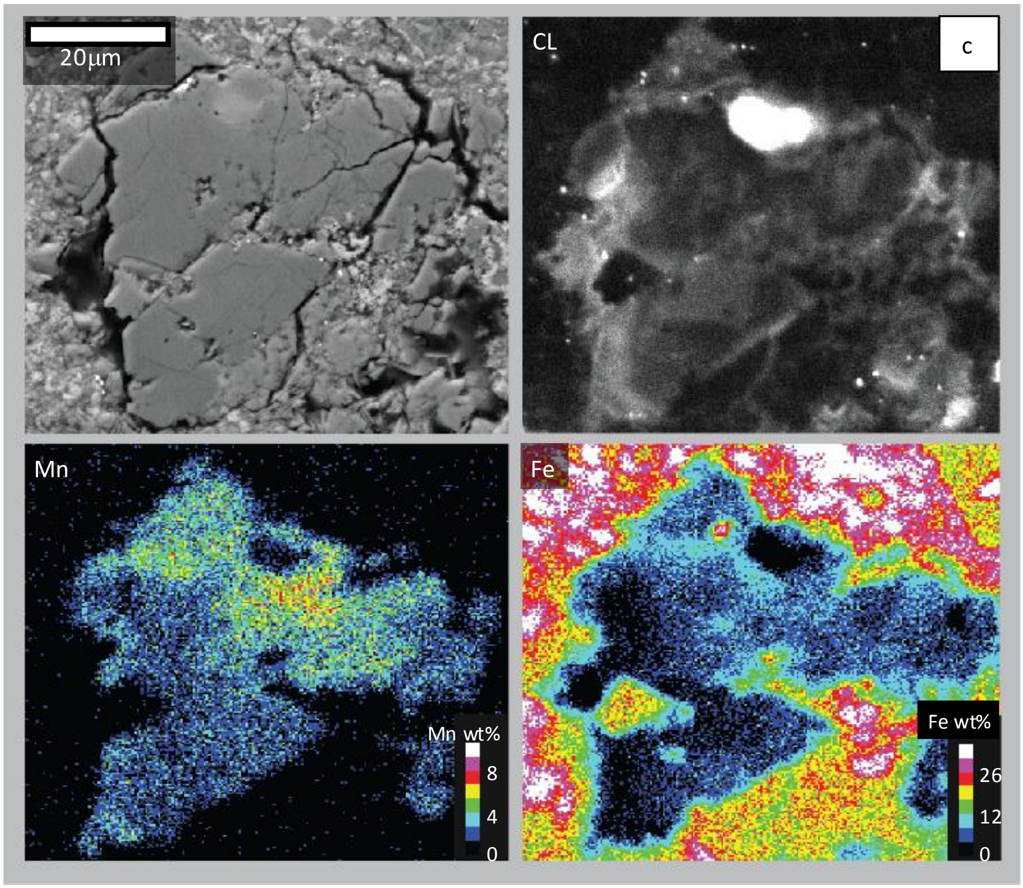
20μm
CL
c
Mn
Fe
Mn wt%
8
4
0
Fe wt%
26
12
0

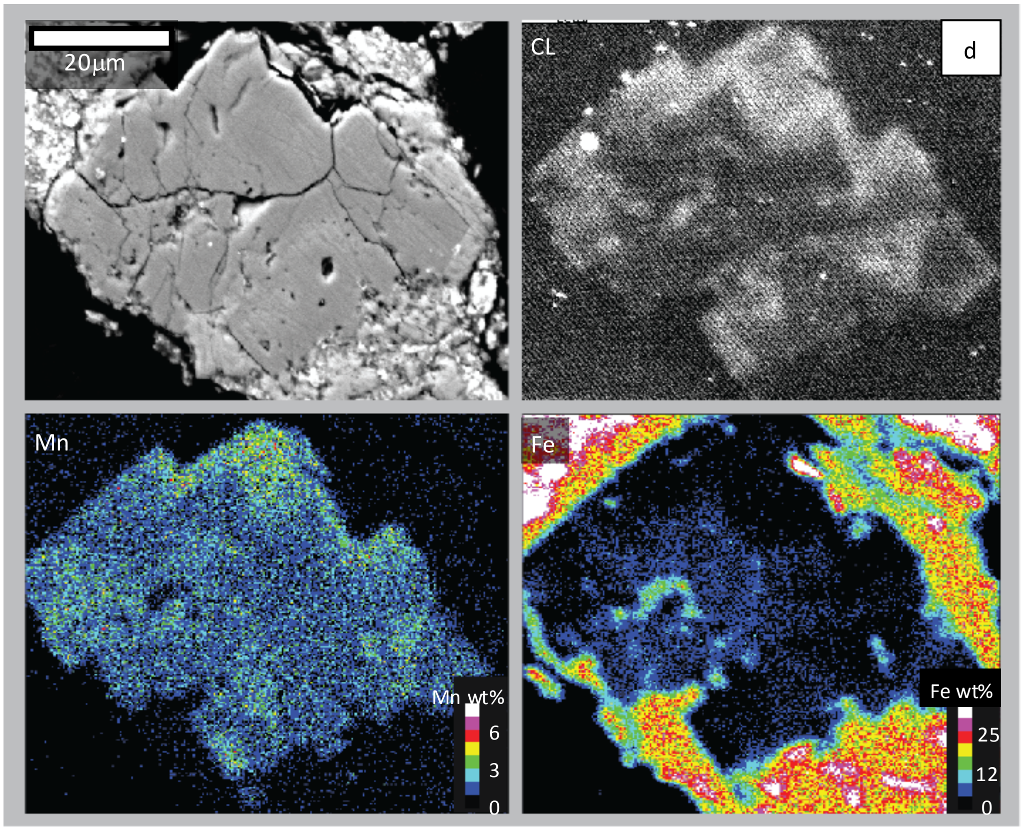
20μm
CL
d
Mn
Fe
Mn wt%
6
3
0
Fe wt%
25
12
0

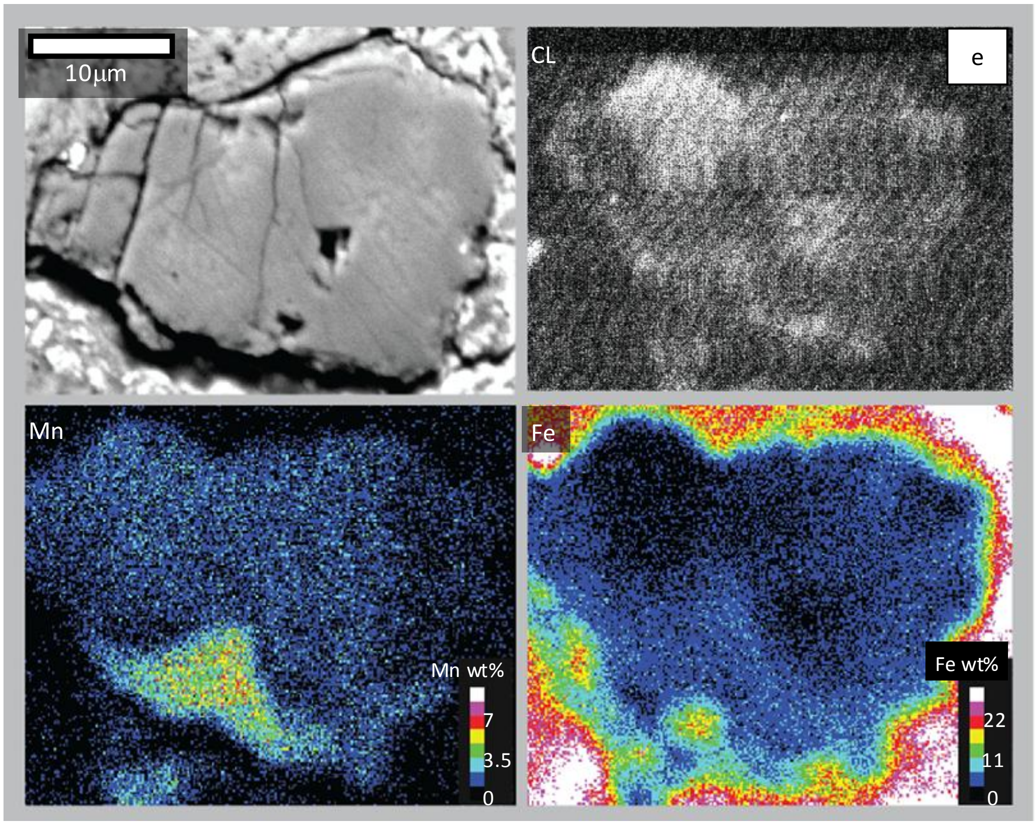
10μm
CL
e
Mn
Fe
Mn wt%
7
3.5
0
Fe wt%
22
11
0

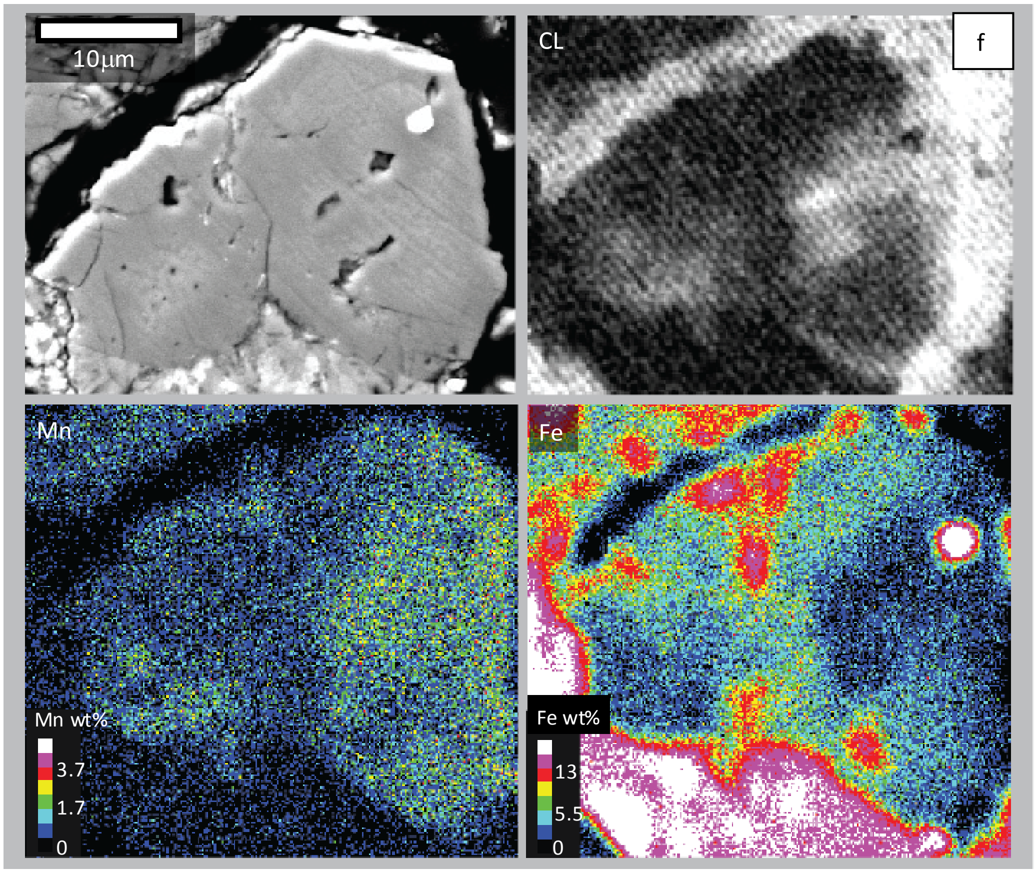
10μm
CL
f
Mn
Fe
Mn wt%
3.7
1.7
0
Fe wt%
13
5.5
0

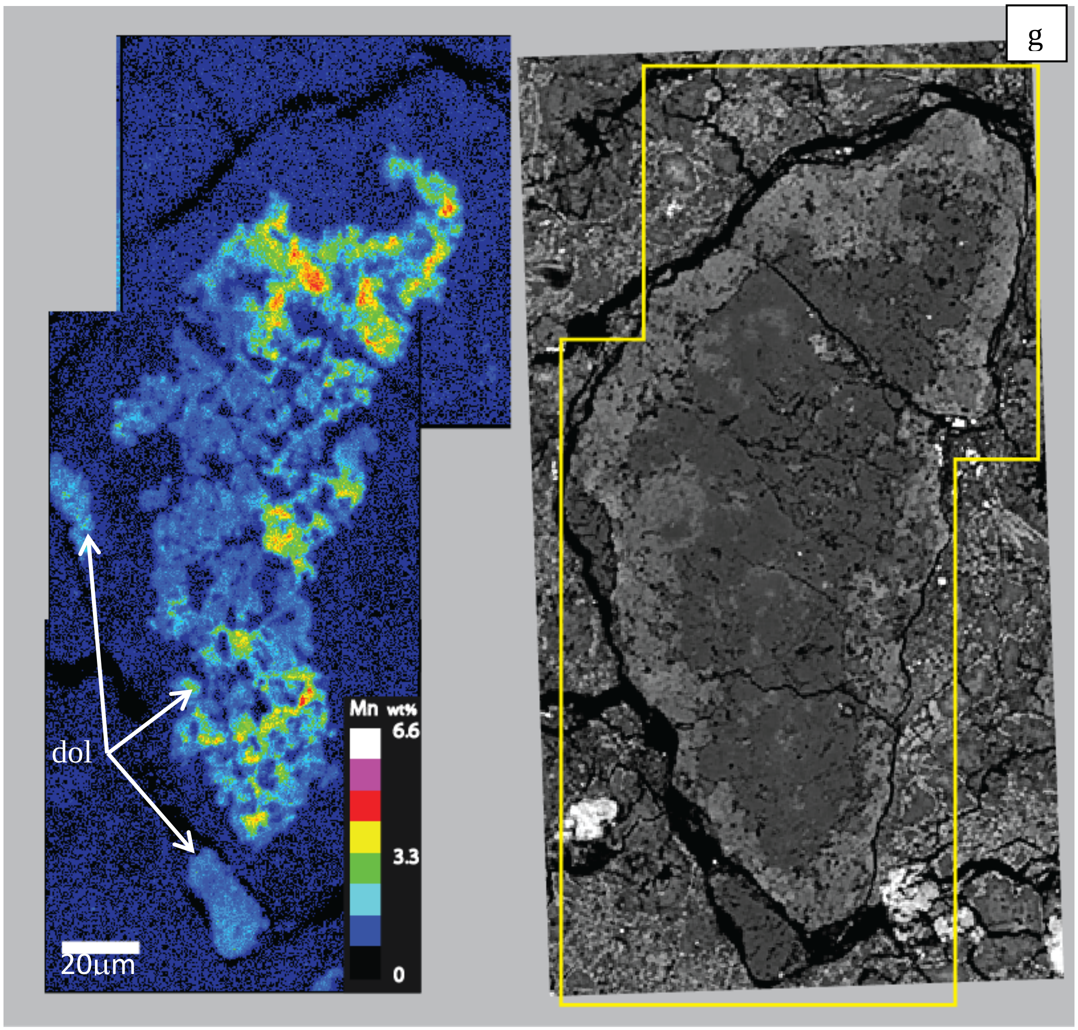
g
Mn wt%
6.6
3.3
0
dol
20μm

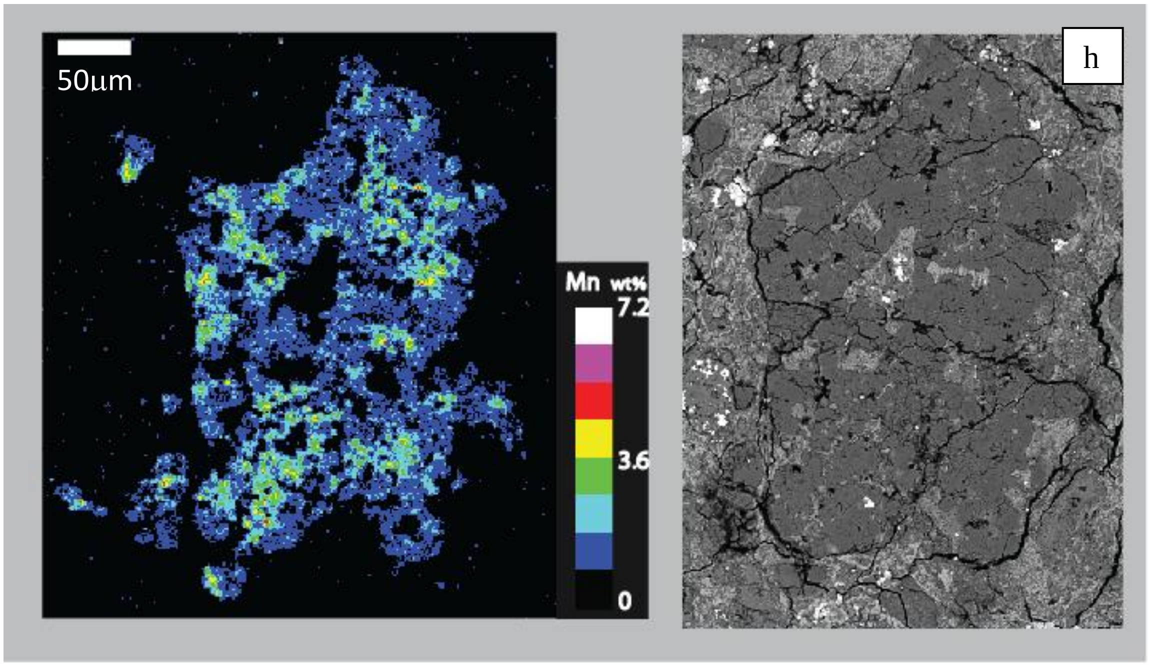
h
50μm
Mn wt%
7.2
3.6
0

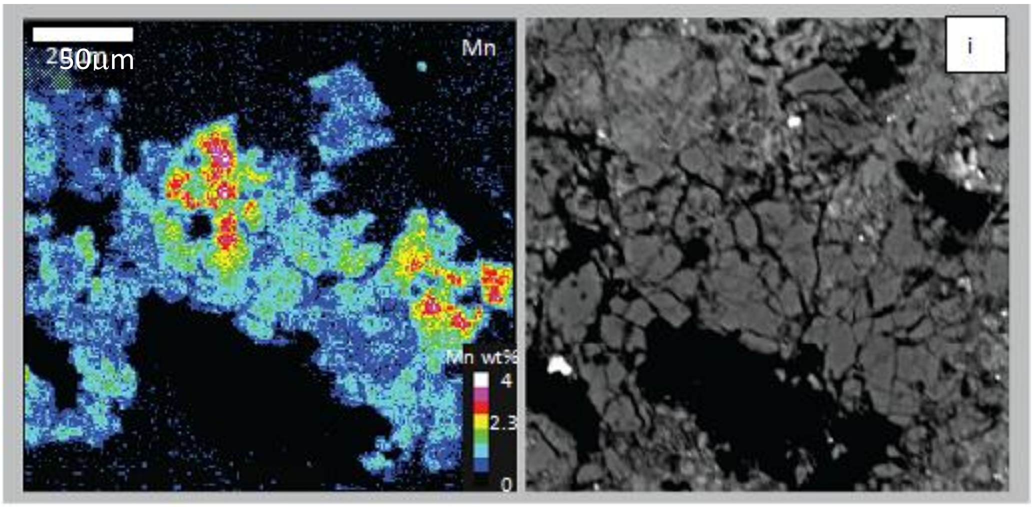
50µm
Mn
Mn wt%
4
2.3
0
i

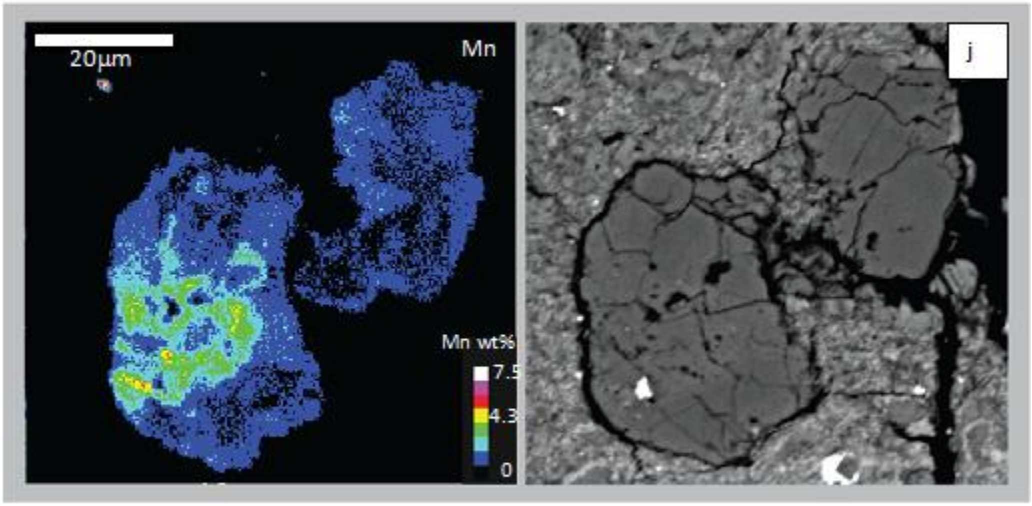
20µm
Mn
Mn wt%
7.5
4.3
0
j

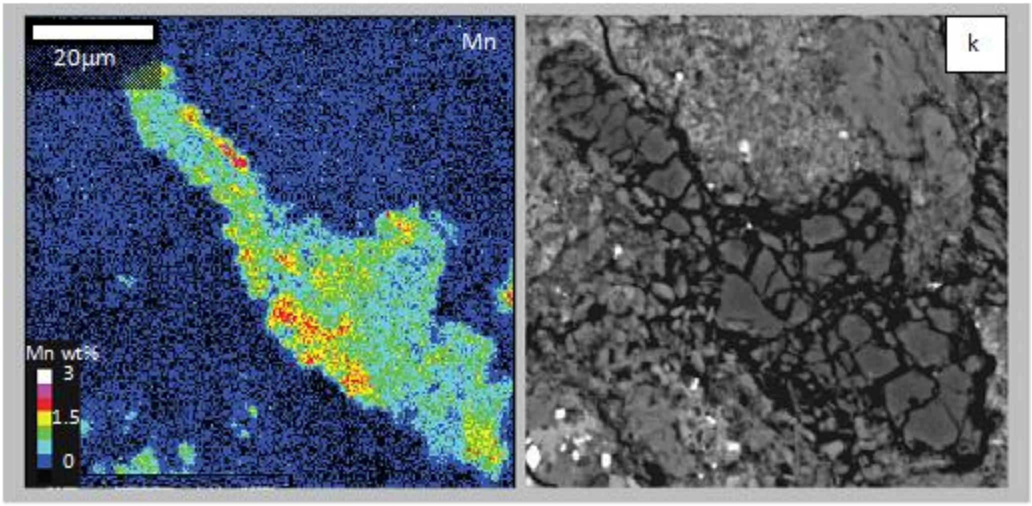
20µm
Mn
Mn wt%
3
1.5
0
k

Figure 5. BSE and CL images of ALH 84051 carbonate grains and EPMA compositional transects of these grains. The transect path is indicated on the carbonate image as arrows. Grain (a) is a matrix grain while (b) and (c) are vein carbonates.

a) Dolomite (in box) and calcite. The CL map is only of the dolomite grain in the box. The transect of dolomite shows an anticorrelation between CaO and both MgO and FeO. MnO is uniform throughout the transect. There is no obvious relationship between CL and elemental abundances.
b) Two transects of one dolomite grain. Unlike Fig. 5a, CaO and MgO trend together and FeO is anticorrelated. Cores are higher in FeO and MnO than rims; CaO and MgO abundances are lower in the core than the rims.
c) Dolomite grain. CaO is anticorrelated with FeO. MnOis relatively flat and MgO content increases across the grain. Note that the first plotted analysis in the transect is 10 μm into the interior of the grain within an area of low CL. The first point of the transect was rejected due to high SiO_2 content.

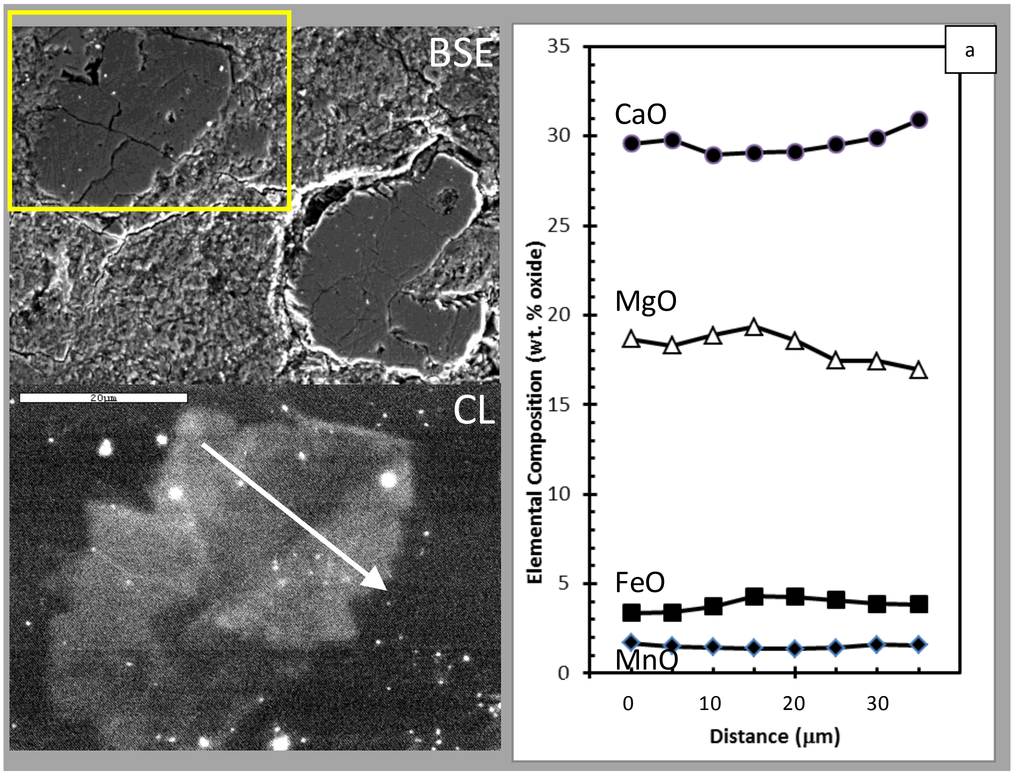

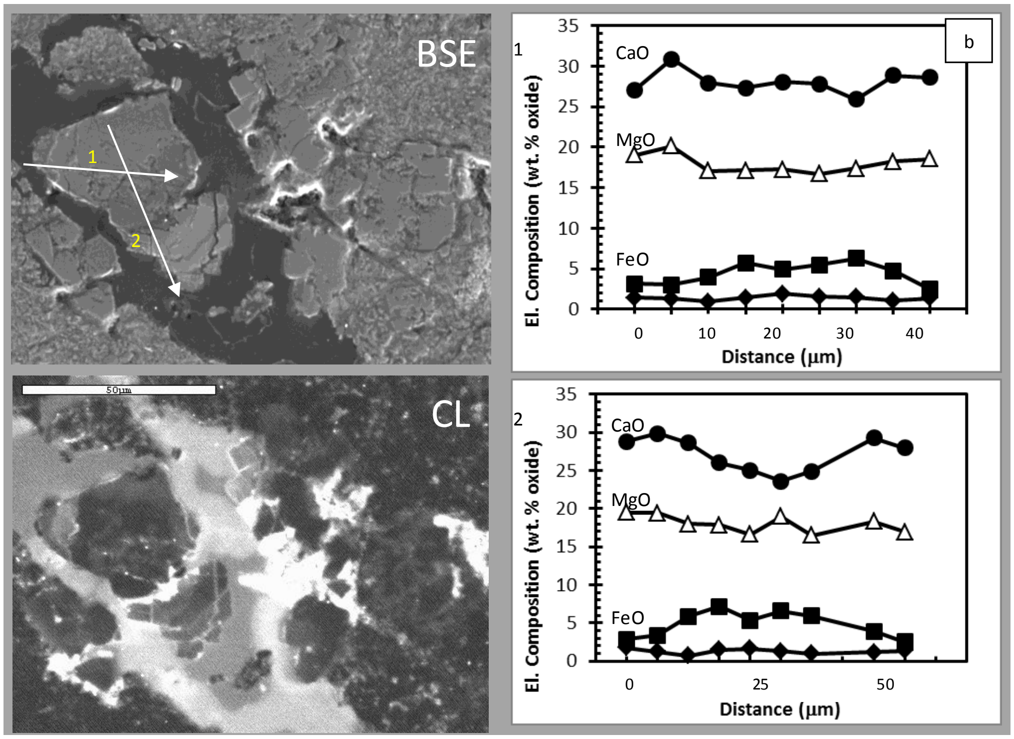
BSE
1
2
CL
50µm
b
1
2
CaO
MgO
FeO
El. Composition (wt.% oxide)
0
5
10
15
20
25
30
35
0
10
20
30
40
0
25
50
Distance (µm)

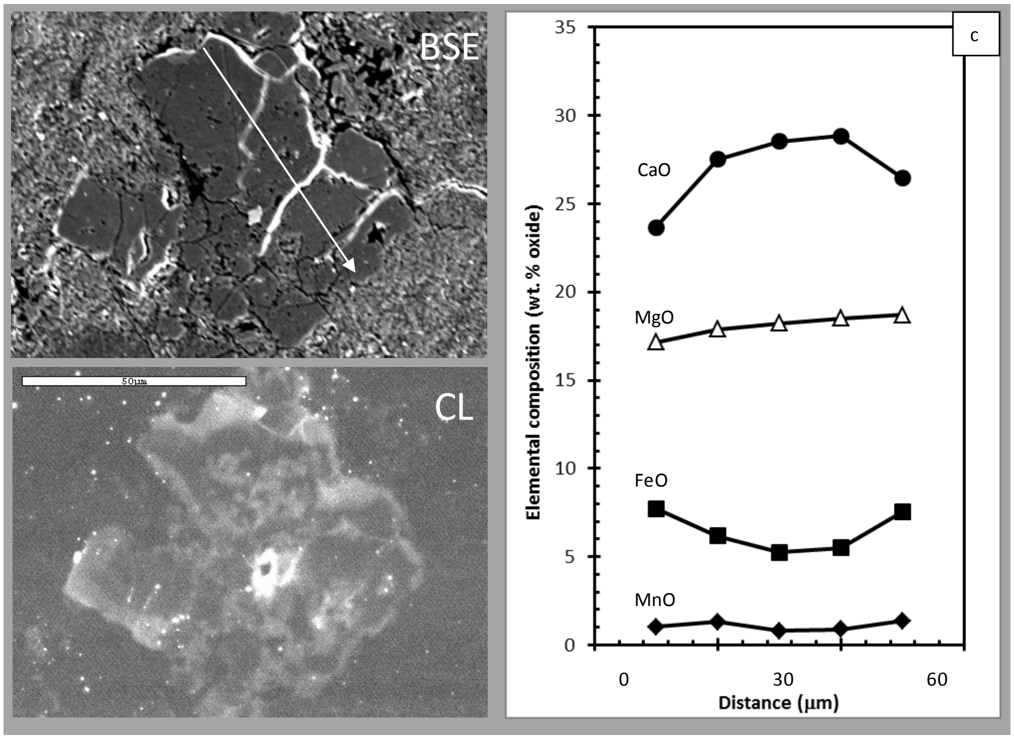
BSE
CL
50µm
c
CaO
MgO
FeO
MnO
Elemental composition (wt.% oxide)
0
5
10
15
20
25
30
35
0
30
60
Distance (µm)

Figure 6. Ternary diagram showing carbonate compositions in dolomite from ALH 84049 and ALH 84051. Data are plotted in mole% of $CaCO_3$, $MgCO_3$, and $(Fe+Mn)CO_3$ components. The shaded area on the large ternary (a) corresponds to the four insets on the right (b-e), and (c), (d), and (e) show data for individual representative grains from ALH 84051.Most data from both samples overlap and lie in a cluster with an approximate composition of 50 mol% $CaCO_3$, 40 mol% $MgCO_3$, and 10 mol% $(Fe+Mn)CO_3$. The range of data for these two samples is slightly greater than that reported by Zolensky et al. (shaded, 1997) and Lee et al. (hashed, 2012), shown in Figure 6b.

In Figure 6 (c-e), points with red rims indicate the rim of a grain and black points indicate cores. There is no obvious core-to-rim relationship amongst these three grains and each grain encompasses a significant part of the total compositional variability.

c) Dolomite grain (shown in Fig. 5a) where the core is enriched in $MgCO_3$ and the rims depleted in $MgCO_3$. The grain composition forms a linear array on the ternary diagram.

d) Dolomite grain (shown in Fig 5b) where the cores contain higher $(Fe+Mn)CO_3$ than the rim.

e) Dolomite grain (shown in Fig 5c) with the opposite trend as 6c; the cores have lower $(Fe+Mn)CO_3$ than the rim. Two core analyses overlap on the diagram

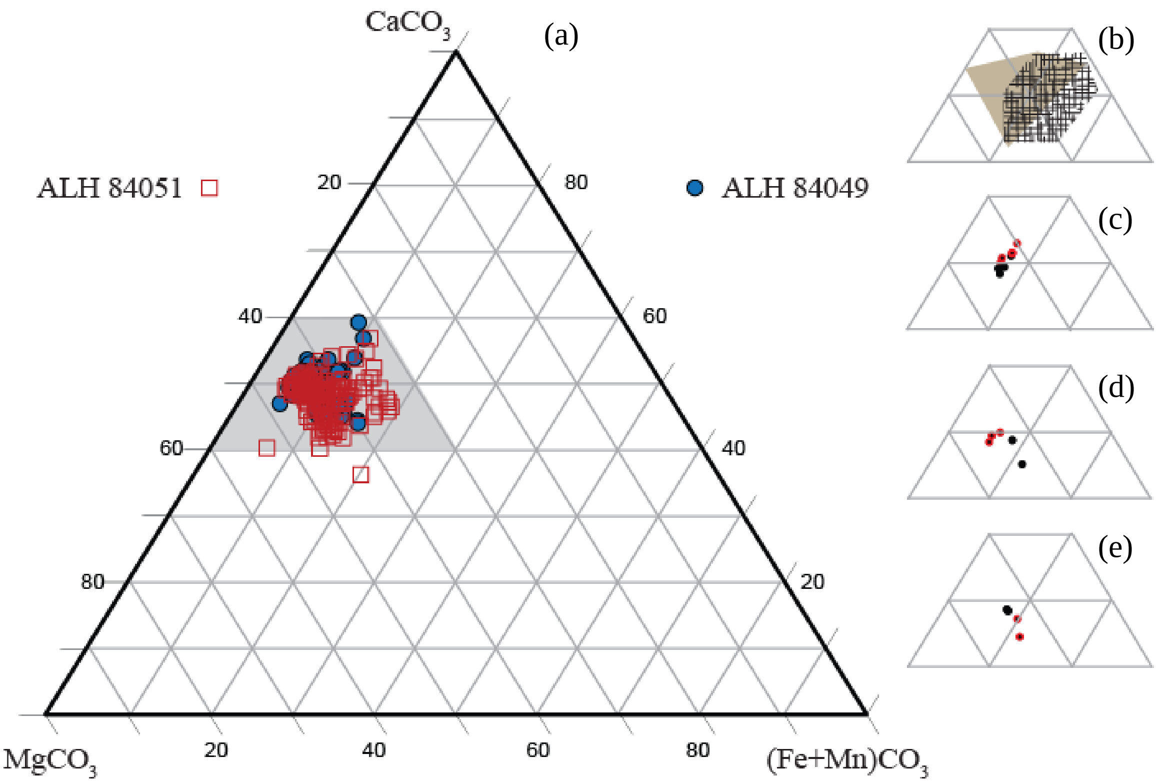

Figure 7. Chemical relationships between the carbonate components within dolomite in ALH 84049 and ALH 84051.Only Figures 7a and 7b have well-defined linear trends. The analytical errors are smaller than the symbols. Blue symbols denote ALH 84049. Red symbols denote ALH 84051.

a) $MgCO_3$-$CaCO_3$. This plot shows a slight relationship between $MgCO_3$ and $CaCO_3$ that is apparent in both samples.

b) $FeCO_3$-$CaCO_3$. This plot shows a well-defined linear relationship between $FeCO_3$ and $CaCO_3$. Data from both samples overlap, although it appears that ALH 84049 compositions cluster more towards the lower $FeCO_3$ end of the trend and ALH 84051 towards the higher $FeCO_3$ end of the data array.

c) $MnCO_3$-$CaCO_3$. In either sample, $MnCO_3$ does not seem to vary with $CaCO_3$.

d) $MgCO_3$-$MnCO_3$. Little covariance between $MgCO_3$ and $MnCO_3$ can be seen in either sample.

e) $MgCO_3$-$FeCO_3$. There is little apparent covariance between $MgCO_3$ and $FeCO_3$, although dolomite in ALH 84049, as noted above, contains less $FeCO_3$.

f) $MnCO_3$-$FeCO_3$. We observe no defined trend in $MnCO_3$ and $FeCO_3$, although ALH 84049 has lower Fe than ALH 84051.

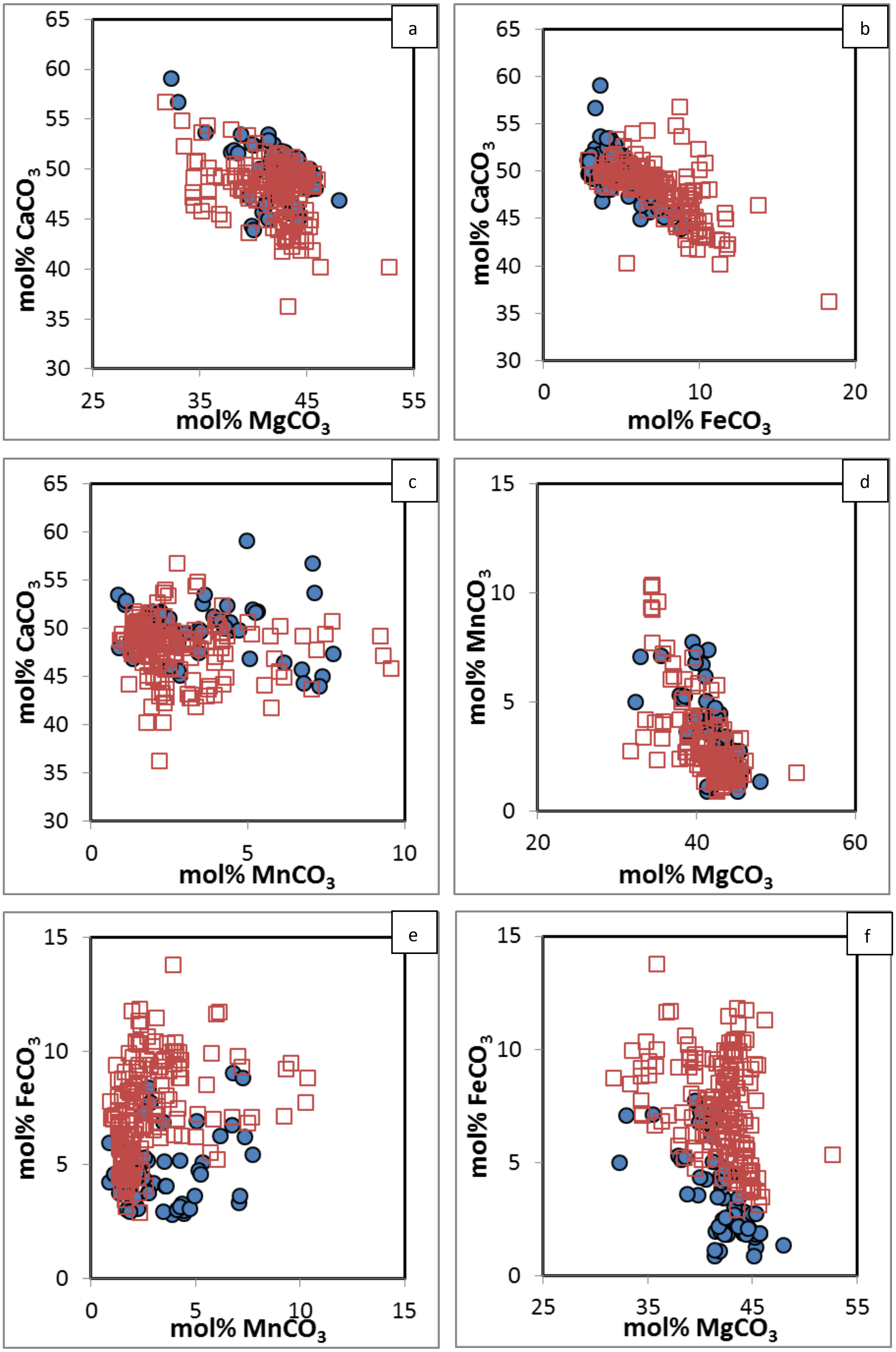
a
mol% CaCO$_3$
65
60
55
50
45
40
35
30
25
35
45
55
mol% MgCO$_3$
b
mol% CaCO$_3$
65
60
55
50
45
40
35
30
0
10
20
mol% FeCO$_3$
c
mol% CaCO$_3$
65
60
55
50
45
40
35
30
0
5
10
mol% MnCO$_3$
d
mol% MnCO$_3$
15
10
5
0
20
40
60
mol% MgCO$_3$
e
mol% FeCO$_3$
15
10
5
0
0
5
10
15
mol% MnCO$_3$
f
mol% FeCO$_3$
15
10
5
0
25
35
45
55
mol% MgCO$_3$

Figure 8. Mn-Cr isochron plot (regressed with error in both axes) of dolomite grains in ALH 84049 (Fig 8a) and ALH 84051 (Fig. 8b). Calculated ^{53}Mn/^{55}Mn initial ratios are indicated on the plots: values for ALH 84049 and ALH 84051 are indistinguishable within error. Larger error in the ALH 84051 isochron could be due to variable formation ages for some dolomite grains which may explain the occurrence of some data points greater than 2σ range from the isochron. The δ^{53}Cr value is defined as δ^{53}Cr = (R_x/R_s-1)1000, where Rx is the measured ^{53}Cr/^{52}Cr ratio and Rs is 0.113457, the terrestrial ratio reported in Birck and Allegre (1988).

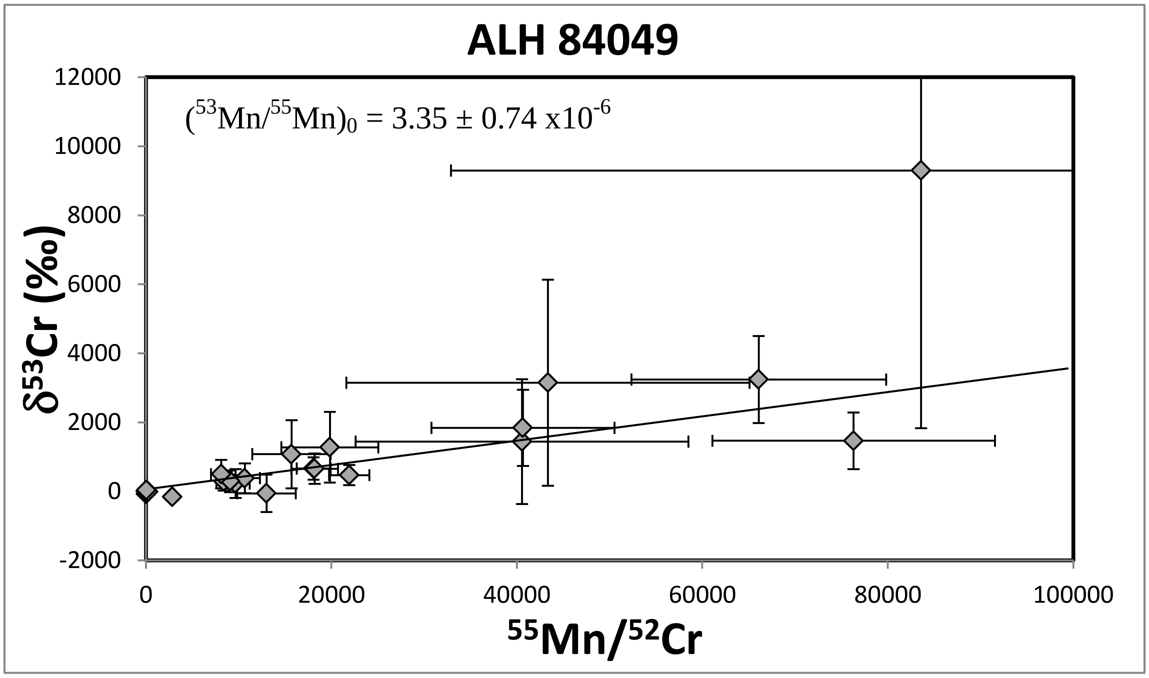
ALH 84049
(^{53}Mn/^{55}Mn)$_0$ = 3.35 ± 0.74 x10^{-6}
δ^{53}Cr (‰)
^{55}Mn/^{52}Cr
12000
10000
8000
6000
4000
2000
0
-2000
0
20000
40000
60000
80000
100000

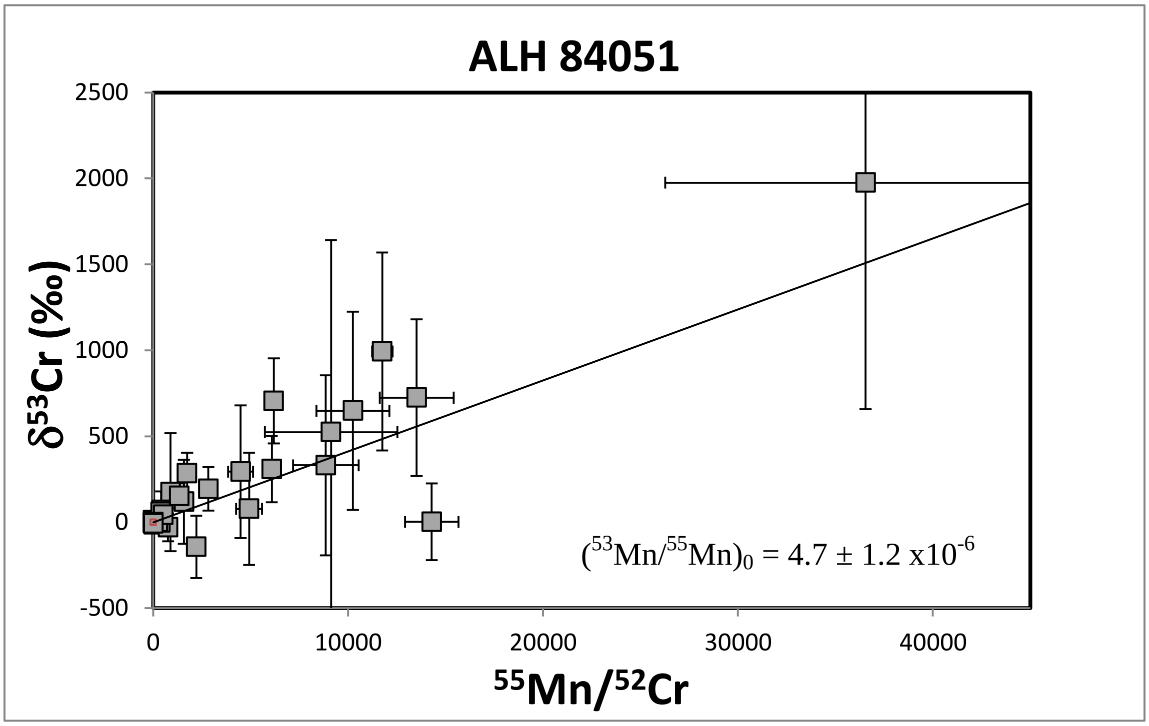
ALH 84051
(^{53}Mn/^{55}Mn)$_0$ = 4.7 ± 1.2 x10^{-6}
δ^{53}Cr (‰)
^{55}Mn/^{52}Cr
2500
2000
1500
1000
500
0
-500
0
10000
20000
30000
40000

Fig. 9. Comparison of CM carbonate ages. Figure 9a shows that all CM Mn-Cr calculated dates overlap in time. Sample name and reference number are denoted on the right side of the figure; all workers used San Carlos olivine as the Mn-Cr standard except Fujiya et al. (2012), who used the calcite standard of Sugiura et al. (2010b). Figure 6b is a comparison of measured age and the alteration grade (2.0-2.5) of Rubin et al. (2007). The apparent relationship between the alteration grade and the age of the carbonates is likely an artifact of the different standard used by Fujiya et al. (2012). References in (a) are as follows: 1) Fujiya et al. (2012), 2) Brearley and Hutcheon (2000), 3) Tyra et al. (2009), 4) de Leuw et al. (2009), 5) Lee et al. (2012), and 6) this work (black symbols).

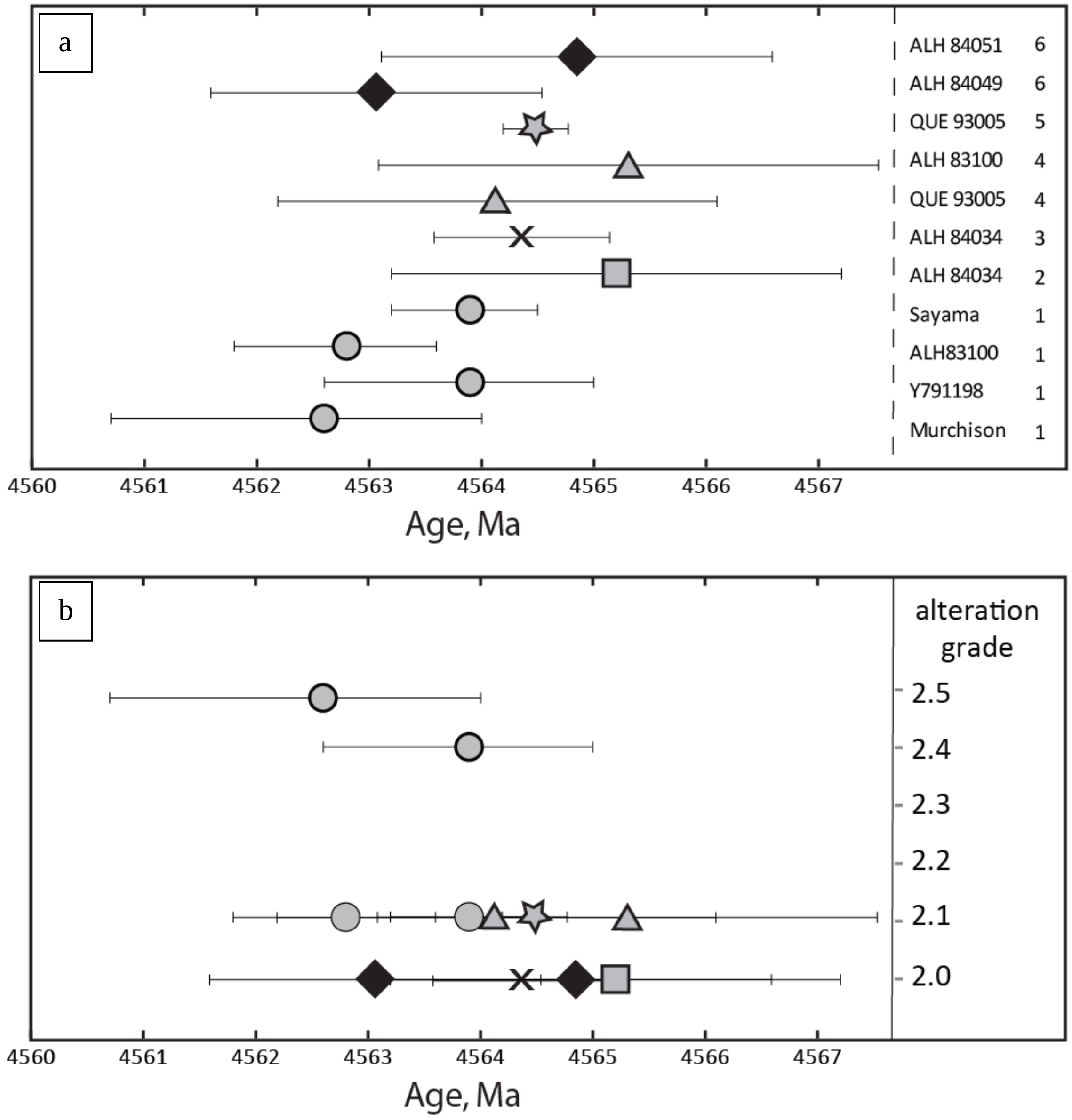

11 APPENDIX

Appendix 1a: Composition of carbonate within ALH 84049

		Wt%						Mol%			
Name	**grain type***	**CaO**	**MgO**	**FeO**	**MnO**	**CO2**	**Total**	**Ca**	**Mg**	**Fe**	**Mn**
a49-13-b4-line	m	27.88	17.67	5.27	3.81	47.71	102.34	46.79	41.25	6.91	5.05
a49-13-b4-line	m	29.92	19.96	3.48	0.98	48.02	102.36	48.90	45.40	4.44	1.26
a49-13-b4	m	28.97	19.61	4.63	0.68	47.58	101.47	47.96	45.16	5.99	0.89
a49-13-b4	m	27.53	20.27	2.84	1.00	46.10	97.75	46.86	48.01	3.78	1.35
a49-13-b6a	m	32.61	18.13	3.33	0.68	47.84	102.59	53.49	41.37	4.26	0.88
a49-13-b6a	m	30.51	17.50	3.42	0.81	46.14	98.39	52.45	41.86	4.59	1.10
a49-13-b6a	m	31.06	17.48	3.45	0.84	46.55	99.37	52.88	41.41	4.58	1.13
a49-13-b6c	m	26.50	17.01	5.02	4.93	46.36	99.82	45.70	40.81	6.76	6.73
a49-13-b6c	m	27.55	16.55	4.05	5.69	45.79	99.62	47.30	39.55	5.43	7.72
a49-13-b6c	m	26.55	17.58	4.70	5.50	46.33	100.66	44.98	41.44	6.22	7.37
a49-13-b6c	m	29.22	17.01	3.89	3.14	45.90	99.15	50.02	40.53	5.20	4.25
a49-13-b6c	m	28.40	18.21	5.27	2.61	47.02	101.51	47.40	42.29	6.86	3.45
a49-13-b6c	m	27.56	17.56	4.77	4.64	46.60	101.12	46.42	41.14	6.27	6.17
a49-13-b6d	m	27.12	19.12	5.97	2.15	47.45	101.80	45.14	44.28	7.75	2.83
a49-13-b6d	m	26.69	18.22	6.29	2.05	46.52	99.77	45.57	43.28	8.38	2.77
a49-13-b6d	m	28.00	19.27	5.72	1.94	47.72	102.66	46.04	44.09	7.35	2.52
a49-13-b2-line1	m	29.61	19.76	2.44	1.42	47.19	100.41	49.25	45.73	3.16	1.86
a49-13-b2-line1	m	30.78	18.38	3.81	1.63	47.95	102.53	50.78	42.19	4.91	2.12
a48-13-b2-line2	m	30.32	19.55	2.63	1.62	48.15	102.27	49.82	44.70	3.38	2.10
a49-6-b6	m	26.14	16.90	6.83	5.07	46.29	101.23	44.32	39.86	9.03	6.79
a49-6-b6	m	29.49	18.56	3.20	2.26	46.83	100.33	49.48	43.33	4.20	2.99
a49-6-b6	m	28.80	19.21	2.89	2.08	46.63	99.59	48.47	44.98	3.79	2.76

a49-6-b6	m	28.89	19.61	2.91	2.09	47.17	100.67	48.07	45.40	3.78	2.75
a49-6-b6-line1	m	30.34	18.81	2.24	3.44	47.85	102.67	49.76	42.92	2.87	4.46
a49-6-b6-line1	m	30.17	18.01	2.27	3.34	46.80	100.59	50.59	42.02	2.97	4.42
a49-6-b6-line1	m	30.56	18.08	2.16	2.94	46.87	100.62	51.17	42.11	2.83	3.89
a49-6-b6-line1	m	30.35	19.08	2.31	2.64	47.71	102.09	49.93	43.67	2.96	3.44
a49-6-b6	m	30.74	16.20	3.89	4.00	47.45	102.29	51.68	37.90	5.11	5.32
a49-6-b6	m	30.94	18.41	2.37	3.18	47.84	102.74	50.78	42.04	3.04	4.13
a49-6-b6-line2	m	30.20	16.57	2.44	3.16	45.32	97.70	52.37	39.99	3.31	4.33
a49-6-b6-line2	m	30.15	18.39	2.45	3.26	47.27	101.53	50.06	42.49	3.18	4.28
a49-6-b6-line2	m	30.31	18.54	2.41	3.65	47.77	102.69	49.79	42.38	3.09	4.73
a49-6-b4-line1	m	30.51	18.07	2.72	1.47	46.25	99.02	51.77	42.66	3.60	1.97
a49-6-b4-line1	m	29.63	17.71	2.27	1.61	45.68	96.88	51.70	42.99	3.09	2.22
a49-6-b4	m	25.72	16.82	6.61	5.39	45.94	100.49	43.93	39.98	8.82	7.28
a49-6-b4-line2	m	29.74	19.32	2.30	1.28	46.63	99.27	50.05	45.23	3.02	1.70
a49-6-b4-line2	m	31.42	19.53	2.31	1.45	48.29	103.00	51.06	44.15	2.93	1.86
a49-6-b3-line1	m	31.04	18.79	3.47	1.59	47.99	102.89	50.76	42.76	4.43	2.05
a49-6-b3-line1	m	30.83	18.48	3.81	1.75	47.79	102.65	50.62	42.22	4.89	2.28
a49-6-b3-line1	m	30.57	17.95	4.36	1.49	47.18	101.54	50.85	41.54	5.66	1.95
a49-6-b3-line1	m	30.21	18.56	4.18	1.58	47.52	102.06	49.89	42.65	5.39	2.06
a49-6-b3-line2	m	30.28	18.60	4.31	1.40	47.65	102.25	49.94	42.68	5.55	1.83
a49-6-b3-line2	m	30.34	18.21	4.44	1.50	47.33	101.81	50.30	41.99	5.74	1.96
a49-6-b3-line2	m	30.95	18.38	3.43	1.92	47.65	102.32	50.97	42.12	4.41	2.50
a49-6-b3-line2	m	29.45	18.97	3.71	1.55	47.06	100.75	49.12	44.00	4.83	2.05
a49-6-b8-line1	m	33.07	13.81	2.48	5.22	46.32	100.90	56.68	32.93	3.32	7.07
a49-6-b8-line1	m	35.16	13.82	2.77	3.75	46.71	102.21	59.08	32.31	3.63	4.98
a49-6-b8-line1	m	31.28	16.56	3.67	3.92	47.31	102.73	51.89	38.22	4.75	5.14
a49-6-b8-line2	m	31.01	16.65	3.53	3.99	47.15	102.32	51.61	38.55	4.59	5.25
a49-6-b8-line2	m	31.54	14.99	2.75	5.29	46.38	100.96	53.71	35.51	3.66	7.12

a49-6-b9-line1	m	30.41	18.51	4.43	1.42	47.92	102.69	50.06	42.40	5.70	1.85
a49-6-b9-line3	m	30.90	16.85	3.08	2.66	46.59	100.09	52.51	39.83	4.08	3.57
a49-6-b9-line3	m	30.85	16.09	3.01	2.64	45.26	97.85	53.49	38.81	4.07	3.62
a49-6-b9-line3	m	29.86	17.99	3.96	2.65	47.14	101.59	49.71	41.66	5.14	3.49
a49-6-b9-line3	m	28.62	18.21	3.90	2.01	45.97	98.71	48.86	43.24	5.19	2.71
a49-6-b10b-line1	m	28.77	19.25	3.09	1.38	46.76	99.25	48.72	45.35	4.08	1.85
a49-6-b10b-line1	m	29.54	18.62	3.64	1.71	47.20	100.70	49.54	43.44	4.76	2.26
a49-6-b10b-line2	m	31.24	18.20	3.45	1.67	48.07	102.63	51.57	41.80	4.45	2.18
a49-6-b10b-line2	m	29.68	19.21	3.41	1.40	47.30	100.99	49.33	44.41	4.42	1.84
a49-60b10a-line1	m	29.40	18.06	4.04	1.93	46.46	99.89	49.66	42.44	5.32	2.57
a49-60b10a-line1	m	28.95	18.38	3.48	1.62	45.92	98.35	49.47	43.70	4.64	2.18
a49-60b10a-line1	m	29.35	20.08	3.34	1.45	48.32	102.55	48.08	45.76	4.28	1.88
a49-60b10a-line1	m	29.61	19.06	2.69	1.58	46.68	99.63	49.78	44.59	3.53	2.10

*grain types include vein dolomite (v), aggregate dolomite (a), and isolated matrix dolomite (m)

Appendix 1b: Composition of carbonate within ALH 84051

			Wt%						Mol%			
	Name	**grain type***	**CaO**	**MgO**	**FeO**	**MnO**	**CO2**	**Total**	**Ca**	**Mg**	**Fe**	**Mn**
dolomite												
	a51-20a-b015	v	29.24	18.76	4.92	1.56	47.47	101.95	48.40	43.20	6.36	2.04
	a51-20a-b015	v	30.61	18.72	2.22	1.78	46.96	100.29	51.19	43.56	2.90	2.35
	a51-20a-b015	v	30.27	18.59	3.12	1.30	46.86	100.14	50.79	43.40	4.09	1.72
	a51-20a-b015	v	30.03	18.43	4.70	1.25	47.40	101.81	49.78	42.50	6.08	1.64
	a51-20a-b015	v	28.56	18.04	4.75	1.15	45.82	98.32	49.01	43.07	6.36	1.56
	a51-20a-b015	v	28.19	18.23	6.06	0.96	46.37	99.81	47.75	42.96	8.01	1.28
	a51-20a-b015	v	26.98	18.50	6.02	1.60	46.12	99.22	45.98	43.86	8.01	2.16
	a51-20a-b015	v	28.84	17.89	5.26	0.72	45.91	98.62	49.38	42.62	7.03	0.98
	a51-20a-b015	v	29.73	17.91	4.33	1.01	46.25	99.23	50.54	42.36	5.75	1.35
	a51-20a-s16	v	29.29	19.88	3.35	1.40	47.63	101.55	48.28	45.59	4.31	1.82
	a51-20a-s16	v	27.95	18.30	4.34	1.26	45.39	97.24	48.36	44.05	5.86	1.72
	a51-20a-s16	v	28.40	17.81	4.93	0.96	45.39	97.49	49.14	42.88	6.66	1.32
	a51-20a-s16	v	27.17	18.37	5.14	1.35	45.43	97.46	47.00	44.21	6.94	1.85
	a51-20a-s16	v	28.19	18.95	5.20	1.02	46.63	99.99	47.44	44.37	6.83	1.36
	a51-20a-s16	v	27.70	18.04	5.91	1.08	45.74	98.47	47.54	43.08	7.92	1.47
	a51-20a-s0	v	29.52	18.71	3.64	1.25	46.65	99.77	49.71	43.84	4.78	1.67
	a51-20a-s0	v	29.43	19.22	3.56	1.18	47.02	100.41	49.14	44.65	4.64	1.56
	a51-20a-s0	v	29.29	19.39	2.38	1.27	46.41	98.74	49.54	45.63	3.14	1.70
	a51-20a-s0	v	29.10	19.22	3.51	1.14	46.71	99.68	48.92	44.96	4.61	1.51
	a51-20a-s0	v	30.15	17.94	3.40	1.16	46.12	98.77	51.38	42.54	4.52	1.56
	a51-20a-s0	v	29.63	19.09	2.80	1.23	46.62	99.37	49.92	44.75	3.68	1.64
	a51-20a-s0	v	29.84	18.32	3.17	1.25	46.23	98.81	50.75	43.35	4.21	1.68
	a51-20a-s0	v	27.99	17.98	6.39	1.57	46.61	100.54	47.25	42.23	8.42	2.10

a51-20a-s9	v	28.04	17.29	4.92	1.90	45.17	97.32	48.82	41.88	6.69	2.61
a51-20a-s9	v	28.88	18.27	4.76	1.04	46.19	99.14	49.09	43.20	6.31	1.40
a51-20a-s9	v	28.82	19.46	2.86	1.71	46.70	99.55	48.45	45.52	3.75	2.27
a51-20a-s9	v	29.87	19.41	3.35	1.19	47.43	101.25	49.42	44.69	4.33	1.56
a51-20a-s9	v	28.62	17.95	5.85	0.68	46.11	99.21	48.76	42.55	7.78	0.91
a51-20a-s9	v	25.97	17.87	7.17	1.45	45.36	97.82	45.11	43.18	9.72	1.99
a51-20a-s9	v	29.25	18.29	3.86	1.13	45.99	98.52	49.91	43.42	5.14	1.53
a51-20a-s9	v	28.90	18.88	2.92	1.20	45.86	97.76	49.49	44.98	3.90	1.62
a51-20a-s7	v	27.83	18.21	5.00	1.09	45.74	97.87	48.04	43.73	6.74	1.49
a51-20a-s7	v	28.20	17.27	4.88	1.79	45.13	97.27	49.08	41.82	6.63	2.46
a51-20a-s7	v	28.08	17.42	4.48	1.88	45.07	96.93	49.01	42.30	6.10	2.59
a51-20a-s7	v	27.24	17.79	6.06	1.37	45.46	97.92	47.12	42.82	8.18	1.87
a51-20a-s7	v	27.36	17.68	6.50	1.10	45.47	98.11	47.25	42.48	8.76	1.50
a51-20a-s7	v	26.32	18.59	6.57	1.34	45.84	98.66	45.09	44.31	8.79	1.81
a51-20a-s7	v	29.16	17.89	4.25	1.12	45.73	98.15	50.06	42.73	5.69	1.51
a51-20a-s12	v	27.49	18.57	6.85	1.79	47.16	101.86	45.75	43.00	8.90	2.35
a51-20a-s12	v	29.30	18.58	4.51	1.03	46.76	100.18	49.26	43.46	5.92	1.37
a51-20a-s12	v	29.18	18.95	4.04	1.19	46.83	100.19	48.93	44.21	5.29	1.58
a51-20a-s12	v	29.22	19.05	2.89	1.06	46.18	98.40	49.67	45.06	3.83	1.43
a51-20a-s12	v	29.61	18.68	2.86	1.24	46.18	98.57	50.35	44.19	3.80	1.67
a51-20a-s12	v	30.39	18.34	4.04	1.10	47.05	100.92	50.71	42.58	5.26	1.45
a51-71-s5	v	29.28	18.49	3.09	1.96	46.33	99.15	49.65	43.63	4.09	2.63
a51-71-s5	v	30.26	18.33	3.44	1.01	46.52	99.56	51.07	43.05	4.53	1.35
a51-71-s5	v	29.12	17.57	4.48	0.98	45.40	97.55	50.35	42.27	6.05	1.34
a51-71-s5	v	29.14	18.30	5.22	0.98	46.67	100.31	49.02	42.83	6.85	1.30
a51-71-s5	v	29.25	19.34	4.50	1.11	47.54	101.74	48.31	44.44	5.80	1.45
a51-70-s11	v	28.48	17.89	5.13	1.30	45.86	98.66	48.76	42.62	6.86	1.76
a51-70-s11	v	29.26	19.11	3.50	1.29	46.77	99.93	49.09	44.61	4.58	1.71

a51-70-s11	v	28.17	18.42	4.94	1.59	46.25	99.37	47.82	43.50	6.55	2.13
a51-70-s11	v	26.60	17.02	6.84	1.63	44.79	96.88	46.74	41.61	9.38	2.26
a51-70-s11	v	28.48	18.01	4.40	1.48	45.65	98.02	48.98	43.10	5.91	2.01
a51-70-s11	v	27.78	17.24	5.48	1.47	44.95	96.92	48.56	41.93	7.48	2.03
a51-70-s7	v	28.79	19.43	2.61	1.22	46.17	98.22	48.94	45.96	3.46	1.64
a51-70-s7	v	29.15	19.13	3.36	1.08	46.50	99.22	49.20	44.93	4.43	1.44
a51-70-s7	v	31.48	18.50	3.37	1.47	47.87	102.69	51.60	42.19	4.31	1.90
a51-70-s7	v	24.28	18.53	8.72	1.42	45.69	98.64	41.87	44.46	11.74	1.94
a51-16-s4	m	26.56	17.35	6.78	1.60	44.96	97.25	46.39	42.16	9.24	2.21
a51-16-s4	m	26.93	17.79	5.86	1.78	45.26	97.62	46.70	42.93	7.93	2.44
a51-16-s4	m	26.84	18.16	6.16	1.42	45.56	98.14	46.25	43.54	8.28	1.93
a51-16-s4	m	20.47	17.56	13.29	1.57	44.74	97.63	36.22	43.23	18.35	2.20
a51-16-s4	m	25.10	17.92	6.70	2.72	45.10	97.54	43.72	43.43	9.11	3.75
a51-16-s4	m	27.48	17.76	6.48	0.96	45.54	98.22	47.37	42.60	8.72	1.31
a51-16-s4	m	29.14	17.74	3.96	1.05	45.44	97.33	50.47	42.75	5.35	1.43
a51-16-s4	m	28.49	18.72	4.26	1.03	46.06	98.56	48.55	44.39	5.67	1.39
a51-16-s4	m	28.63	18.95	3.66	1.12	46.10	98.46	48.74	44.89	4.86	1.51
a51-16-s4	m	29.00	18.63	2.97	1.22	45.75	97.57	49.82	44.53	3.98	1.66
a51-16-s3	m	27.52	17.88	6.17	1.31	45.74	98.62	47.25	42.71	8.27	1.78
a51-16-s3	m	28.53	18.23	5.25	0.79	46.04	98.84	48.67	43.27	6.99	1.07
a51-16-s3	m	28.83	18.51	5.49	0.87	46.74	100.44	48.41	43.24	7.20	1.15
a51-16-s3	m	26.45	18.70	7.55	1.35	46.66	100.71	44.51	43.78	9.92	1.80
a51-12-s8	m	29.57	18.65	3.37	1.70	46.70	99.99	49.70	43.62	4.42	2.26
a51-12-s8	m	29.80	18.29	3.40	1.50	46.48	99.47	50.43	43.07	4.49	2.01
a51-12-s8	m	28.96	18.88	3.72	1.46	46.55	99.57	48.85	44.31	4.90	1.95
a51-12-s8	m	29.08	19.36	4.31	1.40	47.49	101.64	48.08	44.53	5.56	1.83
a51-12-s8	m	29.12	18.57	4.27	1.36	46.60	99.92	49.05	43.52	5.61	1.81
a51-12-s8	m	29.51	17.47	4.09	1.42	45.64	98.13	50.76	41.81	5.49	1.93

a51-12-s8	m	29.91	17.43	3.89	1.60	45.90	98.73	51.16	41.48	5.19	2.16
a51-12-s8	m	30.90	16.96	3.86	1.57	46.13	99.42	52.59	40.16	5.13	2.11
a51-12-s3	a	25.41	18.88	7.90	1.62	46.45	100.26	42.98	44.43	10.43	2.17
a51-12-s6	a	26.18	19.00	5.78	1.48	45.81	98.25	44.91	45.35	7.74	2.01
a51-12-s6	a	25.76	17.92	7.16	1.45	45.15	97.44	44.86	43.42	9.73	2.00
a51-12-s6	a	25.04	17.96	7.60	1.73	45.14	97.47	43.68	43.59	10.35	2.39
a51-12-s6	a	25.08	17.36	7.27	2.73	44.82	97.26	43.95	42.33	9.94	3.78
a51-12-s6	a	23.88	17.54	7.25	4.17	44.99	97.83	41.72	42.64	9.89	5.76
a51-12-s6	a	24.79	17.78	7.37	2.86	45.21	98.01	43.08	42.99	10.00	3.93
a51-12-s6	a	26.50	17.48	6.97	2.09	45.50	98.54	45.76	42.00	9.39	2.85
a51-12-s6	a	24.44	22.99	4.17	1.36	47.70	100.66	40.23	52.65	5.36	1.77
a51-12-s6	a	25.67	18.89	6.97	0.89	45.61	98.03	44.18	45.24	9.36	1.21
a51-12-s6	a	24.07	18.83	6.86	2.43	45.21	97.40	41.83	45.53	9.30	3.34
a51-12-s6	a	25.02	18.58	8.99	1.76	46.55	100.90	42.21	43.61	11.84	2.35
a51-12-s6	a	26.90	17.84	6.72	1.20	45.61	98.27	46.44	42.86	9.06	1.64
a51-12-s6	a	25.35	18.58	8.45	1.79	46.48	100.65	42.81	43.66	11.14	2.39
a51-12-s6	a	25.98	18.07	6.65	3.14	46.17	100.01	44.19	42.76	8.83	4.22
a51-12-s6	a	25.52	18.40	7.88	2.76	46.66	101.22	42.92	43.06	10.35	3.67
a51-12-s6	a	25.21	18.11	8.66	2.35	46.33	100.66	42.71	42.69	11.45	3.15
a51-12-s6	a	25.83	18.72	6.33	1.66	45.65	98.19	44.44	44.81	8.50	2.26
a51-12-s6	a	25.44	18.31	7.87	2.29	46.21	100.12	43.21	43.28	10.43	3.08
a51-12-s6	a	25.82	17.86	6.88	2.37	45.46	98.39	44.58	42.91	9.27	3.24
a51-12-s6	a	24.92	18.28	7.60	1.66	45.40	97.86	43.27	44.16	10.30	2.28
a51-12-s6	a	23.36	19.32	8.42	1.69	45.66	98.45	40.17	46.23	11.30	2.30
a51-12-s6	a	25.89	17.06	7.07	3.15	45.23	98.40	44.92	41.18	9.57	4.32
a51-12-s6	a	25.31	17.25	6.27	4.01	45.04	97.88	44.11	41.83	8.53	5.53
a51-12-s6	m	29.98	17.07	4.38	1.00	45.49	97.92	51.75	40.99	5.90	1.36
a51-12-s6	m	29.35	16.72	4.65	1.40	45.07	97.19	51.18	40.56	6.33	1.93

a51-12-s6	m	29.83	18.48	5.77	1.00	47.77	102.85	49.03	42.26	7.40	1.31
a51-12-s6	m	27.91	17.93	5.35	1.25	45.62	98.06	48.10	43.00	7.20	1.70
a51-12-s6	m	29.03	15.37	5.14	5.57	46.18	101.29	49.35	36.35	6.82	7.48
a51-12-s6	m	27.83	14.58	6.95	6.96	46.35	102.67	47.14	34.36	9.19	9.32
a51-12-s6	m	26.84	14.30	6.55	7.58	45.42	100.69	46.40	34.40	8.84	10.36
a51-12-s6	m	26.66	14.69	7.07	7.05	45.69	101.16	45.82	35.12	9.48	9.58
a51-12-s6	m	28.31	15.25	7.05	5.40	46.53	102.54	47.74	35.78	9.28	7.20
a51-12-s6	m	27.44	16.96	5.25	4.33	45.99	99.97	46.86	40.30	7.00	5.85
a51-12-s6	m	28.71	17.38	5.19	2.33	46.15	99.76	48.84	41.14	6.89	3.13
a51-12-s6	m	28.13	15.73	6.81	3.06	45.33	99.06	48.71	37.90	9.20	4.19
a51-12-s6	m	26.35	15.31	8.63	4.40	45.41	100.10	45.54	36.81	11.64	6.01
a51-12-s6	m	26.53	15.79	8.84	4.59	46.34	102.09	44.94	37.22	11.69	6.15
a51-12-s6	m	31.18	16.59	3.54	1.81	45.87	98.99	53.34	39.49	4.73	2.45
a51-12-s6	m	29.41	17.28	4.69	2.47	46.36	100.21	49.79	40.70	6.20	3.31
a51-12-s6	m	28.82	16.96	4.70	3.23	46.02	99.73	49.15	40.24	6.26	4.35
a51-12-s6	m	29.39	16.74	5.32	3.09	46.52	101.06	49.58	39.29	7.01	4.12
a51-12-s6	m	28.07	17.02	5.62	3.09	45.98	99.78	47.92	40.42	7.49	4.17
a51-12-s6	m	29.07	17.08	6.04	2.83	46.94	101.96	48.62	39.75	7.89	3.74
a51-12-s6	m	29.38	17.54	5.86	2.44	47.30	102.52	48.73	40.48	7.59	3.20
a51-12-s6	m	29.54	17.86	5.88	1.97	47.51	102.76	48.80	41.05	7.58	2.57
a51-12-s6	m	29.19	17.93	6.14	1.88	47.42	102.56	48.32	41.29	7.93	2.46
a51-12-s6	m	29.72	17.76	6.04	1.81	47.53	102.86	49.06	40.79	7.78	2.36
a51-12-s6	m	29.64	17.75	4.13	1.74	46.29	99.55	50.29	41.90	5.47	2.33
a51-12-s6	m	29.43	16.51	4.73	2.94	45.86	99.47	50.38	39.32	6.32	3.98
a51-12-s6	m	29.41	16.41	5.51	3.86	46.77	101.96	49.35	38.31	7.22	5.12
a51-12-s6	m	28.88	16.70	4.17	4.25	46.14	100.14	49.17	39.56	5.54	5.72
a51-12-s6	m	29.52	14.42	5.27	5.65	45.66	100.52	50.75	34.49	7.07	7.68
a51-12-s6	m	28.05	14.12	5.23	6.67	44.78	98.85	49.17	34.44	7.16	9.24

a51-12-s6	m	28.93	15.94	3.86	4.39	45.20	98.32	50.23	38.51	5.23	6.03
a51-12-s6	m	31.30	14.78	4.90	2.43	45.28	98.69	54.33	35.70	6.64	3.33
a51-12-s6	m	28.09	16.83	6.69	3.22	46.52	101.35	47.39	39.51	8.81	4.29
a51-12-s6	m	27.98	16.36	7.23	2.59	45.87	100.03	47.88	38.95	9.66	3.50
a51-12-s6	m	25.54	16.65	7.33	5.20	45.96	100.68	43.63	39.57	9.77	7.02
a51-12-s6	m	26.78	13.88	5.58	7.30	44.11	97.65	47.64	34.35	7.75	10.27
a51-12-s6	m	28.81	15.58	5.31	5.00	45.99	100.69	49.18	37.00	7.07	6.75
a51-12-s6	m	29.59	16.07	4.67	3.71	45.93	99.97	50.56	38.20	6.23	5.01
a51-12-s6	m	30.46	14.04	7.43	3.09	45.72	100.74	52.30	33.54	9.96	4.19
a51-12-s6	m	29.35	14.44	7.66	2.95	45.35	99.75	50.82	34.79	10.35	4.04
a51-12-s6	m	28.94	14.87	7.39	2.98	45.38	99.56	50.11	35.82	9.99	4.08
a51-12-s6	m	31.72	13.85	6.30	2.48	45.43	99.78	54.81	33.30	8.50	3.39
a51-12-s6	m	28.03	17.11	7.28	1.98	46.38	100.78	47.44	40.29	9.62	2.65
a51-12-s6	m	28.62	16.66	7.80	2.21	46.82	102.11	47.99	38.87	10.21	2.93
a51-12-s6	m	28.25	16.55	7.20	2.53	46.23	100.76	47.97	39.10	9.54	3.40
a51-12-s6	m	28.59	16.49	8.08	2.03	46.65	101.84	48.10	38.60	10.61	2.70
a51-12-s6	m	31.64	14.88	6.71	1.73	46.26	101.22	53.67	35.12	8.88	2.32
a51-12-s6	m	32.25	12.97	6.37	1.97	44.82	98.38	56.75	31.76	8.75	2.74
a51-12-s6	m	25.73	17.69	7.60	1.56	45.39	97.97	44.74	42.80	10.32	2.14
a51-12-s6	m	31.63	15.97	4.30	1.76	46.14	99.80	53.98	37.92	5.73	2.37
a51-12-s6	m	29.72	17.25	5.02	1.82	46.45	100.26	50.31	40.63	6.63	2.44
a51-12-s6	a	27.65	15.68	6.61	1.76	46.06	97.76	49.36	38.95	9.21	2.48
a51-12-s6	a	26.80	16.18	6.88	2.85	44.68	97.39	47.07	39.54	9.43	3.96
a51-2-b1-l4	a	28.61	17.88	5.08	1.90	46.37	99.84	48.53	42.20	6.73	2.55
a51-2-b1-l4	a	28.83	17.20	4.86	2.19	45.90	98.98	49.46	41.06	6.51	2.97
a51-2-b1-l4	a	28.19	17.33	5.56	2.24	45.97	99.29	48.26	41.28	7.43	3.03
a51-2-b1-l4	a	29.05	17.63	5.51	2.32	46.89	101.40	48.65	41.08	7.20	3.07
a51-2-b1-l4	a	26.53	18.65	4.94	1.82	45.36	97.30	45.92	44.91	6.67	2.49

	a51-2-b1-l4	a	25.44	19.18	6.96	2.42	46.89	100.89	42.78	44.87	9.13	3.22
	a51-2-b1-l4	a	27.95	17.97	5.96	2.39	46.69	100.96	46.98	42.03	7.82	3.18
	a51-2-b1-l4	a	28.71	16.44	6.01	2.66	45.81	99.63	49.18	39.18	8.04	3.60
	a51-2-b1-l4	a	27.07	15.01	10.29	2.91	45.78	101.06	46.44	35.83	13.78	3.95
calcite												
	a51-12-s8	m	53.47	0.20	0.95	0.28	42.98	97.89	97.72	0.52	1.35	0.41
	a51-12-s8	m	55.51	0.10	0.77	0.28	44.33	100.98	98.31	0.24	1.06	0.39
	a51-12-s8	m	56.00	0.09	0.80	0.43	44.81	102.12	98.10	0.21	1.09	0.59
	a51-12-s8	m	56.14	0.11	0.75	0.52	44.99	102.50	98.00	0.27	1.02	0.71
	a51-12-s8	m	54.92	0.16	0.76	0.52	44.07	100.44	97.80	0.40	1.06	0.74
	a51-12-s8	m	56.31	0.10	0.71	0.54	45.09	102.75	98.05	0.25	0.96	0.74
	a51-12-s8	m	53.73	0.08	0.70	0.48	42.99	97.98	98.10	0.19	1.00	0.70
	a51-12-s8	m	54.06	0.14	0.70	0.46	43.32	98.68	98.01	0.34	0.99	0.65
	a51-12-s8	m	54.66	0.12	0.65	0.39	43.69	99.52	98.22	0.30	0.92	0.56
	a51-12-s8	m	54.73	0.08	0.65	0.36	43.68	99.50	98.38	0.19	0.91	0.51
	a51-12-s8	m	54.74	0.00	0.37	0.09	43.25	98.44	99.36	0.00	0.52	0.13
	a51-12-s8	m	55.19	0.00	0.33	0.06	43.57	99.16	99.44	0.00	0.47	0.09
	a51-12-s8	m	54.27	0.03	0.25	0.09	42.84	97.48	99.43	0.08	0.36	0.13
	a51-12-s8	m	55.03	0.00	0.23	0.03	43.36	98.65	99.64	0.00	0.32	0.05
	a51-12-s8	m	56.26	0.00	0.23	0.04	44.32	100.84	99.64	0.00	0.31	0.05
	a51-12-s8	m	55.49	0.00	0.23	0.01	43.69	99.42	99.66	0.00	0.33	0.01
	a51-12-s8	m	55.24	0.00	0.21	0.01	43.50	98.97	99.68	0.00	0.30	0.02
	a51-12-s8	m	54.99	0.00	0.25	0.07	43.36	98.67	99.54	0.01	0.36	0.10
	a51-12-s8	m	55.63	0.00	0.26	0.08	43.87	99.84	99.53	0.00	0.36	0.11
	a51-12-s8	m	55.35	0.00	0.32	0.09	43.71	99.47	99.42	0.00	0.45	0.13
	a51-12-s8	m	56.59	0.00	0.33	0.09	44.69	101.70	99.42	0.00	0.46	0.12
	a51-12-s8	m	54.87	0.00	0.30	0.10	43.31	98.59	99.42	0.00	0.43	0.15
	a51-12-s8	m	55.17	0.00	0.22	0.02	43.45	98.86	99.66	0.00	0.31	0.03

a51-12-s8	m	55.05	0.03	0.31	0.07	43.46	98.91		99.40	0.07	0.43	0.10
a51-12-s8	m	54.43	0.05	0.43	0.17	43.14	98.21		99.03	0.12	0.60	0.25
a51-12-s8	m	54.86	0.00	0.59	0.10	43.51	99.06		99.03	0.00	0.83	0.14

* grain types include vein dolomite (v), aggregate dolomite (a), and isolated matrix dolomite (m)

CHAPTER 2

Very late timing of CR1 GRO 95577 aqueous alteration: a NanoSIMS ^{53}Mn-^{53}Cr study of siderite

1 Abstract

Petrographic studies of the CR1 chondrite GRO 95577 show that it contains three compositionally-distinct carbonates: calcite, siderite, and rare dolomite. This carbonate assemblage is unique amongst CI, CM, and CR chondrites, but similar to that within Tagish Lake. The siderite is very Mn-rich, has a highly variable composition, and may be chemically zoned. Calcite and dolomite exhibit sharp boundaries between different chemical zones. To constrain the timing of aqueous alteration, we report in-situ Mn-Cr isotopic compositions of siderite obtained by NanoSIMS analyses. The weighted regression of multiple regions of interest from 8 siderite grains shows that the initial ^{53}Mn/^{55}Mn was essentially zero ((-1.38 x10^{-8} ± 4.64) x 10^{-8}, 2σ). If the upper bound of the error defines an isochron, the earliest possible precipitation age consistent with the measured values is 19.5 Myr after the LEW 86010 angrite benchmark (~4538Ma, ~30 Myr after CAIs). This represents the youngest carbonate age measured to date in any carbonaceous chondrite. Low temperature alteration estimates from thermometry of extracted organic matter from GRO 95577 shows that these young ages are not likely to be due to temperature resetting of the Mn-Cr system. The preservation of complex compositional zoning demonstrates that the carbonate grains were never heated to temperatures approaching the closure temperatures for cation diffusion in carbonates. This observation has important implications for the nature of the heat source that warmed the CR parent body. A large parent body capable of retaining heat, such as 2 Pallas, could explain the longevity of liquid water and the young age of siderite. Alternatively, transient heating from impacts could have melted ice late and allowed siderite to precipitate.

2 Introduction

Many meteorites, especially carbonaceous chondrites, have been strongly affected by water. The CR chondrite group has the widest range of aqueous alteration of any of the carbonaceous chondrite groups (Weisberg and Huber, 2007). The CR chondrite population includes rare, unaltered type 3 CR chondrites, common, intermediately altered type 2 chondrites, and only one recognized completely altered type 1 sample, GRO 95577 (Weisberg et al., 1993; Weisberg and Huber, 2007; Abreu and Brearley, 2010). GRO 95577 has undergone extensive aqueous alteration, with pervasive and possibly prolonged fluid activity on its parent body (Weisberg and Huber, 2007). Only a few relict olivine and pyroxene grains remain, generally within the largest chondrules. Carbonates, a direct product of aqueous alteration (Brearley, 2006), are common and distributed throughout. In addition, the abundant, original metal has been replaced by magnetite. Although it is clear that some CRs have experienced extensive alteration, the timing of alteration is poorly constrained. Furthermore, the temporal relationship between alteration on the CR parent body versus other parent bodies is unknown.

CR chondrites are thought to be the most primitive of all carbonaceous chondrites, but many of the components show evidence of the interaction with water. They can be identified by abundant (40-60 vol%) large, layered chondrules (0.2 - 3 mm diameter), matrix (>30 vol%), common chondrule metal, secondary magnetite framboids, and fine-grained dark inclusions (Weisberg et al., 1993). In CRs, dark inclusions are clasts characterized by fine-grained phyllosilicate matrix and rare chondrules (Zolensky et al., 1992; Weisberg et al., 1993; Endress et al., 1994). CR chondrites contain the most primitive organic matter and amino acid species found in carbonaceous chondrites; primitive organic matter has experienced few hydrolysis reactions and may contain anomalous N and H isotope values (Alexander et al., 1998; Busemann et al., 2006; Glavin and Dworkin, 2009). CR chondrites have bulk refractory and moderately volatile element compositions that are similar to CIs, but are depleted in volatile elements like Mn, Na, and K (Weisberg et al., 1995). Additionally, Robert et al. (2006) note that CR chondrites have very high whole rock D/H ratios compared to CI, CM, and CV chondrites. In a three oxygen isotope plot, whole rock (WR) CR chondrites form a line with a $\delta^{18}O/\delta^{17}O$ slope of ~0.7, distinct from the terrestrial fractionation line (TFL), Carbonaceous Chondrite Anhydrous Mixing (CCAM) line, and most other carbonaceous chondrite fields (Weisberg et al., 1993; Schrader et al., 2011). The WR oxygen isotopic compositions of CR chondrites are, in part, the result of the interaction of water with the primary anhydrous minerals within CR meteorites (Clayton and Mayeda, 1984; Clayton and Mayeda, 1999).

Unlike CV, CM, and CI chondrites, little is known of the nature and timing of aqueous alteration within the CR parent asteroid. The ^{53}Mn-^{53}Cr short-lived radionuclide system ($t_{½}$ = 3.7 Myr) has been used to date the formation ages of carbonates in CI1, CM1, and CM2 chondrites, and in Kaidun (a unique polymict breccia) and constrains aqueous alteration to within 10 million years of CAI formation (Endress et al., 1996; Hutcheon and Phinney, 1996; Hutcheon et al., 1998; Brearley and Hutcheon, 2000; Krot et al., 2006; Hoppe et al., 2008; de Leuw et al., 2009; Petitat et al., 2009; Petitat et al., 2011b; Fujiya et al., 2012). These results are consistent with models of aqueous alteration in planetesimals and asteroids that use both the decay of short-lived radionuclides and exothermic hydration reactions as the key heat-producing processes (Clayton and Mayeda, 1984; Grimm and McSween, 1989; Clayton and Mayeda, 1999; Young et al., 1999; Cohen and Coker, 2000; Rosenberg et al., 2001; Young, 2001). Most of these thermal models use ^{26}Al decay as the potential early solar system heat source. At present there is no unequivocal evidence for aqueous alteration in carbonaceous chondrites after ^{26}Al and ^{60}Fe ($t_{½}$ 0.73 and 1.5 Myr respectively) had gone extinct (Kita et al., 2005).

No short-lived radionuclidic system has been used to constrain the formation ages of secondary minerals in CR chondrites, with the exception of the polymict breccia Kaidun (Weisberg et al., 1995). In Kaidun, Hutcheon et al. (1999b) measured Mn-Cr systematics of carbonates in three distinct lithologies (CR, CI, and CM) and Petitat et al. (2011b) also examined carbonates in the CI lithology. Kaidun, however, has experienced heating and brecciation atypical of most CR chondrites (Zolensky et al., 1996). Furthermore, its classification as a CR chondrite may be controversial (Zolensky and Ivanov, 2003). Although its host may indeed be the CR parent body, Kaidun certainly is not representative of the group as a whole.

GRO 95577 provides an excellent opportunity to study the occurrence, distribution, and composition of secondary carbonate minerals in CR chondrites. To date, carbonates in CR chondrites have not been extensively studied (Zolensky et al., 1992; Weisberg et al., 1993). Ca-carbonate (probably calcite) has been described in CR chondrites (Zolensky et al., 1992; Weisberg et al., 1993; Weisberg et al., 1994; Weisberg and Huber, 2007). Three types of secondary carbonate minerals are found in GRO 95577 and are larger than the typical submicron grains reported in most CR chondrites (Weisberg et al., 1993). The larger dimensions of the carbonates in GRO 95577 provide an opportunity to study the carbonate chemistry and isotope composition in a CR chondrite in detail for the first time. In this paper we report the occurrence, distribution, and composition of secondary carbonate minerals in GRO95577. These data provide insights into the chemistry of the parent aqueous fluid(s), the timing of carbonate precipitation, and to help constrain when liquid water was active in the CR parent body.

Understanding the duration of aqueous alteration on the CR chondrite parent body provides input to thermal models and constrains potential early heat sources in asteroids.

3 Samples and Methods

Polished petrographic thin sections of GRO 95577, 30 and GRO 95577, 53 were provided by the Antarctic Meteorite Working Group for use in this study. The samples were first examined by optical microscopy to identify locations of carbonate grains. Multiple petrographic microscopic images were taken in plane, cross-polarized, and reflected light and stitched together using Hugin [Sourceforge] panoramic software. These large format images were used to estimate carbonate location and distribution, and were essential for navigation in subsequent micro and nano-scale analytical studies. These images were also used to evaluate whole rock petrographic textures. Selected carbonate occurrences were then studied in detail using a Scanning Electron Microscope (SEM) using backscattered electron imaging (BSE) and Energy Dispersive Spectroscopy (EDS) X-ray mapping. Quantitative chemical analysis of individual carbonate grains was carried out by Electron Probe Microanalysis (EPMA) prior to Mn-Cr isotopic analysis by Nanoscale Secondary Ionization Mass Spectrometry (NanoSIMS).

SEM imaging and X-ray mapping were carried out on a FEI Quanta 3D Field Emission Gun SEM/Focused Ion Beam (FIB) instrument in the Department of Earth and Planetary Sciences at the University of New Mexico. BSE image mosaics and full spectral imaging X-ray maps of the thin sections were obtained on this instrument, as well as high resolution BSE images of individual grains. The X-ray maps were used to determine the carbonate mineralogy, distribution, and modal abundance, and to provide qualitative compositions of grains on a pixel-by-pixel basis. X-ray mapping was performed with an EDAX Apollo 40 SDD EDS at an accelerating voltage of 30 kV, 32 nA beam current, and 200 μs dwell time with ~90,000 counts per second and ~33% deadtime at a resolution of ~1.7μm per pixel. A full EDS spectrum was obtained for each pixel.

Electron microprobe point analyses and high-magnification quantitative X-ray maps were obtained using a JEOL 8200 Superprobe in the Electron Microbeam Facility at the University of New Mexico. Analyses were obtained at an accelerating voltage of 12 kV and 10 nA beam current using Wavelength Dispersive Spectrometry (WDS). Beam size was set at 1 μm to optimize spatial resolution, minimize the possibility of beam overlap with adjacent phases, and restrict the extent of beam damage within single grains which can affect later Mn-Cr analyses by NanoSIMS. Calibration for the microprobe analyses was performed on spessartine (Si, Mn), celestite (Sr), dolomite (Ca, Mg), and siderite (Fe). Although Sr was analyzed, its concentration was consistently at or below detection limits in almost all analyses. EPMA X-ray maps were taken of individual carbonate grains, typically using 25x25μm field of view at 2 μm/pixel resolution and at running conditions similar to that used during point analyses.

The Mn-Cr isotope abundances of several siderite grains were analyzed using the Lawrence Livermore National Laboratory *Cameca* NanoSIMS 50. A ~70 pA primary O^- beam was rastered over areas between 25×25 μm and 30×30 μm in size to produce quantitative secondary ion images. Positive secondary ions were acquired in a combined peak jumping, multi-collection mode, simultaneously measuring $^{25}Mg^+$, $^{28}Si^+$, $^{44}Ca^+$,

$^{52}Cr^+$, and $^{55}Mn^+$, and subsequently stepping the magnetic field to measure $^{53}Cr^+$ and $^{56}Fe^+$. The secondary ion intensities were corrected for background and counting system dead time. A mass resolving power of ~3600 was used in order to eliminate potential interferences. $^{55}Mn/^{52}Cr$ and $^{53}Cr/^{52}Cr$ ratios were calculated for selected regions of the total image using image processing software (L'Image by L. Nittler). Each ion image was subdivided into three regions of interest (ROIs) based on calculated ^{55}Mn-^{52}Cr ratios. EPMA-damaged areas were digitally removed from consideration. Measured ^{55}Mn-^{52}Cr ion ratios were converted to atomic ratios using a relative sensitivity factor (RSF) of 0.93 which was determined from repeated measurements of San Carlos olivine.

4 Results

4.1 Petrography

4.1.1 Whole rock petrography

The thin sections GRO 95577, 30 and GRO 95577, 53 contain two distinct lithologies, the host CR lithology and dark lithology. Dark lithology (DL) is equivalent to the terms 'dark inclusions' or 'dark clasts' used elsewhere (e.g. Zolensky et al., 1992; Endress et al., 1994); however, because DL is so extensive in our examined sections, the term "lithology" is more correct than "inclusions". This observation differs from that of Weisberg and Huber (2007); they observed predominantly the host CR1 lithology with subordinate dark inclusions in GRO 95577, 11. In both samples, no anhydrous silicates (such as olivine) were observed; both lithologies in both sections are fully aqueously altered and consistent with classification as a CR1 (Weisberg and Huber, 2007). This is in contrast to the observations of Weisberg and Huber (2007), where rare anhydrous grains were observed. Sample GRO 95577, 30 contains completely hydrated DL and host. Most of this sample is CR host lithology, with one ~2 mm sulfide-bounded DL clast and one extensive DL area with diffuse boundaries (see Fig. 1a and b) that constitutes ~1/3 of the section. Sample GRO 95577, 53 is 100% DL with some embedded chondrule fragments and two large (>2 mm) rimmed chondrules present (visible in Figures 1c, 1d, and 2a).

The CR host lithology in GRO 95577, 30 is chondrule supported with matrix interstitial to the chondrule pseudomorphs. Chondrule pseudomorphs range from less than 0.5 mm to almost 2 mm in diameter. Fine-grained rims are visible around chondrules, although some may have been removed through brecciation. Chondrule pseudomorph mineralogy is similar to that observed by Weisberg and Huber (2007), with all chondrules replaced by secondary minerals such as phyllosilicates. The fine-grained matrix in the host CR lithology comprises 30-40 vol% of the sample, similar to that observed in GRO 95577, 11 (Weisberg and Huber, 2007). The matrix is phyllosilicate-dominated with accessory magnetite framboids (~300 nm - 10 μm), pyrrhotite (10-100μm), pentlandite (1-10 μm), and carbonate minerals. Sulfide grains within the host are concentrated in the interstitial matrix and are coarser-grained than those found within the DL (~50 μm maximum diameter vs. ~100 μm maximum size in the host).

In addition to magnetite framboids, large (~150 μm to 1 mm diameter), rounded magnetite grains are also present in GRO 95577, 30 in the host lithology (Figs. 1 and 2). These likely are alteration products of large metal grains. Magnetite associated with chondrules in GRO 95577, 11 occasionally has a core of unaltered metal that has escaped aqueous alteration (Weisberg and Huber, 2007). Although metal is common in CR chondrites, large metal or pseudomorphic magnetite grains have not been described in the

CR chondrite group (e.g. Wasson and Rubin, 2010). Large metal grains, however, are common within CB chondrites (part of the CR chondrite clan), but are associated closely with sulfide (Krot et al., 2002), unlike metal in CR chondrites.

Fine-grained rims up to 100 μm thick and alteration zones surround the large magnetite grains in GRO 95577, 30. In one large magnetite grain (Fig 2c), patchy zoning is visible in the BSE image, likely due to chemical zoning. The large magnetite grain is bordered by sulfide and a fine-grained rim. Two other observed grains (Fig. 2d and 2e) are concentrically zoned. These two grains are also rimmed by fine-grained phyllosilicate, thin sulfide arcs, and, in Figure 2e, scalloped or etched margins. Figure 2f is a magnified image of one such margin which consists mainly of phyllosilicates. A calcium phosphate mineral embedded within this complex magnetite margin was identified by EDS.

The dark lithology in GRO 95577 consists of more fine-grained material (~70 vol% matrix, ~30 vol% chondrules) than the host lithology. Some hydrated chondrules and chondrule relict fragments are observed in the DL, and are more common in GRO 95577, 30 than in the DL of GRO 95577, 53. As noted by Weisberg and Huber (2007) in GRO 95577, 11, many chondrule pseudomorphs resemble altered type 1 chondrules. Two chondrule pseudomorphs in GRO 95577, 53 are quite large at ~3 mm in diameter (Fig. 1, Fig. 2a and 2b). More typical chondrule pseudomorphs in the DL range from ~100-500 μm. Accessory sulfides, magnetite, and carbonates are disseminated throughout the DL, and, as noted above, are often finer-grained than the same phases within the host.

4.1.2 Carbonate petrography and chemistry

Three different carbonate phases, siderite, calcite and dolomite, coexist in GRO 95577, 30 and GRO 95577, 53. Only one other observation of magnesium siderite in the CR3 chondrite MET 00426 has been previously described (Brunner and Brearley, 2011). Calcium carbonate in GRO 95577 is probably calcite, although no test was used to differentiate calcite from aragonite or vaterite. Mineral modal abundances determined from whole thin section X-ray maps of GRO 95577, 53 (Fig 1d) show that calcite makes up 2.9 vol%, siderite 1.0 vol. %, and 7.2 vol% sulfide minerals. Sample GRO 95577, 30 DL has similar modal abundances with 3.0 vol% calcite, 1.5 vol% siderite, and 8.5 vol. % sulfide. GRO 95577, 30 CR host lithology contains 1.7 vol% calcite, 0.6 vol% siderite, and 6.7 vol% sulfide. Dolomite abundances were not resolvable at the 2 μm/pixel resolution of either X-ray map. Very rare dolomite (<2 μm diameter), however, was observed and identified with the SEM and EDS while surveying carbonate-rich areas at high magnification.

Carbonates typically show spatial associations with other secondary minerals. BSE images illustrate characteristic textural characteristics and mineral associations of the carbonates (Fig. 4). Within the DL, calcite, siderite, and pyrrhotite are closely associated. Complex structures, possibly an expression of a three dimensional mesh texture, are apparent in X-ray maps (Fig. 3). Secondary minerals such as carbonates and sulfides are found generally in the matrix; these minerals also may be concentrated on the periphery of chondrule pseudomorphs as shown in Figure 3c. Secondary mineral associations in the CR host lithology are similar to those in DL. Magnetite framboids, also commonly associated with carbonates calcite and siderite, were only observed in the host lithology. Magnetite in the DL often occurs as asymmetrical platelets (Fig. 4b and 4c). Carbonate minerals are common in the matrix of both analyzed thin sections but are not observed inside chondrule pseudomorphs. In the DL, carbonate grains are more uniformly distributed and more common than within the host CR lithology. The host contains sparse, patchy occurrences of carbonate within interstitial matrix.

Figure 4 shows typical associations between carbonate, magnetite framboids, and pyrrhotite in both lithologies. Calcite (Fig. 4a-4c) occurs as irregularly-shaped grains 10-30 μm diameter that typically have a corroded or embayed outline, but can also display a sinuous morphology (Fig. 4c). Calcite and siderite grains in both lithologies and thin sections are commonly corroded. Corroded calcite may also contain inclusions of magnetite framboids (Fig. 4a). Siderite grains are typically smaller (1-10 μm diameter) and less common than calcite grains and occur as patchy, irregularly-shaped grains (Fig. 4b and 4c). Siderite can occur interstitially to the magnetite framboids (Fig. 4d). Siderite grains also commonly surround pyrrhotite (Fig. 4e and 4f); this pyrrhotite typically has corroded or embayed outlines. Patches of corroded, fine grained (<5μm) siderite may extend for tens of microns, or siderite can occur intermingled with phyllosilicate (e.g., Fig. 4b). Siderite often occurs associated with calcite. Figure 4a shows an example of a narrow overgrowth of siderite 2-5 microns thick around the periphery of an embayed calcite grain. Calcite and siderite may be surrounded by voids partially infilled by fibrous phyllosilicates. Many siderite grains surround pyrrhotite in what may be a pseudomorphic texture. For example, Figure 4f shows siderite rimming pyrrhotite.

Dolomite (Fig. 4c) is the least abundant carbonate in both thin sections; only three grains were observed. Dolomite occurs as grains that have a euhedral or blocky morphology and are very fine-grained (1-5μm diameter). Dolomite was only observed in the DL and in every case was found abutting sulfide and associated with nearby calcite and siderite.

High contrast BSE imaging shows that subtle chemical zoning is present in all three carbonate phases in GRO 95577 as shown in Figure 5. The compositional zoning in dolomite (Fig. 5a) and calcite (Fig. 5b) is sharply defined. In the dolomite grain shown in Figure 5a, a darker rhombohedral core is surrounded by brighter, higher Z, dolomite. Calcite, such as that in Figure 5b may be divided into sharply defined zones. Most small siderite grains do not exhibit zoning, although patchy zoning occurs in large grains over 20 μm in diameter. Figure 5c, for instance, shows a large siderite grain where brighter areas have less MgO (~1 wt. %) than dark areas.

Representative compositions of calcite and dolomite determined by EPMA are reported in Table 1; all analyses are given in the Appendix. Calcite compositions show a range of 95.8 - 98.9 mol% $CaCO_3$, 0.3-2.1 mol% $FeCO_3$, 0.2-2.0 mol% $MgCO_3$, and 0-0.4 $MnCO_3$. While calcite is nearly pure, dolomite has significant solid solution with other carbonate components. Four electron microprobe analyses of one dolomite grain show compositions as follows: $CaCO_3$ (45.5-50.1 mol%), $MgCO_3$ (26.0-31.6 mol%), $MnCO_3$ (12.9-17.4 mol. %), and $FeCO_3$ (7.6-9.2 mol. %).

Determination of the chemical composition of siderite grains by EPMA presented some challenges. Although analytical conditions were selected to reduce beam damage and to limit overlap of the interaction volume with adjacent grains, few analyses were completely free of X-ray contributions from adjacent silicate phases, either due to beam overlap or due to secondary fluorescence of adjacent grains. To address this problem, analyses with Si in excess of 2 wt% were discarded. The chemical composition of siderite is compositionally variable, as shown in Figures 5d and 6. $FeCO_3$ ranges from 36.8 – 50.0 mol%, $MgCO_3$ from 25.8-43.2 mol%, $MnCO_3$ from 10.0-32.0 mol%, and $CaCO_3$ from 2.2-6.5 mol% (Table 1). Although we use the term siderite to describe these carbonates, they clearly show significant substitution of Fe by Mg and Mn. Chang et al. (1998) define siderite with ~5-30 mol% $MgCO_3$ as sideroplesite and ~5 to 40 mol% $MnCO_3$ as oligonite. Although GRO 95577 siderite is intermediate in composition between oligonite and sideroplesite and has an extensive range in composition, we continue to call it siderite for the lack of a better term. Regardless of the lithology or the sample, siderite compositions plot in the same area and form a well-defined linear trend on a Fe-Mn-Mg ternary diagram (Fig. 6). The Fe/Mg ratio decreases slightly in siderite as the trend moves towards the Mn apex. Although there is a slight negative correlation of Mg and Ca exists (R^2=0.2), Ca does not vary significantly with Fe or Mn.

4.2 Siderite Mn-Cr isotope systematics

The high concentrations of Mn in siderite in both GRO 95577 samples make it an ideal mineral to analyze the Mn-Cr isotopic composition. We measured the ^{53}Mn-^{53}Cr isotope systematics of three siderite grains from GRO 95577, 53 and five grains from GRO 95577, 30; two grains within the DL and three grains from the host lithology (Appendix 2). The ^{53}Cr/^{52}Cr isotopic compositions of all grains are indistinguishable within error from the terrestrial siderite standard (Table 2, Fig. 7). A Williamson regression of the data gives a $(^{53}Mn/^{55}Mn)_o$ of $(-1.38 \pm 4.64) \times 10^{-8}$. The upper limit for $(^{53}Mn/^{55}Mn)_o$ at the time the siderite formed is $^{53}Mn/^{55}Mn < 8.4 \times 10^{-8}$ based on the 2σ upper bound to the slope of a line fitted to the data and forced through the terrestrial

^{53}Cr/^{52}Cr ratio at Mn/Cr = 0. No significant difference between the Mn-Cr isotope systematics of siderite within the host, DL, or between samples is observed. This is the lowest (^{53}Mn/^{55}Mn)$_o$ measured in any extraterrestrial carbonate to date.

5 Discussion

As shown above, GRO 95577 is highly aqueously altered and divided primarily into two lithologies, the CR host and a finer grained dark lithology (DL). Below we discuss the general petrology to highlight the uniqueness of this meteorite. Carbonates, in particular, are discussed to put them in a petrologic context, evaluate the water chemistry from which they precipitated, and constrain maximum temperatures reached after they formed. This information is important to evaluate Mn-Cr isotope results and affirm that the system has not been disturbed or terrestrially contaminated. Our results suggest that siderite precipitation was extraterrestrial and represents processes that occurred much later in solar system history than any currently recognized secondary alteration in chondrites.

5.1 Petrography of secondary mineralogy in GRO 95577

Both DL and CR host lithologies in GRO 95577 are completely altered, confirming the observations of Weisberg and Huber (2007). We did not observe anhydrous silicate grains, even in large pseudomorphs of the original grains. Nor did we observe relict metal encased within magnetite. Even the large, millimeter scale magnetite bleb (Fig. 2c) contains no relict metal. These observations are atypical of CR2 chondrites because dark inclusions generally show a higher degree of aqueous alteration than the host CR lithology (Zolensky et al., 1992; Weisberg et al., 1993; Endress et al., 1994). GRO 95577, however, shows the same degree of hydration in both lithologies.

High volumes of DL may to be related to higher overall degree of aqueous alteration in GRO 95577. Several authors (e.g., Weisberg et al., 1993; Endress et al., 1994) note that CR chondrites commonly contain hydrated dark inclusions that are mineralogically and texturally distinct from the host CR chondrite. Weisberg and Huber (2007) reported a particularly high abundance of a dark inclusion lithology (DL) in GRO 95577, an observation that is confirmed by our study of two additional thin sections of this meteorite. According to Weisberg and Huber (2007) the fine-grained component of GRO 95577, including CR chondrite matrix and the DL, constituted > 30 vol% of the sample. GRO 95577, 30 contains more than 40% matrix and, as mentioned above, GRO 95577, 53 is entirely DL (~70% matrix). In comparison, the CR2 chondrite Al Rais contains ~70 vol% DL and is also one of the most hydrated and volatile-rich CR chondrites (Kallemeyn and Wasson, 1982; Weisberg et al., 1993). More work, however, would be needed to determine if there could be a causal relationship between abundance of hydrated DL and hydration of the host lithology.

One question that remains is whether aqueous alteration occurred before or after emplacement of the DL within the host lithology. In CR2 chondrites, where the DL is more altered than the CR host, much of the alteration must have occurred before the lithologies were comingled. In GRO 95577, although all the primary components of the host CR lithology and the DL are altered, there are minor differences between the styles of alteration in the two lithologies. For example, although magnetite is common in both lithologies, magnetite framboids are common in the CR host matrix but not within DL.

The absence of magnetite framboids in DL has been observed in other CR chondrites as well (Weisberg et al., 1993). Large magnetite grains are also restricted to the CR host lithology. In addition to magnetite, sulfide minerals in the CR host are noticeably larger than within DL. In other CRs, coarse-grained sulfides tend to be associated with chondrules (e.g., Wasson, 1996; Schrader et al., 2008); fine grained sulfides dominate the matrix and DL (Lee et al., 1992; Abreu and Brearley, 2010). For example, Lee et al. (1992) identified disseminated fine-grained sulfides such as pentlandite throughout the fine grained material of analyzed CR chondrites. Whether these and other mineralogical differences are due to different aqueous alteration histories before the two lithologies were comingled or are simply a reflection of similar alteration affecting the different petrology of the two lithologies is explored more below.

Another difference, as noted in the Results, is that the DL contains more siderite and calcite than the host. Sulfide abundances between the two lithologies, however, are similar, 7.2-8.5 vol% sulfide in DL and 6.7 vol% sulfide in CR host lithology. As we found carbonates solely in fine-grained material, the dissimilarity in carbonate modal abundances is a reflection of the different abundances of fine grained material in both lithologies. Carbonates primarily are restricted to the matrix and DL, perhaps because the chondrules, during alteration, produced microenvironments not conducive to carbonate formation (Brearley, 2006). Furthermore, as noted above, carbonate formation that is limited to the matrix due to favorable geochemical conditions (e.g. higher pH) may also cause the difference in carbonate modal abundance in CR host lithology compared to within DL.

The carbonate assemblage in GRO 95577 of calcite, siderite, and dolomite is unique amongst all carbonaceous chondrites. To our knowledge, occurrences of siderite have been noted in CI chondrites (Endress et al., 1996), in ungrouped Tagish Lake (Zolensky et al., 2002; Izawa et al., 2010), and in the CR 3.0 MET 00426 (Brunner and Brearley, 2011). The siderite found here, however, is a unique composition that is more enriched in Mn than that found in Tagish Lake or in CI1 chondrites. The siderite compositions represent the highest MnO contents of any carbonate found in a CR chondrite. The highest previous concentration of Mn found in a CR chondrite carbonate is 5.6 mole% $MnCO_3$ reported in calcite from a dark lithology in Renazzo (Weisberg et al., 1993). Rare breunnerite (28 wt% CaO, 8.4 wt% FeO, 17.8 wt% MgO, 1.9 wt% MnO), occurs in dark inclusions in Acfer 059/El Djouf 001 (Endress et al., 1994), but has a composition quite different from the carbonate in GRO 95577. In GRO95577, Mn is concentrated in siderite more than any other phase (Fig. 3).

All three carbonates are spatially associated with sulfide minerals, primarily pyrrhotite. Carbonates are also associated with magnetite. Weisberg et al. (1993) observed that calcite may form interstitially within magnetite framboid clusters. Similarly, in the CR host lithology we observe interstitial calcite and siderite in framboids. The correlation of carbonate and sulfides has been observed in CM chondrites primarily as simple associations like sulfide or tochilinite rims around carbonate (e.g., de Leuw et al., 2010). Mineral associations in GRO 95577 are much larger in scale; concomitant sulfides and carbonates are distributed in matrix between chondrule pseudomorphs on a scale of millimeters. In the third dimension, these structures may form a web of associated secondary minerals surrounded by phyllosilicate minerals (Fig.

3). These structures can be seen in the DL as well, although they are less well defined than in the host lithology. Whether this texture is the result of relict chondrules in DL that are now difficult to identify or results from other processes is difficult to determine.

At a finer scale, there are petrographic relationships between carbonates and associated sulfide and magnetite that constrain the timing of mineral precipitation and dissolution events. The timing we report below may not be the only progression possible, as some microchemical environments not have been observed. Disregarding phyllosilicate minerals, magnetite was probably first in the secondary mineral sequence, either through direct oxidation of metal grains or as a product of the serpentinization process (e.g., Bach et al., 2006). Although some sulfides are primary, petrographic relationships show that pyrrhotite overgrew magnetite framboids and so postdated magnetite formation. Figure 4e shows a magnetite inclusion within a large sulfide grain, which implies that sulfide minerals grew after magnetite framboids had formed. Alternatively, these may be primary sulfides located on the periphery of chondrules that later were modified during alteration. Grain boundaries of coincident calcite and pyrrhotite are sharp and pristine. All three observed dolomite grains are also in contact with pyrrhotite and have a sharp boundary between the carbonate and pyrrhotite. Dolomite edges in direct contact with matrix, however, are etched and embayed (e.g., Figs. 4c and 6a). Siderite grains mantle both calcite and pyrrhotite, and therefore siderite is a later phase. There are a few areas where it appears that siderite is replacing pyrrhotite from the grain exteriors inward. Lastly, many pyrrhotite, calcite, and siderite grains are embayed on the edges with voids filled with fibrous phyllosilicate. Some siderite grains even form a patchy mesh texture that appears to be residual siderite and new phyllosilicate intergrowths (see Fig. 4d, e, and f). Based on these observations, the sequence of secondary mineral formation events is:

1. Magnetite formation: included in a few large pyrrhotite grains
2. Pyrrhotite and pentlandite: included in calcite. Troilite, pyrrhotite, and pentlandite are also primary in pristine CR chondrites (Abreu and Brearley, 2010), but some grew later as shown here.
3. Dolomite precipitation: Included within one calcite, sharp boundary with pyrrhotite (grew before later pyrrhotite dissolution event).
4. Calcite precipitation: Like dolomite, evidence of sharp boundaries with pyrrhotite
5. Partial pyrrhotite and calcite dissolution
6. Siderite precipitation: Siderite overgrowth on periphery of calcite, pyrrhotite, and magnetite
7. Late dissolution of pyrrhotite, calcite, and siderite creating voids
8. Emplacement in new void-space of long, fibrous phyllosilicate grains

All siderite compositions lie on a single line on the three component ternary diagram of Figure 6), regardless of lithology and in both samples (GRO 95577, 30 and GRO 95577,53). This trend indicates that the aqueous fluid within GRO 95577 evolved uniformly as siderite precipitated and suggests that some aqueous alteration must have occurred after DL and host were comingled. Furthermore, such chemical homogeneity requires sufficient fluid permeability or communication. Bland et al. (2009) estimate permeability within CI and CM chondrites is very low (10^{-19} to 10^{-17} m^2); lack of fluid flow allowed CI chondrites to be isochemical even though extensive aqueous alteration had occurred. Permeability in GRO 95577, however, must have been sufficient for fluids to remain in communication throughout the rock. Siderite compositional variability may indicate it formed during the final stages of aqueous alteration, as the chemical composition of a small volume of fluid could be affected more easily than larger volumes (low water-rock ratio). A similar scenario for carbonate formation in CM and CI chondrites was hypothesized by Riciputi et al. (1994).

The sequence of secondary mineral precipitation reflects changing geochemical conditions as alteration proceeded. Serpentinization of ultramafic rock creates alkaline and reducing conditions. For example, reacting forsterite and enstatite with water increases alkalinity in aqueous solutions (Palandri and Reed, 2004):

$$Mg_2SiO_4 \text{ (forsterite)} + 2H_2O \rightarrow 2Mg^{2+} SiO_{2aq} + 4OH^-$$

$$MgSiO_3 \text{ (enstatite)} + H_2O \rightarrow Mg^{2+} SiO_{2aq} + 2OH^-.$$

The Mg^{2+} and SiO_2 then can react with water to form serpentine ($3Mg^{2+} + 2SiO_2\,(aq)) + 5H_2O \rightarrow Mg_3Si_2O_5(OH)_4$). In addition to increasing alkalinity, the fluid is reduced from converting ferrous ion in olivine to ferric iron in magnetite (probably in disseminated magnetite framboids). Direct oxidation of Fe^o of metal would reduce the fluid or react further to produce hydrogen gas:

$$3Fe^o + 4H_2O = Fe_3O_4 + 8H^+ + 8e^-$$

$$8H^+ + 8e^- = 4H_2.$$

Although the Fe^o reaction produces acidity (Zolotov and Mironenko, 2008a), some H^+ may be consumed to produce H_2 depending upon conditions. Because of the large abundance of serpentine compared to magnetite (altered metal) in GRO 95577, alkalinity-producing serpentinization reactions should be the more important process.

We used Geochemist's Workbench to calculate the stability fields of the secondary minerals present in GRO 95577. Important parameters for the stability of minerals observed in GRO 95577 (magnetite, pentlandite, pyrrhotite/troilite, calcite, dolomite, and siderite) are pH, Eh, $a[CO_2]$, $a[S]$, $a[Fe]$, $a[Ca]$, $a[Mg]$, $a[Mn]$, and T. Calcite has a large Eh-pH stability field and therefore its presence does not limit Eh-pH conditions as much as the presence of other minerals such as siderite. Additionally, $MgCO_3$ and $MnCO_3$ are not as important as $FeCO_3$, which is an integral component of siderite. Therefore, we can focus solely on Eh, pH, $a[CO_2]$, $a[S]$, and $a[Fe]$ variability to partially constrain thermodynamic conditions during aqueous alteration. While the size of the fields may expand or contract slightly with varying $a[S]$, $a[Fe]$, $a[CO_2]$, and T changes, our work found that the stability fields of the key three components in Eh-pH space do not vary significantly under many conditions. Figure 8 shows an Eh-pH diagram calculated using Geochemist's Workbench which shows that the stability fields of pyrrhotite/troilite, magnetite, and siderite are restricted within Eh-pH space. The occurrence of these three minerals coexisting in GRO 95577 therefore provides robust geochemical constraints on the fluid at the time of precipitation. Temperature differences would change conditions slightly (Fig. 8 caption), however. Since magnetite is older, yet uncorroded, conditions may have remained within its stability field (Fig. 8). Magnetite formation would cease with only slight variations in Eh or pH, and either pyrrhotite or siderite formation would then commence. Because small changes in Eh or pH could destabilize a phase and result in its disappearance, conditions must have remained fairly stable for magnetite, siderite, and sulfide to coexist. In CM chondrites, Tyra et al. (2012) suggest that a decompression event from impact degassing or mechanical failure due to overpressurization (Wilson et al. 1999) would lower $a[CO_2]$ and instantly raise pH and the activity of CO_3^{2-} allowing carbonates to precipitate. As serpentinization proceeds and alkalinity increases, buffering reactions could keep conditions temporarily stable until a component is consumed. Calcite precipitates eight orders of magnitude faster than siderite (Jimenez-Lopez and Romanek, 2004); therefore, calcite formation will be favored until $a[Ca]$ decreases enough for siderite formation to commence (Berner, 1981; Fairen et al., 2004; Jimenez-Lopez and Romanek, 2004; Romanek et al., 2009). As different secondary minerals formed in the progression noted above, it is unlikely that the Eh-pH conditions of the fluid ever changed far from that highlighted in Figure 8.

Many workers have modeled changes in mineral assemblages of CM, CV, and CI chondrites by aqueous alteration (McSween, 1987; Zolensky et al., 1989; Rosenberg et al., 2001; Zolotov and Mironenko, 2008b), but there are no specific models for CR chondrites. All carbonaceous chondrites started with similar materials: chondrules, metal, matrix, water, and minor CAIs, AOAs, and presolar grains (e.g., Brearley and Jones, 1998; Trigo-Rodriguez and Blum, 2009). However, the proportions of each component vary among chondrite groups and the thermal and impact history of each parent body is unique. Many models omit formation of carbonates as they are considered a minor phase. Models that do consider carbonates, however, do not predict the carbonate sequence or the mineral assemblage that we observe in GRO 95577. EQ3/6 computer simulations of a CM chondrite mineral assemblage model consistently that calcite precipitates before dolomite if C concentration in the fluid is 10^{-3} to 10^{-2} m and T between 50°C and 100°C (Zolensky et al., 1989). For a hypothetical CV mineral assemblage, dolomite precipitation preceded calcite at 50°C, but not at 150°C. For either CM or CV chondrite precursors, dolomite never precipitates below 50°C. Furthermore, siderite is never predicted to precipitate in these models. In contrast to CM, CV, and CI chondrites, the observed spatial relationship of degraded FeS and $FeCO_3$ minerals suggests that in GRO 95577, the *a*[Fe] in the fluid increased at the expense of troilite or pyrrhotite, but *a*[S] in the fluid stayed low.

5.2 Mn-Cr derived timing

The Mn-Cr data reported here for siderite grains in GRO 95577 show a $(^{53}Mn\text{-}^{55}Mn)_o$ value of approximately zero which indicates little, if any, ^{53}Mn was present at the time of siderite precipitation in either the CR host lithology or the DL. If one uses the standard LEW 86010 angrite Mn-Cr systematics as an absolute age marker, the slope demarcated by the upper bound of the error envelope (Fig. 7) gives 4538 Ma as the oldest possible age of siderite precipitation in this sample. This is ~19.5 Myr younger than the LEW 86010 crystallization age. These observations indicate that either (i) chromium was mobile in siderite and has been lost due to disturbance of the system or (ii) that siderite precipitated in the CR parent body after the concentration of ^{53}Mn had decayed below detection limits. These two alternatives have profoundly different implications. If the first case were true, the loss of radiogenic Cr implies that the parent body experienced some late stage, possibly localized thermal event, which is not recorded in carbonates in other carbonaceous chondrites. If the second case were true, then the carbonates are significantly younger than any other carbonaceous chondrite carbonates analyzed using the Mn-Cr geochronometer to date. Indeed, this raises the possibility that they could be terrestrial in origin. These different scenarios are discussed in detail below.

5.2.1 Could the Mn-Cr system be disturbed?

The observation that the Mn-Cr isochron for siderite in GRO 95577 is flat, and that the ^{53}Cr/^{52}Cr ratio does not covary with the Mn/Cr ratio, raises the possibility that radiogenic ^{53}Cr was lost from the carbonate structure. Mn-Cr dating has been successfully applied to fayalite in a CV3, and to carbonates in CM2, CM1, and highly-altered CI1 chondrites (Endress et al., 1996; Hutcheon and Phinney, 1996; Hutcheon et al., 1998; Hutcheon et al., 1999a; Brearley and Hutcheon, 2000; Brearley et al., 2001; Hua et al., 2005; Krot et al., 2006; de Leuw et al., 2009; Petitat et al., 2009; Tyra et al., 2009; Tyra et al., 2010; Fujiya et al., 2012). The lack of any covariance between ^{55}Mn and ^{53}Cr* in siderite in GRO 95577 could therefore be interpreted as evidence for disturbance by volume diffusion of the isotopic system or indicates enough time passed for no ^{53}Mn to be available during precipitation. Alternatively, radiogenic Cr could have been lost during dissolution-reprecipitation of siderite. If this were the case, reprecipitated siderite did not incorporate radioactive ^{53}Mn and, therefore, our idea that siderite is young would remain unchanged. We first evaluate the possibility that the isotopic system has been disturbed.

5.2.1.1 Cation diffusion

Experimental data for cation diffusion in carbonates is sparse, especially for the low temperature regimes relevant to aqueously-altered chondrites, and data for Cr diffusion in carbonates is nonexistent. Most diffusion data for carbonates is for Mg^{2+} and Ca^{2+} diffusion in calcite at temperatures ranging from 400 to 900°C (Farver and Yund, 1996; Fisler and Cygan, 1998; Fisler and Cygan, 1999; Kent et al., 2001). We are unaware of any cation diffusivity study for siderite, although this may be in part because siderite decomposes above 400°C (Gallagher and Warne, 1981; Gallagher et al., 1981; Brearley, 2003).

Although no data exist for Cr diffusion in carbonates, we can use parameters such as the valence state and ionic radius of Cr to constrain the expected diffusivity (D) and compare our prediction to the measured diffusivity of other cations in carbonate. The diffusion database of Brady and Cherniak (2010) shows that all measured carbonate cation diffusivity values from 400 to 1000°C lie between 10^{-24} and 10^{-16} m^2/s, respectively. Cations from small 4+ C, to large 3+ REEs, to 2+ cations like Ca and Mg, and 2- anions such as O are included in this range. Second, in general, the higher the absolute value of the valence state, the higher the activation energy and the lower the diffusion rate (Brady and Cherniak, 2010). In all analyzed minerals, for instance, a 1+ cation such as Na is less tightly bound into a mineral structure than a 4+ cation such as Si. Third, a lesser effect is based upon the ionic radius of the cation; the larger the ionic radius, the lower the diffusion rate. This effect, however, is minor in 2+ and 3+ cations as the percentage differences in common ionic radii are small (Brady and Cherniak, 2010). With these rules in place, we can examine the diffusivity of other cations in carbonate and constrain the expected diffusivity of Cr.

We assume that radiogenic ^{53}Cr is in the 3+ valence state in the carbonate structure. As $^{53}Mn^{2+}$ decays to ^{53}Cr by electron capture (Audi et al., 2003), Cr most likely begins as Cr^{3+}. In aqueous fluids, Cr^{2+} is stable at conditions too acidic and reducing for siderite to be stable (Kölling et al., 2000). Cr^{2+} is larger (0.080 nm) than Cr^{3+} (0.063 nm) making it less easily accommodated in six-fold coordination in the carbonate structure (Shannon and Prewitt, 1969; Kleine and Dutrow, 2007). Ionic radii of both Cr^{3+} and Cr^{2+} are comparable to the ionic radii of Fe^{2+} (0.074 nm), Mg^{2+} (0.066 nm), and Mn^{2+} (0.080 nm) (Shannon and Prewitt, 1969), and, therefore, it is unlikely that differences in ionic radii will constrain what species of Cr will be preferred in the structure of siderite. In studies examining ^{53}Mn-^{53}Cr isotope systematics in chondrite olivine and pyroxene, it is assumed that Cr^{3+} is the ion that diffuses after Mn decay (Ito and Ganguly, 2006; Ganguly et al., 2007).

The Cr^{3+} diffusion rate is likely to be similar to or less than that of Mg^{2+}. As noted above, the ionic radius of Cr^{3+} is virtually identical to that of Mg^{2+}. However, Cr^{3+} should diffuse slower than Mg^{2+} because it has a higher valence (e.g. Brady and Cherniak, 2010). In support of this argument, two recent studies show that Cr diffuses slower than Mg (and Fe) in olivine and orthopyroxene (Ito and Ganguly, 2006; Ganguly et al., 2007). Jones and Lofgren (1993), however, noted that Cr diffusion was identical to Fe-Mg interdiffusion in olivine. Altogether, we argue that we would not expect Cr^{3+} to diffuse faster than Mg^{2+} in carbonate. Fisler and Cygan (1998) reported closure temperatures for Mg and Ca within calcite that fall in the 350 to 450 °C range with a cooling rate of 100K/Myr. Kent and Hutcheon (2001) performed diffusion experiments with Mg and Ca in magnesite from 400 to 600°C and obtained similar results at the measured temperatures, but also report an Arrhenius relation that indicates slightly faster diffusion below 400°C than that reported by Fisler and Cygan (1998). Assuming Fisler and Cygan

(1998) Mg^{2+} diffusion values (log D_o = -3.26 m^2/s and E_a = 284 ± 74 kJ/mol) is similar to that of Cr^{3+}, we estimate that Cr only diffuses more than 1 μm in 10 Myr at temperatures above 350°C.

It is unlikely that GRO 95577 ever attained temperatures > 350°C in the parent body as these temperatures would be considered low grade metamorphic temperatures (petrologic type ~3.4 and above in chondrites, Cody et al., 2008) and are not supported by the hydrated petrology seen in GRO 95577. For example, at temperatures above 400°C and at low pressures, siderite itself decomposes (Gallagher and Warne, 1981; Gallagher et al., 1981; Gotor et al., 2000; Brearley, 2003). BSE images show sharp zoning within calcite, dolomite, and siderite grains that is preserved on a micron scale in GRO 95577. EPMA data confirm that there is compositional zoning in Mg, Mn, Ca, and Fe that correspond with BSE intensity (Fig. 6). This zoning cannot be explained by diffusion, because most compositional zones are not parallel to the edges of grains. The chemical zoning is better explained as the preservation of growth features. Furthermore, Tyra et al. (2011b), using Scanning Transmission Electron Microscopy (STEM), showed that measurable chemical zoning (Ca, Mn, Mg, and Fe) occurs in GRO 955577 in very small carbonate grains (±10 μm diameter) and even at the submicron level in one carbonate grain. For example, four chemically-distinct zones with sharp interfaces within a one micron span are reported in “intermediate carbonate” (ankerite) by Tyra et al. (2011b). This evidence shows that carbonates in GRO 95577 have remarkably well-preserved chemical heterogeneity. If Cr^{3+} diffuses slower than Mg^{2+}, as argued above, then it is improbable that radiogenic Cr migrated from where it formed.

Cody et al. (2008) developed organic thermometry on carbonaceous chondrites that is based on the characteristics of the 1s-σ exiton peak in X-ray absorption near-edge spectroscopy (XANES) spectra of extracted insoluble organic matter. This thermometer gives GRO 95577 a peak temperature of 171 ± 64 °C (C-XANES). The authors, using microRaman spectroscopy, also report temperatures of 129 ± 118 °C and 162 ± 120 °C depending upon the calibration used (Cody et al., 2008). These low estimated temperatures affirm that it is highly improbable that resetting by diffusion in siderite has occurred after aqueous alteration ceased. Radiogenic Cr is highly unlikely to have migrated out of siderite as carbonates within GRO 95577 never experienced temperatures to allow measurable migration of cations like Mg^{2+} or Cr^{3+}.

The estimated peak temperature for GRO 95577 is identical within error to that of the CI chondrite Orgueil, the CM chondrites Bells and Murchison, and the ungrouped carbonaceous chondrite Tagish Lake (Cody et al., 2008). The Mn-Cr dating technique has successfully produced isochrons to date secondary carbonates within CI, CM, and Tagish Lake (e.g. Hutcheon and Phinney, 1996; Hoppe et al., 2008; de Leuw et al., 2009; Petitat et al., 2011a). We think it is unlikely that diffusion, driven by the temperatures experienced within GRO 95577, is the cause of the apparent lack of radiogenic ^{53}Cr within siderite grains. Therefore, the most plausible explanation is that radioactive ^{53}Mn did not exist at detectable levels at the time that siderite precipitated.

5.2.2 Could the siderite be terrestrial?

Assuming siderite precipitated after ^{53}Mn was extinct, could it have formed as a result of terrestrial weathering? GRO 95577 was found in a glacial moraine in Antarctica;

therefore water was available from which siderite could precipitate. Terrestrial carbonates have been observed in chondrites in temperate climates (Abreu and Brearley, 2005). Antarctic conditions are also conducive to carbonate formation; some carbonates of terrestrial origin such as calcite, magnesite, and hydrated carbonates like nesquehonite and hydromagnesite have been found on meteorite surfaces and within fractures (Jull et al., 1988; Tyra et al., 2007).

The formation of siderite as a result of Antarctic weathering can be dismissed based on the fact that geochemical conditions are far removed from those conducive to the stabilization of siderite. On Earth, siderite is unstable in oxygenated surface waters such as that present due to the local melting of Antarctic ice. Siderite formation requires reduced aqueous fluid (Kölling et al., 2000). In modern terrestrial environments, siderite precipitates in locations with restricted atmospheric exposure, such as during diagenesis of sedimentary rock in reducing conditions or in areas such as peat bogs (e.g. Berner, 1981; McMillan and Schwertmann, 1998; Rasmussen et al., 1999). In Antarctic meteorites, iron released by weathering typically forms Fe-oxyhydroxides and terrestrial siderite is never observed (Gooding, 1981; Abreu and Brearley, 2010). Furthermore, the survival of micron-sized siderite grains that are uniformly distributed throughout GRO 95577 in an oxidizing Antarctic environment suggests that GRO 95577 has undergone little weathering and siderite is extraterrestrial.

Not only is siderite formation highly improbable in an Antarctic environment, but oxygen isotope compositions of siderite and calcite within GRO 95577 also do not match values expected if they formed at Antarctic conditions. Antarctic water normally has a very negative oxygen isotopic composition, $\delta^{18}O$~-44‰ (Faure et al., 1993). Even if siderite could precipitate in equilibrium with this water at 0°C, which is certainly possible in Antarctica due to insolation heating (Schultz, 1986), it would have an oxygen isotopic composition of $\delta^{18}O_{siderite}$ = -2‰, $\delta^{18}O_{calcite}$ = -6‰ and $\Delta^{17}O_{(calcite\ and\ siderite)} \approx 0$‰ (Zheng et al., 1999). This conclusion holds as long as it is assumed that the water is not rock buffered, which is unlikely as there is no evidence of widespread silicate reaction with terrestrial water. The oxygen isotopic composition of different siderite grains in GRO 95577 is far from that predicted to precipitate in Antarctica and is consistent with precipitation from a non-Antarctic water source (Tyra et al., 2011a, Chapter 4, this work).

5.2.3 Implications of a flat Mn-Cr isochron

From the evidence discussed above, we conclude that the siderite Mn-Cr isotope systematics were not reset and that siderite formation did not occur within a terrestrial environment. Therefore the flat Mn-Cr isochron has real chronological significance for the formation of siderite in the early solar system. Analyzed siderite grains are younger than any carbonate measured to date in a chondritic meteorite. Furthermore, the siderite analyzed in this study has higher concentrations of Mn than any other chondritic carbonates analyzed to date; radiogenic $^{53}Cr^{*}$, therefore, should be easier to analyze. If siderite precipitated 19.5 Myr after LEW 86010, the maximum slope possible within the constraints of the calculated error envelope around the isochron, then a minimum of 30 million years passed from the formation of CAIs to the precipitation of siderite. By then, the primary heat source ^{26}Al and secondary source ^{60}Fe had decayed to insignificance (Ghosh et al., 2006). ^{26}Al decay would become ineffective at heating a planetesimal first, as its half-life is short ($t_{½}$ of ^{26}Al is 0.72Myr and $t_{½}$ of ^{60}Fe is 1.49 Myr) (Scott, 2007).

Additionally, ^{60}Fe heating would also become ineffective by the time GRO 95577 siderite was precipitated.

Not only are the siderites in GRO 95577 young, but their determined ages are also younger than any secondary mineral found before in carbonaceous chondrites. Figure 9 shows ranges of the formation ages of secondary minerals within CM1, CM2, CV3, and CI1 chondrites that have been dated using the Mn-Cr system. This dataset, in its entirety, covers a range of ages from near the time of CAI formation of ~4568 Ma to ~4553 Ma, a range of 15 Myrs (Endress et al., 1996; Hutcheon and Phinney, 1996; Hutcheon et al., 1998; Hutcheon et al., 1999a; Brearley and Hutcheon, 2000; Brearley et al., 2001; Hua et al., 2005; Krot et al., 2006; de Leuw et al., 2009; Petitat et al., 2009; Tyra et al., 2009; Tyra et al., 2010; Fujiya et al., 2012). Prior to this study, CI1 breunnerite from Orgueil was the youngest secondary mineral at 4553.7 ± 0.7 Ma (Petitat et al., 2009). CM1 and CM2 secondary carbonate Mn-Cr ages are identical within error, regardless of technique used, 4564.1 ± 0.9 Ma, including data acquired using a recently synthesized carbonate standard (Chapter 1, this work). Although CV chondritic fayalite formed through a different mechanism than carbonates in CI, CM, and CR chondrites (Krot et al., 1998; Hua et al., 2005), it formed at low temperature and also has been dated by Mn-Cr systematics at ~4561.1 Ma (Hutcheon et al., 1998; Hua et al., 2005). The oldest possible age of GRO 95577 siderite is 4538 Ma, which is 15 Myr younger than the youngest measured secondary mineral in CI chondrites (Petitat et al., 2009). However, because the isochron is essentially flat, we are beyond the limit of age resolution of the Mn-Cr system.

The data show that aqueous alteration on the CR parent body persisted or reoccurred at much later times than on the CI or CM parent body. We propose two mechanisms, discussed below, that could allow liquid water to be present after primary short-lived radionuclides had decayed. In the first case, this meteorite could originate from a parent body large enough to retain heat for long periods of time. Alternatively, a transient heating event warmed part of a cold parent body that contained water ice, producing liquid water that resulted in a late alteration event that ultimately precipitated carbonate.

5.2.3.1 Formation with a large Parent body?

The simplest explanation of late precipitation may be that the CR parent body was large enough to remain warm after ^{26}Al had decayed away. Depending upon the radius of the parent body, time of accretion, initial ^{26}Al ratio, porosity, water content and circulation, regolith thickness, and impact history, large asteroidal bodies could retain heat for hundreds of millions of years. In the case of 4 Vesta, for instance, thermal modeling has shown that large volumes within its interior could maintain temperatures in excess of 1400°C for over a hundred million years after its formation (McSween et al., 2002). Even bodies as small as 50 km in radius could retain volumes (~20 km radius) within the interior with temperatures over 300°C for well over 10 Myr, although smaller bodies may cool off rapidly once ^{26}Al is gone, depending upon the regolith thickness (Grimm and McSween, 1989; Akridge et al., 1998; Bouvier et al., 2007). Although a number of carbonaceous chondrite parent body models assume a diameter of 100 km (Grimm and McSween, 1989; Grimm and McSween, 1993; Cohen and Coker, 2000), models of larger bodies (up to Ceres size) predicts that asteroids with diameters in excess of 100 km could undergo extended aqueous alteration (Young et al., 1999; Young, 2001). Weiss et al. (2009a; 2009b) have suggested that primitive outer shells around large asteroids with differentiated interiors is possible. Therefore, the CR chondrite parent body could in fact be a large differentiated asteroid that retained heat after the Mn-Cr chronometer was dead. Future work on CR chondrites aimed at determining if magnetite and other minerals retain a parent body remnant magnetization could establish if the CR parent body is differentiated.

If the CR parent body is a large asteroid, it is possible that the parent is already known. The CR chondrite Renazzo has reflectance spectra that match 2 Pallas, the 2nd largest asteroid in the solar system with an average diameter of 544 km (Sato et al., 1997; Sato and Miyamoto, 1998; Schmidt et al., 2009). 2 Pallas is thought to be one of the three protoplanets in the asteroid belt and is an “evolved body with planet-like properties” (Schmidt et al., 2009). Furthermore, orbital and spectroscopic characteristics suggest 2 Pallas is the source of the Pallas family of asteroids and near Earth asteroid Phaethon (León et al., 2010). As Phaethon is the source of the annual Geminid meteor shower, this may imply that there is a direct link from 2 Pallas to the Earth. Perhaps some meteors of the Geminid meteor shower survive complete burn up in the atmosphere to become the meteorites that make the CR clan. Alternatively, many bodies in the 2 Pallas family of asteroids are located on or near orbital resonances that produce orbital instability and deliver meteorites to earth (León et al., 2010). Though possible, far more work is needed to determine the CR parent body with certainty. Regardless of what asteroid is the source of CR chondrites, a large parent body could explain the young age of siderite minerals found within GRO 95577.

5.2.3.2 Late heating of the GRO 95577 by a transient heating event

Shock events due to impacts on the parent asteroid of GRO 95577 also may heat an asteroid after the Mn-Cr chronometer had decayed away. There is a significant body of petrologic evidence that shock-induced heating has played an important role in the evolution of a significant number of chondrites, including in CM chondrites (Rubin, 1995; Nakamura, 2005; Nakato et al., 2008; Rubin, 2012). Although Keil et al. (1997) calculated that impact shock heating would only have minor effects, more recent modeling suggests that impact heating could be significant if the impactor is small compared to the host planetesimal (e.g. 1:10 impactor-to-asteroid ratio, Davidson et al., 2010). Impacts that do not disrupt an asteroid can cause localized heating and result in temperature increases of up to ~100°C higher than that prior to impact (Davidson et al., 2010). Considering that that the Late Heavy Bombardment was widespread within the inner solar system, affecting the Moon, Vesta, and the H chondrite parent body until 3.5 Ga, later impacts of carbonaceous chondrite parent bodies elsewhere in the asteroid belt are certainly plausible (Bogard, 1995; Bogard, 2012). These modeling results therefore suggest that impact heating could melt ice to produce liquid water that could interact with the rock and precipitate carbonates.

Additionally to melting ice, impact shock could release bound water from phyllosilicates. This water would then be free to interact with rock and create a fluid from which siderite could precipitate. Shock dehydration experiments show that phyllosilicates lose 20% of their bound water at shock pressures of 20 GPa and ~100% by 60 GPa (Lange et al., 1985; Rubin, 2012). These pressures are far higher than expected in carbonaceous chondrite impacts and also would cause extensive melting (Davidson et al., 2010). Observational evidence, however, shows that particle lineation is directly correlated with aqueous alteration extent in CM and CV chondrites, possibly due to impacts (Zolensky et al., 1997; Rubin, 2012). If lower levels of shock released water from phyllosilicates in the CR parent body, it would then be free to rehydrate dehydrated phyllosilicates, migrate, interact, and potentially precipitate carbonates.

Even if shock-released water was not the fluid from which carbonates precipitated, late stage water could have been involved in other processes. All observed carbonates and many pyrrhotite grains are etched and surrounded by void space and fibrous phyllosilicate infill. If late stage water were acidic, this water could dissolve the margins of calcite, siderite, and pyrrhotite grains in both lithologies of GRO 95577. Alternatively, cooling temperatures increase fluid $a[CO_2]$ which lowers pH and dissolves carbonates (e.g., Stumm and Morgan, 1996). As the solubility of Si decreased as temperature dropped, Si could then precipitate as phyllosilicates in void space left by carbonate dissolution.

6 Conclusions

The secondary mineral assemblage in GRO 95577 indicates complex changes in fluid chemistry as aqueous alteration progressed. GRO 95577 contains three distinct types of carbonate: calcite and siderite with rare dolomite. These phases are scattered randomly through the matrix of the CR host lithology and Dark Lithology (DL). All three carbonate types are compositionally zoned, which indicates that low temperatures after precipitation did not allow detectable cation diffusion. Siderite shares one compositional trend line in both lithologies and in both samples, consistent with pore fluids throughout the rock remaining in communication. Furthermore, aqueous alteration and the carbonates that resulted from alteration must have occurred after host CR lithology and DL comingled. Partial dissolution of all three carbonate types and pyrrhotite suggest that a late acidic fluid may have been present. This fluid could have migrated from elsewhere in the CR parent body, or have been released by impact heating of ice or serpentine. Conversely, acidity could arise simply from cooling aqueous fluid allowing higher $a[CO_{2\,(aq)}]$ and lower pH.

Mn-Cr systematics of several siderite grains have been analyzed by NanoSIMS. The results show that siderite is the youngest secondary mineral found in any carbonaceous chondrite, indicating liquid water existed on its parent body after potential heat sources ^{26}Al and ^{60}Fe had vanished. Sharp compositional zoning indicates temperatures never rose high enough for Cr to diffuse out of grains and reset the Mn-Cr chronometer. Furthermore, based upon siderite stability and oxygen isotope composition, these carbonates are not terrestrial. If siderite in GRO 95577 is significantly younger than carbonates in other carbonaceous chondrites, as our data indicate, liquid water must have been available on the CR parent body for an extended period of time or was remobilized by a thermal event much later in the history of the CR asteroid..

7 Acknowledgements

This work is supported by NASA Grant NNG06GG37G to A.J. Brearley (PI), the N.M. Space Grant (M. Tyra), and under the auspices of the Dept. of Energy by LLNL, Contract DE-AC52-07NA27344.

8 References

Abreu N. M. and Brearley A. J. (2005) Carbonates in Vigarano: Terrestrial, preterrestrial, or both? *Meteoritics & Planetary Science* 40, 609-625.

Abreu N. M. and Brearley A. J. (2010) Early solar system processes recorded in the matrices of two highly pristine CR3 carbonaceous chondrites, MET 00426 and QUE 99177. *Geochimica et Cosmochimica Acta* 74, 1146-1171.

Akridge G., Benoit P. H., and Sears D. W. G. (1998) Regolith and megaregolith formation of H-Chondrites: Thermal constraints on the parent body. *Icarus* 132, 185-195.

Alexander C. M. O. D., Russell S. S., Arden J. W., Ash R. D., Grady M. M., and Pillinger C. T. (1998) The origin of chondritic macromolecular organic matter: A carbon and nitrogen isotope study. *Meteoritics & Planetary Science* 33, 603-622.

Audi G., Bersillon O., Blachot J., and Wapstra A. H. (2003) The Nubase evaluation of nuclear and decay properties. *Nuclear Physics A* 729, 3-128.

Bach W., Paulick H., Garrido C. J., Ildefonse B., Meurer W. P., and Humphris S. E. (2006) Unraveling the sequence of serpentinization reactions: petrography, mineral chemistry, and petrophysics of serpentinites from MAR 15°N (ODP Leg 209, Site 1274). *Geophys. Res. Lett.* 33, L13306.

Berner R. A. (1981) A new geochemical classification of sedimentary environments. *Journal of Sedimentary Petrology* 51, 359-365.

Bland P. A., Jackson M. D., Coker R. F., Cohen B. A., Webber J. B. W., Lee M. R., Duffy C. M., Chater R. J., Ardakani M. G., McPhail D. S., McComb D. W., and Benedix G. (2009) Why aqueous alteration in asteroids was isochemical: High porosity ≠ high permeability. *Earth and Planetary Science Letters* 287, 559-568.

Bogard D. D. (1995) Impact ages of meteorites: A synthesis. *Meteoritics* 30, 244-268.

Bogard D. D. (2012) LHB evidence on asteroids. *Early Solar System Impact Bombardment II*. LPI, Houston, TX.

Bouvier A., Blichert-Toft J., Moynier F., Vervoort J. D., and Albarède F. (2007) Pb–Pb dating constraints on the accretion and cooling history of chondrites. *Geochimica et Cosmochimica Acta* 71, 1583-1604.

Brady J. B. and Cherniak D. J. (2010) Diffusion in minerals: An overview of published experimental diffusion data. *Reviews in Mineralogy and Geochemistry* 72, 899-920.

Brearley A. J. and Jones R. H. (1998) Chondritic Meteorites. In: Papike, J. J. (Ed.), *Planetary Materials*. The Mineralogical Society of America, Washington, DC.

Brearley A. J. and Hutcheon I. D. (2000) Carbonates in the CM1 chondrite ALH84034: Mineral chemistry, zoning and Mn-Cr systematics. *Lunar and Planetary Science Conference* XXXI, abstract #1407.

Brearley A. J., Hutcheon I. D., and Browning L. (2001) Compositional zoning and Mn-Cr systematics in carbonates from the Y791198 CM2 carbonaceous chondrite. *Lunar and Planetary Science Conference* XXXII, abstract #1458.

Brearley A. J. (2003) Magnetite in ALH 84001: An origin by shock-induced thermal decomposition of iron carbonate. *Meteoritics & Planetary Science* 38, 849-870.

Brearley A. J. (2006) The action of water. In: Lauretta, D. S., Leshin, L. A., and McSween, H. Y. Eds.), *Meteorites and the Early Solar System II*. University of Arizona Press, Tucson, AZ.

Brunner C. E. and Brearley A. J. (2011) Microstructural investigation of the crystalline component of matrix in the pristine CR chondrite MET 00426; Implications for diversity in nebular dust *Lunar and Planetary conference* LPI.

Busemann H., Young A. F., Alexander C. M. O. D., Hoppe P., Mukhopadhyay S., and Nittler L. R. (2006) Interstellar chemistry recorded in organic matter from primitive meteorites. *Science* 312, 727-730.

Chang L. L. Y., Howie R. A., and Zussman J. (1998) *Non-Silicates: Sulphates, Carbonates, Phosphates, and Halides*. The Geological Society Publishing House, London.

Clayton R. and Mayeda T. (1999) Oxygen isotope studies of carbonaceous chondrites. *Geochimica et Cosmochimica Acta* 63, 2089-2104.

Clayton R. N. and Mayeda T. K. (1984) The oxygen isotope record in Murchison and other carbonaceous chondrites. *Earth and Planetary Science Letters* 67, 151-161.

Cody G. D., Alexander C. M. O. D, Yabuta H., Kilcoyne A. L. D., Araki T., Ade H., Dera P., Fogel M., Militzer B., and Mysen B. O. (2008) Organic thermometry for chondritic parent bodies. *Earth and Planetary Science Letters* 272, 446-455.

Cohen B. and Coker R. F. (2000) Modeling of liquid water on CM meteorite parent bodies and implications for amino acid racemization. *Icarus* 145, 369-381.

Davidson T. M., Collins G. S., and Ciesla F. J. (2010) Numerical modelling of heating in porous planetesimal collisions. *Icarus* 208, 468-481.

de Leuw S., Rubin A. E., Schmitt A. K., and Wasson J. T. (2009) ^{53}Mn-^{53}Cr systematics of carbonates in CM chondrites: Implications for the timing and duration of aqueous alteration. *Geochimica et Cosmochimica Acta* 73, 7433-7442

de Leuw S., Rubin A. E., and Wasson J. T. (2010) Carbonates in CM chondrites: Complex formational histories and comparison to carbonates in CI chondrites. *Meteoritics & Planetary Science* 45, 513-530.

Endress M., Keil K., Bischoff A., Spettel B., Clayton R. N., and Mayeda T. K. (1994) Origin of dark clasts in the Acfer 059/El Djouf 001 CR2 chondrite. *Meteoritics* 29, 26-40.

Endress M., Zinner E., and Bischoff A. (1996) Early aqueous activity on primitive meteorite parent bodies. *Nature* 379, 701-703.

Fairen A. G., Fernandez-Remolar D., Dohm J. M., Baker V. R., and Amils R. (2004) Inhibition of carbonate synthesis in acidic oceans on early Mars. *Nature* 431, 423-426.

Farver J. R. and Yund R. A. (1996) Volume and grain boundary diffusion of calcium in natural and hot-pressed calcite aggregates. *Contributions to Mineralogy and Petrology* 123, 77-91.

Faure G., Wehn K. S., Montello J. M., Hagen E. H., Strobel M. L., and Johnson K. S. (1993) Isotope composition of the ice and sub-glacial geology near the Allan Hills, Victoria Land, Antarctica. In: Findlay, Unrug, Banks, and Veevers Eds.), *Gondwana Eight*, Balkema, Rotterdam.

Fisler D. K. and Cygan R. T. (1998) Cation diffusion in calcite: Determining closure temperatures and the thermal history for the Allan Hills 84001 meteorite. *Meteoritics & Planetary Science* 33, 785-789.

Fisler D. K. and Cygan R. T. (1999) Diffusion of Ca and Mg in calcite. *Am. Miner.* 84, 1392-1399.

Fujiya W., Sugiura N., Hotta H., Ichimura K., and Sano Y. (2012) Evidence for the late formation of hydrous asteroids from young meteoritic carbonates. *Nat Commun* 3, 627.

Gallagher P. K. and Warne S. S. (1981) Thermomagnetometry and thermal-decomposition of siderite. *Thermochim. Acta* 43, 253-267.

Gallagher P. K., West K. W., and Warne S. S. J. (1981) Use of the Mössbauer effect to study the thermal decomposition of sidewire. *Thermochim. Acta* 50, 41-47.

Ganguly J., Ito M., and Zhang X. Y. (2007) Cr diffusion in orthopyroxene: Experimental determination, Mn-53-Cr-53 thermochronology, and planetary applications. *Geochimica et Cosmochimica Acta* 71, 3915-3925.

Ghosh A., Weidenschilling S. J., McSween H. Y., and Rubin A. E. (2006) Asteroidal heating and thermal stratification of the Asteroid Belt. In: Lauretta, D. S. and McSween, H. Y. Eds.), *Meteorites and the Early Solar System II*. The University of Arizona Press, Tucson.

Glavin D. P. and Dworkin J. P. (2009) Enrichment of the amino acid L-isovaline by aqueous alteration on CI and CM meteorite parent bodies. *P Natl Acad Sci USA* 106, 5487-5492.

Gooding J. L. (1981) Mineralogical aspects of terrestrial weathering effects in chondrites from Allan Hills, Antarctica. *Proc. Lunar Planet. Sci.* 12b, 1105-1122.

Gotor F. J., Macías M., Ortega A., and Criado J. M. (2000) Comparative study of the kinetics of the thermal decomposition of synthetic and natural siderite samples. *Physics and Chemistry of Minerals* 27, 495-503.

Grimm R. E. and McSween H. Y. (1989) Water and the thermal evolution of carbonaceous chondrite parent bodies. *Icarus* 82, 244-280.

Grimm R. E. and McSween H. Y. (1993) Heliocentric zoning of the Asteroid Belt by aluminum-26 heating. *Science* 259, 653-655.

Hoppe P., Macdougall D., and Lugmair G. W. (2008) Extinct manganese-53 in carbonates from the Orgueil meteorite. *New Astronomy Reviews* 52, 467-470.

Hua X., Huss G. R., Tachibana S., and Sharp T. G. (2005) Oxygen, silicon, and Mn-Cr isotopes of fayalite in the Kaba oxidized CV3 chondrite: Constraints for its formation history. *Geochimica et Cosmochimica Acta* 69, 1333-1348.

Hutcheon I. D. and Phinney D. L. (1996) Radiogenic ^{53}Cr* in Orgueil carbonates: Chronology of aqueous activity on the CI parent body. *Lunar and Planetary Science Conference*. Lunar Planet. Inst., Houston, TX.

Hutcheon I. D., Krot A. N., Keil K., Phinney D. L., and Scott E. R. D. (1998) ^{53}Mn-^{53}Cr dating of fayalite formation in the CV3 chondrite Mokoia: Evidence for asteroidal alteration. *Science* 282, 1865-1867.

Hutcheon I. D., Browning L., Keil. K., Krot A. N., Phinney D. L., Prinz M., and Weisberg M. K. (1999a) Time scale of aqueous activity in the early Solar System. *Goldschmidt Conference* 9, CDROM, abstract #971.

Hutcheon I. D., Weisberg M. K., Phinney D. L., Zolensky M. E., Prinz M., and Ivanov A. V. (1999b) Radiogenic ^{53}Cr in Kaidun carbonates; evidence for very early aqueous activity. *Lunar and Planetary Science Conference XXX*. Lunar Planet. Inst., Houston, TX.

Ito M. and Ganguly J. (2006) Diffusion kinetics of Cr in olivine and Mn-53-Cr-53 thermochronology of early solar system objects. *Geochimica et Cosmochimica Acta* 70, 799-809.

Itoh D. and Tomeoka K. (2003) Dark inclusions in CO3 chondrites: new indicators of parent-body processes. *Geochimica et Cosmochimica Acta* 67, 153-169.

Izawa M. R. M., Flemming R. L., King P. L., Peterson R. C., and McCausland P. J. A. (2010) Mineralogical and spectroscopic investigation of the Tagish Lake carbonaceous chondrite by X-ray diffraction and infrared reflectance spectroscopy. *Meteoritics & Planetary Science* 45, 675–698.

Jimenez-Lopez C. and Romanek C. S. (2004) Precipitation kinetics and carbon isotope partitioning of inorganic siderite at 25°C and 1 atm. *Geochimica et Cosmochimica Acta* 68, 557-571.

Jones R. H. and Lofgren G. E. (1993) A comparison of FeO-rich, porphyritic olivine chondrules in unequilibrated chondrites and experimental analogs. *Meteoritics* 28, 213-221.

Jull A. J. T., Cheng S., Gooding J. L., and Velbel M. A. (1988) Rapid growth of magnesium-carbonate weathering products in a stony meteorite from Antarctica. *Science* 242, 417-419.

Kallemeyn G. W. and Wasson J. T. (1982) The compositional classification of chondrites: III. Ungrouped carbonaceous chondrites. *Geochimica et Cosmochimica Acta* 46, 2217-2228.

Keil K., Stoffler D., Love S. G., and Scott E. R. D. (1997) Constraints on the role of impact heating and melting in asteroids. *Meteoritics & Planetary Science* 32, 349-363.

Kent A. J. R., Hutcheon I. D., Ryerson F. J., and Phinney D. L. (2001) The temperature of formation of carbonate in Martian meteorite ALH84001: Constraints from cation diffusion. *Geochimica et Cosmochimica Acta* 65, 311-321.

Kita N. T., Huss G. R., Tachibana S., Amelin Y., Nyquist L. E., and Hutcheon I. D. (2005) Constraints on the origin of chondrules and CAIs from short-lived and long-lived radionuclides. In: Krot, A. N., Scott, E. R. D., and Reipurth, B. Eds.)*Chondrites and the Protoplanetary Disk*. Astronomical Society of the Pacific, Kaua'i, Hawai'i.

Kleine C. and Dutrow B. (2007) *Mineral Science*. Jogn Wiley & Sons.

Kölling M., Ebert M., and Schulz H. D. (2000) A novel approach to the presentation of pe/pH-diagrams. In: Schüring, J., Schulz, H. D., Fischer, W. R., Böttcher, J., and

Duijnisveld, H. M. Eds.), *Redox: Fundamentals, Processes, and Applications*. Springer, New York.

Krot A. N., Petaev M. I., Scott E. R. D., Choi B. G., Zolensky M. E., and Keil K. (1998) Progressive alteration in CV3 chondrites: More evidence for asteroidal alteration. *Meteoritics & Planetary Science* 33, 1065-1085.

Krot A. N., Meibom A., Weisberg M. K., and Keil K. (2002) The CR chondrite clan: Implications for early solar system processes. *Meteoritics & Planetary Science* 37, 1451-1490.

Krot A. N., Hutcheon I. D., Brearley A. J., Pravdivtseva O. V., Petaev M. I., and Hohenberg C. M. (2006) Timescales and settings for alteration of chondritic meteorites. In: Lauretta, D. S., Leshin, L. A., and McSween, H. Y. Eds.), *Meteorites and the early solar system II*. University of Arizona Press, Tucson, AZ.

Lange M. A., Lambert P., and Ahrens T. J. (1985) Shock effects on hydrous minerals and implications for carbonaceous meteorites. *Geochimica et Cosmochimica Acta* 49, 1715-1726.

Lee M. S., Rubin A. E., and Wasson J. T. (1992) Origin of metallic Fe-Ni in Renazzo and related chondrites. *Geochimica et Cosmochimica Acta* 56, 2521-2533.

León J. d., Campins H., Tsiganis K., Morbidelli A., and Licandro J. (2010) Origin of the near-Earth asteoid Phaethon and the Geminids meteor shower. *Astronomy & Astrophysics*, 513, A26.

Lugmair G. W. and Shukolyukov A. (1998) Early solar system timescales according to ^{53}Mn-^{53}Cr systematics. *Geochimica et Cosmochimica Acta* 62, 2863-2886.

McMillan S. G. and Schwertmann U. (1998) Morphological and genetic relations between siderite, calcite and goethite in a Low Moor Peat from southern Germany. *European Journal of Soil Science* 49, 283-293.

McSween H. Y. (1987) Aqueous alteration in carbonaceous chondrites: Mass balance constraints on matrix mineralogy. *Geochimica et Cosmochimica Acta* 51, 2469-2447.

McSween H. Y., Ghosh A., Grimm R. E., Wilson L., and Young E. D. (2002) Thermal evolution models of asteroids. In: Bottke, W. F., Paolicchi, P., Binzel, R. P., and Cellino, A. Eds.), *Asteroids III*. University of Arizona Press, Tucson, AZ.

Nakamura T. (2005) Post-hydration thermal metamorphism of carbonaceous chondrites. *Journal of Mineralogical and Petrological Sciences* 100, 260-272.

Nakato A., Nakamura T., Kitajima F., and Noguchi T. (2008) Evaluation of dehydration mechanism during heating of hydrous asteroids based on mineralogical and chemical analysis of naturally and experimentally heated CM chondrites. *Earth Planets Space* 60, 855-864.

Palandri J. L. and Reed M. H. (2004) Geochemical models of metasomatism in ultramafic systems: serpentinization, rodingitization, and sea floor carbonate chimney precipitation. *Geochimica et Cosmochimica Acta* 68, 1115-1133.

Petitat M., McKeegan K. D., Gounelle M., Mostefaoui S., Marrocchi Y., Meibom A., and Leshin L. A. (2009) Duration and sequence of carbonate crystallization on the Orgueil protolith: ^{53}Mn-^{53}Cr systematics of their evolution in O can C isotopic composition. *Lunar and Planetary Science Conference XL*. LPI, The Woodlands, TX.

Petitat M., Birck J.-L., Luu T. H., and Gounelle M. (2011a) The chromium isotopic composition of the ungrouped carbonaceous chondrite Tagish Lake. *The Astrophysical Journal* 736, 23.

Petitat M., Marrocchi Y., McKeegan K. D., Mostefaoui S., Meibom A., Zolensky M., and Gounelle M. (2011b) ^{53}Mn-^{53}Cr ages of Kaidun carbonates. *Meteoritics & Planetary Science* 46, 275-283.

Rasmussen B., Buick R., and Holland H. D. (1999) Redox state of the Archean atmosphere: Evidence from detrital heavy minerals in ca. 3250-2750 Ma sandstones from the Pilbara Craton, Australia: Reply. *Geology* 27, 1152-1152.

Riciputi L. R., McSween H. Y., Jonson C. A., and Prinz M. (1994) Minor and trace-element concentrations in carbonates of carbonaceous chondrites, and implications for the compositions of co-existing fluids. *Geochimica et Cosmochimica Acta* 58, 1343-1351.

Robert F. (2006) Solar System deuterium/hydrogen ratio. In: Lauretta, D. S. and McSween, H. Y. Eds.), *Meteorites and the Early Solar System II*. University of Arizona Press, Tucson.

Romanek C. S., Jimenez-Lopez C., Navarro A. R., Sanchez-Roman M., Sahai N., and Coleman M. (2009) Inorganic synthesis of Fe-Ca-Mg carbonates at low temperature. *Geochimica et Cosmochimica Acta* 73, 5361-5376.

Rosenberg N. D., Browning L., and Bourcier W. L. (2001) Modeling aqueous alteration of CM carbonaceous chondrites. *Meteoritics & Planetary Science* 36, 239-244.

Rubin A. E. (1995) Petrologic evidence for collisional heating of chondritic asteroids. *Icarus* 113, 156-167.

Rubin A. E. (2012) Collisional facilitation of aqueous alteration of CM and CV carbonaceous chondrites. *Geochimica et Cosmochimica Acta* 90, 181-194.

Sato K., Miyamoto M., and Zolensky M. (1997) Absorption bands near three micrometers in diffuse reflectance spectra of carbonaceous chondrites: Comparison with asteroids. *Meteoritics & Planetary Science* 32, 503-507.

Sato K. and Miyamoto M. (1998) Infrared diffuse reflectance spectra of weathered and unweathered CR2 chondrites: Comparison with Asteroids. *Antarct. Meteorite Res.* 11, 155-162.

Schmidt B. E., Thomas P. C., Bauer J. M., Li J.-Y., McFadden L. A., Mutchler M. J., Radcliffe S. C., Rivkin A. S., Russell C. T., Parker J. W., and Stern S. A. (2009) The shape and surface variation of 2 Pallas from the Hubble Space Telescope. *Science* 326, 275-278.

Schrader D. L., Connolly H. C., and Lauretta D. S. (2008) Opaque phases in type-II chondrules from CR2 chondrites: Implications for CR parent body formation. *Geochimica et Cosmochimica Acta* 72, 6124-6140.

Schrader D. L., Franchi I. A., Connolly H. C., Greenwood R. C., Lauretta D. S., and Gibson J. M. (2011) The formation and alteration of the Renazzo-like carbonaceous chondrites I: Implications of bulk-oxygen isotopic composition. *Geochimica et Cosmochimica Acta* 75, 308-325.

Schultz L. (1986) Allende in Antarctica: Temperatures in Antarctic meteorites. *Meteoritics* 21, 505.

Scott E. R. D. (2007) Chondrites and the protoplanetary disk. *Annu Rev Earth Pl Sc* 35, 577-620.

Shannon R. D. and Prewitt C. T. (1969) Effective ionic radii in oxides and fluorides. *Acta Crystal* B25, 925-946.

Stumm W. and Morgan J. J. (1996) *Aquatic Chemistry: chemical equilibria and rates in natural waters*. John Wiley & Sons, New York.

Trigo-Rodriguez J. M. and Blum J. (2009) The effect of aqueous alteration and metamorphism in the survival of presolar silicate grains in chondrites. *Publications of the Astronomical Society of Australia* 26, 448-453.

Tyra M. A., Farquhar J., Wing B. A., Benedix G. K., Jull A. J. T., Jackson T., and Thiemens M. H. (2007) Terrestrial alteration of carbonate in a suite of Antarctic CM chondrites: Evidence from oxygen and carbon isotopes. *Geochimica et Cosmochimica Acta* 71, 782-795.

Tyra M. A., Brearley A. J., Hutcheon I. D., Ramon E., Matzel J., and Weber P. (2009) Carbonate formation timescales vary between CM1 chondrites ALH84051 and ALH84034. *Lunar and Planetary Science Conference XL*. Lunar Planet. Inst., Houston, TX.

Tyra M. A., Matzel J., Brearley A. J., and Hutcheon I. D. (2010) Variability in carbonate petrography and NanoSIMS ^{53}Mn/^{53}Cr systematics in paired CM1 chondrites ALH 84051, ALH 84049, and ALH 84034. *Lunar and Planetary Science XLI,* abs #2687.

Tyra M. A., Brearley A. J., and Guan Y. (2011a) Oxygen isotopic composition of secondary carbonates in CR1 chondrite GRO 95577*Lunar and Planetary Science Conference*. LPI, The Woodlands, TX.

Tyra M. A., Le Guillou C., and Brearley A. J. (2011b) Deciphering the history of carbonates and associated minerals during secondary alteration within CR1 GRO 95577. *Meteoritical Society Meeting*. LPI, London.

Wadhwa M., Zinner E. K., and Crozaz G. (1997) Manganese-chromium systematics in sulfides of unequilibrated enstatite chondrites. *Meteoritics & Planetary Science* 32, 281-292.

Wasson J. T. (1996) Chondrule Formation: Energetics and Length Scales. In: Hewins, R. H., Jones, R. H., and Scott, E. R. D. Eds.), *Chondrules and the Protoplanetary Disk*. Cambridge University Press, New York.

Wasson J. T. and Rubin A. E. (2010) Metal in CR chondrites. *Geochimica et Cosmochimica Acta* 74, 2212-2230.

Weisberg M. K., Prinz M., Clayton R. N., and Mayeda T. K. (1993) The CR (Renazzo-type) carbonaceous chondrite group and its implications. *Geochimica et Cosmochimica Acta* 57, 1567-1586.

Weisberg M. K., Prinz M., Zolensky M. E., and Ivanov A. V. (1994) Carbonates in the Kaidun chondrite. *Meteoritics* 29, 549-550.

Weisberg M. K., Prinz M., Clayton R. N., Mayeda T. K., Grady M. M., and Pillinger C. T. (1995) The CR chondrite clan. *Proc. NIPR Symp. Antarct. Meteorites* 8, 11-32.

Weisberg M. K. and Huber H. (2007) The GRO 95577 CR1 chondrite and hydration of the CR parent body. *Meteoritics & Planetary Science* 42, 1495-1503.

Weiss B. P., Elkins-Tanton L. T., and Ebel D. S. (2009a) Evidence for internally generated magnetic fields on the CV chondrite parent planetesimal. *Lunar and Planetary Science Conference*. LPI, Houston, TX.

Weiss B. P., Gattecceca J., Stanley S., Rochette P., and Christensen U. R. (2009b) Paleomagnetic records of meteorites and early planetesimal differentiation. *Space Science Reviews*.

Young E., Ash R., England P., and Rumble D. (1999) Fluid flow in chondritic parent bodies: Deciphering the compositions of planetesimals. *Science* 286, 1331-1335.

Young E. D. (2001) The hydrology of carbonaceous chondrite parent bodies and the evolution of planet progenitors. *Phil. Trans. R. Soc. Lond. A.* 359, 2095-2110.

Zheng Y. F., Satir M., Metz P., and Sharp Z. D. (1999) Oxygen isotope exchange processes and disequilibrium between calcite and forsterite in an experimental C-O-H fluid. *Geochimica et Cosmochimica Acta* 63, 1781-1786.

Zolensky M., Weisberg M. K., Buchanan P. C., Prinz M., Reid A., and Barrett R. A. (1992) Mineralogy of dark clasts in CR chondrites, eucrites and howardites. *Lunar and Planetary Science Conference*. Lunar and Planetary Institute, Houston, TX.

Zolensky M., Ivanov A. V., Yang S. V., Mittlefehldt D. W., and Ohsumi K. (1996) The Kaidun meteorite: Mineralogy of an unusual CM1 lithology. *Meteoritics & Planetary Science* 31, 484-493.

Zolensky M., Nakamura K., Gounelle M., Mikouchi T., Kasama T., Tachikawa O., and Tonui E. (2002) Mineralogy of Tagish Lake: An ungrouped type 2 carbonaceous chondrite. *Meteoritics & Planetary Science* 37, 737-761.

Zolensky M. and Ivanov A. (2003) The Kaidun microbreccia meteorite: A harvest from the inner and outer asteroid belt. *Chem Erde-Geochem* 63, 185-246.

Zolensky M. E., Bourcier W. L., and Gooding J. L. (1989) Aqueous alteration on the hydrous asteroids - Results of Eq3/6 computer-simulations. *Icarus* 78, 411-425.

Zolensky M. E., Mittlefehldt D. W., Lipschutz M. E., Wang M. S., Clayton R. N., Mayeda T. K., Grady M. M., Pillinger C. T., and Barber D. (1997) CM chondrites exhibit the complete petrologic range from type 2 to 1. *Geochimica et Cosmochimica Acta* 61, 5099-5115.

Zolotov M. Y. and Mironenko M. V. (2008a) Aqueous alteration of CM2 chondrites evaluated with kinetic models. *Meteoritical Society Meeting*. Meteoritical Society.

Zolotov M. Y. and Mironenko M. V. (2008b) Early alteration of matrices in parent bodies of CI/CM carbonaceous chondrites: Kenetic-thermodynamic modeling *Lunar and Planetary Science XXXIX*. Lunar and Planetary Institute, Houston, TX.

9 Tables

Table 1. Representative carbonate analyses from GRO 95577. The full data set is in Appendix 1.

				Wt%							Mol%		
lithology	**Grain***	**SiO****	**FeO**	**MnO**	**MgO**	**CaO**	**SrO**	**CO_2**	**Total**	**Fe**	**Mn**	**Mg**	**Ca**
siderite	g30-15-b3	0.05	27.19	17.09	11.10	1.93	-	40.96	98.33	40.73	25.93	29.65	3.69
DL	g30-15-b4	0.27	24.24	20.84	9.79	2.48	-	40.80	98.42	36.75	31.99	26.45	4.81
	g30-10-s3	0.13	29.62	14.94	9.73	3.34	-	40.86	98.64	44.62	22.80	26.12	6.45
	g30-15-b2	1.51	30.58	12.71	11.83	2.51	-	43.70	102.83	45.14	19.00	31.12	4.74
	g30-10-s1	1.24	32.91	9.44	13.40	1.90	-	43.96	102.85	47.84	13.90	34.72	3.54
CR	g30-7-b2	0.14	33.43	9.36	12.70	1.17	-	41.28	98.08	49.86	14.13	33.77	2.23
	g30-7-b2	0.05	33.56	9.23	12.84	1.25	-	41.36	98.29	49.80	13.87	33.96	2.37
	g30-7-b3	1.24	28.30	15.57	10.89	1.47	-	41.85	99.32	43.30	24.13	29.70	2.87
	g30-11-b1	1.84	25.65	19.02	9.51	1.75	-	41.96	99.73	40.01	30.05	26.45	3.49
	g30-11-b1	2.15	24.97	19.01	10.10	1.47	-	42.42	100.11	38.95	30.04	28.08	2.94
DL	g53-5-b4	-	31.69	9.91	13.02	2.11	0.04	41.45	98.21	46.85	14.84	34.32	3.99
	g53-5-b17	1.95	27.39	15.37	10.69	2.17	-	42.54	100.12	42.28	24.03	29.40	4.29
	g53-9-b9	0.74	31.56	10.60	12.26	2.68	-	42.49	100.34	46.69	15.89	32.34	5.09
	g53-9-b9	0.74	31.56	10.60	12.26	2.68	-	42.49	100.34	46.69	15.89	32.34	5.09
	g53-9-b9	1.69	31.56	10.26	11.82	2.42	-	42.97	100.71	47.73	15.72	31.87	4.68
dolomite	g30-9-s3	0.74	6.33	10.42	13.08	26.19	-	46.26	103.01	8.58	14.31	31.61	45.50
DL	g30-9-s3	0.33	5.58	9.37	11.84	29.31	-	45.64	102.06	7.56	12.86	28.63	50.94
	g30-9-s3	0.11	6.33	11.73	11.71	26.71	-	45.06	101.66	8.63	16.20	28.49	46.68
	g30-9-s3	-	6.68	12.52	10.61	26.90	-	44.58	101.34	9.19	17.43	26.01	47.37
calcite	g30-10-s6	-	0.72	0.20	0.09	56.07	-	44.67	101.76	0.99	0.28	0.22	98.50
CR	g30-10-s6	0.15	0.77	0.13	0.13	55.47	-	44.45	101.10	1.07	0.18	0.31	98.44
DL	g53-2-b4	-	0.38	0.03	0.31	56.40	-	44.84	101.95	0.52	0.04	0.75	98.69
	g53-2-b4	0.13	0.53	0.07	0.63	56.09	-	45.27	102.72	0.71	0.10	1.52	97.66
	g53-2-b4	0.49	1.10	0.16	0.47	55.22	-	45.34	102.79	1.51	0.22	1.15	97.12

*g30 corresponds to GRO 95577, 30; g53 to GRO 95577, 53; ** Si contamination noted in Wt% but not calculated into mol% calculation

Table 2
Mn-Cr data for selected GRO 95577 siderite grains. DL denotes analyses of a grain from dark lithology and CR from the host CR lithology

Grain	Lithology	ROI	^{55}Mn/^{52}Cr	2σ	^{53}Cr/^{52}Cr	2σ
GRO 95577, 53						
grain 1	DL	4	5.32E+05	5.08E+04	0.1282	0.0293
		3	1.77E+05	1.23E+04	0.1184	0.0202
		2	3.55E+04	1.38E+03	0.1111	0.0109
		1	6.93E+01	4.78E-02	0.1177	0.0002
grain 2	DL	3	1.17E+05	1.64E+04	0.1085	0.0390
		2	1.45E+04	6.70E+02	0.1089	0.0128
		1	1.01E+02	2.14E-01	0.1148	0.0006
grain 3	DL	4	9.19E+03	4.37E+02	0.1180	0.0139
		3	3.58E+03	1.11E+02	0.1145	0.0089
		2	1.72E+03	2.85E+01	0.1140	0.0047
		1	1.80E+02	3.40E-01	0.1155	0.0005
GRO 95577, 30						
grain 1	CR	4	1.06E+05	6.85E+03	0.1139	0.0176
		3	9.84E+03	1.84E+02	0.1101	0.0047
		2	7.97E+02	4.62E+00	0.1120	0.0010
		1	2.00E+02	1.03E+00	0.1127	0.0008
grain 2	CR	4	2.04E+04	2.53E+03	0.1269	0.0352
		3	7.35E+03	5.01E+02	0.1241	0.0190
		2	2.20E+03	5.58E+01	0.1148	0.0066
		1	2.74E+02	2.38E+00	0.1129	0.0020
grain 3	CR	3	8.09E+03	5.32E+02	0.1017	0.0163
		2	1.93E+03	3.65E+01	0.1103	0.0048
		1	2.20E+02	1.30E+00	0.1123	0.0011
grain 4	DL	3	5.53E+02	1.56E+01	0.1216	0.0077
		2	2.39E+02	3.92E+00	0.1139	0.0042
		1	1.23E+02	1.99E+00	0.1126	0.0041
grain 5	DL	3	6.32E+03	3.37E+02	0.1015	0.0132
		2	9.92E+02	1.36E+01	0.1096	0.0034
		1	2.42E+02	1.43E+00	0.1115	0.0010

Duplicate analyses of each grain are from different regions (ROIs). These are delimited by measured ^{55}Mn/^{52}Cr ratio using image processing software.

10 Figures

Figure 1. Optical microscope and X-ray maps of the two thin sections of GRO 95577 examined in this study showing the general textural characteristics of the samples. Figures 1a and 1c are stitched petrographic microscope images in cross-polarized light. In these images, high birefringence grains (light pink) generally are carbonates. Figs. 1c and 1d are mosaic RGB X-ray maps of the two samples where red denotes Mn, green Ca, and blue Si. As the primary carrier of Mn in these samples, siderite is red, Ca-carbonate is green, and phyllosilicates are blue. Two large dark lithology areas (encircled in yellow in 1b) are present in GRO 95577, 30 and DL constitutes the entire GRO 95577, 53 sample.

Figures 1a and 1b show GRO 95577, 30. The circled areas in Figure 1b denote fine-grained DL (~1/3 of sample). Regions outside the circled areas are the CR host lithology with serpentine-rich chondrule pseudomorphs. Carbonates in the CR host are restricted to the matrix and randomly dispersed throughout DL. Two large metal grains are denoted.

Figures 1c and 1d show GRO 95577, 53 where the entire thin section consists of DL. Note the rare chondrules, two of which are ~mm sized. This section resembles a hydrated CV chondrite type A/B dark inclusion in CV chondrites (Itoh and Tomeoka, 2003). Carbonates are disseminated throughout the sample like in the DL within GRO 95577, 53.

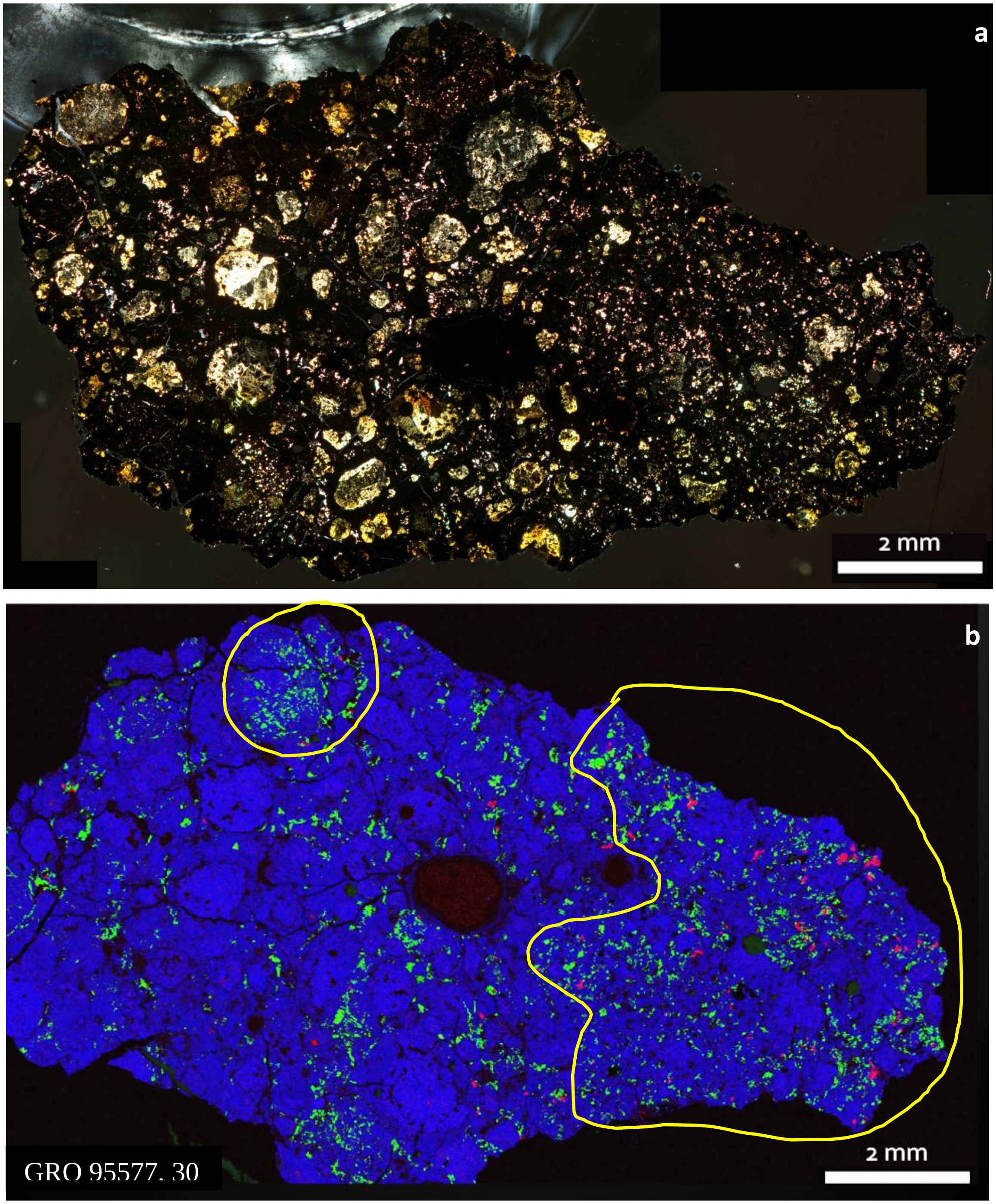
a
2 mm
b
GRO 95577, 30
2 mm

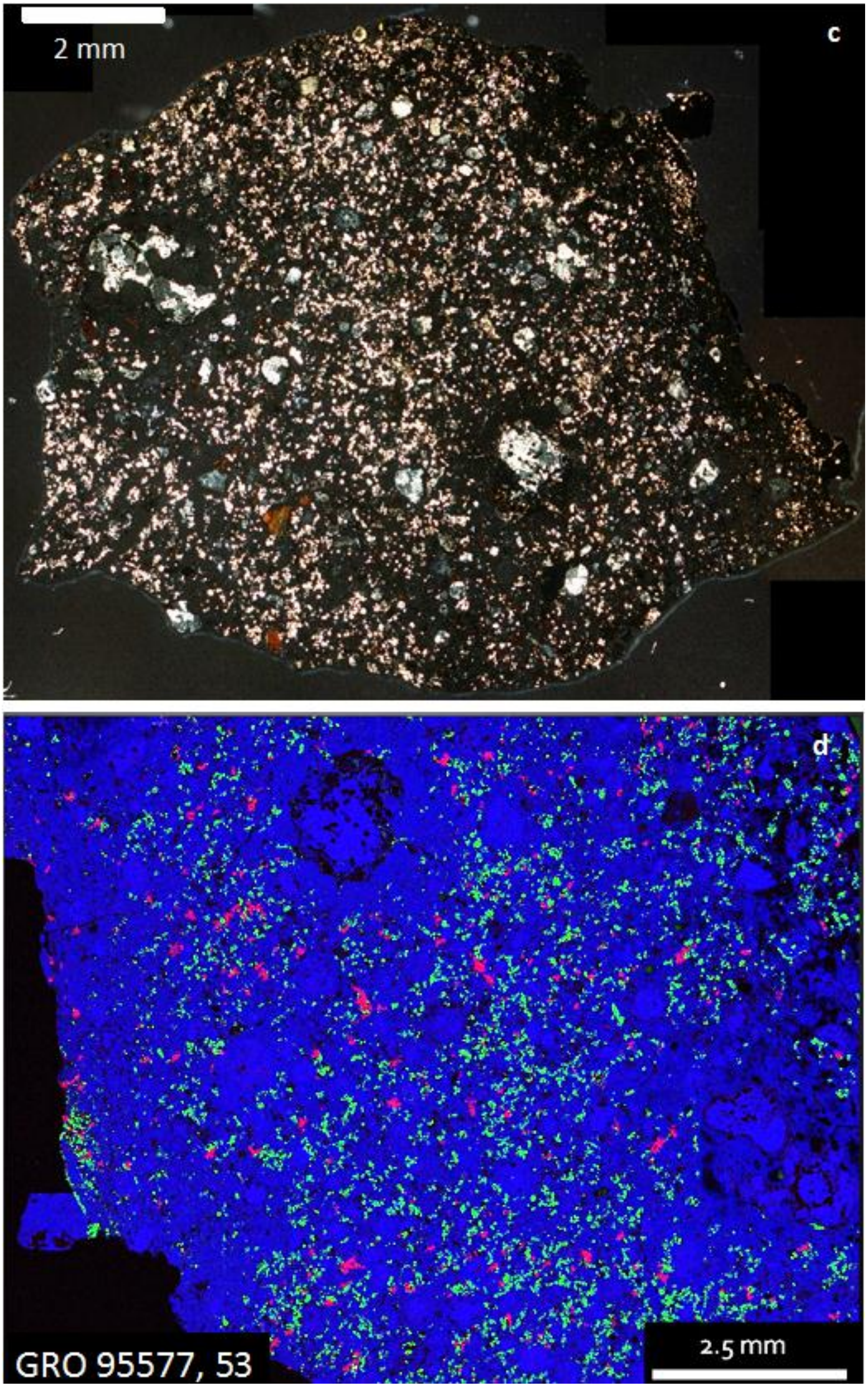
2 mm
c
d
GRO 95577, 53
2.5 mm

Figure 2. BSE images of objects found in GRO 95577. Symbols include mt, magnetite; r-meso, replaced mesostasis; Mg-phyllo, Mg-rich phyllosilicate; and cp, calcium phosphate.

- **a.** This image shows a large chondrule pseudomorph that resembles a type 1 chondrule, and a smaller chondrule fragment. Mg-rich phyllosilicate, altered mesostasis, and common magnetite blebs have replaced forsterite and enstatite, mesostasis, and metal respectively. From GRO 95577, 53 DL.
- **b.** Typical replaced chondrule and chondrule fragment in GRO 95577, 30, host lithology. These also resemble type 1 chondrules.
- **c.** Large magnetite from GRO 95577, 30. The inner area contains more S and O than the pure (very bright in BSE) magnetite rim. Grain is rimmed by fine-grained phyllosilicate. From CR host lithology.
- **d.** Magnetite clast from GRO 95577, 30. Note concentric layering perhaps from episodic oxidation. The scalloped edges suggest conditions (Eh, pH, and/or T) changed after magnetite had formed, leaving magnetite unstable.
- **e.** Magnetite clast. Note the layers visible in the BSE image. This object also has an intensely altered margin from chemical destabilization. The boxed area is shown at a higher magnification in Figure 2f.
- **f.** This image shows a detail of the periphery of the magnetite grain in Figure 2e. The margin contains iron-oxide, phosphate, and phyllosilicate minerals inter-fingering with magnetite.

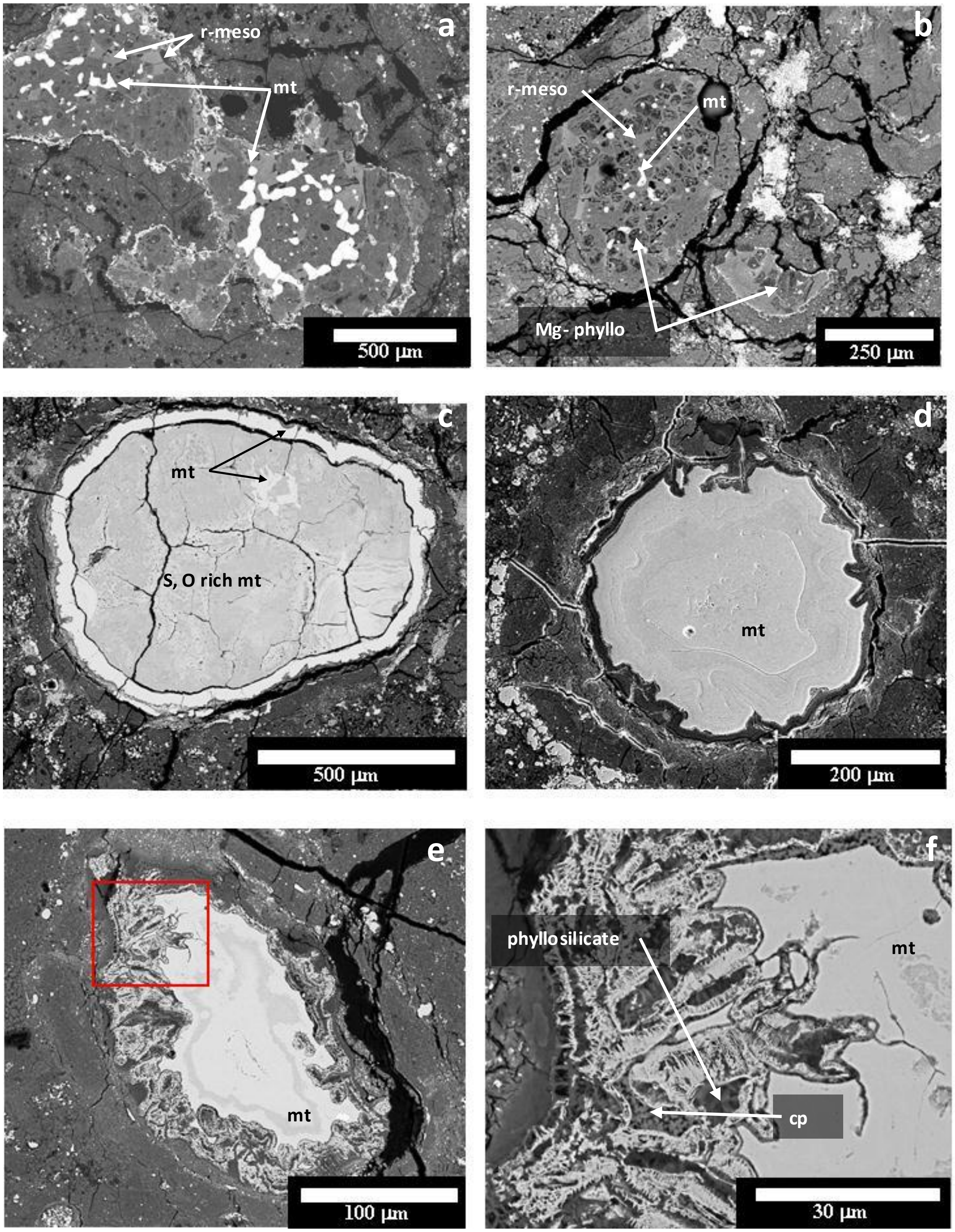
a
r-meso
mt
500 µm
b
r-meso
mt
Mg- phyllo
250 µm
c
mt
S, O rich mt
500 µm
d
mt
200 µm
e
mt
100 µm
f
phyllosilicate
mt
cp
30 µm

Figure 3. Spatial correlation of carbonates and sulfides in GRO 95577, 30 DL. The symbol c designates calcite.

a. Large scale CaFeS RGB map showing texture of associations between sulfides (green) and calcite (yellow). Notice associated secondary minerals wrapping around probable chondrule pseudomorphs.
b. X-ray map delineating calcite (yellow), siderite (red) and sulfide minerals (green) associations
c. X-ray map showing calcite (yellow), siderite (red) and sulfide mineral (green) associations around a chondrule pseudomorph.

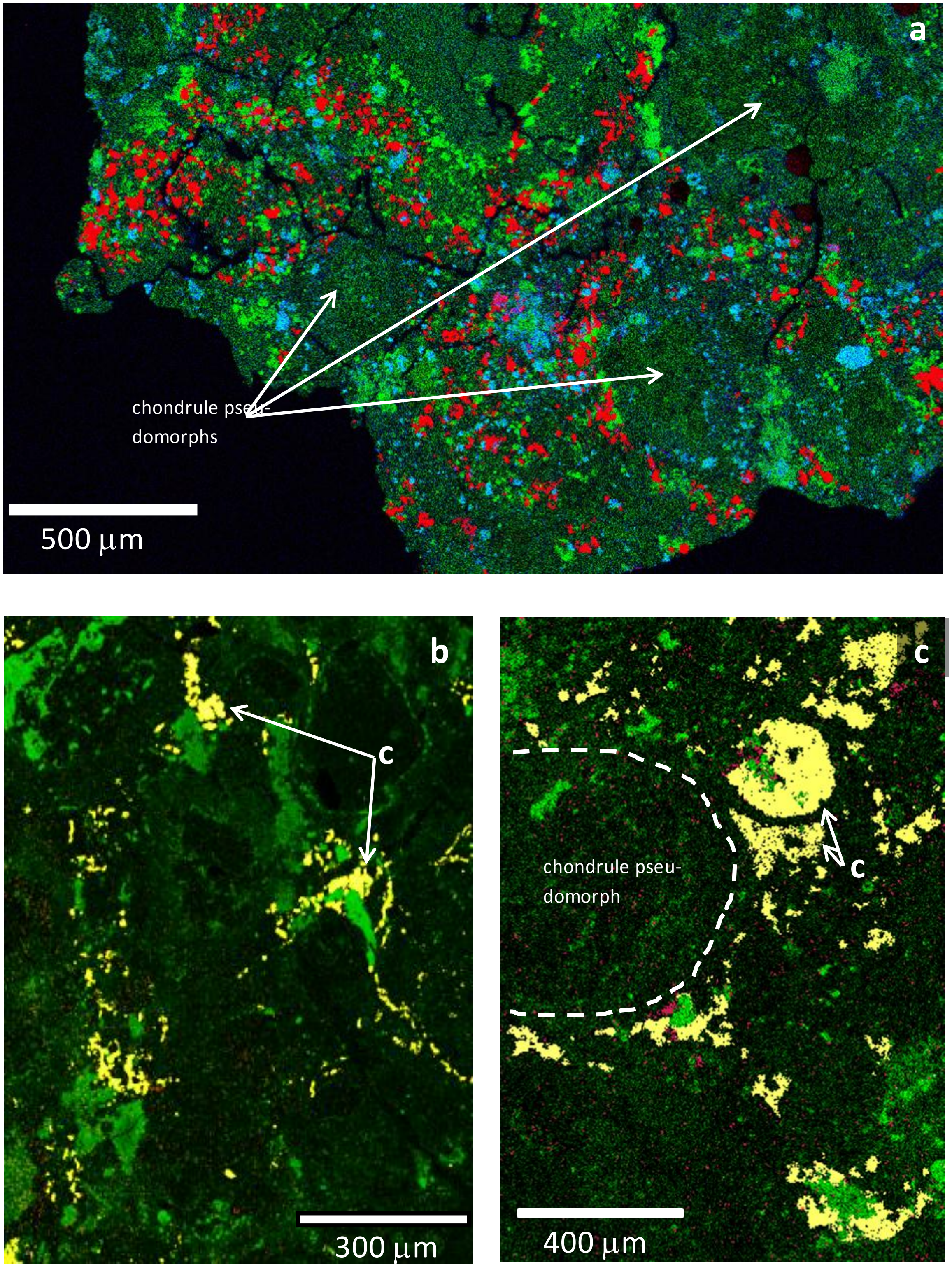
a
chondrule pseu-
domorphs
500 µm
b
c
300 µm
c
chondrule pseu-
domorph
c
400 µm

Figure 4. BSE images showing carbonate morphologies in GRO 95577. Symbols as follows: c = calcium carbonate; s = siderite, d = dolomite, p = pyrrhotite, and m = magnetite.

a. This figure shows a typical calcite associated with magnetite framboids. Siderite mantles calcite and, therefore, is a later phase. Calcite is corroded. From CR host lithology, section 30.

b. A large calcite grain and associated siderite patches. Siderite is separated from calcite by ~10 μm of phyllosilicate minerals that appear to be partial siderite pseudomorphs. Note that siderite has a corroded, mesh texture. From DL, section 53.

c. Coexisting calcite, siderite, dolomite, and associated sulfide. Calcite is corroded and has a sinuous morphology. One siderite grain is 15 μm in diameter with a corroded exterior and is also associated with more-corroded mesh siderite. Dolomite is found abutting a sulfide grain. From DL, section 53.

d. Siderite occurring interstitial to magnetite framboids. The framboids are free from corrosion while siderite, as in the other images, is corroded. From CR host lithology, section 30.

e. Association of magnetite, pyrrhotite, and siderite. The pyrrhotite appears to have grown around magnetite framboids, and siderite rims both pyrrhotite and magnetite. The pyrrhotite is corroded extensively with altered areas intruding into the mineral grain. From CR host lithology, section 30.

f. Example of textural association of siderite with pyrrhotite. Two siderite grains have pyrrhotite cores representing either an overgrowth or replacement of pyrrhotite. From DL, section 30.

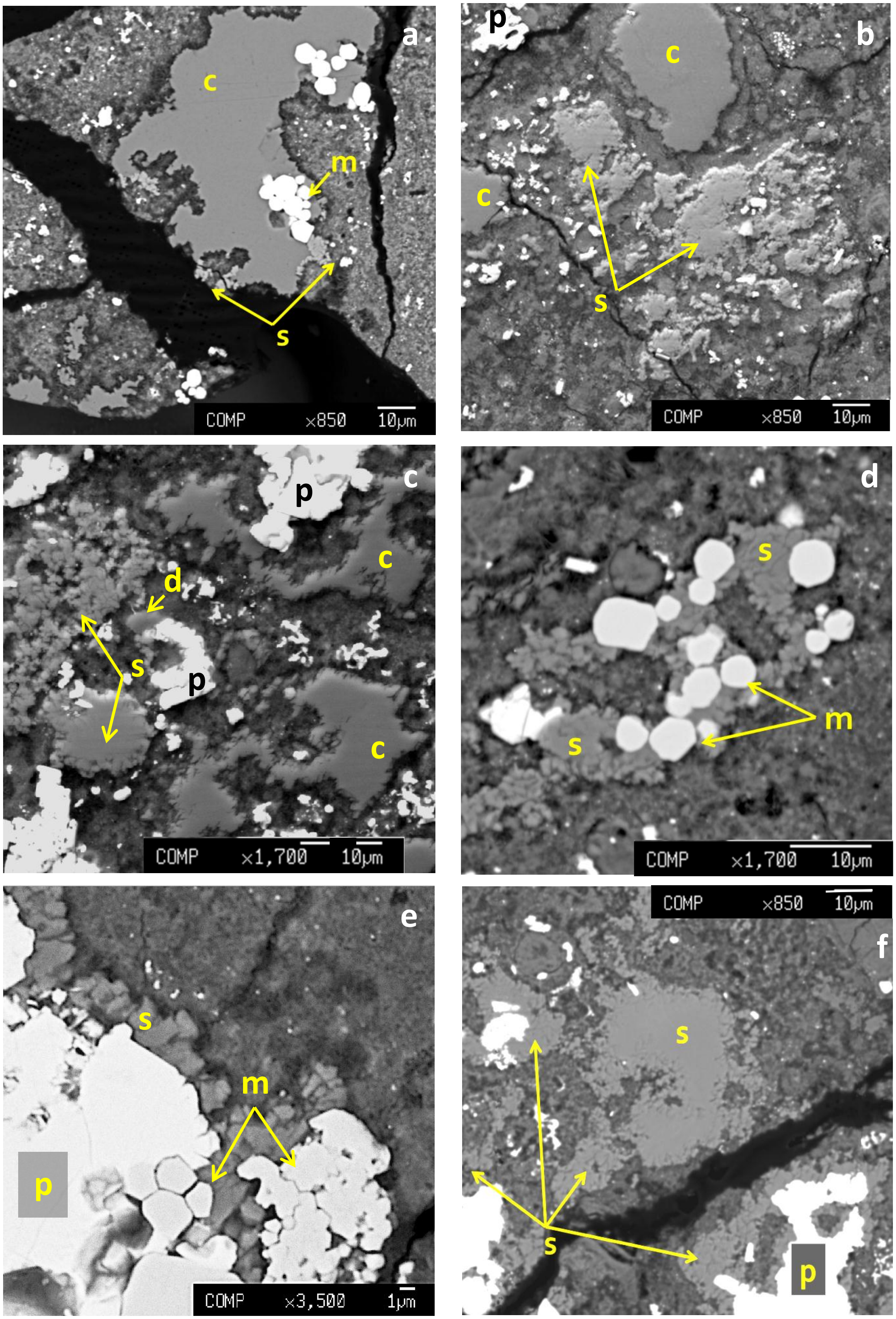
a
c
m
s
COMP ×850 10μm
p
b
c
c
s
COMP ×850 10μm
c
p
c
d
s
p
c
COMP ×1,700 10μm
d
s
m
s
COMP ×1,700 10μm
e
s
m
p
COMP ×3,500 1μm
COMP ×850 10μm
f
s
s
p

Figure 5. High contrast BSE images and microprobe data showing the characteristics of zoning in carbonates in GRO95577.

a) Zoning in dolomite consisting of two well-defined regions with a darker rhomb-shaped area in the center. From GRO 95577, 53 DL.

b) Calcite grain showing four sharply-defined growth zones.

c) Siderite grain with less well defined zoning, with a core darker than the rim. Brighter areas have less MgO. From GRO 95577, 30 DL.

d) EPMA data showing the compositions of labeled spots on Figure 5c. The areas with lower BSE intensity have lower Ca, but higher Mg and Mn compositions, and vice versa for the high BSE regions.

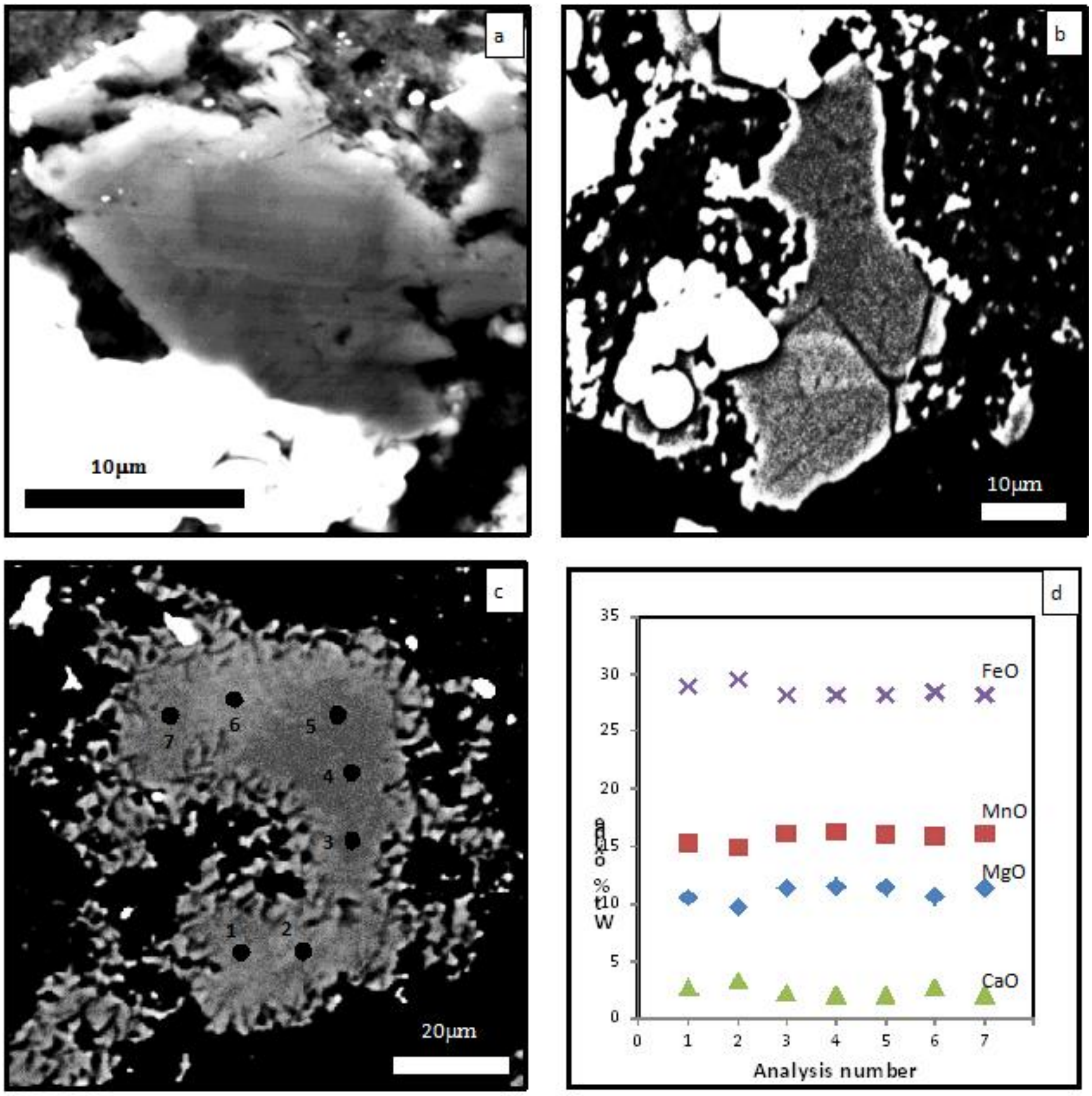
a
10µm
b
10µm
c
7
6
5
4
3
1
2
20µm
d
35
30
25
20
15
10
5
0
FeO
MnO
MgO
CaO
Wt % oxide
0
1
2
3
4
5
6
7
Analysis number

Figure 6. Normalized siderite composition represented on a ternary diagram of mole % Fe, Mn, and Mg in sample GRO 9577. Compositional data are given in Appendix 1. CR host siderite and DL siderite compositions overlap. Siderite composition is variable, but lies on a single trend line, irrespective of the lithology or the sample. Intragrain compositional variability is low compared to that between grains. Mn concentration is strongly inversely correlated with Fe and slightly negatively correlated with Mg. Siderite from Tagish Lake and breunnerite from Acfer 059/El Djouf CR2 dark inclusions (or DL) are included for reference. Siderite from GRO 95577 is compositionally distinct from siderite in these other meteorites (Endress et al., 1994; Zolensky et al., 2002).

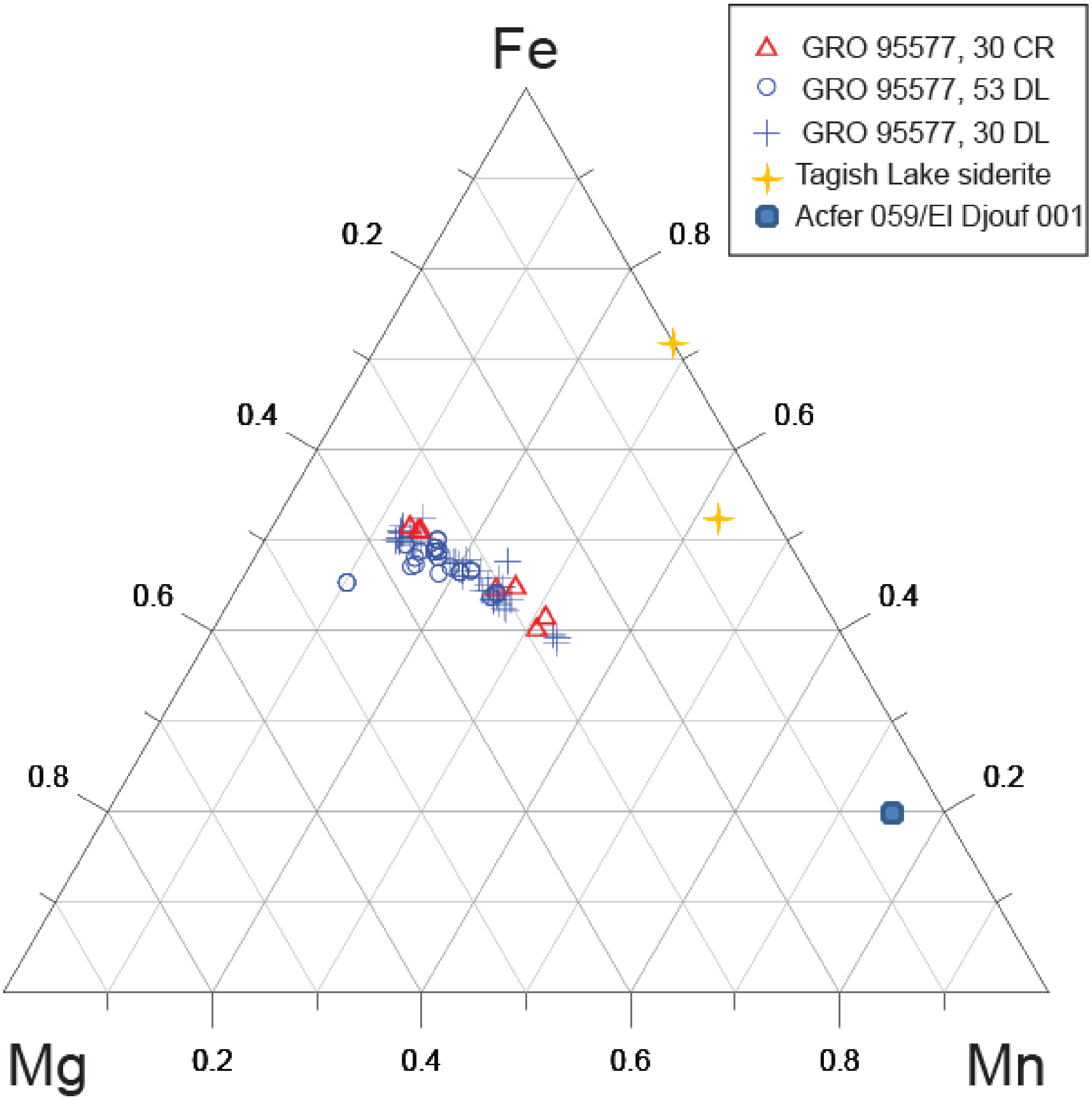

Figure 7. ^{53}Mn-^{53}Cr evolution diagram for siderite grains in GRO 95577, 30 and GRO 95577, 53. The slope of the line fitted to the data gives (solid line) a $^{53}Mn/^{55}Mn_o$ with a slope of (-1.38 ± 4.64) x 10^{-8}. The intercept of this regression is 0.1165 (± 0.0002). The upper bound of the error (dashed line, 3.27 x 10^{-8}) represents the highest $(^{53}Mn/^{55}Mn)_o$ value permissible within the uncertainty of the given data. Note the extremely wide range of Mn-Cr ratios of the data. Figure 7a shows the entire range of the data and Figure 7b shows an expanded region of Figure 7a, illustrating the details of the data with low $^{55}Mn/^{52}Cr$.

a

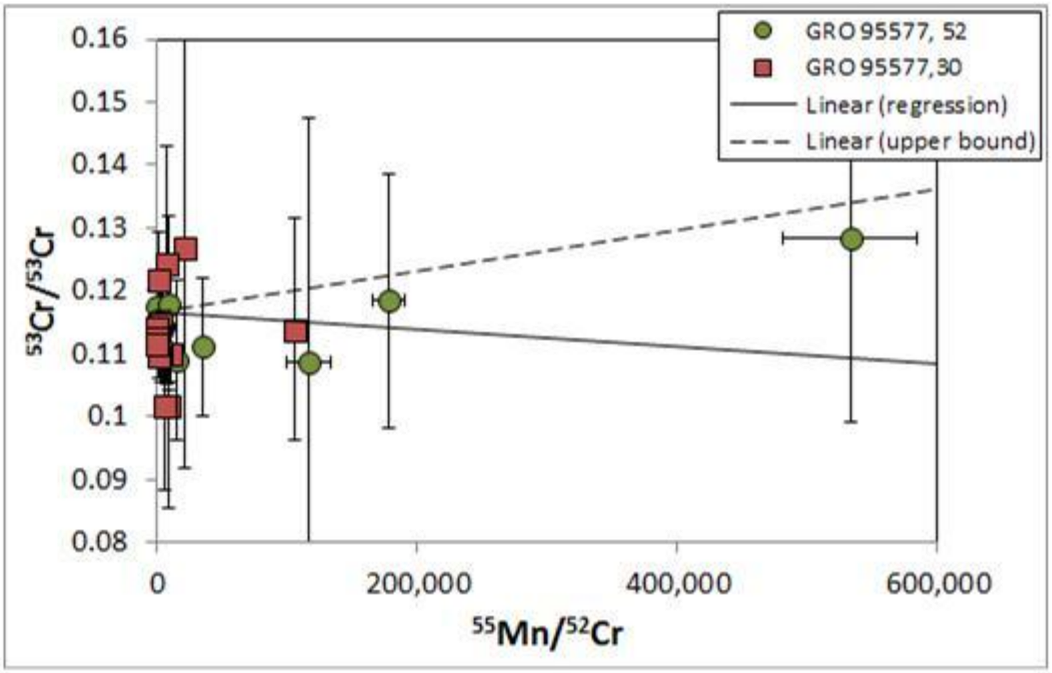

0.16
0.15
0.14
0.13
0.12
0.11
0.1
0.09
0.08
0
200,000
400,000
600,000
$^{53}Cr/^{53}Cr$
$^{55}Mn/^{52}Cr$
● GRO 95577, 52
■ GRO 95577,30
Linear (regression)
Linear (upper bound)

b

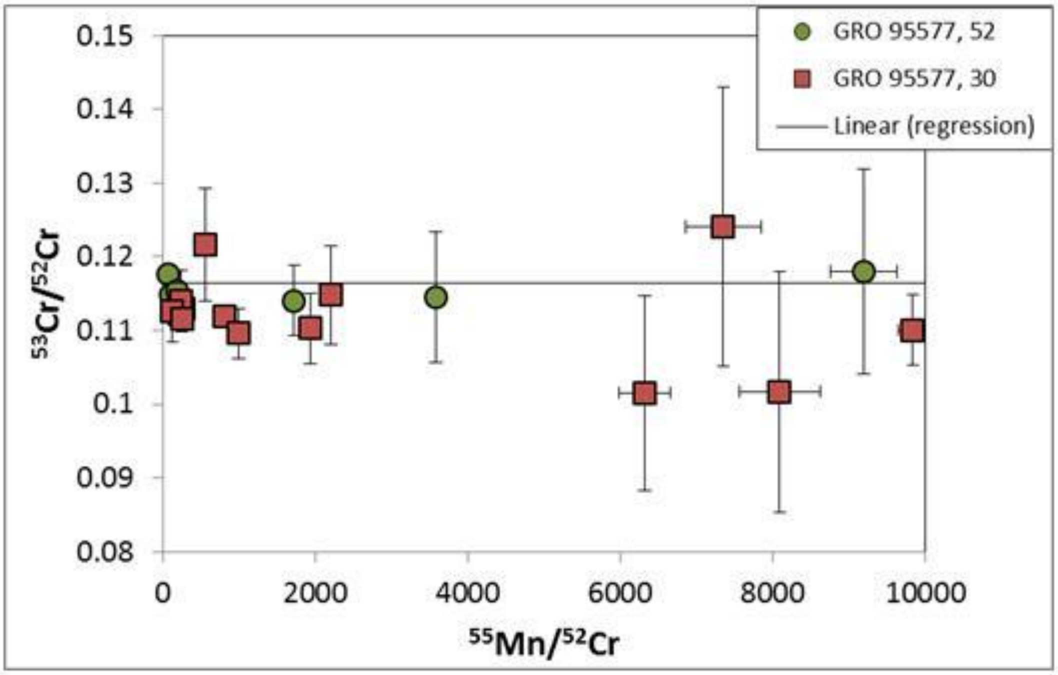

0.15
0.14
0.13
0.12
0.11
0.1
0.09
0.08
0
2000
4000
6000
8000
10000
$^{53}Cr/^{52}Cr$
$^{55}Mn/^{52}Cr$
● GRO 95577, 52
■ GRO 95577, 30
Linear (regression)

Figure 8. Eh-pH diagram showing stability fields of common minerals (shaded) in GRO 95577. Minerals are defined as py (pyrite), tro (troilite, FeS), sd (siderite), mt (magnetite), and hem (hematite). Mt, sd, and tro are stable in fields subparallel to the lower limit of the water stability field and are located under reducing conditions. Increasing $a[SO_4]$, will increase the area of the stability field of troilite at the expense of siderite and pyrite. Similarly, decreasing $a[CO_2]$ will expand both mt and tro mostly at the expense of sd. The general Eh-pH stability area of all three minerals, however, will remain very similar to that displayed above, except due to changing T. For instance, decreasing T to 100°C will drive the Fe^{2+} field to the right at the expense of mt, sd, and tro minerals to a pH ~ 8. Diagram created in Geochemist's Workbench with T=150°C, P = 15 bars, $a[H_2O] = 1$, $a\ [SO_4^{2-}] = 10^{-17}$, $a[CO_{2aq}] = 10^{-1.7}$.

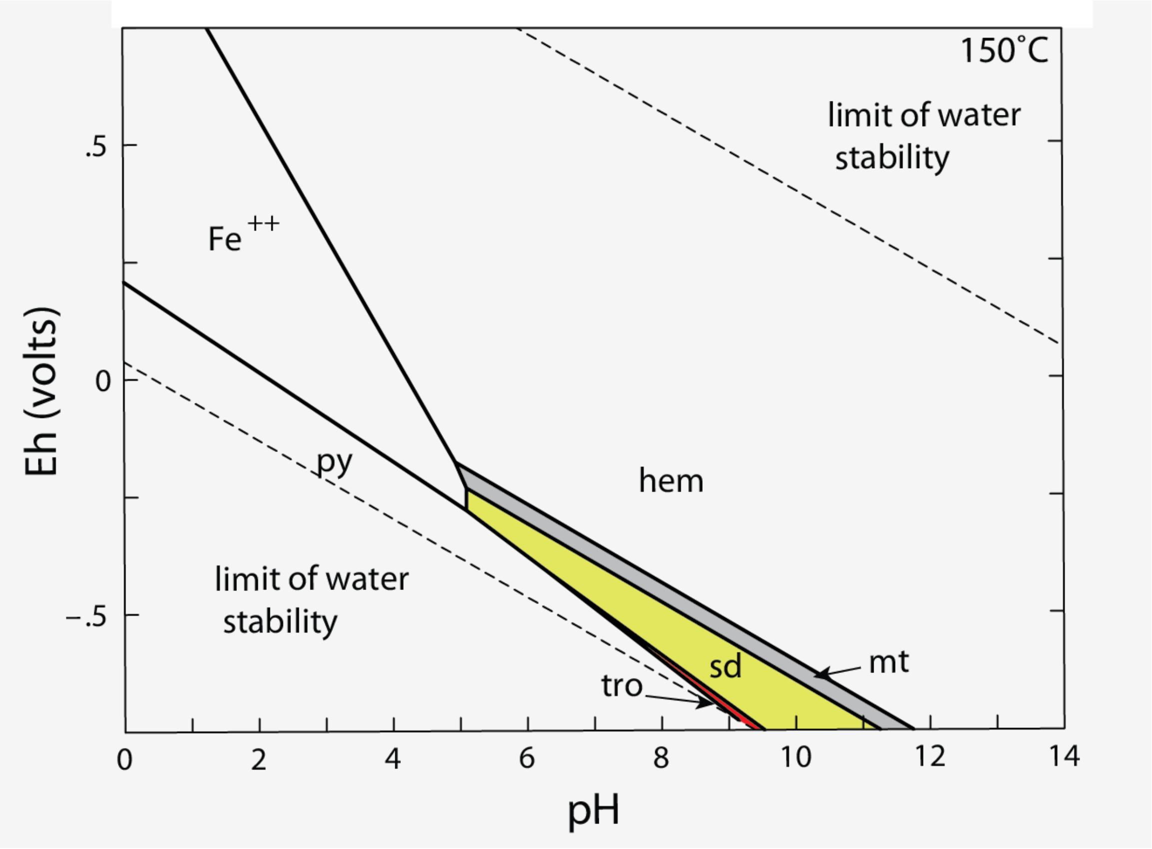

Figure 9. Mn-Cr system age data for secondary minerals in different carbonaceous chondrite groups. The diamond (GRO 95577) depicts the earliest possible age of siderite, given the error on the regression, although may be younger as indicated by the arrow. The formation age of siderite is anomalous from all data cited (Endress et al., 1996; Hutcheon and Phinney, 1996; Hutcheon et al., 1998; Hutcheon et al., 1999a; Brearley and Hutcheon, 2000; Brearley et al., 2001; Hua et al., 2005; Krot et al., 2006; de Leuw et al., 2009; Petitat et al., 2009; Tyra et al., 2009; Tyra et al., 2010; Fujiya et al., 2012). The lower x axis shows ages relative to LEW 86010, which is our anchor for the Mn-Cr isotope system and the upper axis the absolute age (Lugmair and Shukolyukov, 1998). Shaded times of CAI and chondrule formation from Kita et al. (2005) are included for reference.

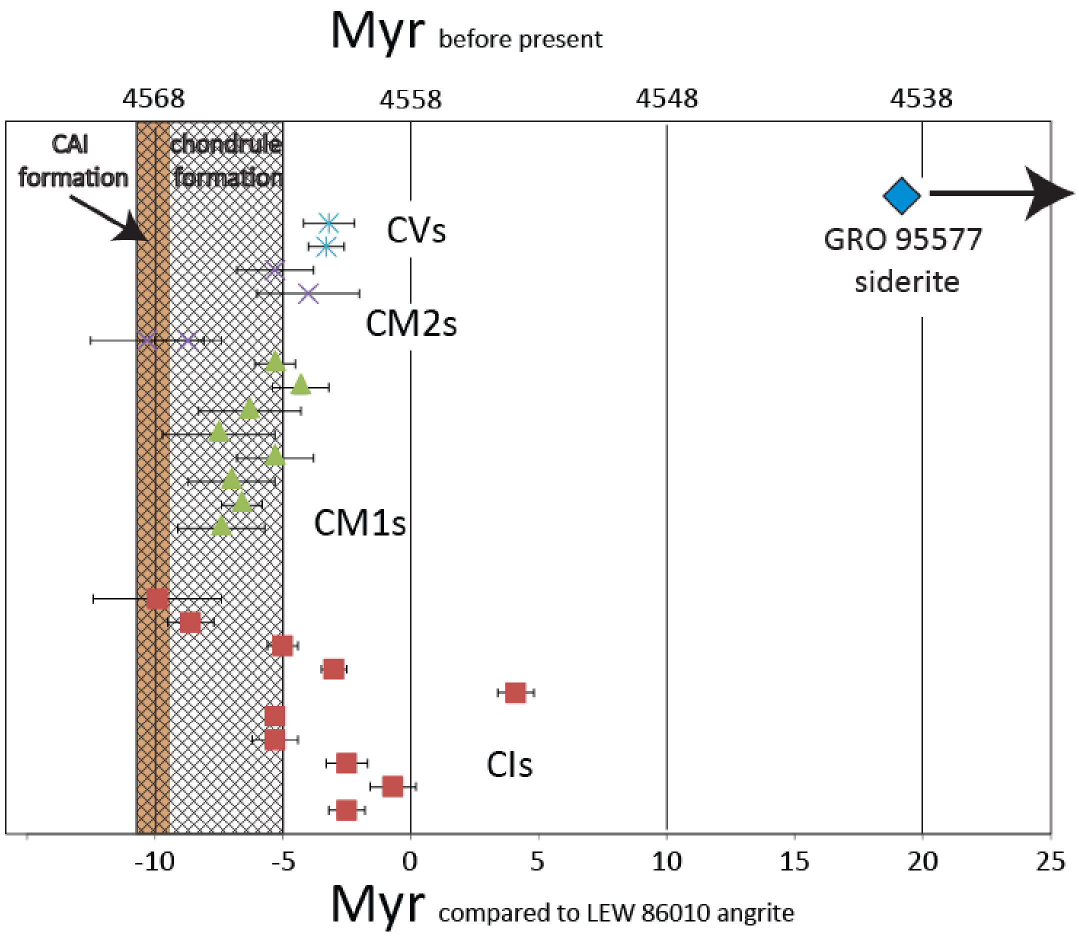

Appendix 1 EPMA-derived carbonate compositions in GRO 95577

		Wt%								Mol%			
lithology	**Grain***	**SiO_2****	**FeO**	**MnO**	**MgO**	**CaO**	**SrO**	**CO_2**	**Total**	**Fe**	**Mn**	**Mg**	**Ca**
siderite													
DL	g30-15-b3	0.05	27.19	17.09	11.10	1.93	bdl	40.96	98.33	40.73	25.93	29.65	3.69
	g30-15-b3	0.11	27.32	16.85	11.13	1.95	bdl	41.02	98.37	40.95	25.58	29.73	3.74
	g30-15-b4	0.27	24.24	20.84	9.79	2.48	bdl	40.80	98.42	36.75	31.99	26.45	4.81
	g30-10-s3	0.13	29.62	14.94	9.73	3.34	bdl	40.86	98.64	44.62	22.80	26.12	6.45
	g30-10-s3	0.04	28.47	15.86	10.67	2.61	0.05	41.06	98.77	42.55	24.00	28.44	5.01
	g30-15-b5	0.09	33.69	8.80	12.09	2.70	bdl	41.54	98.91	49.83	13.18	31.87	5.11
	g30-10-s3	-	28.21	16.10	11.39	1.98	bdl	41.25	98.92	41.89	24.21	30.14	3.76
	g30-15-b3	0.55	27.41	16.33	11.15	2.04	bdl	41.50	98.98	41.26	24.90	29.92	3.93
	g30-15-b2	0.27	28.34	16.00	10.94	2.15	bdl	41.31	99.01	42.42	24.26	29.19	4.13
	g30-10-s3	0.04	28.19	16.03	11.44	1.99	bdl	41.32	99.01	41.85	24.11	30.27	3.78
	g30-15-b5	0.58	33.13	8.44	12.79	2.17	bdl	42.05	99.16	49.26	12.71	33.90	4.13
	g30-15-b2	0.13	28.48	16.16	11.20	1.89	bdl	41.38	99.25	42.36	24.34	29.70	3.60
	g30-15-b2	0.55	29.28	14.21	11.30	2.24	bdl	41.66	99.26	43.91	21.58	30.21	4.30
	g30-10-s3	-	28.21	16.22	11.50	2.00	bdl	41.47	99.40	41.67	24.27	30.28	3.78
	g30-15-b2	0.45	28.58	15.39	11.32	2.10	bdl	41.72	99.56	42.63	23.26	30.10	4.01
	g30-15-b2	0.45	30.51	13.02	11.27	2.62	bdl	41.78	99.65	45.45	19.64	29.92	5.00
	g30-15-b4	0.52	24.55	20.61	9.61	2.99	bdl	41.42	99.69	36.99	31.45	25.80	5.76
	g30-10-s1	0.23	33.04	9.70	12.90	1.81	bdl	42.11	99.80	48.46	14.41	33.72	3.41
	g30-15-b4	0.61	24.92	20.39	9.78	2.60	bdl	41.52	99.81	37.58	31.13	26.28	5.01
	g30-10-s3	0.20	28.25	16.09	11.39	2.18	bdl	41.72	99.82	41.77	24.08	30.03	4.12
	g30-15-b5	0.44	32.85	8.25	13.60	2.23	bdl	42.48	99.86	48.10	12.23	35.48	4.19
	g30-15-b2	0.77	32.83	8.44	13.58	1.75	bdl	42.69	100.08	48.40	12.60	35.69	3.31
	g30-15-b2	0.79	32.82	8.35	13.71	1.70	bdl	42.74	100.11	48.34	12.46	36.00	3.20
	g30-10-s3	0.71	29.00	15.30	10.56	2.66	bdl	41.91	100.15	43.46	23.22	28.21	5.11

	g30-15-b2	0.58	30.16	13.16	11.89	2.27	bdl	42.24	100.30	44.63	19.72	31.35	4.30
	g30-15-b5	0.66	33.39	8.31	13.40	2.17	bdl	42.90	100.83	48.77	12.29	34.88	4.06
	g30-15-b5	0.95	32.90	8.39	13.74	1.78	bdl	43.16	100.93	48.26	12.47	35.93	3.35
	g30-10-s1	0.84	33.45	8.08	13.46	2.10	bdl	43.08	101.01	48.97	11.98	35.11	3.94
	g30-15-b2	0.58	30.04	13.51	12.07	2.28	bdl	42.60	101.08	44.07	20.07	31.57	4.29
	g30-15-b2	1.01	33.27	8.31	13.39	2.09	bdl	43.28	101.37	48.76	12.34	34.98	3.92
	g30-15-b5	0.84	33.08	8.16	13.93	1.97	0.08	43.34	101.39	48.15	12.02	36.16	3.67
	g30-10-s1	0.86	33.26	9.39	13.09	1.76	bdl	43.12	101.46	48.66	13.91	34.14	3.29
	g30-10-s1	0.55	33.11	9.51	13.29	2.09	bdl	43.12	101.66	47.92	13.94	34.28	3.87
	g30-15-b2	1.06	29.97	14.08	11.18	2.68	bdl	42.96	101.94	44.34	21.10	29.49	5.07
	g30-15-b3	1.56	27.90	16.96	10.70	1.84	bdl	43.01	101.95	41.96	25.83	28.68	3.54
	g30-10-s1	0.97	34.22	8.12	13.42	1.81	bdl	43.49	102.02	49.82	11.98	34.83	3.37
	g30-15-b2	1.49	30.80	12.93	11.46	2.25	bdl	43.34	102.26	45.83	19.48	30.40	4.29
	g30-15-b5	1.29	33.47	8.11	13.39	2.30	bdl	43.85	102.40	48.86	11.98	34.85	4.31
	g30-15-b2	1.30	30.91	12.36	12.00	2.40	bdl	43.50	102.49	45.53	18.44	31.50	4.52
	g30-15-b2	1.25	33.72	8.25	13.62	1.82	bdl	43.90	102.55	49.09	12.16	35.35	3.40
	g30-15-b2	1.39	28.82	15.15	11.64	2.14	bdl	43.47	102.60	42.60	22.67	30.67	4.05
	g30-15-b2	1.65	28.80	14.98	11.14	2.57	bdl	43.54	102.68	42.90	22.60	29.59	4.91
	g30-15-b2	1.66	30.70	12.14	12.18	2.22	bdl	43.83	102.77	45.44	18.20	32.15	4.22
	g30-10-s1	1.14	32.78	9.27	13.47	2.17	bdl	43.92	102.77	47.52	13.61	34.83	4.04
	g30-15-b2	1.51	30.58	12.71	11.83	2.51	bdl	43.70	102.83	45.14	19.00	31.12	4.74
	g30-10-s1	1.24	32.91	9.44	13.40	1.90	bdl	43.96	102.85	47.84	13.90	34.72	3.54
CR	g30-7-b2	0.14	33.43	9.36	12.70	1.17	bdl	41.28	98.08	49.86	14.13	33.77	2.23
	g30-7-b2	0.86	33.07	8.36	12.76	1.44	bdl	41.75	98.23	50.02	12.81	34.39	2.78
	g30-7-b2	0.05	33.56	9.23	12.84	1.25	bdl	41.36	98.29	49.80	13.87	33.96	2.37
	g30-7-b3	1.24	28.30	15.57	10.89	1.47	bdl	41.85	99.32	43.30	24.13	29.70	2.87
	g30-11-b1	1.84	25.65	19.02	9.51	1.75	bdl	41.96	99.73	40.01	30.05	26.45	3.49
	g30-11-b1	2.15	24.97	19.01	10.10	1.47	bdl	42.42	100.11	38.95	30.04	28.08	2.94

	g30-7-b1	2.53	27.90	16.36	9.99	1.58	bdl	43.10	101.48	43.38	25.76	27.70	3.15
DL	g53-5-b4	-	31.69	9.91	13.02	2.11	0.04	41.45	98.21	46.85	14.84	34.32	3.99
	g53-5-b16	0.69	30.04	12.12	12.07	2.08	bdl	41.74	98.73	45.17	18.47	32.35	4.01
	g53-0-b6	0.40	31.12	10.22	13.60	1.90	bdl	42.33	99.58	45.66	15.19	35.57	3.57
	g53-0-b6	0.79	30.84	10.00	13.74	1.86	bdl	42.72	99.96	45.46	14.93	36.11	3.51
	g53-5-b17	1.95	27.39	15.37	10.69	2.17	bdl	42.54	100.12	42.28	24.03	29.40	4.29
	g53-9-b9	0.74	31.56	10.60	12.26	2.68	bdl	42.49	100.34	46.69	15.89	32.34	5.09
	g53-9-b9	0.74	31.56	10.60	12.26	2.68	bdl	42.49	100.34	46.69	15.89	32.34	5.09
	g53-0-b6	2.24	30.53	9.61	13.02	1.75	bdl	43.53	100.69	46.45	14.81	35.32	3.42
	g53-9-b9	1.69	31.56	10.26	11.82	2.42	bdl	42.97	100.71	47.73	15.72	31.87	4.68
	g53-9-b9	1.69	31.56	10.26	11.82	2.42	bdl	42.97	100.71	47.73	15.72	31.87	4.68
	g53-5-b16	1.34	27.86	15.69	10.89	2.50	bdl	42.61	100.88	41.98	23.94	29.25	4.83
	g53-9-b7	1.02	31.08	11.21	12.44	2.33	bdl	42.89	100.98	45.99	16.80	32.80	4.41
	g53-9-b7	1.02	31.08	11.21	12.44	2.33	bdl	42.89	100.98	45.99	16.80	32.80	4.41
	g53-9-b7	1.09	31.41	10.96	12.24	2.43	bdl	42.91	101.04	46.57	16.46	32.35	4.62
	g53-9-b7	1.09	31.41	10.96	12.24	2.43	bdl	42.91	101.04	46.57	16.46	32.35	4.62
	g53-5-b16	1.49	27.67	15.47	11.16	2.45	bdl	42.83	101.08	41.70	23.60	29.97	4.73
	g53-9-b8	2.43	29.58	6.57	16.27	1.53	bdl	44.71	101.08	44.02	9.90	43.17	2.91
	g53-9-b8	2.43	29.58	6.57	16.27	1.53	bdl	44.71	101.08	44.02	9.90	43.17	2.91
	g53-6-b6	1.15	29.69	13.43	11.41	2.83	bdl	42.88	101.39	44.15	20.22	30.25	5.39
	g53-6-b6	1.15	29.69	13.43	11.41	2.83	bdl	42.88	101.39	44.15	20.22	30.25	5.39
	g53-9-b7	2.36	30.92	10.54	12.24	2.25	bdl	44.07	102.38	46.64	16.10	32.91	4.35
	g53-9-b7	2.36	30.92	10.54	12.24	2.25	bdl	44.07	102.38	46.64	16.10	32.91	4.35
	g53-5-b4	2.89	31.46	8.55	13.09	1.87	bdl	44.57	102.43	47.77	13.15	35.44	3.63
	g53-6-b6	2.04	29.70	12.88	11.85	2.31	bdl	43.93	102.73	44.44	19.52	31.61	4.43
	g53-6-b6	2.04	29.70	12.88	11.85	2.31	bdl	43.93	102.73	44.44	19.52	31.61	4.43
	g53-5-b16	2.17	29.84	11.73	12.69	2.11	bdl	44.24	102.78	44.51	17.72	33.75	4.02

*g30 corresponds to GRO 95577, 30; g53 to GRO 95577, 53; ** Si contamination noted in Wt% but not within mol% calculation (Si not in carbonate structure)

						Wt%						Mol%	
lithology	**Grain***	**SiO_2****	**FeO**	**MnO**	**MgO**	**CaO**	**SrO**	**CO_2**	**Total**	**Fe**	**Mn**	**Mg**	**Ca**
dolomite													
DL	g30-9-s3	0.74	6.33	10.42	13.08	26.19	bdl	46.26	103.01	8.58	14.31	31.61	45.50
	g30-9-s3	0.33	5.58	9.37	11.84	29.31	bdl	45.64	102.06	7.56	12.86	28.63	50.94
	g30-9-s3	0.95	6.39	10.20	11.77	27.57	bdl	46.13	103.02	8.76	14.15	28.73	48.37
	g30-9-s3	0.11	6.33	11.73	11.71	26.71	bdl	45.06	101.66	8.63	16.20	28.49	46.68
	g30-9-s3	-	6.68	12.52	10.61	26.90	bdl	44.58	101.34	9.19	17.43	26.01	47.37
calcite													
CR	g30-10-s6	-	0.72	0.20	0.09	56.07	bdl	44.67	101.76	0.99	0.28	0.22	98.50
	g30-10-s6	0.15	0.77	0.13	0.13	55.47	bdl	44.45	101.10	1.07	0.18	0.31	98.44
DL	g53-2-b4	-	0.38	0.03	0.31	56.40	bdl	44.84	101.95	0.52	0.04	0.75	98.69
	g53-2-b4	0.13	0.53	0.07	0.63	56.09	bdl	45.27	102.72	0.71	0.10	1.52	97.66
	g53-2-b4	0.49	1.10	0.16	0.47	55.22	bdl	45.34	102.79	1.51	0.22	1.15	97.12
	g53-2-b4	1.07	1.41	0.07	0.42	52.16	bdl	43.85	98.97	2.05	0.10	1.07	96.78
	g53-2-b4	1.16	1.38	0.16	0.75	51.21	bdl	43.65	98.31	2.02	0.23	1.95	95.80
	g53-2-b4a	0.00	0.38	0.03	0.31	56.40	bdl	44.84	101.95	0.52	0.04	0.75	98.69
	g53-2-b4a	0.13	0.53	0.07	0.63	56.09	bdl	45.27	102.72	0.71	0.10	1.52	97.66
	g53-2-b4a	0.49	1.10	0.16	0.47	55.22	bdl	45.34	102.79	1.51	0.22	1.15	97.12
	g53-2-b4a	1.07	1.41	0.07	0.42	52.16	bdl	43.85	98.97	2.05	0.10	1.07	96.78
	g53-2-b4a	1.16	1.38	0.16	0.75	51.21	bdl	43.65	98.31	2.02	0.23	1.95	95.80
	g53-2-b4b	0.69	1.41	0.06	0.82	53.70	bdl	44.94	101.60	1.96	0.08	2.03	95.92
	g53-2-b4b	0.69	1.41	0.06	0.82	53.70	bdl	44.94	101.60	1.96	0.08	2.03	95.92
	g53-5-b17	0.30	0.60	0.23	0.45	54.74	bdl	44.41	100.74	0.83	0.32	1.12	97.72
	g53-5-b17	-	0.39	0.31	0.16	56.65	bdl	45.07	102.58	0.53	0.42	0.40	98.65
	g53-6-b	0.00	0.27	0.26	0.55	55.34	bdl	44.35	100.77	0.38	0.36	1.34	97.92

g53-6-b	-	0.23	0.20	0.16	52.71	bdl	41.81	95.11	0.33	0.30	0.43	98.94
g53-6-b3	0.13	0.61	0.29	0.32	56.62	bdl	45.52	103.48	0.83	0.39	0.78	98.01
g53-6-b3	0.06	0.30	0.27	0.43	56.51	bdl	45.26	102.84	0.41	0.37	1.05	98.17
g53-6-b3	0.00	0.38	0.25	0.46	55.52	bdl	44.46	101.07	0.53	0.35	1.12	98.00
g53-6-b3	-	0.38	0.25	0.46	55.52	bdl	44.46	101.07	0.53	0.35	1.12	98.00
g53-6-b3	-	0.27	0.26	0.55	55.34	bdl	44.35	100.77	0.38	0.36	1.34	97.92
g53-6-b3	0.16	0.25	0.23	0.60	54.89	bdl	44.26	100.38	0.35	0.33	1.48	97.84
g53-6-b3	0.00	0.30	0.23	0.25	54.51	bdl	43.38	98.67	0.43	0.32	0.63	98.62
g53-6-b3	-	0.30	0.23	0.25	54.51	bdl	43.38	98.67	0.43	0.32	0.63	98.62
g53-6-b3	0.12	0.29	0.26	0.95	54.14	bdl	44.05	99.82	0.41	0.36	2.36	96.87
g53-6-b3	0.12	0.29	0.26	0.95	54.14	bdl	44.05	99.82	0.41	0.36	2.36	96.87
g53-6-b3	0.05	0.25	0.26	0.75	52.34	bdl	42.26	95.90	0.37	0.38	1.93	97.33
g53-6-b3	0.02	0.16	0.19	0.00	52.32	bdl	41.31	94.01	0.24	0.29	0.00	99.47
g53-6-b3	0.00	0.33	0.22	0.28	52.27	bdl	41.66	94.75	0.49	0.32	0.72	98.47
g53-6-b3	-	0.33	0.22	0.28	52.27	bdl	41.66	94.75	0.49	0.32	0.72	98.47
g53-6-b3	1.70	1.20	0.19	0.48	52.10	bdl	44.76	100.43	1.74	0.28	1.25	96.73
g53-6-b3	1.70	1.20	0.19	0.48	52.10	bdl	44.76	100.43	1.74	0.28	1.25	96.73
g53-6-b3	-	0.21	0.24	0.33	51.62	bdl	41.15	93.55	0.31	0.36	0.89	98.45
g53-6-b3	-	0.18	0.22	0.28	50.14	bdl	39.90	90.71	0.28	0.34	0.76	98.62
g53-6-b3	0.06	0.30	0.27	0.43	56.51	bdl	45.26	102.84	0.41	0.37	1.05	98.17
g53-6-b3	0.16	0.25	0.23	0.60	54.89	bdl	44.26	100.38	0.35	0.33	1.48	97.84
g53-6-b3	0.00	0.23	0.20	0.16	52.71	bdl	41.81	95.11	0.33	0.30	0.43	98.94
g53-6-b3	0.05	0.25	0.26	0.75	52.34	bdl	42.26	95.90	0.37	0.38	1.93	97.33
g53-6-b3	0.02	0.16	0.19	0.00	52.32	bdl	41.31	94.01	0.24	0.29	0.00	99.47
g53-6-b6	0.61	0.67	0.35	1.09	54.46	bdl	45.45	102.63	0.92	0.49	2.66	95.93
g53-6-b6	0.61	0.67	0.35	1.09	54.46	bdl	45.45	102.63	0.92	0.49	2.66	95.93

*g30 corresponds to GRO 95577, 30; g53 to GRO 95577, 53; ** Si contamination noted in Wt% but not within mol% calculation (Si not in carbonate structure)

Appendix 2 NanoSIMS target Regions of Interest (ROIs). BSE images. All grains are siderite.

a. g53-5-b4a and g53-5-b4b; DL

b. g53-5-16b; DL

c. g30-10-s3a and g30-10-s3b; DL

d. g30-10-s1b; DL

e. g30-11-b1a and g30-11-b1b; CR

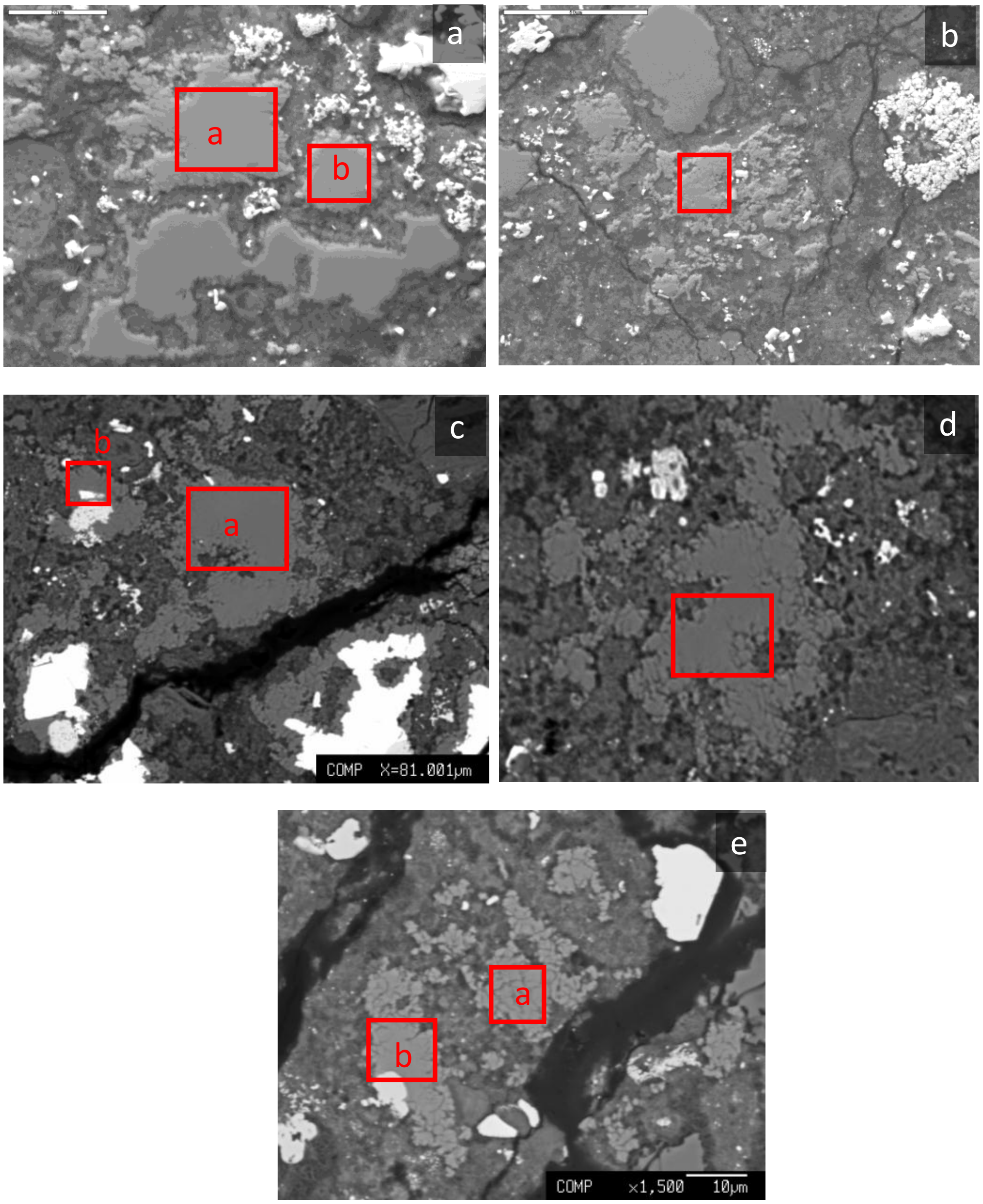

CHAPTER 3

Episodic carbonate precipitation in the CM chondrite ALH 84049: An ion microprobe analysis of O and C isotopes

1 Abstract

We have determined the oxygen and carbon isotope composition of dolomite grains and the carbon isotope composition of calcite grains in the highly altered CM1 chondrite, ALH 84049 using Secondary Ion Mass Spectrometry (SIMS). Chemically-zoned dolomite constitutes 0.8 vol% of the sample and calcite 0.9 vol%. Thirteen separate dolomite grains have δ^{13}C values that range from 23 to 60 (± 2) ‰, δ^{18}O values from 25 to 32 (± 3) ‰, and δ^{17}O values from 10 to 16 (± 3) ‰. Intragrain δ^{13}C values in dolomite vary up to 10 ‰. Three calcite grain δ^{13}C values are distinct from dolomite and range from 10 to 13 (± 2) ‰. Calcite and dolomite appear to record different precipitation episodes. Carbon isotope values of both dolomite and calcite in this single sample encompass much of the previously reported range for CM chondrites. Our results show that bulk carbonate C and O isotope analyses may oversimplify the history of carbonate precipitation. Multiple generations of carbonates with variable isotope compositions exist in ALH 84049 and, perhaps, in many CM chondrites. This work shows that one should exercise caution when using a clumped isotope approach to determine the original temperature and the isotopic compositions of water for CM chondrite carbonates. Less altered CM meteorites with more homogeneous carbonate isotope compositions, however, may be suited for bulk carbonate analyses, but detailed carbonate petrologic and isotopic characterization of individual samples is advised.

2 Introduction

CM chondrites preserve material from the early Solar System and record extensive interaction with water. Although a few CM chondrites have been thermally altered (Nakamura, 2005; Schmidt et al., 2005; Nakato et al., 2008), most range from moderately aqueously altered type 2 (CM2) to extensively altered type 1 (CM1) (Zolensky et al., 1997; Rubin et al., 2007; Howard et al., 2009). During aqueous alteration of CM chondrites, water reacts with the fine-grained matrix to form phyllosilicates, and also reacts with larger chondrule olivine, pyroxene, and other primary anhydrous minerals to varying degrees (Brearley, 2006). Progressive alteration changes the composition of matrix phyllosilicates from Fe-rich to Mg-rich as elements are redistributed during the alteration process (McSween, 1979; Tomeoka and Buseck, 1985; Browning et al., 1996; Howard et al., 2009).

CM1 chondrites are highly altered meteorites with essentially 100% alteration of the primary phases and represent the final stage of progressive aqueous alteration of a CM2-like precursor (Zolensky et al 1997). The mineralogy and whole-rock oxygen isotope composition of CM1 chondrites indicate slightly higher alteration temperatures and, paradoxically, lower water/rock ratios than CM2 chondrites (Zolensky et al. 1997, Rubin et al 2007). In ordinary chondrites burial depth may correlate with petrologic type, though this correlation is not perfect (Scott and Krot, 2005); perhaps CM1 chondrites were buried deeper and subsequently experienced higher temperatures of alteration than CM2 chondrites.

Carbonates are ubiquitous in CM2 (DuFresne and Anders, 1962; Fuchs et al., 1973; Bunch and Chang, 1980; Johnson and Prinz, 1993; Benedix et al., 2003; Lee et al., 2012) and CM1 chondrites (Riciputi et al., 1994; Zolensky et al., 1997; de Leuw et al., 2010; Lindgren et al., 2012). Calcite is common in most CM2 chondrites, irrespective of their degree of alteration, and is joined by dolomite in highly altered CM2 chondrites like Cold Bokkeveld (e.g., Brearley, 2006; Rubin et al., 2007; Lee and Ellen, 2008). Aragonite also has been observed in CM2 chondrites such as Murray but is rare (Lee and Ellen, 2008). Similarly, CM1 chondrites contain primarily calcite, but also contain dolomite (usually embayed) and other carbonates such as breunnerite (Zolensky et al., 1997; de Leuw et al., 2010; Lee et al., 2011). With each study, the story of aqueous alteration and resultant carbonate precipitation becomes more complex and suggests that carbonates precipitated in multiple stages from a changing fluid(s) (e.g. Brearley, 1998; Brearley, 2006; de Leuw et al., 2010; Lee et al., 2011; Lee et al., 2012; Tyra et al., 2012).

The bulk oxygen isotope compositions of CM2 chondrites have been used to track the isotopic evolution of water from high δ^{18}O, δ^{17}O and Δ^{17}O values to lower values as interaction with primary anhydrous silicates progressed (e.g. Clayton and Mayeda, 1984; Clayton and Mayeda, 1999). Carbonate bulk oxygen isotope analyses have been used to evaluate progressive aqueous alteration in CM chondrites (Clayton and Mayeda, 1988; Clayton and Mayeda, 1999; Benedix et al., 2003; Tyra et al., 2007). Benedix et al. (2003) adapted the oxygen isotope model of Clayton and Mayeda (1984; 1999) to explain the isotopic behavior of carbonate. Even though bulk techniques essentially average the grain scale isotopic heterogeneity of carbonates, there remains a considerable range in reported isotopic values, even within single samples. For instance, Benedix et al. (2003) found that

$\delta^{18}O$ of different calcite aliquots of Murchison vary by 6‰, suggesting that large oxygen isotope heterogeneities exist, at least in this meteorite.

Ion microprobe analyses of the stable isotopic compositions of individual carbonate grains have allowed workers to evaluate isotope heterogeneity at a very fine scale. Brearley et al (1999) and Bonal et al. (2010) used Secondary Ionization Mass Spectrometry (SIMS) to analyze calcite in the type 2.5 CM2 chondrite Murchison and found considerable oxygen isotope heterogeneity. Additionally, Tyra et al. (2012) analyzed individual carbonates in a set of Antarctic CM2 chondrites (all type 2.2, paired with EET 96006). They found that oxygen isotope compositions of Ca-carbonates from one individual meteorite rival the bulk carbonate heterogeneity reported for *all* CM2 chondrites. Tyra et al. (2012) also showed that at least two precipitation events occurred. None of these workers, however, considered if compositional variability, including zoning, corresponds to isotope composition. Compositional zoning has been found to be ubiquitous in individual dolomite grains in ALH 84049 and ALH 84051 (Tyra et al., 2010a; Chapter 1, this work).

Carbonate bulk carbon isotope composition ($\delta^{13}C$) is also related to aqueous alteration, an effect that is postulated to be related to the production of methane during serpentinization (Guo and Eiler, 2007). Guo and Eiler (2007) applied carbonate “clumped isotope thermometry” to CM2 chondrite carbonates and noted a possible link between serpentinization and carbonate $\delta^{13}C$ composition where

$$\text{ol/pyx} + H_2O \rightarrow H_2 + \text{serpentine}. \qquad (1)$$

Hydrogen then reduces dissolved bicarbonate to produce methane, which escapes the asteroid:

$$4H_2 + HCO_3^- \rightarrow CH_4 + OH^- + 2H_2O \qquad (2)$$

Methane production removes ^{12}C preferentially, which raises $\delta^{13}C$ values of remaining carbon in the fluid (Richet et al., 1977; Horita, 2001; Guo and Eiler, 2007). Due to non-equilibrium fractionation, methane $\delta^{13}C$ is hypothesized to be ~90‰ lower than bicarbonate (Guo and Eiler, 2007). Therefore, as serpentinization progresses, methane production and removal drives the remaining bicarbonate towards higher $\delta^{13}C$ values. This change of bicarbonate composition should be reflected in the carbon isotope composition of carbonates that precipitate from the fluid (Guo and Eiler, 2007).

Here, we present the results of carbon and oxygen isotope analyses of carbonate grains within ALH 84049 whose petrographic context, mineral chemistry, and compositional zoning are well constrained. Oxygen and carbon isotope data for these carbonates can provide useful constraints on the conditions and processes of carbonate formation. Carbonate isotope compositions ($\delta^{13}C$ and $\delta^{18}O$) of CM1 chondrites have been measured in bulk samples by phosphoric acid dissolution (Benedix et al 2003, Grady et al 1988), but no in-situ measurements of isotopic compositions at the grain scale using SIMS have been reported to date. This study addresses several questions: 1) Does the compositional zoning of dolomite correspond to variations in isotope composition that may reflect changes or evolution of the fluid with time? 2) Do the C and O isotope values of carbonates covary in a way that can be used to constrain processes that affect both the carbonate anion and water? 3) Do C and O isotopic compositions of carbonates record evidence of different populations of carbonates with distinct isotopic compositions? If such populations exist then isotope differences may reflect precipitation at different times during progressive alteration and constrain if the carbonate phases coprecipitated from the same fluid. Alternatively, highly localized variations or differences in isotopic composition may reflect local chemical microenvironments within the meteorite, in which individual carbonates grew from isolated reservoirs of fluid.

3 Samples and Methods

3.1 ALH 84049

A thin section of ALH 84049 (1”diameter, 30 μm thick) was provided by the Antarctic Meteorite Working Group from the NASA Johnson Space Center Antarctic Meteorite Collection. Approximately 29.4g of this sample was collected in Antarctica, and it was determined to have a weathering grade of Ae with a fracturing grade of B (Score and Lindstrom, 1990). ALH 84049 dolomite was analyzed for its Mn-Cr isotopic systematics in Tyra et al. (2010b; Chapter 1, this work): in this study we determined that the sample is fully hydrated and classified it as a CM1. All analyzed dolomite grains in ALH 84049 are compositionally zoned in Fe, Mn, Ca, and Mg (Tyra et al., 2010b; Chapter 1, this work).

3.2 Imaging and chemical analyses

We imaged the entire sample with a digital camera attached to a petrographic microscope. Reflected light, plane-polarized transmitted light, and cross-polarized transmitted light modes were used to image the sample. The images in each mode were stitched together into one composite image using Hugin [sourceforge] software, correcting for lens aberrations. These maps form a baseline to locate carbonate grains, to aid navigation on the SIMS, and to document general petrographic textures in the sample. Potential carbonates (usually bright pink in the cross-polarized light maps) were verified either optically or through energy dispersive Xray spectroscopy (EDS) on a scanning electron microscope (see below).

Following optical microscope characterization, ALH 84049 was imaged with a FEI Quanta 3D Field Emission Gun SEM/Focused Ion Beam (FIB) instrument located in the Department of Earth and Planetary Sciences at the University of New Mexico. Backscattered electron (BSE) images were taken on the SEM using a beam current of 4 nA, accelerating voltage of 30kV at 100x magnification, and with a 100 ms dwell time per pixel. The images were combined into a mosaic of the entire thin section using EDAX software (Fig. 1). Carbonate grains were verified by energy-dispersive spectroscopy (EDS) using an EDAX Apollo 40 silicon drift detector.

Many carbonate grains were analyzed with wavelength dispersive spectrometry (WDS) X-ray mapping using a JEOL 8200 Superprobe Electron Probe Micro-analyzer (EPMA) at the University of New Mexico. Dolomite grains were mapped at 15 kV, 20 nA, and with a 1 μm beam to determine their composition and characterize chemical zoning. We performed WDS quantitative analyses and calibrated for Mn, Mg, Fe, Ca, Sr, and Si using spessartine (Mn), dolomite (Ca, Mg), siderite (Fe), celestite (Sr) and quartz (Si) standards. Silicon was included in the element list to define the edges of the carbonate grain as accurately as possible. Point compositional analyses of carbonates were performed after SIMS analysis to avoid electron beam damage to the minerals that could affect isotope results. Point analyses were performed adjacent (usually within a couple of microns) to the SIMS pits and averaged to estimate the chemical composition of the spot area. However, because the SIMS spots and EPMA analyses were not exactly coincident, the results may not match the composition of the excavated area exactly.

3.3 Ion microprobe work

We selected dolomite and calcite grains with few or no inclusions, determined either through BSE imaging or X-ray maps, because an inclusion could have a different oxygen isotope composition or cause variable Instrumental Mass Fractionation (IMF). Selected carbonate grains were analyzed by ion microprobe to determine C isotope (δ^{13}C in ten dolomites and three calcium carbonates) and O (δ^{17}O and δ^{18}O in eight dolomite grains) compositions. Figure 1, a BSE mosaic of the entire ALH 84049 thin section used in this study, shows the locations and identifying numbers of each analyzed grain within a 3 mm area.

To determine the C and O isotope composition of carbonates, we used the Cameca IMS 7f-GEO SIMS at Caltech (Cs$^+$ primary beam, 10 keV, ~0.1 nA, ~10 μm spot size). Secondary ions of -10 keV were collected at a mass resolving power (m/Δm) of ~5500 to separate ^{17}O$^-$ from the ^{16}O^{1}H$^-$ interference. The ^{16}O$^-$ signal was measured with a Faraday cup (FC), and the ^{17}O$^-$ and ^{18}O$^-$ signals with an electron multiplier (EM). The ^{12}C$^-$ signal was measured with a Faraday cup (FC), and the ^{13}C$^-$ signals with an electron multiplier (EM). Sample charging was compensated with a negative electron gun (NEG) at -10 keV. Sample data were calibrated for instrumental mass fractionation (IMF) and matrix effects with suitable calcite and siderite standards.

After SIMS work was completed, the analyzed grains were re-examined by SEM using BSE imaging (Quanta 3D FEG Dualbeam SEM at 15kVand a current of 0.19 nA). These images (Fig. 2) were then scrutinized to ensure that the SIMS analysis spot was located entirely within the target grain and had not sputtered down to any inclusion minerals below the sample surface.

4 Results

4.1 Petrology

The petrology of the carbonates in ALH 84049 has been discussed in detail in Chapter 1 (this work); only a brief description is provided here. Calcite and dolomite are both found in ALH 84049, at near equal proportions (0.8 vol% dolomite, 0.9 vol% calcite; Chapter 1, this work). Both carbonate minerals range from 10 to 50 μm in diameter and are distributed randomly throughout the sample. The calcite grains in ALH 84049 are consistent with the “type 1 calcite” classification from Tyra et al. (2012); type 1 calcites contain few mineral inclusions, are 10-50 μm in diameter, subhedral, and disseminated throughout the matrix. In less altered CM chondrites, type 1 calcites may have tochilinite rims ($6Fe_{0.9}S \cdot 5(Fe,Mg)(OH)_2$), but these are absent in ALH 84049 and ALH 84051. Unlike in the paired chondrite ALH 84051 (Tyra et al., 2009; Tyra et al., 2010b), no vein dolomite or large dolomite aggregates were observed in ALH 84049.

Compositionally, calcite grains are essentially pure $CaCO_3$, with very low minor element concentrations (<0.5 wt%). We do not differentiate calcite from its polymorphs aragonite or vaterite, both of which have been found to be minor components of CM chondrites (Lee and Ellen, 2008). Rare calcite grains with corroded or embayed margins have been found included within dolomite (Chapter 1, this work). Dolomites show complex, often asymmetric, chemical zoning: MnO, CaO, FeO and MgO can vary by as much as 4 wt% within a single grain. The edges of distinct compositional zones are abrupt and show no consistent core-to-rim relationship (Chapter 1, this work).

4.2 Dolomite oxygen and carbon isotope composition

Table 1 reports the chemical compositions of individual carbonate grains along with their oxygen and carbon isotope compositions. The $\delta^{18}O$ compositions of dolomite grains are variable and range from 25 to 32 (± 3) ‰ and $\delta^{17}O$ from 10 to 16 (± 3) ‰; errors are 2σ. Intragrain isotope variability may be significant. For example, we obtained two oxygen isotope SIMS analyses of dolomite a49-5-b5 and spot 1 had a $\delta^{18}O$ of 25.38 ‰ and spot two 32.31 ‰, the lowest and highest values of the entire data set. The two analyses in grain a49-5-b12 also have a significant oxygen isotope range, but the two analyses in grain a49-5-b13 are identical.

Dolomite C isotope compositions in ALH 84049 are heterogeneous. Dolomite $\delta^{13}C$ values show a large range from 37 to 60‰ (± 2‰) (Table 1). Three grains were analyzed twice in separate locations; one grain, the dolomite a49-6-b3, $\delta^{13}C$ composition varied by ~10‰ (40.2‰ vs. 50.5‰) between the two analyses. Calcite $\delta^{13}C$ values range from 9.8 to 13.7 ‰, a much smaller range than dolomite.

4.3 Isotopic composition vs. carbonate chemistry

The evidence of compositional zoning in ALH 84049 carbonates suggests that there may have been different periods of carbonate growth. In order to establish if compositionally-distinct growth zones record different carbon isotopic compositions, we compared the chemical composition of areas of grains that are proximal to the SIMS analysis spots. The results are presented with isotope compositions in Table 1. Standard deviations on the analyses were larger than EPMA analytical error and therefore are reported in Table 1.

Figures 3a and 3b compare compositional data for individual carbonate grains with the measured oxygen isotope composition of the grains. Isotope results do not appear to show any systematic variation with Mn, Fe, or Mg content of the carbonate. Additionally, the oxygen isotope results do not seem to vary with Ca composition, though there may be a weak ($R^2 = 0.35$) relationship where increasing $\delta^{18}O$ values correspond to lower mol% Ca. Like oxygen isotope compositions, carbon isotope compositions do not vary with the chemical composition of the dolomite (Figs. 3c and 3d). Furthermore, multiple analyses from the same grain also show no correlation between elemental composition and either O or C isotope; pairs of analyses from the same grain are highlighted in Table 1.

Our results differ from those of Riciputi et al. (1998), who observed a strong relationship of oxygen, sulfur, and carbon stable isotope values in carbonates with composition, implying that compositionally-induced matrix effects occurred during their SIMS analyses. As there is little indication here that composition (Ca, Mg, Fe, or Mn) covaries with O or C isotope results, we suggest that chemical-composition induced matrix effects have not affected our reported oxygen isotope results.

5 Discussion

Below, we explain that although the oxygen isotope composition of dolomite fits with expected models of oxygen isotope response to fluid evolution, the difference in carbon isotope values between dolomite and calcite is unexpected. Additionally, the variation in both oxygen and carbon isotope composition within an area 3 mm wide (Fig. 1) is remarkable, as is the isotopic variation in three of four dolomite grains with two analyses. We also evaluate if O and C isotope composition and chemical composition varied together to examine how water evolved as it precipitated carbonates. Furthermore, we discuss the relationship between the oxygen isotope compositions of carbonates in the CM1 chondrite ALH 84049 with those determined for less altered CM2s. We evaluate carbon isotope evolution and determine mechanisms, including the possibility of methane formation between the precipitation events that formed calcite and dolomite, to explain the difference between calcite and dolomite δ^{13}C compositions.

5.1 Oxygen isotopes in carbonates

Oxygen isotopes have been used as a marker of aqueous alteration in CM chondrites because they track the interaction of water with chondrite minerals. In carbonaceous chondrites oxygen resided in essentially two distinct reservoirs: ^{16}O-depleted water created by nebular UV ray self-shielding (Kuramoto and Yurimoto, 2005) and ^{16}O-rich anhydrous silicates (Clayton et al., 1973). In the CM chondrite parent body, water oxygen isotope composition evolved to lower δ^{18}O, δ^{17}O and Δ^{17}O values with progressive interaction with anhydrous silicates (Clayton and Mayeda, 1999; Benedix et al., 2003).

Previous oxygen isotopic studies have shown that different morphologies of calcite in CM chondrites have different oxygen isotope compositions (Tyra et al., 2007; Tyra et al., 2012). These different calcite types are grouped by morphology: Type 1 calcite grains are smaller (10-50 μm) grains interspersed throughout the matrix. Type 2 calcite grains are larger aggregates that range from 50-250 μm in diameter and contain small sulfide or phyllosilicate inclusions. Type 3 calcite grains are veins that may infill cracks. Based on their oxygen isotope compositions, Tyra et al. (2012) showed that type 3 calcite in the CM 2.2 EET 96006 paired set are terrestrial in origin. Subsequent work, however, has discovered calcite veins in CM2 chondrites that are not terrestrial, including bimineralic calcite-dolomite veins (Lindgren et al., 2011; Lee et al., 2012). Some of these calcite veins may have oxygen isotope compositions similar to type 2 calcite aggregate grains (M. Lee, personal communication).

Type 1 calcite grains have similar oxygen isotope compositions in the CM2 chondrites Murchison and in the EET 96006 paired set, samples with a large range in degree of aqueous alteration (2.5 to 2.2; Rubin et al., 2007; Tyra et al., 2012). Brearley et al. (1999) determined calcite δ^{18}O compositions of seven grains ranging from 27 to 37 ‰ which reside on the terrestrial fractionation line (TFL). Bonal et al. (2010) analyzed five calcite grains and determined calcite oxygen δ^{18}O ranges from, including error, 34 to 37.5‰ and δ^{17}O from 16.5 to18.5‰; all data plot slightly below the TFL. The results of both Bonal et al. (2010) and Brearley et al (1999) overlap that of one of the two carbonate isotope reservoirs, type 1 calcite, reported in the EET 96006 CM2 chondrite paired set (Tyra et al., 2012). Furthermore, the petrographic description of analyzed grains in both studies is analogous to type 1 grains. Type 2 calcite was not observed by Bonal et al. (2010) and Brearley et al (1999), although grains that fit the description of type 2 calcite were documented in Murchison by Benedix et al. (2003). Tyra et al. (2012) argued that the bulk carbonate isotope results of Benedix et al. (2003) imply that both type 1 and type 2 calcites are present in many CM2 chondrites including Murchison (2.5), Murray (2.4/2.5), Nogoya (2.2), and Cold Bokkeveld (2.2). We did not analyze calcite grains in ALH 84049 for their oxygen isotope composition. It is not reasonable, however, to assume that the oxygen isotope composition of type 1 calcite in ALH 84049 is similar to type 1 grains in other CM chondrites, unless it can be established that they formed under similar conditions. As discussed below, three major variables, temperature, extent of alteration, and water – rock (W:R) ratio could have produced the differences in the oxygen isotope compositions of carbonates between CM1 and CM2 chondrites.

Different temperatures of formation would influence the oxygen isotope values recorded in carbonate due to differences in fractionation. Both □17O and □18O values of carbonates, for instance, would lie closer to the oxygen isotope composition of water in CM1 chondrites if temperatures were higher than that in CM2 chondrites (assuming the same source water). Temperatures during alteration of CM chondrites are not well known. Clayton and Mayeda (1984) examined the oxygen isotopic composition of carbonates and phyllosilicates in CM2 chondrites to calculate temperature, but it was later found that phyllosilicates and carbonates were not in isotopic equilibrium, invalidating calculated temperatures except in Nogoya (0-25°C) (Benedix et al., 2003). Guo and Eiler (2007) used C and O clumped isotopes to determine temperatures of precipitation between 20 and 71 °C; although problems with this technique are discussed further below. Cody et al. (2008) used organothermometry to determine maximum temperatures experienced in CM2 chondrites Bells (77 ± 93 °C) and Murchison (96 ± 65 °C) but did not examine any CM1 chondrites. There is some evidence that temperatures may have been higher in CM1 chondrites, but this is far from certain. Zolensky et al. (1997) noted that the most aqueously altered CM chondrites (like CM1s) do not have tochilinite. This can be attributed to temperatures above 120°C, high $f O_2$, or low $f S_2$ destabilizing tochilinite (Zolensky, 1984; Zolensky et al., 1997). High temperatures over 120°C are not needed, however; EQ3/6 geochemical modeling of CM and CV chondrites showed that tochilinite disappeared between 25°C and 50°C (Zolensky et al., 1989).

In addition to temperature influencing recorded oxygen isotope compositions in carbonates, both the W:R ratio and amount of aqueous alteration in the chondrite changes the composition of water as it interacted with anhydrous mineral. The effect of both situations is similar: water will take on the isotope characteristics of the silicates (become more rock dominated) and have lower $\delta^{18}O$, $\delta^{17}O$, and $\Delta^{17}O$ compositions. A temperature rise, conversely, would just cause a mass dependent fractionation of the $\delta^{18}O$ and $\delta^{17}O$ (not $\Delta^{17}O$) values of the precipitating carbonates.

The oxygen isotope composition ($\delta^{18}O$, $\delta^{17}O$) of dolomite in ALH 84049 overlaps or is lower than the oxygen isotope composition of type 1 calcites in CM2 chondrites (Fig. 4); $\Delta^{17}O$ values are equivalent. The inset in Figure 4 illustrates the progression of the composition of water with time and alteration. Figure 4 then relates types 1 and 2 calcite isotope compositions analyzed previously to dolomite analyzed here. Bulk carbonate oxygen isotope data in CM2s suggest that dolomite may have precipitated later than calcite or from more evolved water (Benedix et al., 2003). In this study, we did not analyze the oxygen isotope values of type 1 calcite grains. Therefore, we cannot compare the calcite composition to dolomite to ascertain its place in the oxygen isotope model described above. However, given the similarity between the fractionation factors of dolomite and calcite (1000lnα (at 25°C) calcite-H_2O = 28.38‰ (O'Neil et al., 1969), 1000lnα (at 25°C) dolomite-H_2O=30.97‰ (Vasconcelos et al., 2005), differences in fractionation at constant temperature cannot be responsible for observed differences in oxygen isotope composition.

Even though dolomite grains in ALH 84049 have oxygen isotope compositions that are similar to calcite in other CM chondrites, dolomite and calcite did not precipitate concurrently. Petrographic evidence presented in Tyra et al. (Chapter 1, this work) shows that calcite grains are included in dolomite and, consequently, precipitated earlier. Observed calcite grains are also embayed and dolomite grains are relatively pristine, suggesting that calcite precipitated before dolomite. However, because dolomite is more resistant to acid, this conclusion is not unequivocal. Furthermore, calcite precipitation is kinetically faster than dolomite precipitation and therefore would precipitate first and consume available CO_3^{2-}(Chou et al., 1989; Arvidson and Mackenzie, 1999; Arvidson and Mackenzie, 2000). This argues against cogenetic precipitation and contrasts with the observations of de Leuw et al.(2010), who observed that calcite precipitated after corroded dolomite in highly altered CM1 chondrites such as MET 01070. The strongest argument against dolomite and calcite co-precipitation, however, is their very different carbon isotope compositions.

5.2 Carbon Isotopes in carbonates

This is the first ion probe study of carbon isotope ratios in carbonates in CM chondrites. Sampling individual grains allows us to examine heterogeneities unseen in bulk analyses that may differentiate carbonate types. Figure 5 compares the carbon isotope composition of calcite and dolomite in ALH 84049, as well as comparing our data to bulk CM, CI, CV, CO, and CR carbonaceous chondrite groups (reported in Grady et al., 1988; Guo and Eiler, 2007). Although the δ^{13}C composition of only three calcite grains were analyzed, these are significantly distinct from the δ^{13}C compositions of dolomite (T-test assuming unequal variances, $p=1.2 \times 10^{-4}$). Calcite and dolomite carbon isotope compositions are distinct.

5.2.1 δ^{13}C variations in individual carbonate grains

Carbon isotope heterogeneity in carbonates (calcite and dolomite) of one sample, ALH 84049, encompasses much of the aggregated data spread seen in all bulk analyses of CM, CR, and CI chondrites (Fig. 5). As noted in the Results, dolomite δ^{13}C values cover a range of almost 40‰ and variability of up to 10‰ was observed within individual grains. This observed carbon isotope heterogeneity would be lost during bulk analyses; however, there are large δ^{13}C heterogeneities in bulk CM2 chondrite samples (Grady et al., 1988; Guo and Eiler, 2007) which may arise from varying abundances of separate carbonate populations.

Carbon isotope heterogeneity could arise because there are many potential carbon sources that have variable δ^{13}C compositions (Grady et al., 1988; Alexander et al., 1998; Sephton, 2002). For instance, different species of organic matter have unique δ^{13}C compositions; oxidation of these species, therefore, may have affected the local isotope composition of aqueous carbon. Although organic matter δ^{13}C has been primarily examined through bulk techniques such as pyrolysis, some studies have found considerable δ^{13}C variability in both soluble and insoluble organic matter (Alexander et al., 1998; Sephton et al., 2003; Alexander et al., 2007). There is abundant petrographic evidence that chemical microenvironments exist in CM chondrites (Brearley, 2006; Palmer and Lauretta, 2011; Chapter 1, this work). Because the diffusivities of CO_3^{2-} and cations that define microenvironments such as Mn^{2+}, Fe^{2+}, Mg^{2+}, and Ca^{2+} are comparable (assuming 25°C, 35 ppt salinity, and 1 atm pressure) (Boudreau, 1997), there is no reason that isotopic microenvironments could not also exist as well.

5.2.2 Calcite vs. dolomite

Calcite grains have $\delta^{13}C$ values from 10 to 13 (± 2) ‰, much lower than dolomite (37 to 60‰). At similar temperatures, $\delta^{13}C$ fractionation factors for calcite are very similar to dolomite. For example, calculated fractionation between dolomite and calcite at 100°C (assuming 1 atm pressure) is 1.5‰ and at 200°C is 1.0‰ (Sheppard and Schwarcz, 1970). Small differences between the fractionation factors between of both species (and between dissolved carbonate and both species) is not sufficient to account for the large differences in carbon isotope composition observed here. Different carbon sources for the two carbonate populations are necessary.

We consider the most likely cause of the difference in $\delta^{13}C$ composition is, as explained in the Introduction, that methane formed between the formation of calcite and dolomite. Methane formation and escape would drive the $\delta^{13}C$ composition of the remaining C to higher values (Guo and Eiler, 2007). The distinct difference in $\delta^{13}C$ values implies that calcite and dolomite could not have precipitated at equilibrium from the same fluid and, therefore, formed at different times. If methane evolution drove the $\delta^{13}C$ composition of dissolved carbonate to higher values, then calcite precipitated before dolomite. Methane evolution and removal, coincidentally, could also explain the lack of tochilinite as this process could raise the oxygen fugacity of remaining fluid above the stability range of tochilinite, although magnetite, an expected result of tochilinite breakdown, is not observed (van de Vusse and Powell, 1983; Browning and Bourcier, 1996).

If future analyses uphold the small range of $\delta^{13}C$ composition reported here for calcite, then little carbon isotope evolution occurred in the fluid during calcite precipitation. Conversely, the large range of dolomite $\delta^{13}C$ compositions, along with that reported in bulk analyses such as Tyra et al. (2007), may indicate changing $\delta^{13}C_{fluid}$ with time. Dolomite may have precipitated from isolated fluids, precipitated at different times during continual methane formation, or precipitated after spatially-heterogeneous methane formation caused a wide range of $\delta^{13}C$ of available carbon. Dolomite in ALH 84049 precipitated from the final fraction of a rapidly-evolving brine and calcite precipitated earlier when porosity and permeability were higher (Chapter 1, this work).

5.3 Dolomite oxygen and carbon isotope covariance

There is little covariance between O and C isotope results and the two elements do not seem to be coupled. Figure 6 compares oxygen and carbon isotopes for the six dolomite grains which were successfully analyzed for both isotopes; there is no noticeable trend in the data. If methane production after calcite formation drove $\delta^{13}C$ higher than when type 1 calcite precipitated, as hypothesized above, then this process must have ceased during dolomite formation because a trend would be expected of increasing $\delta^{13}C$ with decreasing $\delta^{18}O$ and $\delta^{17}O$. Conversely, if local carbon sources controlled the carbon available for carbonate formation, then we would not expect a consistent relationship between C and O isotopes. In Figure 6, our data are compared with the bulk carbonate data for CM chondrites of Guo and Eiler (2007). The two sets of data are almost indistinguishable except, perhaps, the bulk oxygen isotope compositions are slightly heavier than analyses of dolomite in-situ. This may be a coincidence, as explained below.

Guo and Eiler (2007) used bulk carbonate O and C isotopes to determine temperatures of precipitation and proposed that methane formation could explain a relationship between the two isotopes independent of temperature. A difficulty with the application of clumped isotopes to thermometry in CM chondrites, however, is that our work shows that the carbonates present in CM chondrites are isotopically heterogeneous. Furthermore, even at the temperature (25°C) used in the phosphoric acid extraction by Guo and Eiler (2007), dolomite, if present, can contaminate released CO_2 gas by up to 20% in the nominal 24 hour extraction time (Al-Aasm et al., 1990). The abundance of each carbonate population, therefore, will influence the calculated temperature obtained from this bulk technique. In ALH 84049, we observed 0.9 vol% calcite and 0.8 vol% dolomite, very similar proportions. Our work shows that calcite and dolomite are very different in C isotope composition. Additionally, calcite also may have different oxygen isotope populations depending upon morphology (Tyra et al., 2012). It is well known that bulk techniques miss local mineralogical heterogeneity; in this case the ramifications are significant. Depending upon the proportions of each generation and type of carbonate in individual samples, the bulk carbonate isotopic compositions may vary considerably.

5.4 Composition and isotopes

Although dolomite grains are compositionally zoned, neither oxygen nor carbon isotope compositions change in concert with this zoning. One reason for this may be simply that we did not obtain isotope data for the most extreme chemical compositions. In Chapter 1 (this work) we note that Mn-rich zones are usually found at grain peripheries, unless they occupy porous interior areas which may be a sign of recrystallization. This study observed dolomite $MnCO_3$ contents as high as 7.72 mol%. For the isotope analyses, the majority of dolomites have Mn contents only 1-3 mol% $MnCO_3$. SIMS spot placement near a grain edge, where more extreme chemical compositions often occur, risks beam overlap with adjacent grains. We therefore made most isotope analyses near grain centers. Therefore, a relationship between chemical composition and isotope composition may not have been observed due to sampling bias.

Although sampling bias is a possibility, it is likely that the lack of a correlation between the chemical composition and the isotope composition may be that, although oxygen is a major component of water itself, cations are not (reservoir size effect). Cation consumption during carbonate precipitation and phyllosilicate formation allowed for a wide range of fluid cation compositions which are preserved in carbonates. Additionally, chemical microenvironments formed through the reaction of water with the heterogeneous mineralogy of CM chondrites (Brearley, 2006). This can be seen not only in the chemical variability of individual dolomite grains, but it is also apparent in the large carbon isotope variability in dolomites separated by only hundreds of microns (for example, grains 6-b10a and 6-b10b). Fluid flow that could homogenize chemical compositions and locally-sourced inorganic carbon that would be incorporated in carbonates could not have been very significant.

6 Conclusions

This work has advanced the understanding of aqueous alteration, specifically carbonate precipitation, in the CM parent body. We show that when calcite precipitated first, fluid carbonate $\delta^{13}C$ values were probably homogeneous. With progressing aqueous alteration, fluids became more chemically heterogeneous and isolated resulting in chemically variable and zoned dolomite. This reinforces observations of other workers that fluids in the CM and CI chondrite parent bodies were distinct and evolved chemically (Fredriksson and Kerridge, 1988; Johnson and Prinz, 1993; Riciputi et al., 1994). Available carbon $\delta^{13}C$ values rose and became more heterogeneous. Our study has provided several new observations that constrain the chemical and isotopic evolution of fluids during carbonate precipitation, as follows:

1. The $\delta^{13}C$ compositions of dolomite in this one sample span much of the range of bulk analyses of a few different carbonaceous chondrite groups. Dolomite and calcite carbon isotope compositions are distinct with dolomite $\delta^{13}C$ values ranging from ~35-60 ‰ and calcite at ~10‰. Single dolomite grains can have $\delta^{13}C$ values that vary by 10‰. The analyzed carbonate grains occur within a very spatially restricted area, demonstrating that there were highly localized variations in the isotopic composition of carbon that was incorporated into dolomite.

2. Measured $\delta^{13}C$ values in calcite are far lower than those in dolomite. Also, the $\delta^{13}C$ of the carbon source for calcite may have been homogenous while that of

dolomite varied markedly. We attribute this phenomenon to discontinuous methane formation that removed ^{12}C preferentially, as well as the oxidation of isotopically variable organic species that released C, which was incorporated on a highly localized scale into dolomite.

3. This is the first measurement of dolomite oxygen isotopic compositions in-situ. The oxygen isotope compositions of measured grains slightly overlap the composition of CM chondrite type 1 calcite, measured in prior studies. Even though dolomite (measured here) and type 1 calcite oxygen isotope compositions measured in other CM chondrites overlap, their different $\delta^{13}C$ compositions make it unlikely that they precipitated together.

4. Of six dolomite grains where both carbon and oxygen isotopes were measured in the same grain, values are similar to bulk CM chondrite carbonate measured by Guo and Eiler (2007). Because of the very different $\delta^{13}C$ of calcite and dolomite, and noted differences in $\delta^{18}O$ in type 1 and type 2 calcite throughout CM chondrites, the bulk methodology of Guo and Eiler (2007) may result in inaccurate temperature estimates for carbonate precipitation. To determine temperature accurately, in-situ characterization of both oxygen and carbon isotope compositions of individual grains is needed.

7 Acknowledgements

This work is supported by NASA Grant NNG06GG37G to A.J. Brearley (PI), the Moore Foundation to Y. Guan, the N.M. Space Grant (M. A. Tyra), and a 2010

Meteoritical Society student travel award (M. A. Tyra). I am also grateful for discussions with Scott Jasechko, Maarten de Moor, and Rena Ford.

8 References

Al-Aasm I. S., Taylor B. E., and South B. (1990) Stable isotope analysis of multiple carbonate samples using selective acid extraction. *Chemical Geology: Isotope Geoscience section* **80**, 119-125.

Alexander C. M. O. D., Russell S. S., Arden J. W., Ash R. D., Grady M. M., and Pillinger C. T. (1998) The origin of chondritic macromolecular organic matter: A carbon and nitrogen isotope study. *Meteoritics & Planetary Science* **33**, 603-622.

Alexander C. M. O. D., Fogel M., Yabuta H., and Cody G. D. (2007) The origin and evolution of chondrites recorded in the elemental and isotopic compositions of their macromolecular organic matter. *Geochimica et Cosmochimica Acta* **71**, 4380-4403.

Arvidson R. S. and Mackenzie F. T. (1999) The dolomite problem: Control of precipitation kinetics by temperature and saturation state. *American Journal of Science* **299**, 257-288.

Arvidson R. S. and Mackenzie F. T. (2000) Temperature dependence of mineral precipitation rates along the $CaCO_3$-$MgCO_3$ join. *Aquat. Geochem.* **6**, 249-256.

Benedix G. K., Leshin L. A., Farquhar J., Jackson T., and Thiemens M. H. (2003) Carbonates in CM2 chondrites: Constraints on alteration conditions from oxygen isotopic compositions and petrographic observations. *Geochimica et Cosmochimica Acta* **67**, 1577-1588.

Bonal L., Huss G. R., Krot A. N., and Nagashima K. (2010) Chondritic lithic clasts in the CB/CH-like meteorite Isheyevo: Fragments of previously unsampled parent bodies. *Geochimica et Cosmochimica Acta* **74**, 2500-2522.

Boudreau B. P. (1997) *Diagenetic models and their implementation: modelling transport and reactions in aquatic sediments*. Springer, New York.

Brearley A. J. (1998) Carbonates in CM carbonaceous chondrites: Complex zoning revealed by high resolution cathodoluminescence studies. *Lunar and Planetary Science XXIX*. LPI, Houston, TX.

Brearley A. J., Saxton J. M., Lyon I. C., and Turner G. (1999) Carbonates in the Murchison CM chondrite: CL characteristics and oxygen isotopic compositions. *Lunar and Planetary Science* **XXX**, 1301.pdf.

Brearley A. J. (2006) The action of water. In: Lauretta, D. S., Leshin, L. A., and McSween, H. Y. Eds.), *Meteorites and the Early Solar System II*. University of Arizona Press, Tucson, AZ.

Browning L., McSween H., and Zolensky M. (1996) Correlated alteration effects in CM carbonaceous chondrites. *Geochimica et Cosmochimica Acta* **60**, 2621-2633.

Browning L. B. and Bourcier W. L. (1996) Tochilinite: A sensitive indication of alteration conditions on the CM asteroidal parent body*Lunar and Planetary Science Conference XXVII*. Lunar and Planetary Institute.

Bunch T. E. and Chang S. (1980) Carbonaceous chondrites .2. Carbonaceous chondrite phyllosilicates and light-element geochemistry as indicators of parent body processes and surface conditions. *Geochimica et Cosmochimica Acta* **44**, 1543-1577.

Chou L., Garrels R. M., and Wollast R. (1989) Comparative study of the kinetics and mechanisms of dissolution of carbonate minerals. *Chemical Geology* **78**, 269-282.

Clayton R. and Mayeda T. (1999) Oxygen isotope studies of carbonaceous chondrites. *Geochimica et Cosmochimica Acta* **63**, 2089-2104.

Clayton R. N., Grossman L., and Mayeda T. K. (1973) Component of primitive nuclear composition in carbonaceous meteorites. *Science* **182**, 485-488.

Clayton R. N. and Mayeda T. K. (1984) The oxygen isotope record in Murchison and other carbonaceous chondrites. *Earth and Planetary Science Letters* **67**, 151-161.

Clayton R. N. and Mayeda T. K. (1988) Isotopic composition of carbonate in EETA-79001 and its relation to parent body volatiles. *Geochimica et Cosmochimica Acta* **52**, 925-927.

Cody G. D., Alexander C. M. O. D., Yabuta H., Kilcoyne A. L. D., Araki T., Ade H., Dera P., Fogel M., Militzer B., and Mysen B. O. (2008) Organic thermometry for chondritic parent bodies. *Earth and Planetary Science Letters* **272**, 446-455.

de Leuw S., Rubin A. E., and Wasson J. T. (2010) Carbonates in CM chondrites: Complex formational histories and comparison to carbonates in CI chondrites. *Meteoritics & Planetary Science* **45**, 513-530.

DuFresne E. R. and Anders E. (1962) On the chemical evolution of the carbonaceous chondrites. *Geochimica et Cosmochimica Acta* **26**, 1085-1114.

Fredriksson K. and Kerridge J. F. (1988) Carbonates and sulfates in CI chondrites--formation by aqueous activity on the parent body. *Meteoritics* **23**, 35-44.

Fuchs L. H., Olsen E., and Jensen J. (1973) Mineralogy, mineral-chemistry, and compositon of the Murchison (C2) meteorite. *Smithsonian Contributions to the Earth Sciences* **10**, 1-38.

Grady M. M., Wright I. P., Swart P. K., and Pillinger C. T. (1988) The carbon and oxygen isotopic composition of meteoritic carbonates. *Geochimica et Cosmochimica Acta* **52**, 2855-2866.

Guo W. and Eiler J. M. (2007) Temperatures of aqueous alteration and evidence for methane generation on the parent bodies of the CM chondrites. *Geochimica et Cosmochimica Acta* **71**, 5565-5575.

Horita J. (2001) Carbon isotope exchange in the system CO_2-CH_4 at elevated temperatures. *Geochimica et Cosmochimica Acta* **65**, 1907-1919.

Howard K. T., Benedix G. K., Bland P. A., and Cressey G. (2009) Modal mineralogy of CM2 chondrites by X-ray diffraction (PSD-XRD). Part 1: Total phyllosilicate abundance and the degree of aqueous alteration. *Geochimica et Cosmochimica Acta* **73**, 4576-4589.

Johnson C. A. and Prinz M. (1993) Carbonate compositions in CM and CI chondrites, and implications for aqueous alteration. *Geochimica et Cosmochimica Acta* **57**, 2843-2852.

Kim S.-T. and O'Neil J. R. (1997) Equilibrium and nonequilibrium oxygen isotope effects in synthetic carbonates. *Geochimica et Cosmochimica Acta* **61**, 3461-3475.

Kuramoto K. and Yurimoto H. (2005) Oxygen isotopic heterogeneity in the Solar System: The molecular cloud origin hypothesis and its implications for meteorites and the planets. In: Krot, A. N., Scott, E. R. D., and Reipurth, B. Eds.), *Chondrites and the Protoplanetary Disk*. Astronomical Society of the Pacific, San Francisco, CA.

Lee M. R. and Ellen R. (2008) Aragonite in the Murray (CM2) carbonaceous chondrite: Implications for parent body compaction and aqueous alteration. *Meteoritics & Planetary Science* **43**, 1219-1231.

Lee M. R., Sofe M. R., and Lindgren P. (2011) Evolution of carbonate mineralization in the CM2 carbonaceous chondrites. *Lunar and Planetary Science Conference XLII*. LPI, The Woodlands, TX.

Lee M. R., Lindgren P., Sofe M. R., O'D Alexander C. M., and Wang J. (2012) Extended chronologies of aqueous alteration in the CM2 carbonaceous chondrites: Evidence from carbonates in Queen Alexandra Range 93005. *Geochimica et Cosmochimica Acta* **92**, 148-169.

Lindgren P., Lee M. R., Sofe M., and Burchell M. J. (2011) Microstructure of calcite in the CM2 carbonaceous chondrite LON 94101: Implications for deformation history during and/or after aqueous alteration. *Earth and Planetary Science Letters* **306**, 289-298.

Lindgren P., Lee M. R., and Sofe M. (2012) Evidence for multiple fluid pulses in the CM1 carbonaceous chondrite parent body. *Lunar and Planetary Science Conference*. LPI, Houston, TX

McSween H. Y. (1979) Alteration in CM carbonaceous chondrites inferred from modal and chemical variations in matrix. *Geochimica et Cosmochimica Acta* **43**, 1761-1770.

Nakamura T. (2005) Post-hydration thermal metamorphism of carbonaceous chondrites. *Journal of Mineralogical and Petrological Sciences* **100**, 260-272.

Nakato A., Nakamura T., Kitajima F., and Noguchi T. (2008) Evaluation of dehydration mechanism during heating of hydrous asteroids based on mineralogical and chemical analysis of naturally and experimentally heated CM chondrites. *Earth Planets Space* **60**, 855-864.

O'Neil J. R., Clayton R. N., and Mayeda T. K. (1969) Oxygen Isotope Fractionation in Divalent Metal Carbonates. *The Journal of Chemical Physics* **51**, 5547-5558.

Palmer E. E. and Lauretta D. S. (2011) Aqueous alteration of kamacite in CM chondrites. *Meteoritics & planetary science* **46**, 1587-1607.

Richet P., Bottinga Y., and Javoy M. (1977) Review of hydrogen, carbon, nitrogen, oxygen, sulfur, and chlorine stable isotope fractionation among gaseous molecules. *Annu Rev Earth Pl Sc* **5**, 65-110.

Riciputi L. R., McSween H. Y., Jonson C. A., and Prinz M. (1994) Minor and trace-element concentrations in carbonates of carbonaceous chondrites, and implications for the compositions of co-existing fluids. *Geochimica et Cosmochimica Acta* **58**, 1343-1351.

Riciputi L. R., Paterson B. A., and Ripperdan R. L. (1998) Measurement of light stable isotope ratios by SIMS: Matrix effects for oxygen, carbon, and sulfur isotopes in minerals. *Int J Mass Spectrom* **178**, 81-112.

Rubin A. E., Trigo-Rodriguez J. M., Huber H., and Wasson J. T. (2007) Progressive aqueous alteration of CM carbonaceous chondrites. *Geochimica et Cosmochimica Acta* **71**, 2361-2382.

Schmidt M., Xeflide S., Botz R., and Mann S. (2005) Oxygen isotope fractionation during synthesis of CaMg-carbonate and implications for sedimentary dolomite formation. *Geochimica et Cosmochimica Acta* **69**, 4665-4674.

Score R. and Lindstrom M. M. (1990) Guide to the U.S. collection of Antarctic meteorites 1976-1988. *Antarctic Meteorite Newsletter* **13**, 40,41,88.

Scott E. R. D. and Krot A. N. (2005) Chondritic meteorites and the high-temperature nebular origins of their components. In: Krot, A. N., Scott, E. R. D., and Reipurth, B. Eds.), *Chondrites and the Protoplanetary disk*. ASP Conference Series.

Sephton M. A. (2002) Organic compounds in carbonaceous meteorites. *Nat Prod Rep* **19**, 292-311.

Sephton M. A., Verchovsky A. B., Bland P. A., Gilmour I., Grady M. M., and Wright I. P. (2003) Investigating the variations in carbon and nitrogen isotopes in carbonaceous chondrites. *Geochimica et Cosmochimica Acta* **67**, 2093-2108.

Sheppard S. F. and Schwarcz H. (1970) Fractionation of carbon and oxygen isotopes and magnesium between coexisting metamorphic calcite and dolomite. *Contributions to Mineralogy and Petrology* **26**, 161-198.

Tomeoka K. and Buseck P. R. (1985) Indicators of aqueous alteration in CM carbonaceous chondrites: Microtextures of a layered mineral containing Fe, S, O, and Ni. *Geochimica et Cosmochimica Acta* **49**, 2149-2163.

Tyra M. A., Farquhar J., Wing B. A., Benedix G. K., Jull A. J. T., Jackson T., and Thiemens M. H. (2007) Terrestrial alteration of carbonate in a suite of Antarctic CM chondrites: Evidence from oxygen and carbon isotopes. *Geochimica et Cosmochimica Acta* **71**, 782-795.

Tyra M. A., Brearley A. J., Hutcheon I. D., Ramon E., Matzel J., and Weber P. (2009) Carbonate formation timescales vary between CM1 chondrites ALH84051 and ALH84034. *Lunar and Planetary Science Conference XL*. Lunar Planet. Inst., Houston, TX.

Tyra M. A., Brearley A. J., and Guan Y. (2010a) SIMS in-situ carbon and oxygen isotopic composition of dolomite and calcite in CM1/2 ALH 84049. *73rd annual Meteoritical Society Meeting*. Lunar and Planet. Inst., New York, NY.

Tyra M. A., Matzel J., Brearley A. J., and Hutcheon I. D. (2010b) Variability in carbonate petrography and NanoSIMS ^{53}Mn/^{53}Cr systematics in paired CM1 chondrites ALH 84051, ALH 84049, and ALH 84034. *Lunar and Planetary Science XLI*, abs #2687.

Tyra M. A., Farquhar J., Guan Y., and Leshin L. A. (2012) An oxygen isotope dichotomy in CM2 chondritic carbonates—A SIMS approach. *Geochimica et Cosmochimica Acta* **77**, 383-395.

van de Vusse R. and Powell R. (1983) The interpretation of pyrrhotite-pentlandite-tochilinite-magnetite-magnesite textures in serpentines from Mount Keith, Western Australia. *Mineral. Mag.* **47**, 501-505.

Vasconcelos C., McKenzie J. A., Warthmann R., and Bernasconi S. M. (2005) Calibration of the delta O-18 paleothermometer for dolomite precipitated in microbial cultures and natural environments. *Geology* **33**, 317-320.

Zolensky M. E. (1984) Hydrothermal Alteration of CM Carbonaceous Chondrites - Implications of the Identification of Tochilinite as One Type of Meteoritic Pcp. *Meteoritics* **19**, 346-347.

Zolensky M. E., Bourcier W. L., and Gooding J. L. (1989) Aqueous alteration on the hydrous asteroids - Results of Eq3/6 computer-simulations. *Icarus* **78**, 411-425.

Zolensky M. E., Mittlefehldt D. W., Lipschutz M. E., Wang M. S., Clayton R. N., Mayeda T. K., Grady M. M., Pillinger C. T., and Barber D. (1997) CM chondrites exhibit the complete petrologic range from type 2 to 1. *Geochimica et Cosmochimica Acta* **61**, 5099-5115.

9 Tables

Table 1. Isotopic and chemical composition of carbonate grains

grain	$\delta^{18}O$ (‰)	1σ (‰)	$\delta^{17}O$ (‰)	1σ (‰)	$\Delta^{18}O$ (‰)	1σ (‰)	$\delta^{13}C$ (‰)	1σ (‰)	$CaCO_3$*	$MgCO_3$*	$FeCO_3$*	$MnCO_3$*
dolomite												
a49-5_b5_1	27.9	1.8	14.1	1.5	-0.4	1.6	--	--	49.45	44.86	3.13	2.56
a49-5_b55_1	28.8	1.7	15.9	1.6	0.9	1.6	--	--	51.09	42.48	4.54	1.88
a49-5_b6_1	29.4	1.7	14.5	1.5	-0.8	1.6	--	--	51.48	42.69	3.78	2.04
a49-5_b8_1	25.4	1.7	11.8	1.4	-1.4	1.5	43.1	3.2	51.00	43.42	3.21	2.37
a49-5_b8_2	32.3	1.8	15.3	1.5	-1.5	1.6	46.7	1.4	48.86	43.75	5.31	2.08
a49-5_b88_1	29.4	1.7	13.2	1.6	-2.1	1.7	--	--	51.09	41.72	5.41	1.78
a49-5_b9_1	26.4	1.7	10.6	1.3	-3.1	1.4	37.4	0.8	52.54	39.56	5.83	2.06
a49-5_b12_1	25.9	1.6	10.3	1.5	-3.1	1.5	59.8	1.1	50.70	42.99	4.29	2.02
a49-5_b12_2	30.4	1.6	15.0	1.4	-0.8	1.4	54.5	1.1	47.19	39.71	8.18	4.91
a49-5_b13_1	28.9	1.6	13.3	1.4	-1.7	1.5	56.5	1.1	49.49	42.12	5.74	2.64
a49-5_b13_2	29.6	1.7	15.9	1.6	0.4	1.6	--	--	48.66	42.00	7.39	1.94
a49_6_b3_1	--	--	--	--	--	--	40.2	0.8	50.93	43.19	3.83	2.06
a49_6_b3_2	--	--	--	--	--	--	50.5	1.0	50.93	43.19	3.83	2.06
a49_6_b4_1	--	--	--	--	--	--	45.9	0.8	44.41	40.22	8.46	6.91
a49_6_b6_1	--	--	--	--	--	--	49.5	1.0	49.15	43.60	3.14	4.12
a49-6-b9_1	--	--	--	--	--	--	37.0	1.3	50.62	41.48	4.72	3.17
a49-6-b10a_1	--	--	--	--	--	--	52.7	1.2	49.16	44.64	4.02	2.19
a49-6-b10b_2	--	--	--	--	--	--	39.3	1.0	48.91	44.26	4.71	2.12
calcite	--	--	--	--	--	--						
a49_2_b7cal	--	--	--	--	--	--	13.7	0.8	98.06	0.49	1.32	0.13
a49_5b2a_1	--	--	--	--	--	--	11.9	0.7	98.82	0.24	0.88	0.06
a49_6_b5_2	--	--	--	--	--	--	9.7	1.2	98.46	0.21	0.92	0.42

Shaded areas denote multiple analyses of one grain. Compositions are adjacent to SIMS spots but not exactly coincident. *mol %.

10 Figures

Figure 1. Locations of carbonate grains analyzed by SIMS within thin section ALH 84049, a1. Fig. 1a shows an optical microscope overview of the entire thin section taken in cross polarized light; horizontal distance across the sample is 1.4 cm. Most analyzed carbonates are visible in the image in bright pink colors. The two white boxes show areas where carbonates were analyzed by ion microprobe and are in Figures 1b and 1c. Fig. 1b and 1c are reflected light images of the sample at higher magnification. In reflected light, carbonates have relatively high reflectivity and can be distinguished from the surrounding silicate material quite easily. In Fig. 1c, analyzed grains are identified by text to the right of each grain.

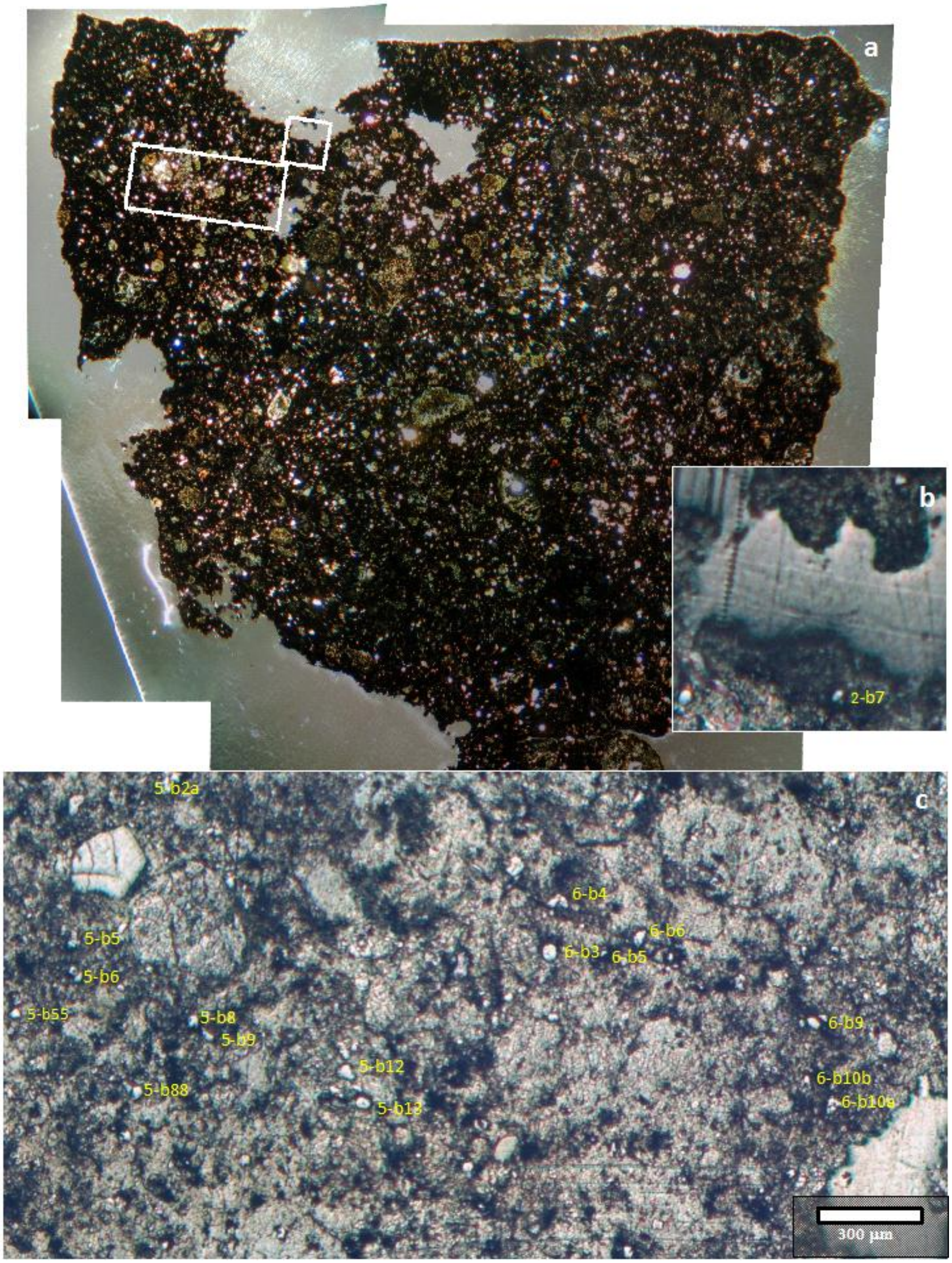
a
b
2-b7
c
5-b2a
6-b4
6-b6
5-b5
6-b3
6-b5
5-b6
5-b55
5-b8
5-b9
6-b9
5-b12
6-b10b
5-b88
5-b13
6-b10a
300 μm

Figure 2. BSE images of carbonates analyzed by SIMS. Green ellipses denote areas analyzed for $\delta^{13}C$ and orange ellipses were analyzed for oxygen isotope composition. Unlike many CM2 chondrite calcite grains, none of the grains are rimmed by tochilinite; “dol” is dolomite and “cal” is calcite.

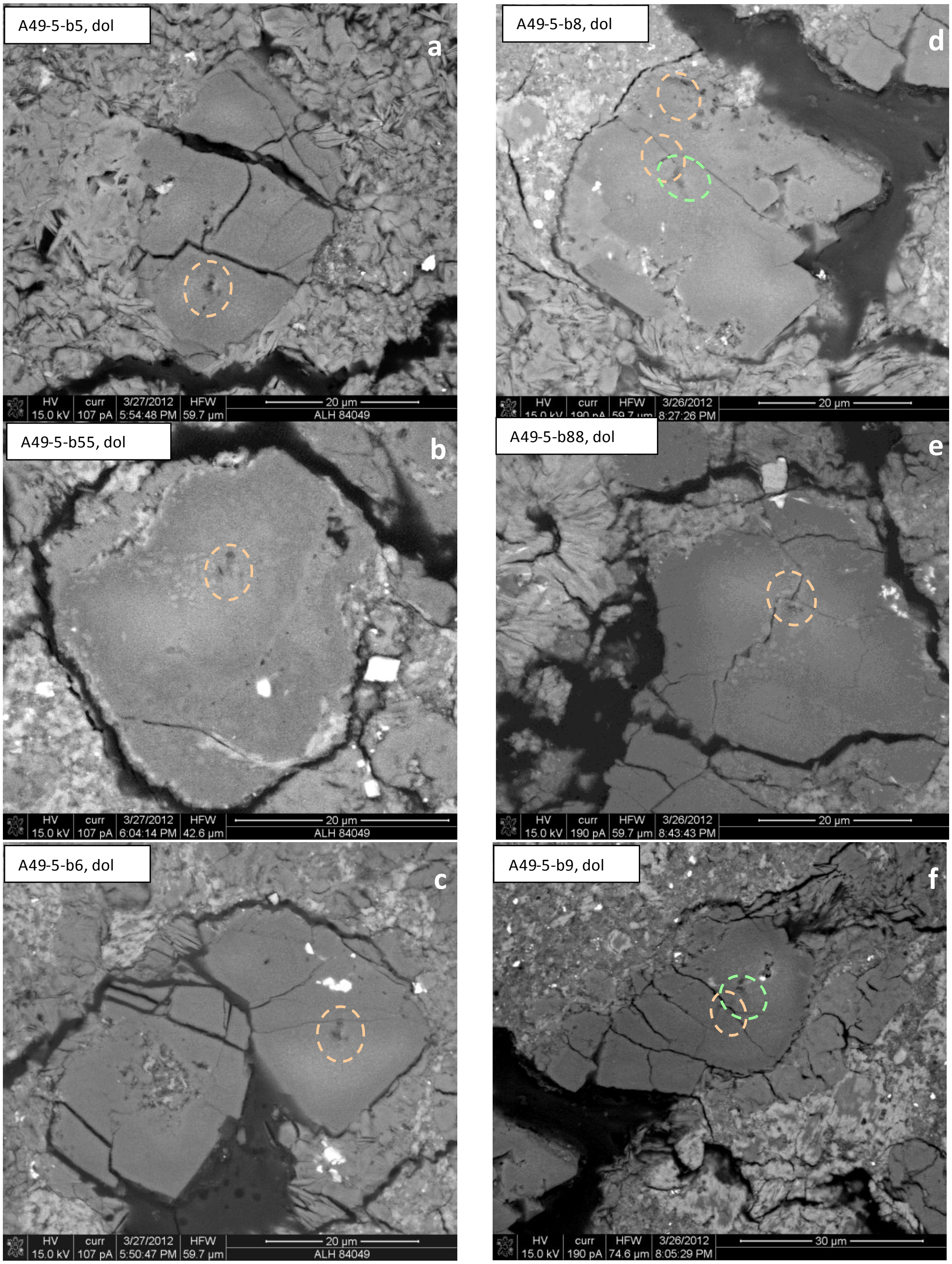
A49-5-b5, dol
a
HV 15.0 kV | curr 107 pA | 3/27/2012 5:54:48 PM | HFW 59.7 µm | 20 µm | ALH 84049
A49-5-b55, dol
b
HV 15.0 kV | curr 107 pA | 3/27/2012 6:04:14 PM | HFW 42.6 µm | 20 µm | ALH 84049
A49-5-b6, dol
c
HV 15.0 kV | curr 107 pA | 3/27/2012 5:50:47 PM | HFW 59.7 µm | 20 µm | ALH 84049
A49-5-b8, dol
d
HV 15.0 kV | curr 190 pA | HFW 59.7 µm | 3/26/2012 8:27:26 PM | 20 µm
A49-5-b88, dol
e
HV 15.0 kV | curr 190 pA | HFW 59.7 µm | 3/26/2012 8:43:43 PM | 20 µm
A49-5-b9, dol
f
HV 15.0 kV | curr 190 pA | HFW 74.6 µm | 3/26/2012 8:05:29 PM | 30 µm

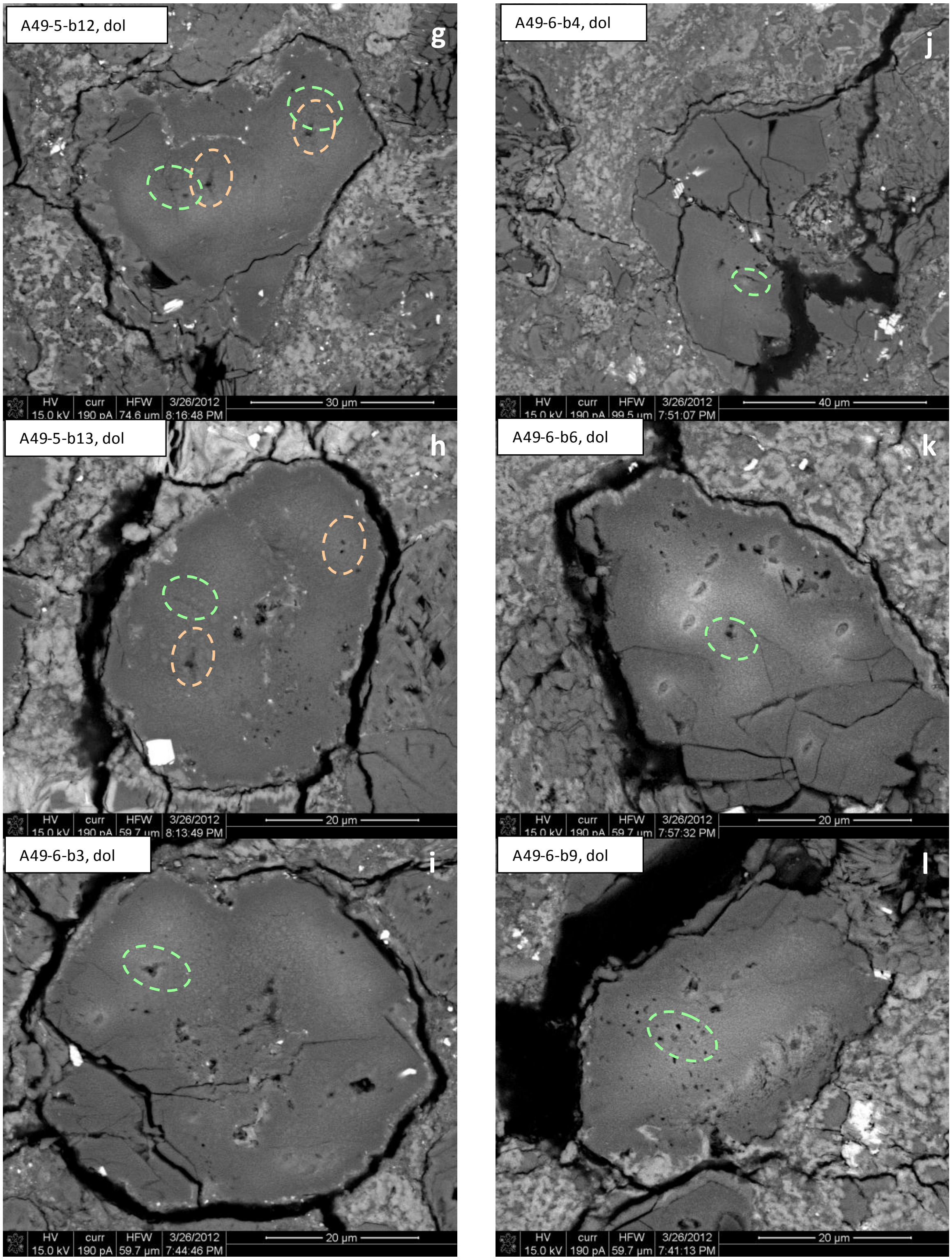
A49-5-b12, dol
g
HV 15.0 kV | curr 190 pA | HFW 74.6 µm | 3/26/2012 8:16:48 PM | 30 µm
A49-6-b4, dol
j
HV 15.0 kV | curr 190 pA | HFW 99.5 µm | 3/26/2012 7:51:07 PM | 40 µm
A49-5-b13, dol
h
HV 15.0 kV | curr 190 pA | HFW 59.7 µm | 3/26/2012 8:13:49 PM | 20 µm
A49-6-b6, dol
k
HV 15.0 kV | curr 190 pA | HFW 59.7 µm | 3/26/2012 7:57:32 PM | 20 µm
A49-6-b3, dol
i
HV 15.0 kV | curr 190 pA | HFW 59.7 µm | 3/26/2012 7:44:46 PM | 20 µm
A49-6-b9, dol
l
HV 15.0 kV | curr 190 pA | HFW 59.7 µm | 3/26/2012 7:41:13 PM | 20 µm

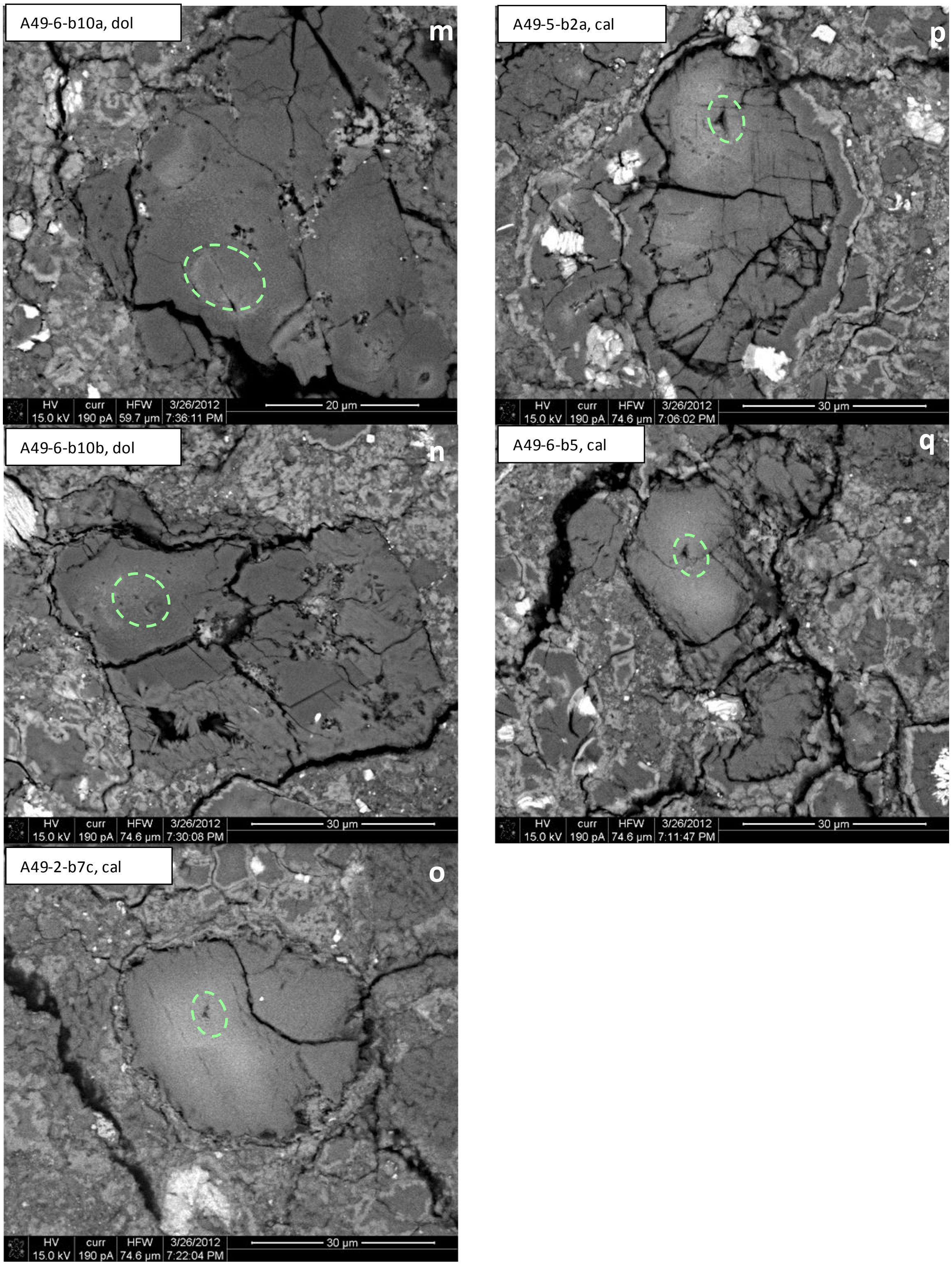
A49-6-b10a, dol
m
HV 15.0 kV | curr 190 pA | HFW 59.7 µm | 3/26/2012 7:36:11 PM
20 µm
A49-5-b2a, cal
p
HV 15.0 kV | curr 190 pA | HFW 74.6 µm | 3/26/2012 7:06:02 PM
30 µm
A49-6-b10b, dol
n
HV 15.0 kV | curr 190 pA | HFW 74.6 µm | 3/26/2012 7:30:08 PM
30 µm
A49-6-b5, cal
q
HV 15.0 kV | curr 190 pA | HFW 74.6 µm | 3/26/2012 7:11:47 PM
30 µm
A49-2-b7c, cal
o
HV 15.0 kV | curr 190 pA | HFW 74.6 µm | 3/26/2012 7:22:04 PM
30 µm

Figure 3. Figures 3a and 3c show dolomite oxygen isotope compositions compared to the chemical composition (Ca, Mg, Fe, and Mn) of the area analyzed. Figures 3b and 3d compare carbon isotope composition to the composition of the area analyzed. All four plots show little correlation between isotope composition and chemical composition except in Figure 3a, where there may be a weak relationship between Ca concentration and oxygen isotope composition ($R^2 = 0.35$). Gray lines tie two analyses from single grains together. Oxygen and carbon isotope compositions are in permil (‰) vs. VSMOW for oxygen and PDB for carbon. The cation compositions are reported in mol%. Isotope errors are 1σ and EPMA error is smaller than the symbol sizes.

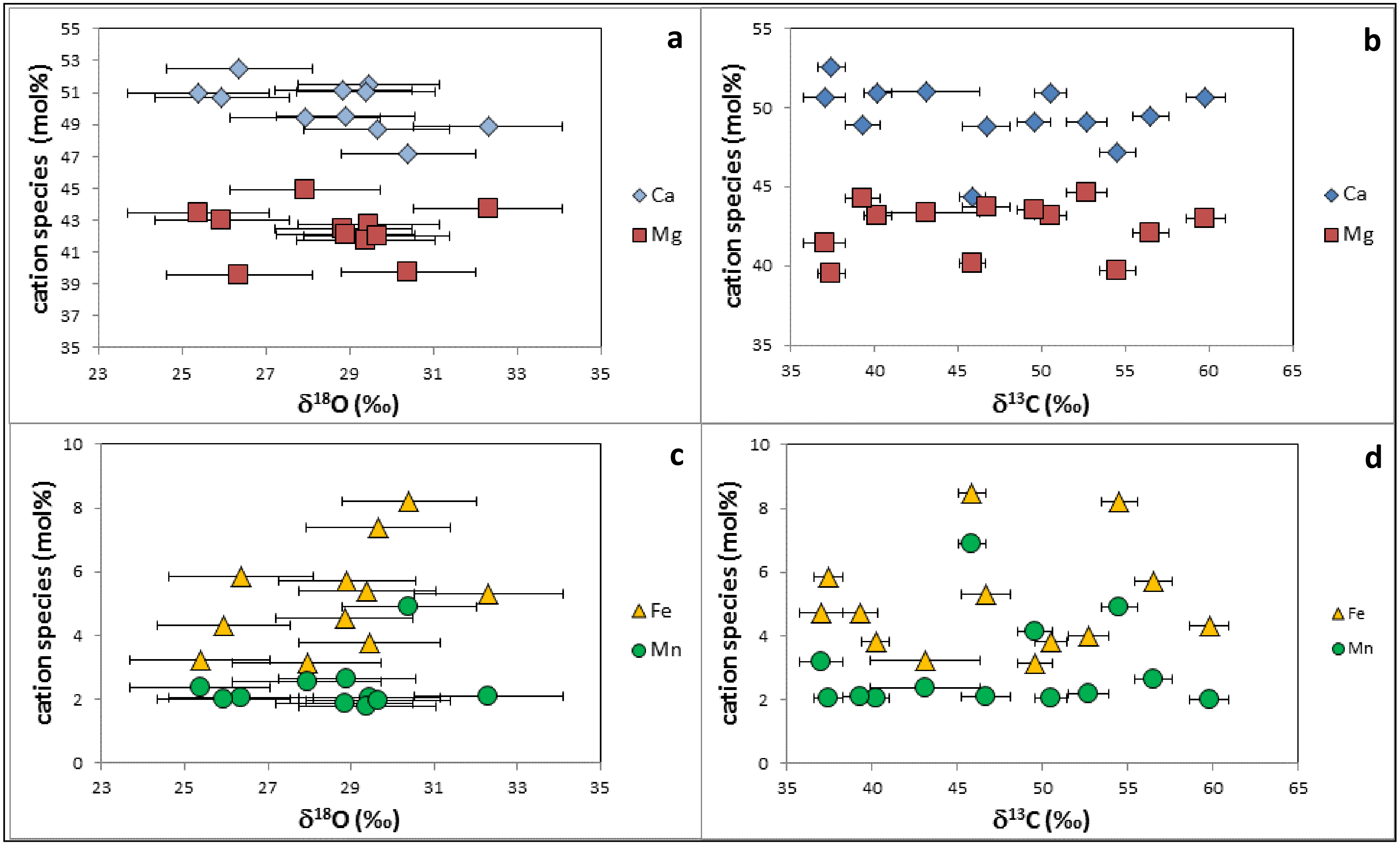a
cation species (mol%)
55
53
51
49
47
45
43
41
39
37
35
23
25
27
29
31
33
35
δ18O (‰)
◇ Ca
■ Mg
b
cation species (mol%)
55
50
45
40
35
35
40
45
50
55
60
65
δ13C (‰)
◆ Ca
■ Mg
c
cation species (mol%)
10
8
6
4
2
0
23
25
27
29
31
33
35
δ18O (‰)
▲ Fe
● Mn
d
cation species (mol%)
10
8
6
4
2
0
35
40
45
50
55
60
65
δ13C (‰)
▲ Fe
● Mn

Figure 4. Comparison of the oxygen isotope composition of analyzed dolomite of ALH 84049 with literature data (SIMS analyses) for calcite in the CM2 chondrites Murchison (Brearley et al., 1999) and the EET 96006 paired set (Tyra et al., 2007). Type 1 calcites are small matrix grains found throughout all CM chondrites and type 2 calcites are larger aggregates. The dolomite compositions in ALH 84049 overlap the composition of type 1 calcite grains in the two CM2 chondrites.

The inset shows a closed system model where water interacts with anhydrous silicate and evolves, producing progressively lower oxygen isotope values for both. As the water evolves it becomes lighter in δ^{18}O, and δ^{17}O. The oxygen fractionation factors of water – calcite and water – dolomite are similar (O'Neil et al., 1969; Kim and O'Neil, 1997; Vasconcelos et al., 2005); if dolomite formed from the same water as calcite then it may have precipitated with type 1 calcite. Perhaps less likely, dolomite could have formed from a later pulse of water with similar oxygen isotope values as that from which calcite precipitated and the closed system model does not apply. The analyses are reported with respect to VSMOW.

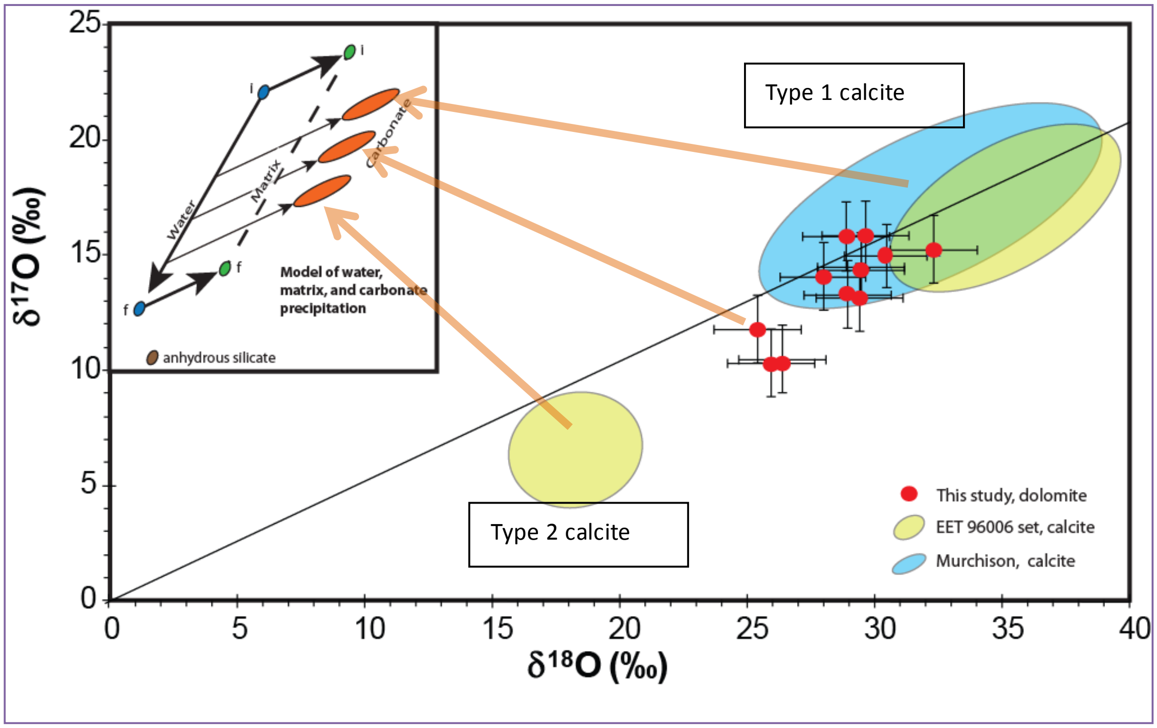

Figure 5. Carbon isotope compositions for dolomite and calcite from this study (circles) compared to published bulk carbonate data for different carbonaceous chondrite groups (Grady et al., 1988; Guo and Eiler, 2007). Note the distinct separation of $\delta^{13}C$ values for calcite and dolomite in ALH 84049, and how results from individual carbonate grains in one sample encompass much of the heterogeneity reported from many samples. Uncertainties for the data are smaller than the symbols (see Table 1 for details). The letter "c" is calcite and "d" is dolomite.

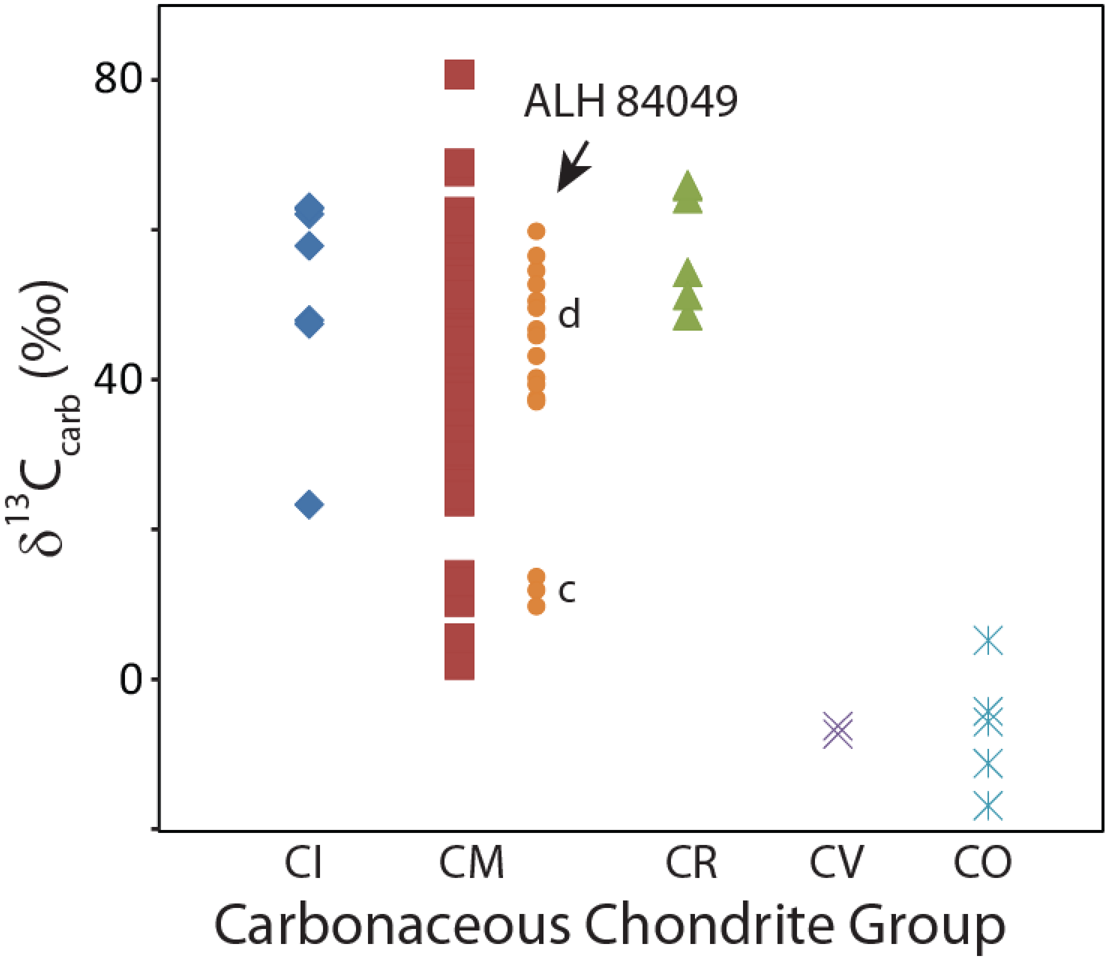

Figure 6. Plot showing the δ^{13}C and δ^{18}O compositions of single grains of dolomite from ALH 84049 (round, filled symbols). There is no apparent relationship between oxygen and carbon isotope compositions in dolomite. Also plotted are bulk CM2 chondrite carbonate data (stars) from Guo and Eiler (2007), which show a similar range to that found in individual dolomite grains. Oxygen isotope compositions are plotted in relation to VSMOW and carbon isotopes to PDB.

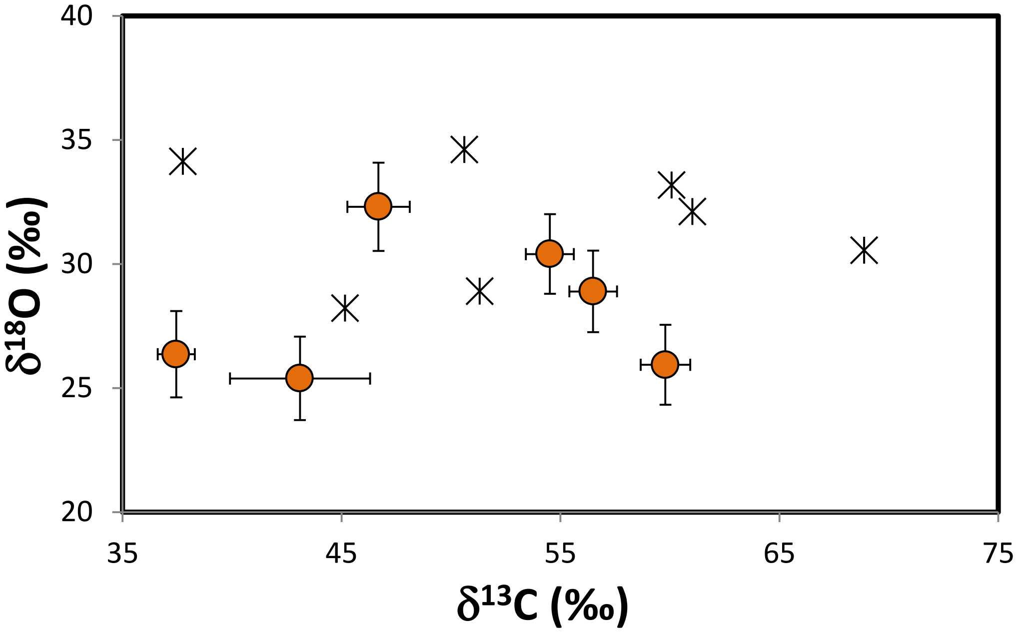

CHAPTER 4

Siderite and calcite oxygen isotope composition in CR1 chondrite GRO 95577: SIMS approach

1 ABSTRACT

Manganese-chromium age dating of siderite grains in the CR1 chondrite GRO 95577 indicate that it crystallized much later than any carbonate analyzed to date in a carbonaceous chondrite. Here, we report the first in situ oxygen isotope compositions of the secondary minerals siderite and calcite in this chondrite measured by SIMS. Oxygen isotope values of carbonates in GRO 95577 are similar to those reported in CI, CM1, and CM2 chondrites. The $\delta^{18}O$ values of calcite range from 23.6 to 34.0 ‰ and $\delta^{17}O$ values range from 14.1 to 18.0 ‰. Siderite $\delta^{18}O$ value ranges from 15.4 to 27.3 ‰ and $\delta^{17}O$ compositions range from 8.5 to 15.5 ‰. These data show that the carbonates could not have precipitated from Antarctic water during terrestrial weathering and therefore confirms that both carbonates are extraterrestrial in origin. Oxygen isotope values do not vary in tandem with the very heterogeneous carbonate chemical compositions at the spatial and analytical resolution of the ion microprobe used. These observations suggest that the cation chemistry of the fluid from which carbonates grew evolved independently of oxygen isotope composition. The heterogeneous carbonate compositions implies that geochemical environment within GRO 95577 was spatially variable; perhaps due to microenvironments controlled by localized dissolution reactions involving coarse-grained primary silicate phases in chondrules. Oxygen isotope compositions can be explained by a simple model where water evolved as it interacted with silicates. The chemical environment during carbonate precipitation within GRO 95577 was complex and heterogeneous, whereas the oxygen isotope system evolved in a comparatively simple manner.

2 INTRODUCTION

GRO 95577 is distinct amongst CR chondrites; it is the sole sample that represents the most advanced stage of aqueous alteration, type 1 (Weisberg and Huber, 2007). With the addition of GRO 95577, CR chondrites are the only group that show a full range of petrologic types from unaltered type 3.0 (Abreu and Brearley, 2010) to type 1, where aqueous alteration has completely replaced the original primary mineralogy (Weisberg et al., 1993; Weisberg et al., 1995; Weisberg and Huber, 2007). Nearly all primary minerals, including what once were large chondrule olivine and metal grains, have been replaced by secondary minerals. Consequently, GRO 95577 and less-altered CR chondrites allow us to study aqueous alteration from incipient low temperature hydrothermal alteration to full hydration of protolith minerals.

GRO 95577 contains siderite, calcite, and minor dolomite (Chapter 2, this work). Calcite grains as large as 200μm occur, although <50 μm diameters are more typical. Siderite grains are usually less than 40 μm in diameter (most less than 10μm) and dolomite is less than 20 μm. In siderite, microscale and even nanoscale chemical variability between grains and compositional zoning ($MgCO_3$, $MnCO_3$, $FeCO_3$, and $CaCO_3$ components) within grains have been noted (Tyra et al., 2010b; Tyra et al., 2011; Chapter 2, this work). This suggests that chemical environments within GRO 95577 were heterogeneous. Compositional relationships between Mn, Fe, and Mg within siderite, however, are linear; this implies that aqueous fluid was in communication throughout the sample during siderite formation (Chapter 2, this work). Calcite grains are relatively pure, 96 to 100 mol% $CaCO_3$, regardless of sample number or lithology studied (Weisberg and Huber, 2007; Chapter 2, this work).

Oxygen isotope compositions of carbonates can constrain isotope evolution of aqueous fluids in chondrite parent bodies (Grady et al., 1988; Clayton and Mayeda, 1999; Benedix et al., 2003; Tyra et al., 2007b). For example, in CM chondrites, lower δ^{18}O values are consistent with increasing aqueous alteration as water progressively interacted with ^{16}O-rich silicates and followed a mixing line from high δ^{18}O to lower values. Previous SIMS measurements of carbonates in CM1 and CM2 chondrites have shown that oxygen isotope heterogeneity is present on a grain-to-grain scale (Brearley et al., 1999; Tyra et al., 2007a; Tyra et al., 2010a; Chapter 3, this work). Calcite and siderite in GRO 95577 may show similar isotopic diversity that can be used to place constraints on the formation of these carbonates.

Although no in-situ oxygen isotope analyses of carbonates in CR chondrites have been undertaken to date, Bonal et al. (2010) analyzed dolomite and magnesite oxygen isotope compositions in-situ in hydrated lithic clasts of the CB/CH chondrite Isheyevo. CB and CH chondrites are tied to the CR chondrite group by their petrology, bulk REE abundances, and oxygen isotope compositions (Weisberg et al., 1995; Krot et al., 2002). It is unclear, however, if CR, CB, and CH chondrites are from the same parent body. Bonal et al. (2010) reported that carbonate δ^{18}O ranged from 26.0 ± 1.0‰ to 32.2 ± 0.6‰ and δ^{17}O from 12.9 ± 1.1‰ to 13.9 ± 1.0‰; these ranges overlap carbonate isotope compositions in the CI1 chondrite Orgueil and also CM2 chondrite carbonates (Kallemeyn and Wasson, 1982; Grady et al., 1988; Benedix et al., 2003). Determining the carbonate oxygen isotope composition of CR chondrites will help determine if models of aqueous alteration for other carbonaceous chondrites apply to CR chondrites.

Few models for aqueous alteration and coincident carbonate formation exist for CR chondrites. In this study, we explore if systematic relationships exist between carbonate chemistry and oxygen isotope composition which could reflect chemical and isotopic changes in parent body fluids with time. We have analyzed individual carbonate grain (calcite and siderite) oxygen isotope compositions in situ via ion microprobe. Our data affirm that calcite and siderite in GRO 95577 are extraterrestrial and provide constraints on the extent of water-mineral interactions. Our data are the first oxygen isotope measurements of individual secondary minerals in CR chondrites and provide a foundation towards understanding the oxygen isotope evolution of CR chondrites during alteration from type 3 to type 1.

3 METHODS

3.1 Samples

We examined two 1 inch round, polished petrographic thin sections, GRO 95577, 30 and GRO 95577, 53. The samples were acquired courtesy of the Antarctic Meteorite Working Meteorite Group from the Antarctic Meteorite Collection at NASA Johnson Space Center. These are the same two thin sections used in Chapter 2 (this work) for a study of the ^{53}Mn-^{53}Cr systematics of siderite. Prior to electron and ion beam analyses, the samples were imaged with a petrographic microscope to locate potential carbonate grains. The images taken in crossed polarized light, plane light, and reflected light provided a navigational aid when using the Electron Probe Microanalyzer (EPMA) and the Secondary Ion Mass Spectrometer (SIMS). The samples were carbon-coated under standard operating conditions to ~20 nm with an Emitech K950X Turbo Evaporator unit in preparation for electron beam and ion beam analysis.

3.2 Chemical analysis

Full spectral X-ray maps of each thin section were acquired using an EDAX Apollo 40 SDD detector attached to a FEI Quanta 3D FEG SEM (30 kV accelerating voltage , 23 nA beam current, ~200 μs dwelltime per pixel, 1.7 μm/pixel resolution, ~30% deadtime). These maps were used to determine the distribution, abundance, and chemistry of carbonates in the samples. In addition, the X-ray maps allowed the largest siderite and Ca-carbonate grains to be located and selected for additional chemical and isotopic analysis.

The composition of each grain selected for isotopic analysis was determined by electron probe microanalysis prior to ion microprobe analysis. Analyses were carried out using the JEOL 8200 EPMA located at the University of New Mexico. Analysis conditions were 12kV accelerating voltage, 10nA beam current, with a ~1μm beam size. SIMS analyses were performed at locations adjacent to where the microprobe analyses were performed.

3.3 Isotopic analyses

We measured oxygen isotopic compositions of both siderite and Ca-carbonate within GRO 95577. To determine the oxygen isotopic composition of carbonates, we used the Cameca IMS 7f-GEO SIMS at the California Institute of Technology (Cs^+ primary beam, 10 keV, ~0.1 nA, ~10 μm spot size). The $^{16}O^-$ signal was measured with a Faraday cup (FC), and the $^{17}O^-$ and $^{18}O^-$ signals with an electron multiplier (EM). Counting times of 2s for ^{16}O, 10s for ^{17}O, and 4s for ^{18}O allowed a typical count rate of ~25 million counts-per-second for ^{16}O. Sample charging was compensated with a negative electron gun (NEG) at -10 keV. Background correction, though negligible, was applied to the three O masses. Electron multiplier dead-time correction was applied to mass ^{17}O and ^{18}O.

We used a N_2(l) cold trap to reduce the OH^- signal by a factor of 10, field apertures to ensure steep sides of the peaks which cuts tail input, and a high mass resolving power (MRP) of 6500 (M/ΔM). This ensured that the ^{16}OH tail to the ^{17}O peak was less than 0.1‰. During the siderite oxygen isotopic analyses, pre-sputtering was performed for 120s at 0.6 nA and each analysis encompassed 30 cycles at 0.3 nA. Pre-sputtering removes surface contamination and the carbon coat from the region of interest. Repeated analyses of the siderite standard gave an uncertainty of 2.3‰ (2σ) for $\delta^{18}O$ and 1.8‰ (2σ) for $\delta^{17}O$. The siderite grains within GRO 95577, however, are not pure siderite. Siderite Fe ranges from 44-62 mole %, Mn from 12-38 mole %, and Mg from 17.5-30 mole % (Chapter 2, this work). Sample data were calibrated for instrumental mass fractionation (IMF) and matrix effects with suitable calcite (optical calcite) and siderite standards. The elemental compositions of individual siderite grains are compared with oxygen isotope values and potential matrix effects are discussed below in sections 4.2 and 5.1.

For the calcite SIMS analyses, we first pre-sputtered at 0.6 nA for 120s before reducing the current to 0.3 nA for the analytical run (30 cycles). A higher current (and spot size) than the siderite analyses was possible as the calcite grains were larger. This procedure improved the counting statistics. Measured Ca-carbonates were, on average, 98.4 mole % $CaCO_3$, 1.1 wt. % $FeCO_3$, 0.35 wt% $MnCO_3$, and 0.15 wt. % $MgCO_3$. This nearly pure composition is close enough to the Optical Calcite standard for matrix effects to be negligible.

4 RESULTS

4.1 Petrography

Tyra et al. (Chapter 2, this work) described carbonate petrography in GRO 95577. In addition to the host CR lithology (large chondrules, ~30% matrix), GRO 95577 also contains a significant component of a fine-grained “dark lithology” (DL). Calcite, siderite, and rare dolomite are present in matrix between chondrules within the host and the DL (Fig. 1; Weisberg and Huber, 2007; Tyra et al., 2010b). GRO 95577, 30 contains 3.2 vol. % calcite and 0.15 vol% siderite. GRO 95577, 53 has 2.9 vol% calcite and 0.17 vol% siderite, essentially identical results. Carbonates are often associated with magnetite and pyrrhotite and exhibit embayed and corroded textures on the periphery of all observed grains.

Ranges in chemical and isotope composition of carbonates analyzed are shown in Table 1. In summary, calcium carbonate compositions ranged from 0.2 to 0.3 mol% $MgCO_3$; 0 to 0.2 mol% $MnCO_3$; 0 to 1.1 mol% $FeCO_3$; and 98.4 to 98.6 mol% $CaCO_3$. Ca-carbonate grain compositions were indistinguishable, whether the grain occurs in the CR host lithology or the DL. Dolomite ranged from 26.0 to 31.6 mol%, $MgCO_3$; 12.9 to 17.4 mol% $MnCO_3$; 7.6 to 9.2 mol% $FeCO_3$; and 45.5 to 50.9 mol%, $CaCO_3$.

4.2 Oxygen isotopes

Figure 2 shows SIMS analysis spots on one calcite and three siderite grains. Analyzed calcite grains are far larger than SIMS spots (each spot was ~10 μm in diameter). Careful selection of siderite grains was required, as few siderite grains are larger than 10 μm in diameter. Backscatter electron images of all siderite SIMS analysis spots are shown in the appendix for reference.

Siderite and calcite oxygen isotopic compositions are distinct. The $\delta^{18}O$ of calcite (10 spots in 10 grains), ranges from 23.6 to 34.0 ‰ and $\delta^{17}O$ values range from 14.1 to 18.0 ‰. Siderite $\delta^{18}O$ values (11 spots in 8 grains), range from 15.4 to 27.3 ‰ and $\delta^{17}O$ compositions range from 8.5 to 15.5 ‰. Measured carbonate isotopic compositions in the DL and CR host lithologies are identical within error; Table 1 gives chemical compositions, isotope compositions, and the location (i.e. DL or host lithology) of each carbonate analyzed. Both siderite and calcite oxygen isotope compositions lie on the terrestrial fractionation line. They overlap slightly, but the majority of siderite oxygen isotopic values ($\delta^{17}O$ and $\delta^{18}O$) are lower than calcite. The data and calculated errors are listed in Table 1. Figure 3 compares chemical compositions to oxygen isotope values, and Figure 4 illustrates data relationships.

5 DISCUSSION

5.1 Chemistry

The variable chemistry of calcite and siderite was discussed and related to fluid evolution in Tyra et al. (Chapter 2, this work). Based on the oxygen isotopic compositions of carbonates in GRO 95577, we argue below that oxygen isotope $\delta^{18}O$ values of fluids evolve to lower values as interaction with anhydrous silicates progressed. However, variations in carbonate chemistry cause matrix effects during SIMS oxygen isotope analyses of minerals (e.g., Leshin et al., 1998; Rollion-Bard and Marin-Carbonne, 2011). Therefore, interpretation of the oxygen isotope evolution requires understanding if and how chemical composition correlates with isotope values, independent of matrix effects.

Matrix effects can significantly affect reported oxygen isotope values. For example, Leshin et al. (1998) measured the oxygen isotope composition of carbonates in ALH 84001; matrix effects over the large chemical range of analyzed grains were discernible. Consequently, the authors used a correction assuming that oxygen isotope values correlate linearly with chemical variations in the carbonates, especially variations in Mg. In this study, the SIMS analytical conditions differed from that of Leshin et al. (1998). Although we describe isotope variations within single grains, the results shown in Table 1 and Figure 3 imply that the tuning of the SIMS produced minimal matrix effects in oxygen isotope values obtained. Nevertheless, if we applied the same correction used by Leshin et al. (1998) to our data, then over the ~20 mol% variation in $MgCO_3$ reported here in siderite, a maximum correction of ~2‰ would be applied. For example, a hypothetical grain 1 with an $MgCO_3$ content 20 mol% higher than grain 2 would have a $\delta^{18}O$ composition 2‰ lower. We observe, however, no systematic variation of $\delta^{18}O$ or $\delta^{17}O$ with composition. Furthermore, the spread of data shown in Figure 4 far exceeds what can be explained by matrix effects. Therefore, the variation in oxygen isotope values that we report in this paper cannot be explained by matrix effects.

Assuming that the matrix effects caused minimal instrumental mass fractionation (IMF), our data suggest that differences in oxygen isotope composition and chemistry exist within individual grains. For instance, as reported in Table 1 Grain g30-11-b has a $\Delta^{17}O$ between +1 and 2 ‰ (± 1‰) at 33.51 mol% Mg and a slightly negative $\Delta^{17}O$ of ~ -0.3 ‰ (± 1‰) in a location with 26.45 mol% Mg. This effect is interesting as it seems to be a non-mass dependent relationship which cannot be created by matrix effects. However, more analyses are needed: at present, the observed relationship is barely visible at a 1σ level and insignificant at a 2σ level. Consequently, it can only be stated that siderite precipitated from a fluid with either heterogeneous or evolving chemical composition that has no definitive correlation with oxygen isotope composition.

5.2 Terrestrial Siderite?

Based on the Mn-Cr systematics, the siderite grains in GRO 95577 have younger crystallization ages than any secondary carbonate mineral measured in carbonaceous chondrites to date. Tyra et al. (2010b) and Chapter 2 (this work) suggest that siderite precipitated at least 24 Myr after CAI formation. Because this age is based upon the error envelope about an essentially flat Mn-Cr isochron, this unique result raises the possibility that siderite within GRO 95577 is not extraterrestrial in origin, but may have formed by weathering in the Antarctic before the meteorite was collected. Several studies demonstrate that carbonates (e.g. nesquehonite, hydromagnesite, calcite) can precipitate during extended residence within Antarctic ice (e.g. Jull et al., 1988; Tyra et al., 2007b).

Although some terrestrial carbonates do form in meteorites, chemical conditions are not favorable for siderite precipitation. Tyra et al. (Chapter 2, this work) argue that the terrestrial surface environment is too oxidizing for siderite formation to have occurred while GRO 95577 rested on and within Antarctic ice. Terrestrial siderite precipitation is restricted to somewhat reduced, methanogenic geochemical conditions (Garrels and Christ, 1965; Hem, 1985; Romanek et al., 2009).

The δ^{18}O compositions of calcite and siderite are also inconsistent with terrestrial formation in Antarctica. To our knowledge, there is no published measurement of δ^{18}O of ice at Grosvenor Hills near the Trans-Antarctic Mountains, the location where GRO

95577 was recovered. Surface snow $\delta^{18}O$ adjacent to the Trans-Antarctic Mountains averages from -40 to -45‰ (Lorius, 1983; Cassidy and Whillans, 1988). Furthermore, modern Antarctic precipitation on the East Antarctic ice sheet adjacent to the Transantarctic Mountains is modeled to average -40‰ with a seasonal variation of ±10‰ (Helsen et al., 2007). It is likely, however, that the water available to interact with GRO 95577 was much lighter in composition. The sample was collected from exposed blue ice at the Grosvenor Mountain inner Mt. Cecily ice field (Grossman, 1998). Glacial blue ice originates from the East Antarctic highlands which, depending upon age, is significantly lighter than local precipitation in Grosvenor Mountains. This ice $\delta^{18}O$ composition is commonly <-60‰ (Watanabe et al., 2003). Typical temperatures at meteorite stranding surfaces remain well below freezing; however, during the summer low albedo meteorites at Allan Hills in Antarctica may reach 5°C a couple of days per year (Schultz, 1986). At 5°C, the fractionation (1000 ln(α)) is 36.78‰ between calcite and water and 39.93‰ between siderite and water. If the water available within GRO 95577 ranged from -40‰ to -60‰, then the measured compositions in GRO 95577 of both siderite and calcite lie far outside of the range of in-situ precipitation at probable Antarctic temperatures (Fig. 5; Zheng, 1999). Terrestrial water could react with minerals in GRO 95577 and change the oxygen isotope composition of water (rock buffering); however no petrographic evidence has been found to support extensive terrestrial water-rock interaction.

We demonstrate in Figure 5 the isotopic compositional range of potential carbonate which would precipitate from melted Antarctic ice. For the purpose of this demonstration, we use -40‰ as Antarctic water, 5°C for the temperature, and the fractionation factors mentioned above. Neither the composition of siderite nor calcite is consistent with formation from Antarctic water. If the interior temperature were higher, or if the initial water were lighter, then the carbonate would have oxygen isotopic compositions even lower than that displayed. Measured carbonates in GRO 95577, with δ^{18}O values > 20‰, are distinct from carbonates produced by terrestrial weathering in Antarctica. Therefore, we conclude that the carbonate assemblages in GRO 95577 are extraterrestrial in origin.

5.3 Siderite and calcite oxygen isotope differences caused by temperature changes?

Although during aqueous alteration there may have been periods of carbonate dissolution and reprecipitation (Zolensky et al., 1989; Johnson and Prinz, 1993; Brearley and Hutcheon, 2000; de Leuw et al., 2010), it is unlikely that oxygen isotope compositions of carbonate minerals changed after their final precipitation. Tyra et al. (Chapter 2, this work) present evidence using enhanced contrast BSE imagery that all classified carbonate types, Ca-carbonate, dolomite, and siderite, contain observable zoning. We argue that zoning on the micron scale in carbonate grains can only have been preserved if post formational temperatures remained below the closure temperature (350 to 450 °C at a 100K/Myr cooling rate, Fisler and Cygan, 1999) for diffusion of Mg, Mn, Ca, and Fe cations. Organo-thermometry (e.g. Cody et al., 2008) and a lack of metamorphic textures also strongly suggest that temperatures remained low (< ~250 °C). Furthermore, the diffusion coefficient of oxygen in carbonates is similar to that of Mg (Cherniak, 2010). Assuming oxygen isotopic diffusion in carbonates occurs at similar rates to cations, these observations indicate that the primary (i.e., preterrestrial) oxygen isotopic compositions of carbonates in GRO 95577 should be preserved.

Temperature differences at the time of precipitation between calcite and siderite could explain the reported oxygen isotope differences between these two carbonate phases. Precipitation at a lower temperature would produce a carbonate that shows more isotopic fractionation from asteroidal water than if the carbonate formed at a higher temperature. For example a calcite precipitating at 25°C from a fluid with a δ^{18}O of 0‰ would have a δ^{18}O composition of 31.19‰ (33.95‰ for siderite) and at 175°C a δ^{18}O composition of 11.28‰ (12.57‰ for siderite), a difference of about 20‰ (Zheng et al., 1999). The lower δ^{18}O values of siderite could have arisen because siderite precipitated at warmer temperatures than calcite. Fractionation effects caused by differences in temperature of formation are mass-dependent and so our reported isotope compositions lying along a mass-dependent fractionation line are indeed consistent with siderite and calcite precipitating at different temperatures. The petrography of GRO 95577 shows that siderite must have precipitated after most calcite in this sample (Tyra et al., 2011; Chapter 2, this work). Therefore, if temperatures increased after calcite formation, siderite would precipitate with lower δ^{18}O and δ^{17}O values than older calcite.

Estimates of CR chondrite alteration temperature are variable. Clayton and Mayeda (1977) used the oxygen-isotope equilibrium fractionation between magnetite and phyllosilicates to estimate that CR chondrites (Renazzo in particular) experienced alteration at a temperature of ~300°C. This temperature estimate requires that magnetite and phyllosilicates formed concurrently and in equilibrium with the fluid. In Chapter 2, we note that, within the CR1 chondrite GRO 95577, siderite is zoned in Mn, Mg, and Ca. We (Chapter 2, this work) argue that the fine scale (sub-micron) zoning is inconsistent with diffusion. To preserve 1 μm zoning from diffusion at ~300°C, the cooling rate would need to be faster than 800K/Myr (Fisler and Cygan, 1998). It is far more likely that submicron zoning is the result of precipitation from a fluid of changing composition at temperatures that never exceeded 200°C. Furthermore, the preservation of temperature sensitive organic matter, as shown by the organic thermometry measurements by Cody et al. (2008), is most consistent with a temperature that is less than 200°C for all measured CR chondrites (171 ± 64°C).

5.4 Siderite and calcite oxygen isotope differences a result of fluid isotope evolution?

5.4.1 Closed system

The range in calcite oxygen isotope compositions in GRO 95577 implies that calcite precipitated from water that varied in its oxygen isotope composition. Because water evolves toward lighter oxygen isotope values (explained below), one can say that in a closed system a carbonate with lower oxygen isotopic values precipitated after a grain with higher oxygen isotopic values if the fluid was homogeneous. Carbonate oxygen isotope heterogeneity could also originate from precipitation from localized fluid reservoirs isolated from each other and evolving differently due to reactions with heterogeneous silicate minerals. As calcite and siderite chemical compositional ranges are indistinguishable in both samples and in both lithologies, isolation due to low permeability is unlikely, however (Bland et al., 2009). Perhaps mineralogical heterogeneity repeats on a mm-scale (for instance, from one chondrule through the matrix to the next chondrule). In this scenario, similar microenvironments and the fluid response to these microenvironments repeat throughout the sample and isotopic and chemical similarities do not necessitate fluid communication. A final scenario could be that chondrules had already hydrated to phyllosilicates before carbonate precipitated.

Chondrule minerals, because of their large size, react relatively slowly, creating areas in CM2 chondrites with a different microenvironment than the adjacent matrix (Brearley, 2006). If all minerals had already reacted with water before carbonate precipitation, then the microenvironments would not exist. The fact that siderite and calcite oxygen isotopic compositions both lie on a mass dependent line and do not noticeably change in $\Delta^{17}O$ also would be expected if all anhydrous silicates had reacted. Otherwise, carbonates would preserve progressively decreasing $\Delta^{17}O$ and $\delta^{18}O$ values that arose from reacting anhydrous silicates changing the water composition. If geochemical microenvironments did not exist, then it is difficult to explain the siderite chemical heterogeneity.

Benedix et al. (2003) tailored the closed system two-component model of Clayton and Mayeda (1984) to explain calcite oxygen isotope compositions in CM chondrites. In these models, asteroidal water evolved from higher to lower values of $\delta^{18}O$, $\delta^{17}O$, and $\Delta^{17}O$ as water interacted with anhydrous silicates. Carbonates record the evolution of the water. Benedix et al. (2003) used concepts outlined in Clayton and Mayeda (1984; 1999) of whole rock oxygen isotopic composition evolution to explain measured bulk carbonate oxygen isotope data. Below we use a similar rationale to model the evolution of water in the CR parent body.

Figure 6 shows a modified version of the schematic shown in Benedix et al. (2003). We present water oxygen isotopic evolution and minerals that formed in equilibrium with this water (siderite, calcite, and phyllosilicates) in a $\delta^{18}O$ vs. $\delta^{17}O$ framework. To emphasize trends, we have exaggerated the y-axis, as the water regression slopes reported by Clayton and Mayeda(1999) and the TFL vary by < 0.2. The TFL is generally a slope of 0.52 and the CR water evolution slope ranges from 0.6 (Clayton and Mayeda, 1999) to 0.7 (Choi et al., 2009; Schrader et al., 2011). In the figure, water begins initially at 'i' and trends to 'f' as it exchanges and reacts with anhydrous minerals, thus becoming $\delta^{18}O$ and $\delta^{17}O$ depleted with time. Assuming water leaves the system, the whole rock composition becomes isotopically heavier as secondary minerals precipitate (Fig. 6 inset).

At a given temperature, the first calcite precipitating from the same water reservoir would have a heavier isotopic value than a later one (see Fig. 6). As the siderite and calcite oxygen fractionation factors at 25°C vary by ~3‰, at 100°C by ~2‰, and at 200°C by ~1‰, differences between siderite and calcite can only be explained by the water composition changing between calcite precipitation and the onset of siderite precipitation. Calculated $\delta^{18}O$ values between calcite and siderite vary by 3.3‰ at 0°C and 1.8‰ at 100°C, using fractionation factors by Zheng (1999). As calcite and siderite $\delta^{18}O$ values vary by up to 17‰, the isotopic differences between the two phases cannot be wholly attributed to cogenetic precipitation at equilibrium from the same fluid. The simplest explanation is that calcite precipitated first and siderite second from water of evolving O isotopic composition, with a transitional period when coprecipitation occurred.

5.4.2 Unidirectional fluid flow or circulation?

The simple closed system of Clayton and Mayeda is consistent with results reported here. However, the fluid flow model of Young et al. (1999; 2001) could also explain the similarity of results presented here with those for the CM and CI chondrites. In essence, the Young planetesimal hydrological model suggests that each body had comparable starting material and water. If the interior of the body heats enough, then water ice will melt or be released through metamorphism and begin flowing down-temperature and down pressure towards the outside of the body. The flow outward creates similar temperature and fluid isotope composition zones at similar radial distances from the center of the body. A fundamental point that the model makes is that because a single body can have many oxygen isotope zones, similar oxygen isotope values in two meteorites does not necessitate that they originated on the same body. The oxygen isotope compositions of carbonates in CI, CM, and now CR chondrites are remarkably similar, and they all have comparable degrees of aqueous alteration. Perhaps this quality is the result of parallel evolution of fluid on different bodies within the early solar system, consistent with the model of Young et al. (1999; 2001).

Fluid flow, however, may not be unidirectional. Palgutta et al. (2010) modeled convective hydrological systems, assuming that water did not escape an asteroid into space. Water heats in the interior, moves outward and cools, and sinks back toward the asteroid interior. The results are similar to Young (2001), where water of homogeneous composition may reside in one area of the planetesimal, even though many different isotopic regimes exist within the entire body. The biggest difference between the two models is that while Young et al (2001) predict areas of similar isotope composition that is depth-dependent, Palgutta et al (2010) envisage vertical bands of similar alteration and isotope composition that depend on the location where water is either rising or descending as part of a convective cell.

Similarly to the model of Young et al. (2001), the model of Palgutta et al. (2010) could also explain the similarity of carbonate oxygen isotope compositions of the CR1 GRO 95577 to that in other carbonaceous chondrite classes, but more work is needed to determine which scenario is more likely. Models accounting for potential low permeability of chondrite matrix (Bland et al., 2009), preferential fluid flow through impact fractures (carbonate veins, Tyra et al., 2009), continual impact disturbance, and that account for changing permeability conditions as alteration continues are needed.

6 Conclusions

GRO 95577 is an intriguing meteorite. Tyra et al (Chapter 2, this work) and this paper show that siderite within GRO 95577 exhibits large chemical variability. This spread in chemical composition is consistent with variable geochemical microenvironments, as envisioned by Brearley et al. (2006). Although fluids from which siderite precipitated were chemically heterogeneous, the oxygen isotope composition of the fluid followed an evolution that can be explained by a two-component closed system model. The best explanation is that while chemistry in the CR parent body was quite variable due to the heterogeneous distribution of minerals at the tens of microns scale, oxygen isotopes evolved in parallel within these microenvironments. The chemistry is a complex system; the oxygen isotope system is not.

Our data show that the variations in, and differences between, siderite and calcite oxygen isotope compositions were not caused by analytical artifacts such as matrix effects and, further cannot be attributed to terrestrial formation or temperature differences at the time of precipitation from a fluid. Petrographic observations show that siderite precipitated after calcite. We conclude that siderite formed from a fluid that had evolved to δ^{18}O and δ^{17}O values lower than that from which calcite precipitated (Chapter 2, this work). This confirms that the isotopic evolution of water in CR chondrites was similar to that observed within CI and CM chondrites. Although a closed system model can explain these observations, our results do not exclude parallel oxygen isotope evolution in different meteorite parent bodies as the result of fluid flow processes like that modeled by Young (2001) and Palgutta et al. (2010).

More work is needed to determine if our results apply to other CR chondrites. A finer beamed ion microprobe, such as a NanoSIMS, would allow better comparison of grain composition with isotope composition on the micron scale. Furthermore, GRO 95577 contains abundant magnetite, much of which is associated with siderite. Analyzing the oxygen isotope composition of magnetite and also the abundant phyllosilicates within GRO 95577 may reveal more information about the isotope evolution of water in GRO 95577.

7 Acknowledgements

This work is supported by NASA Grant NNG06GG37G (A.J. Brearley) and the New Mexico Space Grant (M. Tyra).

8 REFERENCES

Abreu N. M. and Brearley A. J. (2010) Early solar system processes recorded in the matrices of two highly pristine CR3 carbonaceous chondrites, MET 00426 and QUE 99177. *Geochimica et Cosmochimica Acta* **74**, 1146-1171.

Benedix G. K., Leshin L. A., Farquhar J., Jackson T., and Thiemens M. H. (2003) Carbonates in CM2 chondrites: Constraints on alteration conditions from oxygen isotopic compositions and petrographic observations. *Geochimica et Cosmochimica Acta* **67**, 1577-1588.

Bland P. A., Jackson M. D., Coker R. F., Cohen B. A., Webber J. B. W., Lee M. R., Duffy C. M., Chater R. J., Ardakani M. G., McPhail D. S., McComb D. W., and Benedix G. (2009) Why aqueous alteration in asteroids was isochemical: High porosity ≠ high permeability. *Earth and Planetary Science Letters* **287**, 559-568.

Bonal L., Huss G. R., Krot A. N., and Nagashima K. (2010) Chondritic lithic clasts in the CB/CH-like meteorite Isheyevo: Fragments of previously unsampled parent bodies. *Geochimica et Cosmochimica Acta* **74**, 2500-2522.

Brearley A. J., Saxton J. M., Lyon I. C., and Turner G. (1999) Carbonates in the Murchison CM chondrite: CL characteristics and oxygen isotopic compositions. *Lunar and Planetary Science* **XXX**, 1301.pdf.

Brearley A. J. and Hutcheon I. D. (2000) Carbonates in the CM1 chondrite ALH84034: Mineral chemistry, zoning and Mn-Cr systematics. *Lunar and Planetary Science Conference* **XXXI**, abstract #1407.

Brearley A. J. (2006) The action of water. In: Lauretta, D. S., Leshin, L. A., and McSween, H. Y. Eds.), *Meteorites and the Early Solar System II*. University of Arizona Press, Tucson, AZ.

Cassidy W. A. and Whillans I. M. (1988) *Workshop on Antarctic Meteorite Stranding Surfaces*. Lunar and Planetary Institute, Houston, TX.

Cherniak D. J. (2010) Diffusion in carbonates, fluorite, sulfide minerals, and diamond. *Reviews in Mineralogy and Geochemistry* **72**, 871-897.

Choi B. G., Ahn I., Ziegler K., Wasson J. T., Young E. D., and Rubin A. E. (2009) Oxygen isotopic compositions and degree of alteration of CR chondrites. *Meteoritics & Planetary Science* **44 (supplement)**, A50.

Clayton R. and Mayeda T. (1999) Oxygen isotope studies of carbonaceous chondrites. *Geochimica et Cosmochimica Acta* **63**, 2089-2104.

Clayton R. N. and Mayeda T. K. (1977) Oxygen isotopic compositions of separated fractions of the Leoville and Renazzo carbonaceous chondrites. *Meteoritics* **12**, 199.

Clayton R. N. and Mayeda T. K. (1984) The oxygen isotope record in Murchison and other carbonaceous chondrites. *Earth and Planetary Science Letters* **67**, 151-161.

Cody G. D., Alexander C. M. O. D., Yabuta H., Kilcoyne A. L. D., Araki T., Ade H., Dera P., Fogel M., Militzer B., and Mysen B. O. (2008) Organic thermometry for chondritic parent bodies. *Earth and Planetary Science Letters* **272**, 446-455.

de Leuw S., Rubin A. E., and Wasson J. T. (2010) Carbonates in CM chondrites: Complex formational histories and comparison to carbonates in CI chondrites. *Meteoritics & Planetary Science* **45**, 513-530.

Fisler D. K. and Cygan R. T. (1998) Cation diffusion in calcite: Determining closure temperatures and the thermal history for the Allan Hills 84001 meteorite. *Meteoritics & Planetary Science* **33**, 785-789.

Fisler D. K. and Cygan R. T. (1999) Diffusion of Ca and Mg in calcite. *Am. Miner.* **84**, 1392-1399.

Garrels R. M. and Christ C. L. (1965) *Solutions, Minerals, and Equilibria*. Harper and Rowe, New York.

Grady M. M., Wright I. P., Swart P. K., and Pillinger C. T. (1988) The carbon and oxygen isotopic composition of meteoritic carbonates. *Geochimica et Cosmochimica Acta* **52**, 2855-2866.

Grossman J. N. (1998) The Meteoritical Bulletin, No. 82, 1998 July. *Meteoritics & Planetary Science* **33**, A221-A239.

Helsen M. M., Van de Wal R. S. W., and Van den Broeke M. R. (2007) The isotopic composition of present-day Antarctic snow in a Lagrangian atmospheric simulation. *Journal of Climate* **20**, 739-756.

Hem J. D. (1985) Study and interpretation of the chemical characteristics of natural water. In: Survey, U. G. (Ed.). US Geological Survey.

Johnson C. A. and Prinz M. (1993) Carbonate compositions in CM and CI chondrites, and implications for aqueous alteration. *Geochimica et Cosmochimica Acta* **57**, 2843-2852.

Jull A. J. T., Cheng S., Gooding J. L., and Velbel M. A. (1988) Rapid growth of magnesium-carbonate weathering products in a stony meteorite from Antarctica. *Science* **242**, 417-419.

Kallemeyn G. W. and Wasson J. T. (1982) The compositional classification of chondrites: III. Ungrouped carbonaceous chondrites. *Geochimica et Cosmochimica Acta* **46**, 2217-2228.

Krot A. N., Meibom A., Weisberg M. K., and Keil K. (2002) The CR chondrite clan: Implications for early solar system processes. *Meteoritics & Planetary Science* **37**, 1451-1490.

Leshin L. A., McKeegan K. D., Carpenter P. K., and Harvey R. P. (1998) Oxygen isotopic constraints on the genesis of carbonates from Martian meteorite ALH84001. *Geochimica et Cosmochimica Acta* **62**, 3-13.

Lorius C. (1983) Antarctica: Survey of near-surface mean isotopic values. In: Robin, G. d. Q. (Ed.), *The Climate Record in Polar Ice Sheets*. Cambridge University Press.

Palguta J., Schubert G., and Travis B. J. (2010) Fluid flow and chemical alteration in carbonaceous chondrite parent bodies. *Earth and Planetary Science Letters* **296**, 235-243.

Rollion-Bard C. and Marin-Carbonne J. (2011) Determination of SIMS matrix effects on oxygen isotopic compositions in carbonates. *J. Anal. At. Spectrom.* **26**, 1285-1289.

Romanek C. S., Jiménez-López C., Navarro A. R., Sánchez-Román M., Sahai N., and Coleman M. (2009) Inorganic synthesis of Fe–Ca–Mg carbonates at low temperature. *Geochimica et Cosmochimica Acta* **73**, 5361-5376.

Schrader D. L., Franchi I. A., Connolly H. C., Greenwood R. C., Lauretta D. S., and Gibson J. M. (2011) The formation and alteration of the Renazzo-like carbonaceous chondrites I: Implications of bulk-oxygen isotopic composition. *Geochimica et Cosmochimica Acta* **75**, 308-325.

Schultz L. (1986) Allende in Antarctica: Temperatures in Antarctic meteorites. *Meteoritics* **21**, 505.

Tyra M. A., Farquhar J., Guan Y., and Leshin L. A. (2007a) Using SIMS to evaluate oxygen isotopes in CM chondritic carbonate. *Lunar and Planetary Science Conference XXXVIII*, Houston, TX.

Tyra M. A., Farquhar J., Wing B. A., Benedix G. K., Jull A. J. T., Jackson T., and Thiemens M. H. (2007b) Terrestrial alteration of carbonate in a suite of Antarctic CM chondrites: Evidence from oxygen and carbon isotopes. *Geochimica et Cosmochimica Acta* **71**, 782-795.

Tyra M. A., Brearley A. J., Hutcheon I. D., Ramon E., Matzel J., and Weber P. (2009) Carbonate formation timescales vary between CM1 chondrites ALH84051 and ALH84034. *Lunar and Planetary Science Conference XL*. Lunar Planet. Inst., Houston, TX.

Tyra M. A., Brearley A. J., and Guan Y. (2010a) SIMS in-situ carbon and oxygen isotopic composition of dolomite and calcite in CM1/2 ALH 84049. *73rd annual Meteoritical Society Meeting*. Lunar and Planet. Inst., New York, NY.

Tyra M. A., Brearley A. J., Matzel J., and Hutcheon I. D. (2010b) Types and timescales of secondary carbonates in CR1 chondrite GRO 95577. *Lunar and Planetary Science Conference*.

Tyra M. A., Le Guillou C., and Brearley A. J. (2011) Deciphering the history of carbonates and associated minerals during secondary alteration within CR1 GRO 95577. *Meteoritical Society Meeting*. LPI, London.

Watanabe O., Jouzel J., Johnsen S., Parrenin F., Shoji H., and Yoshida N. (2003) Homogeneous climate variability across East Antarctica over the past three glacial cycles. *Nature* **422**, 509-512.

Weisberg M. K., Prinz M., Clayton R. N., and Mayeda T. K. (1993) The CR (Renazzo-type) carbonaceous chondrite group and its implications. *Geochimica et Cosmochimica Acta* **57**, 1567-1586.

Weisberg M. K., Prinz M., Clayton R. N., Mayeda T. K., Grady M. M., and Pillinger C. T. (1995) The CR chondrite clan. *Proc. NIPR Symp. Antarct. Meteorites* **8**, 11-32.

Weisberg M. K. and Huber H. (2007) The GRO 95577 CR1 chondrite and hydration of the CR parent body. *Meteoritics & Planetary Science* **42**, 1495-1503.

Young E., Ash R., England P., and Rumble D. (1999) Fluid flow in chondritic parent bodies: Deciphering the compositions of planetesimals. *Science* **286**, 1331-1335.

Young E. D. (2001) The hydrology of carbonaceous chondrite parent bodies and the evolution of planet progenitors. *Phil. Trans. R. Soc. Lond. A.* **359**, 2095-2110.

Zheng Y. F. (1999) Oxygen isotope fractionation in carbonate and sulfate minerals. *Geochem J* **33**, 109-126.

Zheng Y. F., Satir M., Metz P., and Sharp Z. D. (1999) Oxygen isotope exchange processes and disequilibrium between calcite and forsterite in an experimental C-O-H fluid. *Geochimica et Cosmochimica Acta* **63**, 1781-1786.

Zolensky M. E., Bourcier W. L., and Gooding J. L. (1989) Aqueous alteration on the hydrous asteroids - Results of Eq3/6 computer-simulations. *Icarus* **78**, 411-425.

9 Tables

Table 1.Chemical and oxygen isotopic compositions of analyzed grains. Chemical data (mol% $FeCO_3$, $MnCO_3$, $MgCO_3$, and $CaCO_3$) were obtained via EPMA and isotopic data (in ‰) via SIMS. The dashed lines separate individual grains.

mineral	grain	lithology	Mg	Mn	Ca	Fe	$\delta^{18}O$	1σ	$\delta^{17}O$	1σ	$\Delta^{17}O$	1σ
siderite	g30-11-B1a@1	CR	33.51	26.24	1.91	38.35	24.36	1.38	14.51	1.07	1.85	0.97
	g30-11-B1a@2	CR	"	"	"	"	24.35	1.27	13.43	1.09	0.77	0.95
	g30-11-B1a@3	CR	"	"	"	"	22.48	1.26	13.16	1.03	1.47	0.89
	g30-11-B1a@4	CR	"	"	"	"	20.68	1.28	12.49	1.10	1.73	0.96
	g30-11-B1b@6	CR	26.45	30.05	3.49	40.01	23.03	1.31	11.78	1.15	-0.20	1.03
	g30-11-B1b@7	CR	"	"	"	"	23.53	1.29	11.87	1.04	-0.37	0.90
	g30-10-S2_1	DL	34.28	13.94	3.87	47.92	20.72	1.93	12.06	1.65	1.29	1.74
	g30-10-S2_3	DL	34.72	13.90	3.54	47.84	21.94	2.05	12.86	2.42	1.45	2.51
	g30-10-S2_6	DL	34.72	13.79	3.21	48.27	22.77	1.29	12.02	1.21	0.18	1.10
	g30-10-S2_6@1	DL	"	"	"	"	20.89	1.66	11.87	1.05	1.01	1.07
	g30-10-S2_6@2	DL	"	"	"	"	24.30	1.37	12.76	1.27	0.12	1.19
	g30-10-S2_6@3	DL	"	"	"	"	27.26	1.41	15.49	1.27	1.32	1.20
	g30-10-S3_2	DL	30.27	24.27	3.78	41.66	21.12	1.35	9.80	1.20	-1.19	1.10
	g30-10-S3_5@1	DL	26.12	22.80	6.45	44.62	24.09	1.31	13.34	1.19	0.81	1.08
	g30-10-S3_5@2	DL	"	"	"	"	24.54	1.41	14.30	1.12	1.54	1.04
	g30-10-S3_5@3	DL	"	"	"	"	22.72	1.27	12.79	1.02	0.98	0.87
	g30-15-B2-003_3	DL	30.10	23.26	4.01	42.63	19.86	1.34	10.06	1.06	-0.27	0.95
	g30-15-B2-003_4	DL	"	"	"	"	20.05	1.28	11.35	1.09	0.93	0.96
	g30-15-B2-003_5	DL	"	"	"	"	21.34	1.36	11.32	1.04	0.22	0.93
	g30-15-B2-008@0	DL	35.68	12.60	3.31	48.40	20.22	1.32	11.87	1.25	1.35	1.15
	g30-15-B2-008@1	DL	"	"	"	"	17.42	1.38	9.45	1.16	0.39	1.07
	g30-15-B2-008@2	DL	"	"	"	"	15.36	1.35	8.47	1.12	0.48	1.01
	g30-15-B2-008@3	DL	"	"	"	"	18.41	1.46	10.58	1.08	1.00	1.01
	g30-15-B2-008@4	DL	"	"	"	"	18.99	1.49	9.71	1.09	-0.16	1.04
	g30-15-B2-009@1	DL	31.47	19.77	4.10	44.65	21.16	1.26	9.44	1.03	-1.57	0.88
	g30-15-B2-009@2	DL	"	"	"	"	19.44	1.32	9.87	1.12	-0.24	1.00
	g30-15-B2-009@3	DL	"	"	"	"	18.07	1.25	9.16	1.09	-0.23	0.95
	g30-15-B2-009@4	DL	"	"	"	"	17.56	1.23	8.80	1.06	-0.33	0.90
	g30-15-B2-005@0	DL	32.37	22.06	3.56	42.00	21.83	1.45	12.54	1.07	1.19	1.00
	g30-15-B2-005@1	DL	"	"	"	"	20.57	1.23	12.00	1.09	1.31	0.94
	g30-15-B2-005@2	DL	"	"	"	"	20.94	1.28	12.00	1.17	1.12	1.04
	g30-15-B2-005@3	DL	"	"	"	"	22.66	1.27	12.05	1.03	0.26	0.88
calcite	g30-11-b1a	CR	0.27	0.13	98.38	1.23	26.36	1.18	14.43	1.23	0.72	1.72
	g30-11-b1b	CR	0.20	0.28	98.42	1.10	33.04	1.20	17.04	1.22	-0.15	1.71
	g30-11-b1c	CR	0.30	0.09	98.55	1.06	30.27	1.19	16.83	1.25	1.09	1.73
	g30-10-s001	DL		N/A			28.34	1.22	17.21	1.23	2.47	1.73
	g30-10-s4	DL		N/A			33.99	1.47	17.93	1.62	0.26	2.07
	g30-10-s5	DL		N/A			26.77	1.13	15.99	1.21	2.07	1.70
	g30-10-s6	DL	0.22	0.28	98.50	0.99	23.66	1.39	14.09	1.32	1.78	1.83
	g30-16(14)-b1	DL		N/A			32.34	1.18	17.01	1.22	0.19	1.71
	g30-18-b1	DL		N/A			31.41	1.15	18.04	1.19	1.70	1.69
	g30-18-b2	DL		N/A			31.96	1.20	16.42	1.20	-0.20	1.70

10 Figures

Figure 1. Examples of carbonates within GRO 95577. Backscatter electron images 1a and 1b are from GRO 95577,53 and images 1c-1e are from GRO 95577,30. The different carbonate minerals are spatially associated with each other and also with magnetite (m) framboids (Fig 1e) and pyrrhotite (p). Note that siderite (s) is often fragmented and patchy, although the grains shown in Figures 1a and 1c have clean regions. Calcite (c), and dolomite (d) are also indicated.

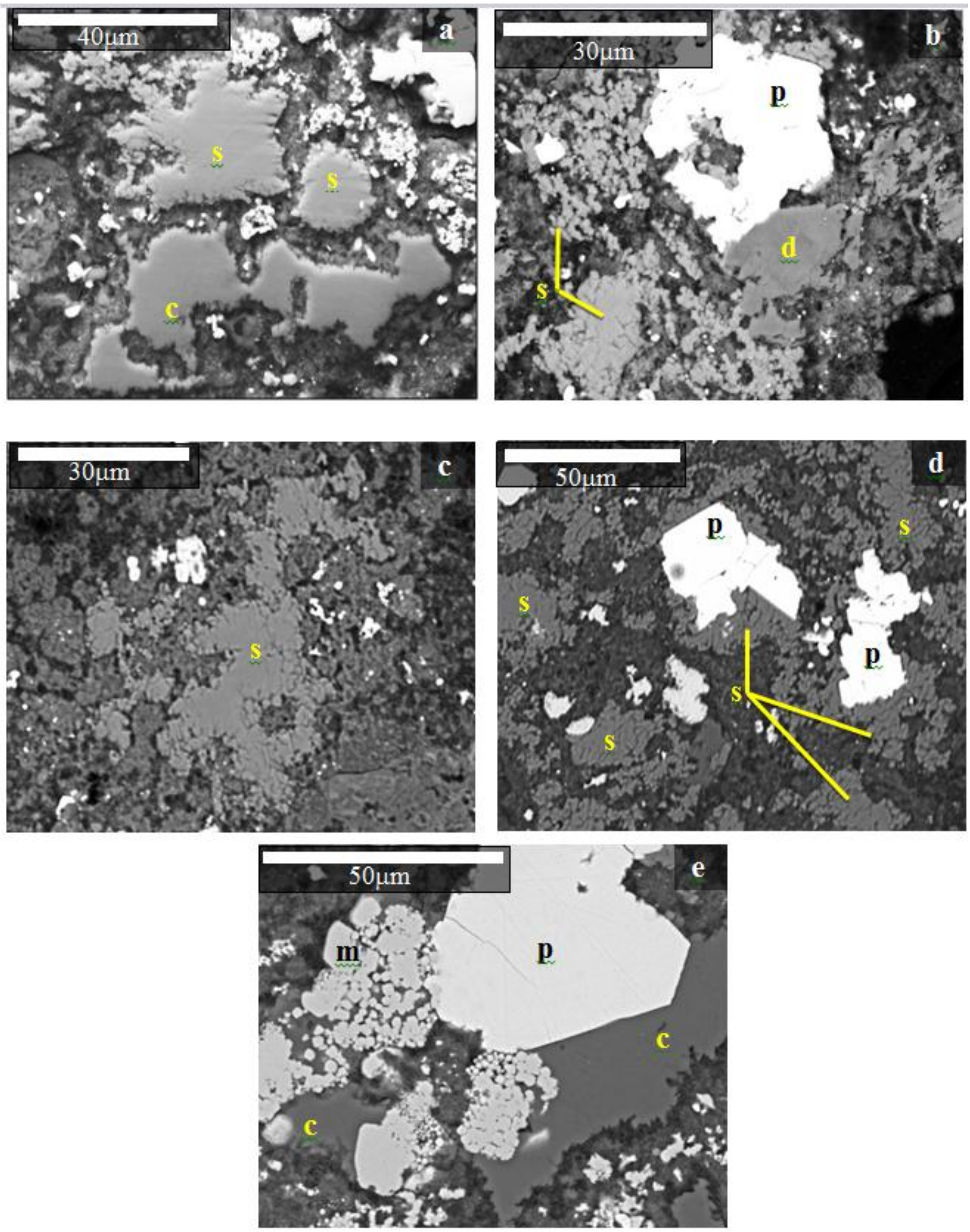

Figure 2. BSE images of SIMS spots in carbonate grains. Figure 2a shows two SIMS spots in a ~200 µm diameter calcite; Figures 2b to 2d show SIMS spots in siderite. Calcite (c) grains were far larger than siderite (s). Therefore, precise placement of the ion beam was necessary for SIMS analysis on siderite minerals. We monitored Si closely when placing SIMS spots, and employed apertures where necessary to narrow the beam and ensure only carbonate was being analyzed. BSE images of all SIMS spots in siderite are shown in the Appendix.

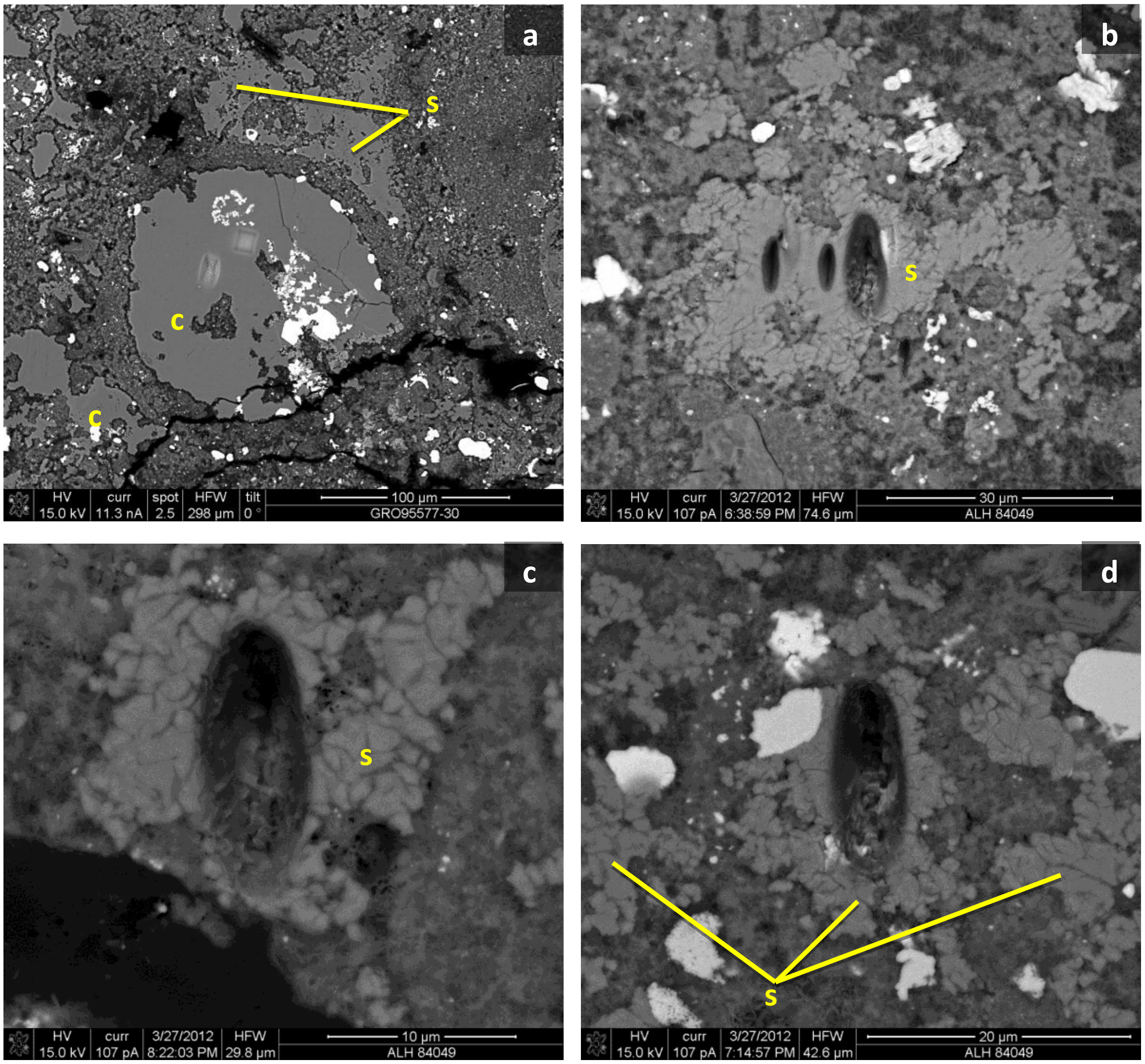

Figure 3. Comparison of siderite grain chemistry and oxygen isotopic composition. No significant correlations are apparent between the elemental composition (Mg, Fe, Ca, and Mn) of siderite with either δ^{18}O (a through d) or Δ^{17}O (e). At a 1σ error level, compositionally induced matrix effects are not apparent over the compositional ranges of cations present in the siderite. Chemical composition does not correlate with oxygen isotope composition within single grains.

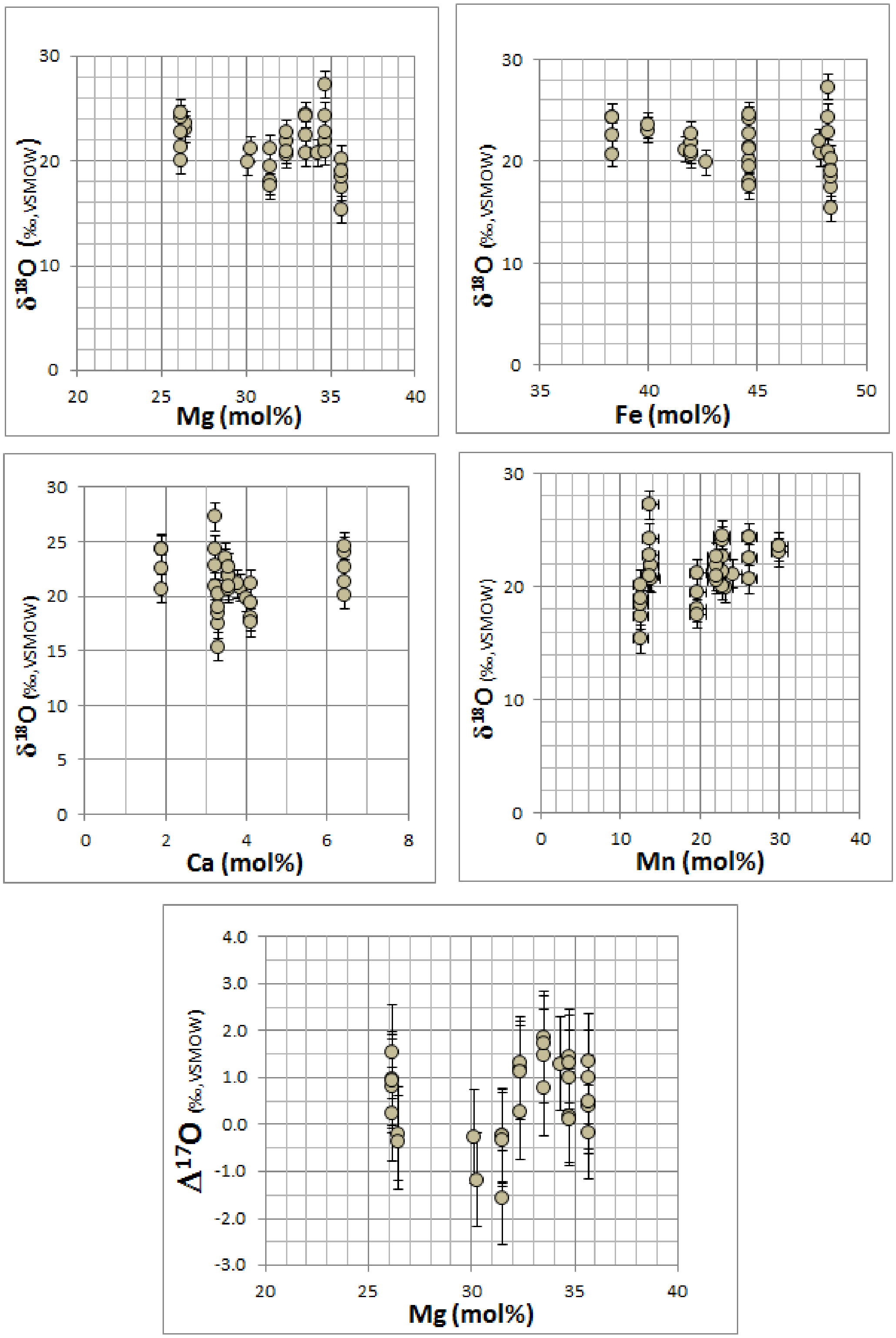

Figure 4.Oxygen isotopic compositions of calcite and siderite. Both lie on the terrestrial fractionation line which could indicate that they formed cogenetically. This is unlikely, however, as their fractionation factors could not account for differences observed between the two carbonate minerals. Either there were large temperature differences between the times of formation from fluids of identical compositions, or an evolving source fluid is possible. The shaded ellipse illustrates ion microprobe results of magnesite and dolomite in Isheyevo (CB/CH chondrite) lithic clasts (Bonal et al., 2010). These carbonates overlap our results for calcite. All values reported in reference to the VSMOW isotope standard.

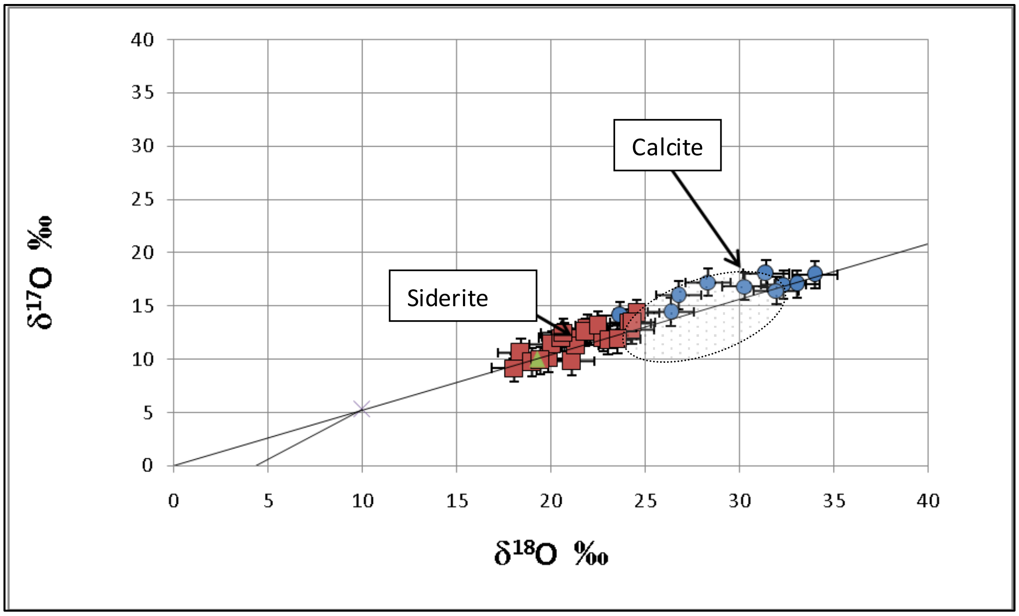

Figure 5. Diagram that contrasts the hypothetical oxygen isotopic composition of carbonate precipitated from Antarctic water as a result of terrestrial weathering and measured carbonate from this study. Given a hypothetical water composition (see text), terrestrial siderite (red) and calcite (blue) would form with compositions near the origin in the figure (both axes are relative to VSMOW). Measured siderite and calcite compositions, however, have higher $\delta^{18}O$ values than that possible in Antarctic conditions. This confirms the chemical arguments of Tyra et al. (Chapter 2, this work) that the carbonates in GRO 95577 are extraterrestrial in origin.

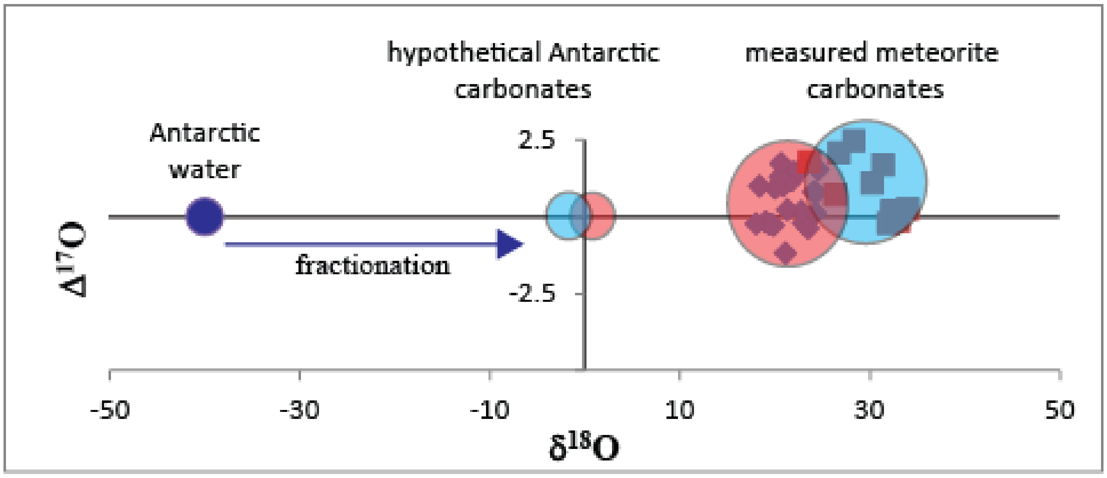

Figure 6. Diagram illustrating a simplified model, derived from Benedix et al. (2003), that gives an overview of the projected precipitation of Ca-carbonate and siderite in GRO 95577. The initial oxygen isotopic composition of water is at the blue ‘i’ and ends at ‘f’; the slope of this line is exaggerated to better illustrate that the trajectory of water is actually only slightly steeper than that of a mass dependent line. Matrix phyllosilicates would form along the parallel dotted line, their composition changing in tandem with water. Carbonates would form to the right of the expected matrix composition along mass dependent fractionation lines. Ellipses that represent carbonate isotope compositions are caused by temperature variation and/or composition affecting fractionation. The inset shows that as more phyllosilicates form, the whole rock composition of the chondrite would follow the trajectory outlined in red towards the final phyllosilicate value. The three arrows are guidelines that show the relationship with anhydrous silicate and bulk phyllosilicate compositions at three points in time, initial (i), midway through alteration, and at the end of alteration (f).

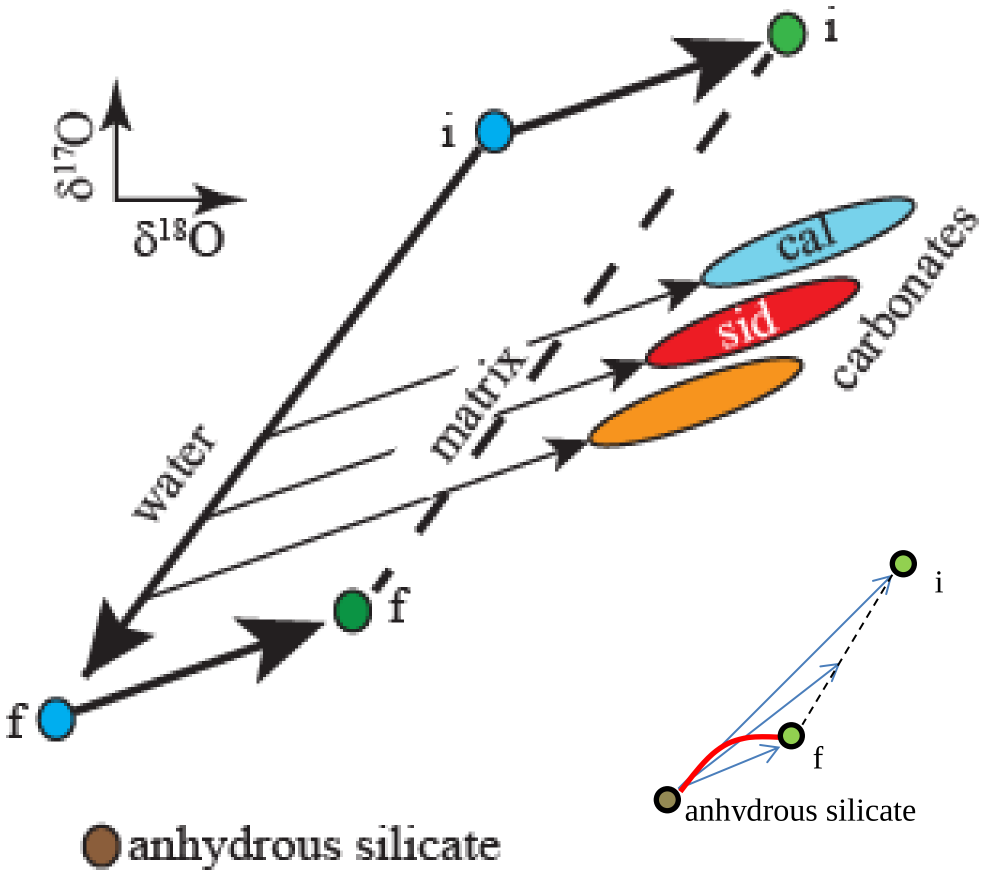

11 APPENDIX

Backscattered electron images of SIMS spots of analyzed siderite grains. Every grain shown in Table 1 is included. Below are the grain designations of each figure and a description of the spot.

a. G30-11-b1a, clean spot.
b. G30-11-b1b, mostly good spot, although slight overlap on one side (<10% overlap)
c. G30-10-s2, three clean spots
d. G30-10-s3, three clean spots. Middle spot not included in Table 2.
e. G30-15-b2, tiny sulfide inclusion visible (white), but should not affect oxygen isotopic analysis. Otherwise, clean.
f. G30-15-b2-008, interior is clean, but slight overlap with phyllosilicate on periphery.
g. G30-15-b2-009, slight overlap on periphery, but beam was focused on deep area of pit (near top).
h. G30-15-b2-005, slightest overlap of sulfide grain, but otherwise clean.

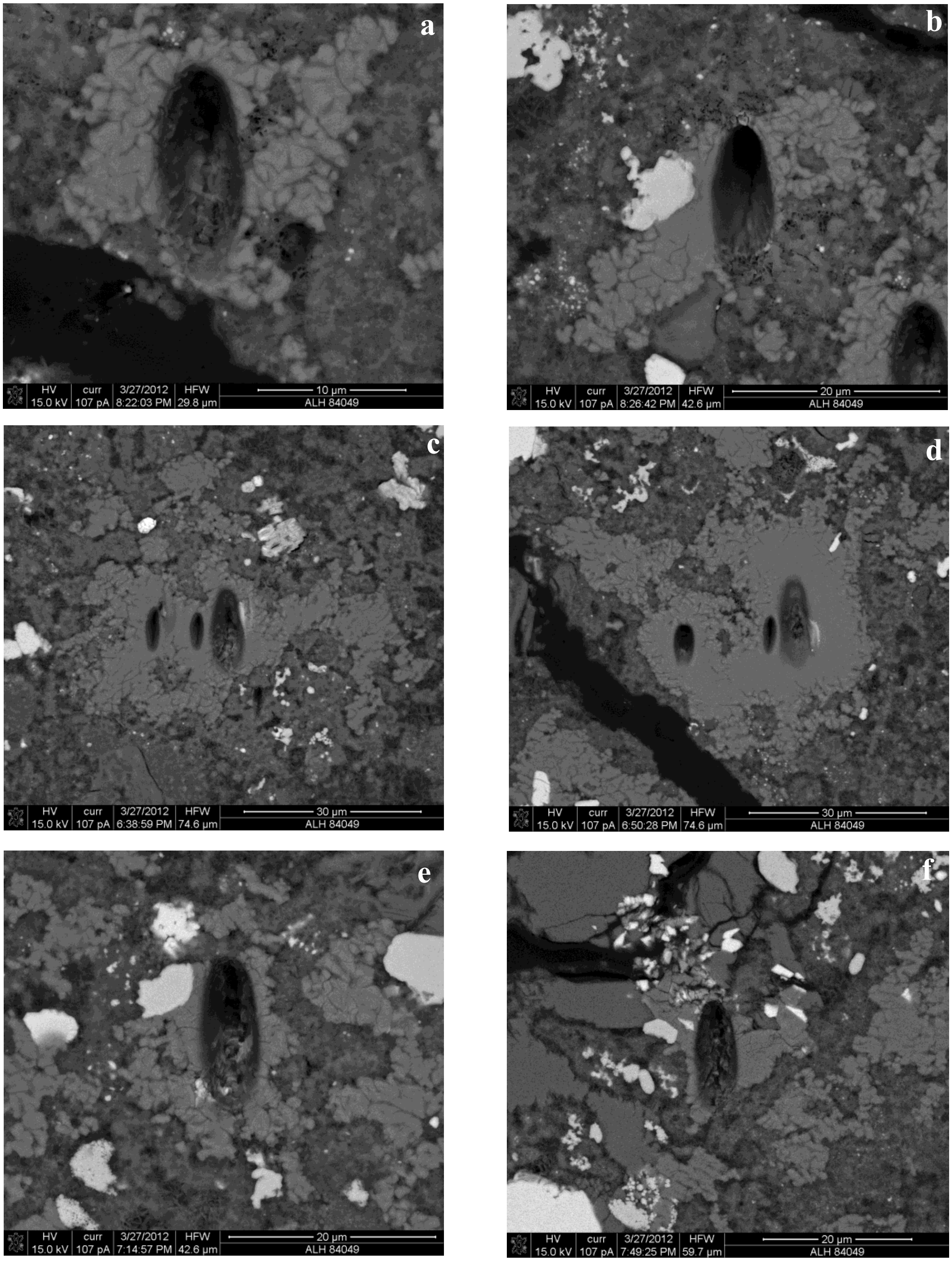
a
HV 15.0 kV
curr 107 pA
3/27/2012 8:22:03 PM
HFW 29.8 µm
10 µm
ALH 84049
b
HV 15.0 kV
curr 107 pA
3/27/2012 8:26:42 PM
HFW 42.6 µm
20 µm
ALH 84049
c
HV 15.0 kV
curr 107 pA
3/27/2012 6:38:59 PM
HFW 74.6 µm
30 µm
ALH 84049
d
HV 15.0 kV
curr 107 pA
3/27/2012 6:50:28 PM
HFW 74.6 µm
30 µm
ALH 84049
e
HV 15.0 kV
curr 107 pA
3/27/2012 7:14:57 PM
HFW 42.6 µm
20 µm
ALH 84049
f
HV 15.0 kV
curr 107 pA
3/27/2012 7:49:25 PM
HFW 59.7 µm
20 µm
ALH 84049

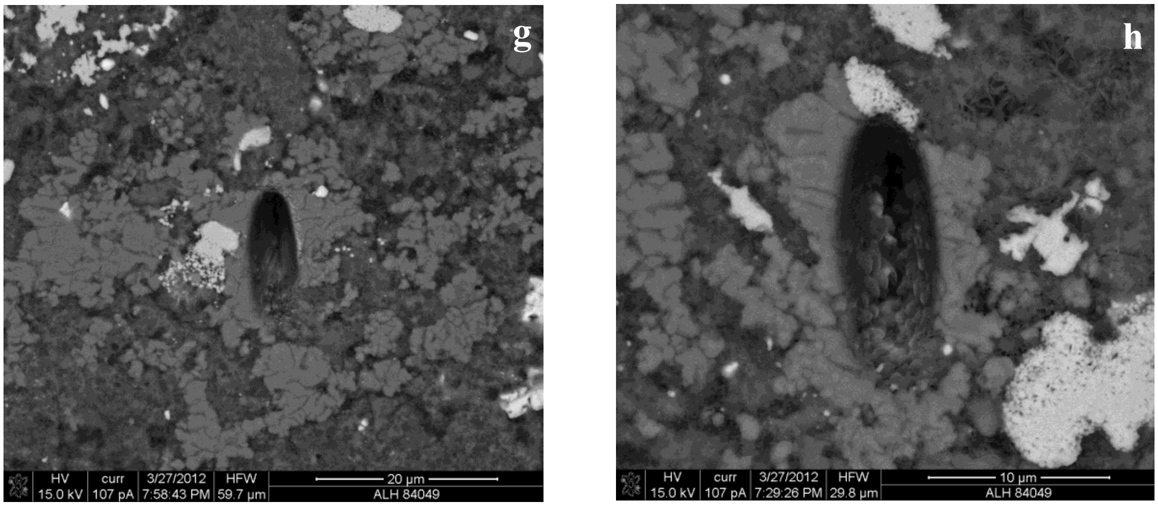
g
HV
15.0 kV
curr
107 pA
3/27/2012
7:58:43 PM
HFW
59.7 µm
20 µm
ALH 84049
h
HV
15.0 kV
curr
107 pA
3/27/2012
7:29:26 PM
HFW
29.8 µm
10 µm
ALH 84049